MULTIPARAMETER ENGINEERING OF LAYERED COMPOSITES

by

Jian Zhu

A dissertation submitted in partial fulfillment
of the requirements for the degree of
Doctor of Philosophy
(Chemical Engineering)
in the University of Michigan
2013

Doctoral Committee:

Professor Nicholas Kotov, Chair
Professor Mark A. Burns
Associate Professor A. John Hart
Assistant Professor Charles W. Monroe

To my parents, *ZHU guiqing and Yu cuihua*

献给我的父亲 朱桂清 和 母亲 于翠华

ACKNOWLEDGMENTS

First and foremost I owe forever my sincerest gratitude to my advisor Prof. Nicholas A. Kotov. He guided me into the wonderful world of nanotechnology, encouraged me to overcome the setbacks, gave me the freedom to execute new ideas, and helped me polish the research skills and expertise. He set a good example for me as a brilliant researcher, innovator and leader. Without his selfless support, I cannot realize my full potential as a PhD researcher.

The research presented in this dissertation is only possible due to the assistance from many places across the university. Dr. Kai Sun, Dr. Haiping Sun, and Dr. Ying Qi in EMAL provided me training and support for most equipment used for this thesis. Prof. Adam Matzger and Dr. Antek Wong-Foy in Department of Chemistry gave me a great deal of assistance for XRD analyses. Prof. Ellen Arruda and her graduate student Keqing Cao in the Department of Mechanical Engineering provided me the generous assistance for mechanical measurement. My close collaboration with Prof. Joerg Lahann's research group also contributed to the success of this thesis. In addition, Prof. John Hart, Prof. Mark A. Burns, and Prof. Charles W. Monroe in my dissertation committee deserve my genuine gratefulness for their assistance and useful comments on my research.

Further, I would like to thank former and current colleagues in Prof. Kotov's research groups. Dr. Bongsup Shim, Dr. Paul Podsiadlo, Dr. Edward Jan, Dr. Peter Ho

gave me a lot of aid when I just started as a graduate student. Dr. Ming Yang, Dr. Yunlong Zhou and Dr. Bongjun Yeom closely collaborated with me for several projects and stimulated a number of good scientific discussions. I enjoyed the beneficial research environment with Christine M. Andres, Huanan Zhang, Yeomseob Kim, Xinyu Li, Terry Shy, Yichun Wang, Tao Hu, Guangxiang Ma, Xiaoming Hao, Yajie Liu and Jishu Han. I thank the undergraduate researcher, Douglas Watts, for his assistance in one of my projects. Of the specific mention here is Christine M. Andres, who not only provided support for my research projects, but presented me the wonderful American cultures and encouraged me as a true friend to overcome my limits in various aspects.

Finally, I would like to acknowledge my family and friends. My parents, ZHU Guiqing and YU Cuihua always stand behind me and give generous love and encouragement throughout my pursuit of dream and happiness. My roommates, Vichet In, Shashank Kadetotad, and Carey Wiese, gave me a home-like environment and stimulated my interest in business, entrepreneurship, and love. My friends, Yu Chen, Hao Chen, Ming Qin, Hongliang Xin, Jing Liu, Yuhui Shi, Xu Wang, made my stay in Ann Arbor a wonderful experience. I am deeply grateful for every support they have offered.

TABLE OF CONTENTS

LIST OF FIGURES

Chapter I

Chapter II

Chapter III

Chapter IV

LIST OF TABLES

ABSTRACT

Many technological challenges facing humanity require the development of high performance nanocomposites. The desirable multiparameter combination of those composites relies on the inclusion of high content well-dispersed nanomaterials with tailored interface and ordered architecture. Natural biomaterials, such as wood, bone, silk, and nacre, exemplify such a design strategy, and accordingly give rise to satisfactory collective properties. Biomimicking such materials to obtain appealing synthetic composites, however, requires advanced manufacturing techniques with multiscale controllability, adaptability and scalability.

This thesis shows that layer-by-layer assembly (LBL) and its alternatives as effective and versatile approaches to fabricate layered nanocomposites with attractive multifunctional properties. First, an LBL assembled single walled carbon nanotube (SWNT) transparent coating is designed as an indium tin oxide replacement. A new type of SWNT doping by sulfonated polyetheretherketone (SPEEK) led to a conductivity of 1.1×105 S/m. This property was better than those of other conventional SWNT composites and translated to a surface conductance of 920 ohms/sq and transmittance of 87%. The coating also revealed high temperature resilience up to 500 °C, low roughness of 3.5 nm, and high strength of 366 MPa. Next, a combination of better strength and toughness than other layered assemblies was shown for polyvinyl alcohol (PVA)

/reduced graphene composites made by both LBL and vacuum assisted flocculation (VAF) technique. Composites by those methods showed similarities in the mechanical properties, but striking difference in the in-plane electrical conductivity. These observations were explained in terms of structures and interfaces. A unique pseudonegative thermal expansion was identified in the graphene oxide (GO) layered assemblies due to fast water exchange with the environment. This property was exploited to tune the thermal expansion of PVA/GO composites through VAF. Finally, aramid nanofiber (ANF) hydrogel network was constructed by a solvent-exchange process. This network was impregnated with epoxy by a gelation-assisted LBL technique. The resulting ANF/epoxy composite demonstrates an ultimate strength of 505 MPa, and toughness of 50.1 MJ/m3 with high damping property and close-to-zero thermal expansion. Either the strength or toughness is higher than those of quasi-isotropic carbon or aramid microfiber reinforced composites.

CHAPTER I

Introduction

1.1 A Historical Perspective of Composites

One of the hallmarks of human history is the appearance of innovative materials in different eras to boost productivity and efficiency. The name of the material is even used to represent the related historic stage, such as the Stone Age, Bronze Age and Iron Age.[1] In the modern time, a myriad of new materials are desired to satisfy the demands of industrial and information revolution. Among those modern materials, composites receive tremendous attention due to their high performance. A composite is defined as a heterogeneous combination of two or more materials. Monolithic materials, such as metal, ceramic, or polymer, cannot deliver the range of performance needed in many critical situations.[2] By combining two materials together, their individual properties can be synergized to get far better characteristics.

The 20th century has witnessed the development of modern composite materials. Palucka et al. have characterized this period into four generations.[3] The first generation (1940s) is characterized by the discovery of glass fiber and its reinforced composites. The second generation (1960s) is marked by the better performance composites made from carbon and aramid fiber. The third generation (1970s &1980s) aimed to search for new application markets and methods to synergize the properties. The fourth generation

(1990s) is the development of nanocomposites and the application of biomimetic strategies. Those developments of composite materials was largely driven by 1) high-strength, low weight materials for aerospace industry and military 2) expansion of polymer market for new applications 3) the impetus to realize the theoretical strength of certain materials.

The microfiber reinforced composites are well-developed in the first three historic generations. E-glass, carbon, aramid (Kevlar 49) and polyethylene (Spectra 900) microfibers are typical materials used to combine with a variety of thermoplastic and thermosetting polymers.[4] Those microfibers typically have high modulus and tensile strength with low density. Carbon fiber, for example, has tensile modulus (E) of 231GPa, and ultimate strength (σ_u) of 3.65 GPa.[4] Their integration with epoxy can give rise to E of 215 GPa, and σ_u of 1.24 GPa.[4] Those performances can be better than or comparable to the best steel, aluminum, titanium, and nickel alloys but with much less density.[4] The availability of a range of matrix materials offers the flexibility of material design process. When a set of functions are needed for certain applications, one can combine different resins and reinforcements for the specific requirements. This "materials by design" process for composites can be a distinct advantage over other materials.[3]

The introduction of nanomaterials into composites field generate new excitement over high performance and multifunctional materials, which is the focus of fourth generation development of composites. Nanomaterials are materials with one or more dimensions in the nanometer range. The associated quantum effect leads to such materials not only with superior mechanical properties, but with interesting thermal, electrical, optical and other properties as well. Carbon nanotube, a sheet of carbon atoms

rolled into a long hollow cylinder, can exhibit E of 0.64TPa, and σ_u of 37 GPa,[5] which are 3 and 10 times higher than that of carbon fibers, respectively. Its thermal conductivity is higher than diamond, and electrical conductivity is close to copper.[6] Its thermal stability is up to 2800°C in vacuum, and optical absorption can be easily tuned by CNT types[7] or other external stimuli.[8] All those characteristics lead to applications of CNT in various fields including high strength/high modulus materials, energy storage devices, electronic systems, biosensors, and drug delivery systems.

The nanomaterials' greater interfacial interaction with the matrix ascribing to high ratio of their surface area to volume leads to performance enhancement even at very low reinforcement volume fractions. Toyota researchers pioneered the nylon-clay nanocomposite technology in the early 1990s. At only 4.2wt% clay, the E doubled, and σ_u was increased by more than 50% in comparison to nylon.[9, 10] However, few nanocomposites till now can match up with the mechanical properties of microfiber reinforced composites even though they can have other advanced electrical or optical properties. The reasons include insufficient dispersion, alignment, and low volume fraction of the nanoreinforcement as well as the poor bonding and load transfer interfaces with the matrices.[11] The high surface areas of nanomaterials make them easy to agglomerate with each other. Thus it is extremely challenging to include large fraction of nanomaterials in the composites. Mechanical properties usually show a maximum at a very low reinforcing content, and gradually degrade with further increase of nanomaterials.[12, 13] The agglomerated reinforcing phase tends to be split when subjected to external force, thus causing the premature failure.

Such a challenge is associated with the technology to process and manufacture the nanocomposites. Using traditional compounding techniques to prepare a homogenous dispersion of nanomaterials in a polymer matrix is very difficult due to the strong tendency for those materials to agglomerate. Therefore, developing the new manufacturing technologies able to scale-up for commercialization will be one of the biggest challenges towards next-generation nanocomposite development.

1.2 Bioinspired Approach towards Nanocomposites Research

Natural composites, such as mollusk shells, bones, and wood, closely and elegantly associate different components to build advanced structural materials with outstanding mechanical behavior.[14] Those composites exemplify a perfect nanocomposite model taking into account of the good dispersion and alignment, high content nano building blocks and their interfaces. The association of compositional and architectural engineering makes those natural composites amazing. Despite the limited resources from natural environment, biological materials fulfill their specific demands by evolving the hierarchical structures. For instance, nacre is a kind of sandwich material made of layers of aragonite ($CaCO_3$) nanoplatets (95 vol%) alternating with organic layers of proteins (5 vol%).[15] The laminated architecture together with optimum interface shear force makes the fracture strength and toughness 20-30 times higher than synthetically produced monolithic $CaCO_3$.[14]

The amazing feature of biological material is not an exceptional single property. In fact, the fracture strength or toughness alone can be easily matched with synthetic materials. However, the concept of combing different properties together, especially the

generally mutually exclusive ones, such as the strength and toughness, is remarkably attractive. Without appropriate fracture resistance, the strong and hard structural materials can have little use.[16] In addition to nacre, other biological materials, such as bone,[17, 18] silk[19, 20] and cuticular coating of byssal threads[21, 22] can also effectively manage this property trade-off. Despite much effort has been into studying those hierarchical structures of biological properties, it is still challenging even for today to completely copy nature's wonderful designs and performances.[23] In addition to the magnificent combination of mechanical behaviors, nano/micro architecture of the natural materials has been shown to provide unusual optical,[24] magnetic,[25] actuating[26] and surface[27] properties.

This structure induced optimum combination of properties for natural materials indicates pathways to obtain high-performance bio-inspired nanocomposites with a whole new set of unprecedented properties.[28] This implication actually coincides with the multifunctionality desired for the next generation nanocomposites. Materials in the Modern Age are needed to meet a wide range of energy efficient applications with light weight, high mechanical strength, required color, electrical, thermal properties and environmental stability. Applications can be as diverse as biological implants, electronic packages, flexible displays, aircraft components, and energy generating /storage devices. Multifunctional nanocomposites by design require platform technologies to fabricate nanocomposites with similar biological architectures.

Nature uses spontaneous association of molecules into stable structures in the design of biological hybrid materials. This molecular self-assembly can rely on all sorts of non-convalent interactions, such as electrostatic interaction, hydrogen bonds, van der

Waals interactions to form stable linkage of molecules into large scale structures. This process inspired an artificial engineering process, layer-by-layer (LBL) assembly.[29, 30] With this approach, a transparent clay nanocomposite with record-high strength (σ_u=400 MPa) and stiffness (E=106 GPa) was obtained.[31] A similar LBL deposition approach assisted by spin-coating can lead to chitosan/alumina nanosheets composites with high strength (σ_u=300 MPa) and ductility (ε~ 20%).[32] In addition to molecular self-assembly approach, nature also uses proteins as templates to grow hybrid structures,[15] material scientists can also use templates, or precisely a percolation network consisting of nanomaterials in which they insert organic or metal matrices. An alumina scaffold with lamellar pores formed by freeze casting[33] was infiltrated with polymethyl methacrylate. The final hybrid material has high yield strength and fracture toughness similar to those of aluminum alloys.[34]

1.3 Towards optimal multiparameter engineering

Understanding structure and property relationship is essential for engineering nanocomposites with desired properties. Here, I review several microstructure characteristics important for material design.

1.3.1 Mechanical properties.

A material's Young's modulus (E), ultimate strength (σ_u), toughness (K) are essential mechanical features for engineering design. These parameters can be obtained by a uniaxial tensile test. The nominal stress (σ) is defined by force per unit initial area, which is the internal resisting stress applied to avoid sample breakage. The nominal strain (ε) is the elongation divided by the initial length of the sample. At the beginning of a

stress-strain curve, σ is linearly related to ε by a constant E obeying Hooke's Law. Since the polymer or polymer nanocomposite is not pure elastic solid, the overall mechanical behavior is not linear. An elastic region can be followed by a plastic region, and then fracture. The ultimate strength (σ_u) is the maximum stress that a material can withstand before fracture. The work done during stretching the film is stored (elastic region) or dissipated (plastic region) in the deformed material. This quantity can be calculated by integrating the area under the stress-strain curve of a material, can be considered as the measure of the toughness (K).

Young's modulus (E) and Elasticity E is mainly dependent on the composition, structure and nature of the bonding of the constituents. It is a measure of the easiness of the deformation. The metallic, ionic, and covalent bonds are generally much stronger than the van der Waals (vdW) bonds. The polymers, where vdW interactions dominate, usually have lower E than those of metals and ceramics. The stress-strain relationship can be contributed by both the energy and entropy parts.[2] In the crystalline metal or ceramics, the structure remains essentially unchanged by the deformation, so that the energy part is predominant. In amorphous polymers, such as the rubber, the mechanical behavior can be usually defined by the entropic behavior. In a polymer nanocomposites, both energy and entropy contribution exists due to the composite nature.

On a microscopic level, the molecule movements contributing to the elasticity and thus E can differ in terms of bonding environment. In metals, ceramics, and glassy polymers, the deformation is based on the completely reversible modification of the atomic distance and angles, or stretching and rotating of molecular bonds.[35, 36] The elastomers, however, involve the uncoiling of randomly coiled polymer chains during the

elastic deformation.[2] In the polymer nanocomposites, such as PVA/graphene composite, *E* is contributed by the force to overcome 1) covalent bond in PVA backbone and graphene sheet 2) vdW or covalent bonds between PVA chains or in the PVA/Graphene interphase. In other words, the *E* is dependent on the *E* of polymer, graphene, and the strength of the interphase.

A primary challenge in composite engineering is to ensure the strong interphase between the filler and matrix. A filler surface is usually chemically modified, or coated to ensure good wetting by polymers. The poor wetting can lead to the generation of voids at the interface. The good wetting is necessary, but not sufficient to guarantee strong bonding. A pure vdW bonded interface can resort to a mechanical interlocking effect at a rough interface. The high surface area of nanofillers can especially facilitate this type of interaction. An even stronger interface can be reached by covalently crosslinking the filler and the matrix. In PVA/clay composite, glutaraldehyde can crosslink the interface to make the combination reach the theoretical modulus.[31] The upper bound of *E* that can be achieved by nanocomposites is determined by the rule of mixtures or Voigt model.

In addition to the interphase strength, alignment and high aspect-ratio of anisotropic fillers are essential for achieving high *E*. Higher aspect-ratio can lead to smaller proportion of the length to carry loads well beyond its loading carrying potential, since the tensile strength of the nanofillers are built up from each end according a shear-lag model.[37] The alignment can ensure high packing density and take advantage of the stiffer direction of the filler. It is essentially important when large fraction of fillers need to be incorporated to boost electrical or thermal functions of composites. The alignment of 2D platelets, such as graphene or clay in the plane is relatively easy, and can be

achieved by LBL assembly,[31] vacuum assisted assembly,[38] or electrically induced assembly.[39] It takes more efforts to confine 1D nanofiller into the same direction, external forces, such as shear[40] or magnetic field,[41] or assembly approaches such as Langmuir-Blodgett[42] or Langmuir-Schaefer[43] have to be used. With less demanding processing technique, 1D nanofillers can be aligned across a 2D plane get quasi-isotropic nanocomposite.

To be noted here, although E is evaluated in the linearly elastic region, elastic behavior is not always linear. Rubber, or biological materials such as actin or collagen[44] show interesting non-linear elasticity. In addition, the deformation can be drastically affected by loading history and rate, thus the stress-strain curve can be a function of time or frequency. These mechanical behaviors are attributed to the viscoelasticity associated with time-dependent microscopic processes in the deformation. Viscoelasticity can also result in different trajectories for loading and unloading, forming a hysteresis loop. A fully recoverable loop warrants the definition of elasticity. Also remember that the loop is also time/frequency dependent, and might take time to be fully recovered.

Ultimate Strength (σ_u) and *Toughness (K)* Adding stiff nanofiller into the polymer can generally increase E, however, not necessarily σ_u. A dominant factor is the number of structural defects. Those defects can come from inhomogeneity (matrix rich or filler rich region), voids, microcracks, and debonded interfaces. The number of defects can also scale with the size of the sample.[45] The defects can serve as seeds for material failure through localized stress concentration. During the stretching, the stress at the tip of a crack can lead to the propagation of a crack when exceeding the theoretical cohesive strength of the material. Multiple defects then collapse together into a larger crack and

finally a fracture. On some occasions, however, the polymer can undergo plastic deformation at the crack, and a shape crack tip can be blunted due to the plastic strain. This type of microstructure change can usually make the material tough and flaw-tolerant.

It is expected that a combination of high E and high extension or ultimate strain (ε_u) can give rise to a very high σ_u. However, it is very unusual for a material to have both of them. Unidirectional carbon fiber composites can have a σ_u of 2 GPa contributed by a high E of 142 GPa but a low ε_u of 1.3%.[46] In contrast, silk fibers typically have a σ_u of 1-2 GPa contributed by a high ε_u of 50-60% but a relatively low E of 10 GPa.[23] As discussed above, the high E is an indication of strong attractive forces even at the interface. The fracture thus occurs with little sliding of constituents against each other or a low extension, while weak interface can facilitate plastic relocation or a large extension, but a low E. Accordingly, if the aim is to exploit the high stiffness and load-bearing capacity of the nanoreinforcement, one has to engineer strong interfacial bonding. However, this strategy might make the material intolerant of defects, and cause the premature failure. On the other hand, the interfacial bonding can be engineered to be weak, so that an advancing crack gets deflected, and components can be capable of movement to absorb more stretching energy. In addition to engineering the bonding force, the hierarchical structure is important to gradually unfold the structure in the micron, submicron, nanometer, and molecular scale.[47] Strain hardening with the molecules align with each other at the final stage is important to get high σ_u.

Combining high σ_u and K in a nanocomposite similar to natural silk is vital for structural materials, since catastrophic fracture is unacceptable in most safety critical

applications.[16] A candidate composite should contain well-oriented and dispersed nanofiller. The strong covalent or ionic bonding in the interface should be controlled to a proper extent. Interfacial vdW bonds including hydrogen bonds are more suitable to give a tough material. In addition, mechanical interlocking from the large and rough surface area can be an important structural feature to explore. Hierarchical polymers, such as semicrystalline polymers, can be used as a matrix to enable multiscale unfolding of polymer chains. Thermodynamic studies for the polymer on the surface can be used to predict proper nanofiller content to avoid brittle nature.

Combining all the three parameters E, σ_u and K in a composite can be more demanding. Some of the above criteria can generally be followed. In addition, the polymer should be required to have a high modulus and strength to avoid the breakage of the chains before the plastic sliding of the components.

1.3.2 Electrical properties.

The electrical property of a polymer composite is affected by the volume fraction (φ) and the proximity of conductive fillers. Highest φ relies on the alignment to ensure the highest packing density. The dependence of conductivity (σ_c) on φ is understood as a percolation phenomenon arising from the connectivity between adjacent conductive nanoparticles. There is a percolation threshold (φ_c) at which the conductivity increases sharply and the composite is transformed into a conductor from an insulator. When $\varphi > \varphi_c$, the conductivity increases as $(\varphi-\varphi_c)^t$, where t is a critical exponent.[48] SWNT and graphene generally have a low φ_c of 0.1–0.4 vol % due to their high aspect ratio.[49, 50] Well-dispersed and exfoliated nanofillers increase the chance of forming a connective network.

The connectivity range increases with the ease of charge transport between conductive fillers. A direct contact would benefit the flow of charges. On most cases, the nanofillers are in close proximity spaced by insulating host polymer matrix. The electrical conduction can be controlled by electron hopping under the applied electric field. Sometimes, the electron hopping is also known as tunneling when no energy exchange is involved during the electron transfer from the valance to conduction band. The hopping mechanism can also contribute to the non-linear voltage-current relationship due to the effect of localized polarization and space-charge induced effects.[51] The hopping probability is dependent on the temperature, spatial tunneling distance, electronic states, and the contact barrier. By controlling those parameters, one could control and optimize the conductivity of nanocomposites.

When conductive fillers are physically in contact with each other, the nanocomposite exhibits band-type conduction.[51] This conduction mode can be distinguished from the previous electric conducting mode by comparing the conductive behaviors under DC and AC excitations. The AC conductivity from hopping mechanism invariably exhibits higher AC conductivity with increasing frequency.[52]

Optimal σ_c can thus be achieved by placing large volume of well oriented and dispersed conductive nanofillers with minimal contact barrier in the polymer. The ideal condition is achieved when conductive fillers can have bare contact with each other. Conventional mixing and casting, however, usually covers the conductive nanofiller with a thin layer of insulating coating. Methods such as layer-by-layer assembly[53] or back-diffusion of polymers into a percolation conductive network[54] can lead to some degree of direct contact.

Combining high mechanical and electrical properties together in a composite is by no means an easy task. Including polymers into the conductive network invariably decreases the conductivity due to the reduction of contacts. Polymer is nevertheless needed to increase the toughness or strength of the conductive filler network. To minimize the effect of tradeoff, the intrinsic conductivity of conductive fillers, such as carbon nanotube or graphene, can be improved by small molecule, oxide, or polymer dopants.[53, 55, 56] The general approaches to optimize the mechanical and electrical properties, such as the alignment and dispersibility of nanofillers, are similar. Making the performance lean more towards either mechanical or electrical properties is dependent on the interfacial engineering. The tradeoff between those two properties relies on the desired requirements in the application.

1.4 The Layer-by-Layer (LBL) Assembly Technique for Multifunctional nanocomposites

As mentioned in the last section, the LBL assembly technique is inspired by the molecule assembly process ubiquitous in biological material synthesis. This approach is based on the sequentially alternative adsorption of polymers or nanomaterials with complementary interactions on a substrate. As a bottom-up assembly method with deposition of several nanometers thick material at a time, it offers fine control over structures of tunable functional materials as well as incorporation of a variety of desired components at a large content with ease. With the sequential deposition fashion, this method is likely to generate a stratified structure on the substrate with good alignment and interfacial interactions. Therefore, this technique can be an effective and universal

pathway for making multifunctional nanocomposites with architecture similar to biological materials. LBL is a major focus of this thesis, thus it requires adequate review in this section.

The LBL concept was first demonstrated by Iler[57] in 1966 for oppositely charged particles, but didn't receive interest in the scientific community until Decher's pioneering work[29, 30] on the alternative assembly of oppositely charged polyelectrolytes in early 1990s. This area has grown at an unusually rapid pace since then, introducing a broad range of new fundamental sciences and applications. Several complementary interactions have been discovered to build multilayer films. Those interactions include electrostatic forces[30], charge transfer interactions[58], coordination chemistry[59], hydrogen bonding[60] or stepwise covalent bonding[61] and many more.[62, 63] The thickness of the film is usually linearly dependent on the deposition cycles. This linearity is related with the outer surface adsorption of species,[64] which are kinetically "locked" to result in charge reversal or overcompensation of interactions. Upon rising, the loosely adsorbed material at the interface is removed to leave a single "monolayer" adsorption. Actually, the highly interpenetrating polymer chains enable the molecular level blending with a limited number of adjacent layers.[29]

Rather than the linear growth of the film, an unusual exponential growth of LBL (or eLBL) film, introduced by Elbert et al[65], has aroused lots of interest due to the high speed of film fabrication process. An "in and out" model was proposed by Picart et al[66, 67] to illustrate this unusual growth pattern. In these systems, the polycations are able to diffuse into the film during the deposition, then out of the film during the rinsing step, and further out during the polyanions deposition.[65-67] Therefore, the polyanions interact

not only with the outer polycations at the interface, but also some diffusible polycations inside the films. Polymer chains in these eLBL films get redistributed with each alternating cycles, resulting a film with less stratified structure despite a fast growing rate of several micrometers after only a few tens of deposition.[64]

The linear growth fashion is more commonly used for fabricating multifunctional layered nanocomposites, although eLBL is also adopted to introduce hardness,[65] toughness,[68] responsiveness[69] as well as faster growth rate for the final product. A dipping coating process is often resorted due to the simplicity (Figure 1.1 A). The repetitive nature of LBL also leads to the development of autorobots, such as slides stainer or nanoStrata for continuously depositing hundreds or even thousands of layers at a time.

Only a few layers of coatings can lead to the modification and functionalization of surfaces. Several interesting applications have been suggested, including superhydrophobic[70, 71] or superhydrophilic surfaces,[72, 73] antireflective coating,[49, 62-64], transparent conductors,[53, 74, 75] and neural interfaces. Perhaps one of the most promising applications is the use of the a few layers of LBL coating on porous materials and complex surfaces. For example, LBL films have been used to coat microneedles, stents, bandages, or fabrics to generate biological, electrical, and sensing functions. With the simple dipping technique, LBL microcapsules can also be made by templating on the micro or micro scale objects for regulated drug delievery and release.

More than a micron thick LBL films can be made by repeating necessary cycles. Clay[31, 65, 76] and CNT LBL thick freestanding films have been widely studied.[31, 65, 74, 77, 78] Due to good interfacial interaction and alignment on the plane, significant improvement

of mechanical properties has been achieved.[31, 77] The added beneficial properties of CNTs, such as the electrical conductivity, have further led to the investigations of use of those freestanding thin films for strain and corrosion sensing,[79] fuel cell membranes[80] and optoelectronic devices.[75] In addition to the function of reinforcing phase, the clay can also play a role in preventing oxygen penetration for anti-flammability and packaging purposes.[81, 82]

The introduction of eLBL into multifunctional nanocomposites has led to responsive films[69] as well as further tunability of layered structure for specific purposes.[65, 76, 83] Interestingly, the micro periodicity appears after introducing the exponential growth of polymeric pairs (poly(diallyldimethylammonium chloride) or PDDA and poly(acrylic acid) or PAA) into the linearly grown PDDA/Clay pairs.[76] Such a fast incorporation of polymer pairs for layered nanocomposites demonstrates another dimension of controllability of the LBL assembly.

Despite the remarkable progress of the LBL assembly technique as to fundamental science and engineering applications, one of the key challenges for its translation to industrial applications is still the ability to cost-effectively fabricate these thin films at adequately high throughput. Typical adsorption times range from 5 to 30 min in traditional dip coating LBL, leading to typical cycle times of 45 min. Additional manufacturing constraints include film uniformity as well as potential out-diffusion of components over the long dipping time.[84]

Spin assisted LBL (Figure 1.1 B), introduced by Cho et al[85], was suggested to offer high-speed processing.[41, 64, 65] In this process, dilute solutions of polymers or nanomaterials are spin coated onto a planar substrate, followed by a rinse cycle to remove

the loosely bonded components. The adsorption, rearrangement and selective elimination of adsorbed chains on the surface are achieved almost simultaneously at a high spinning rate over a short time period in comparison to the self-diffusion process dominated in the dip coating LBL. The molar concentration of assembling components in solution during the short period is significantly increased upon rapid elimination of water during the spinning process, yielding thick layers. In addition, mechanical factors, such as the centrifugal force and air shear force can usually afford some degree of lateral chain orientation and stratification. The spin assisted LBL is a very promising process to build multilayers on planar surfaces. An automatic machine for this process has also been developed.[86] However, this technique is not able to coat 3-D, porous, or otherwise complex substrate. It is also not amenable to for very large surfaces, such as a window or a display.[84]

Another assembly mode, spray assisted LBL (Figure 1.1 C) was first demonstrated by Schlenoff et al[87] to further overcome the scale-up challenges of LBL assembly. In this process, misted layering of polyelectrolytes with misted rinse leads to linear build-up of multilayer thin films. The structure and properties of the produced films can be similar to those produced by dip coating LBL.[87-89] An automated machine for this process was first developed by Hammond Group.[89] A controlled pressure drop can also be coupled with spraying for porous substrate to obtain functional asymmetrical coatings.[90] The spray deposition allows regular multilayer growth even under conditions for which dipping fails to produce homogeneous films, such as extremely short contact times[91] or hydrophobic surfaces.[89] It can also shorten the time for assembling by removing the washing step, as the drainage constantly removes some excess materials

arriving at the surface. The cycle times for the generation of LBL films can be order of tens of seconds rather than 45 min in the conventional system. Such a fast processing makes feasible the industrial fabrication of a large range of thick multilayered films. In addition, this manufacturing process can have no limit on the substrate size, thus can be highly accessible and preferable to industry.[87]

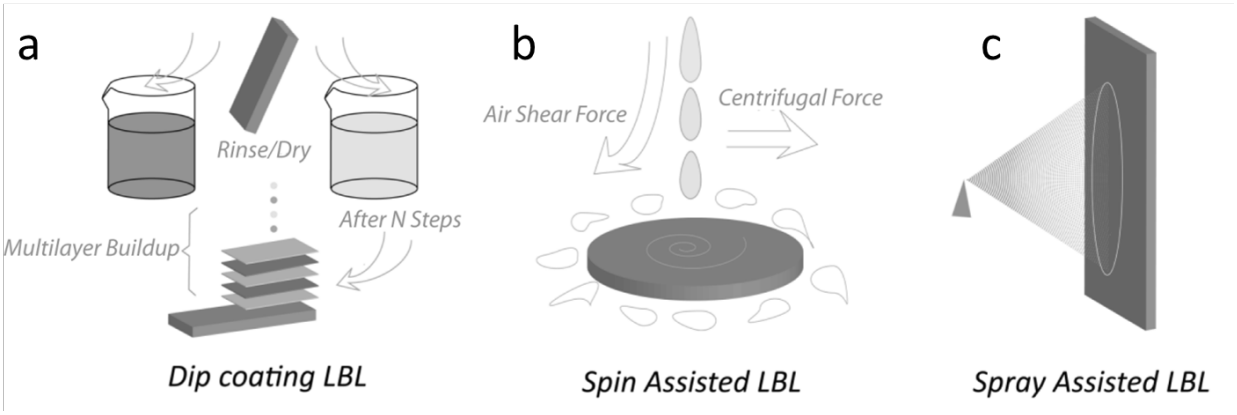

Figure 1.1 a) Dip coating LBL technique. b) Spin assisted LBL technique. c) Spray assisted LBL technique.

1.5 Purpose and Research Overview

As discussed in the previous sections, a set of properties rather than a single property is of interest for real world applications. Therefore, fundamental studies of mechanical, electrical, thermal, optical, and chemical properties are required along the exploration of uses of multifunctional nanocomposites. Both the constituents and structures need be designed as a whole for the required materials. LBL assembly is a cost-effective and versatile approach to assemble a bank of polymers and nanomaterials together to form a structure similar to natural composites with superior mechanical behaviors as well as other properties enhancement. However, this approach also faces challenges of scale-up and sustainability. In addition, water solubility for both components is usually an inevitable prerequisite for the LBL assembly. Such a stringent demand can eliminate many polymers or nanomaterials insoluble in water. To expand the range of selections for *materials by design* and attract more commercial interest of this approach, an improvement and adaptation of this method is required.

The focus of this work is on the layered composites for the engineering of multi-properties. Not only LBL assembly, but other adapting or alternative approaches with fast processing ability will be demonstrated in the following chapters. Mutually exclusive property pairs, such as conductivity and strength, strength and toughness, strength and transparency will be engineered to avoid big trade-off in the layered nanocomposites. Other engineering parameters, such as controllable thermal expansion, can also be associated with this elegant lamellar architecture.

Chapter II discusses LBL assembly as an efficient approach for managing multi-parameters required for flexible transparent conductor. Single-walled carbon nanotube

(SWNT) coatings are being considered as replacements for indium tin oxide (ITO) as transparent conductors (TCs). The problems of TC coatings from SWNT and similar materials include poor mechanical properties, high roughness, low temperature resilience, fast loss of conductivity, and consequently, short device lifetime. The required degree of structural control and simultaneous realization of many desirable characteristics can be achieved using LBL assembly. A new type of SWNT doping based on electron transfer from valence bands of nanotubes to unoccupied levels of SPEEK through π- π interactions is identified for this system.

Chapter III discusses an alternative approach for LBL assembly: vacuum assisted flocculation (VAF) method. In Chapter 3.1, polyvinyl alcohol (PVA) and reduced graphene (RG) composites are made and found to have an optimum combination of high strength and toughness. Similar composites using the conventional LBL assembly are comparatively made, and systematically evaluated their structure, mechanical, and electrical properties. In Chapter 3.2, I show that a unique negative thermal expansion (NTE) is associated with the layered architecture of graphene oxide (GO) assemblies. This NTE behavior is owing to unique themrohydration processes related with fast transport of water between the GO sheets, amphiphilic nature of nanochannels. This discovery makes the tuning of thermal expansion of GO/PVA layered composites possible.

Chapter IV deliberates an alteration of conventional LBL assembly: high-speed gelation assisted LBL deposition for aramid composites. In Chapter 4.1, I introduce a 3D percolated nanoscale network (PNN) made of aramid nanofibers (ANFs) that have the ability to branch and bifurcate unlike other fibrous nanomaterials. Such morphology

makes them nearly ideal for forming PNNs. ANFs can easily form hydrogel or aerogels with open highly porous framework that can be subsequently filled with other polymers. In Chapter 4.2, the ANF gel is further exploited to develop high-speed LBL deposition technique. A controlled thickness of ANF gel can be deposited on the substrate, and any polymer of choice is then allowed into the network. The process can be repeated to get multilayer deposition. Unlike the traditional LBL assembly, which usually requires highly charged polymer and nanoparticle (NP) aqueous solutions, this gelation assisted LBL deposition technique can combine the NP network and thermosetting polymers with efficiency, allowing wider control of structures thus properties. The demonstrated ANF and epoxy composites show fracture strength higher than steel and toughness better than the Kevlar® microfiber.

The final chapter concludes this work and suggests some future research directions.

1.6 References

1. Rowley-Conwy, P., *From Genesis to Prehistory: The Archaeological Three Age System and Its Contested Reception in Denmark, Britain, and Ireland*. Oxford University Press: Oxford; New York, **2007**; pp 362.
2. Meyers, M. A.; Chawla, K. K.; Hosford, W. F.; MyiLibrary, *Mechanical Behavior of Materials*. Cambridge University Press: Cambridge ; New York, **2009**; pp 856.
3. Palucka, T.; Bensaude-Vincent, B., Composites Overview. *authors.library.caltech.edu/5456/1/hrst.mit.edu/hrs/materials/public/composites/Composites_Overview.htm* **2002**.
4. Mallick, P. K., *Fiber-Reinforced Composites: Materials, Manufacturing, and Design*. CRC Press: Boca Raton, FL, **2008**; pp 619
5. Baughman, R. H.; Zakhidov, A. A.; de Heer, W. A., Carbon Nanotubes - the Route toward Applications. *Science* **2002**, 297, 787-792.
6. Ebbesen, T. W.; Lezec, H. J.; Hiura, H.; Bennett, J. W.; Ghaemi, H. F.; Thio, T., Electrical Conductivity of Individual Carbon Nanotubes. *Nature* **1996**, 382, 54-56.
7. Green, A. A.; Hersam, M. C., Colored Semitransparent Conductive Coatings Consisting of Monodisperse Metallic Single-Walled Carbon Nanotubes. *Nano Lett.* **2008**, 8, 1417-1422.
8. Wu, Z. C.; Chen, Z. H.; Du, X.; Logan, J. M.; Sippel, J.; Nikolou, M.; Kamaras, K.; Reynolds, J. R.; Tanner, D. B.; Hebard, A. F.; Rinzler, A. G., Transparent, Conductive Carbon Nanotube Films. *Science* **2004**, 305, 1273—1276.
9. Usuki, A.; Koiwai, A.; Kojima, Y.; Kawasumi, M.; Okada, A.; Kurauchi, T.; Kamigaito, O., Interaction of Nylon-6 Clay Surface and Mechanical-Properties of Nylon-6 Clay Hybrid. *J. Appl. Polym. Sci.* **1995**, 55, 119-123.
10. Kojima, Y.; Usuki, A.; Kawasumi, M.; Okada, A.; Fukushima, Y.; Kurauchi, T.; Kamigaito, O., Mechanical-Properties of Nylon 6-Clay Hybrid. *J. Mater. Res.* **1993**, 8, 1185-1189.
11. Dzenis, Y., Materials Science - Structural Nanocomposites. *Science* **2008**, 319, 419-420.
12. Hussain, F.; Hojjati, M.; Okamoto, M.; Gorga, R. E., Review Article: Polymer-Matrix Nanocomposites, Processing, Manufacturing, and Application: An Overview. *Journal of Composite Materials* **2006**, 40, 1511-1575.
13. Gao, J. B.; Itkis, M. E.; Yu, A. P.; Bekyarova, E.; Zhao, B.; Haddon, R. C., Continuous Spinning of a Single-Walled Carbon Nanotube-Nylon Composite Fiber. *J. Am. Chem. Soc.* **2005**, 127, 3847-3854.
14. Meyers, M. A.; Chen, P. Y.; Lin, A. Y. M.; Seki, Y., Biological Materials: Structure and Mechanical Properties. *Prog Mater Sci* **2008**, 53, 1-206.
15. Marin, F.; Le Roy, N.; Marie, B., The Formation and Mineralization of Mollusk Shell. *Front Biosci (Schol Ed)* **2012**, 4, 1099-125.
16. Ritchie, R. O., The Conflicts between Strength and Toughness. *Nat. Mater.* **2011**, 10, 817-822.
17. Fantner, G. E.; Hassenkam, T.; Kindt, J. H.; Weaver, J. C.; Birkedal, H.; Pechenik, L.; Cutroni, J. A.; Cidade, G. A. G.; Stucky, G. D.; Morse, D. E.; Hansma, P. K.,

Sacrificial Bonds and Hidden Length Dissipate Energy as Mineralized Fibrils Separate During Bone Fracture. *Nat. Mater.* **2005**, 4, 612-616.
18. Peterlik, H.; Roschger, P.; Klaushofer, K.; Fratzl, P., From Brittle to Ductile Fracture of Bone. *Nat. Mater.* **2006**, 5, 52-55.
19. Shao, Z. Z.; Vollrath, F., Materials: Surprising Strength of Silkworm Silk. *Nature* **2002**, 418, 741-741.
20. Liu, Y.; Shao, Z.; Vollrath, F., Relationships between Supercontraction and Mechanical Properties of Spider Silk. *Nat. Mater.* **2005**, 4, 901-905.
21. Holten-Andersen, N.; Fantner, G. E.; Hohlbauch, S.; Waite, J. H.; Zok, F. W., Protective Coatings on Extensible Biofibres. *Nat. Mater.* **2007**, 6, 669-672.
22. Harrington, M. J.; Masic, A.; Holten-Andersen, N.; Waite, J. H.; Fratzl, P., Iron-Clad Fibers: A Metal-Based Biological Strategy for Hard Flexible Coatings. *Science* **2010**, 328, 216-220.
23. Vollrath, F.; Porter, D.; Holland, C., The Science of Silks. *Mrs Bull* **2013**, 38, 73-80.
24. Aizenberg, J.; Sundar, V. C.; Yablon, A. D.; Weaver, J. C.; Chen, G., Biological Glass Fibers: Correlation between Optical and Structural Properties. *Proc. Natl. Acad. Sci. U. S. A.* **2004**, 101, 3358-3363.
25. Faivre, D.; Schuler, D., Magnetotactic Bacteria and Magnetosomes. *Chem. Rev. (Washington, DC, U. S.)* **2008**, 108, 4875-4898.
26. Fratzl, P.; Barth, F. G., Biomaterial Systems for Mechanosensing and Actuation. *Nature* **2009**, 462, 442-448.
27. Koch, K.; Bhushan, B.; Barthlott, W., Diversity of Structure, Morphology and Wetting of Plant Surfaces. *Soft Matter* **2008**, 4, 1943-1963.
28. Studart, A. R., Towards High-Performance Bioinspired Composites. *Adv. Mater.* **2012**, 24, 5024-5044.
29. Decher, G., Fuzzy Nanoassemblies: Toward Layered Polymeric Multicomposites. *Science* **1997**, 277, 1232-1237.
30. Decher, G.; Schmitt, J., Fine-Tuning of the Film Thickness of Ultrathin Multilayer Films Composed of Consecutively Alternating Layers of Anionic and Cationic Polyelectrolytes. In *Trends in Colloid and Interface Science Vi*, **1992**; pp 160-164.
31. Podsiadlo, P.; Kaushik, A. K.; Arruda, E. M.; Waas, A. M.; Shim, B. S.; Xu, J. D.; Nandivada, H.; Pumplin, B. G.; Lahann, J.; Ramamoorthy, A.; Kotov, N. A., Ultrastrong and Stiff Layered Polymer Nanocomposites. *Science* **2007**, 318, 80-83.
32. Bonderer, L. J.; Studart, A. R.; Gauckler, L. J., Bioinspired Design and Assembly of Platelet Reinforced Polymer Films. *Science* **2008**, 319, 1069-1073.
33. Deville, S.; Saiz, E.; Nalla, R. K.; Tomsia, A. P., Freezing as a Path to Build Complex Composites. *Science* **2006**, 311, 515-518.
34. Munch, E.; Launey, M. E.; Alsem, D. H.; Saiz, E.; Tomsia, A. P.; Ritchie, R. O., Tough, Bio-Inspired Hybrid Materials. *Science* **2008**, 322, 1516-1520.
35. Ehrenstein, G. W., *Polymeric Materials: Structure, Properties, Applications*. Hanser Gardner Publications: **2001**.
36. Bowden, P. B., The Elastic Modulus of an Amorphous Glassy Polymer. *Polymer* **1968**, 9, 449-454.

37. Jackson, A. P.; Vincent, J. F. V.; Turner, R. M., The Mechanical Design of Nacre. *Proceedings of the Royal Society of London. Series B. Biological Sciences* **1988**, 234, 415-440.
38. Walther, A.; Bjurhager, I.; Malho, J.-M.; Pere, J.; Ruokolainen, J.; Berglund, L. A.; Ikkala, O., Large-Area, Lightweight and Thick Biomimetic Composites with Superior Material Properties Via Fast, Economic, and Green Pathways. *Nano Lett.* **2010**, 10, 2742-2748.
39. Koerner, H.; Jacobs, J. D.; Tomlin, D. W.; Busbee, J. D.; Vaia, R. A., Tuning Polymer Nanocomposite Morphology: Ac Electric Field Manipulation of Epoxy–Montmorillonite (Clay) Suspensions. *Advanced Materials* **2004**, 16, 297-302.
40. Shim, B. S.; Kotov, N. A., Single-Walled Carbon Nanotube Combing During Layer-by-Layer Assembly: From Random Adsorption to Aligned Composites. *Langmuir* **2005**, 21, 9381-9385.
41. Erb, R. M.; Libanori, R.; Rothfuchs, N.; Studart, A. R., Composites Reinforced in Three Dimensions by Using Low Magnetic Fields. *Science* **2012**, 335, 199-204.
42. Tao, A.; Kim, F.; Hess, C.; Goldberger, J.; He, R.; Sun, Y.; Xia, Y.; Yang, P., Langmuir−Blodgett Silver Nanowire Monolayers for Molecular Sensing Using Surface-Enhanced Raman Spectroscopy. *Nano Letters* **2003**, 3, 1229-1233.
43. Cao, Q.; Han, S. J.; Tulevski, G. S.; Zhu, Y.; Lu, D. D.; Haensch, W., Arrays of Single-Walled Carbon Nanotubes with Full Surface Coverage for High-Performance Electronics. *Nat Nanotechnol* **2013**, 8, 180-186.
44. Storm, C.; Pastore, J. J.; MacKintosh, F. C.; Lubensky, T. C.; Janmey, P. A., Nonlinear Elasticity in Biological Gels. *Nature* **2005**, 435, 191-194.
45. Bazant, Z. P., Scaling Theory for Quasibrittle Structural Failure. *Proc. Natl. Acad. Sci. U. S. A.* **2004**, 101, 13400-13407.
46. Cambridge Materials Selector Database (Grantadesign.Com).
47. Giesa, T.; Arslan, M.; Pugno, N. M.; Buehler, M. J., Nanoconfinement of Spider Silk Fibrils Begets Superior Strength, Extensibility, and Toughness. *Nano Lett.* **2011**, 11, 5038-5046.
48. Ambrosetti, G.; Balberg, I.; Grimaldi, C., Percolation-to-Hopping Crossover in Conductor-Insulator Composites. *Phys Rev B* **2010**, 82.
49. Stankovich, S.; Dikin, D. A.; Dommett, G. H. B.; Kohlhaas, K. M.; Zimney, E. J.; Stach, E. A.; Piner, R. D.; Nguyen, S. T.; Ruoff, R. S., Graphene-Based Composite Materials. *Nature* **2006**, 442, 282-286.
50. Kyrylyuk, A. V.; Hermant, M. C.; Schilling, T.; Klumperman, B.; Koning, C. E.; van der Schoot, P., Controlling Electrical Percolation in Multicomponent Carbon Nanotube Dispersions. *Nat Nano* **2011**, 6, 364—369.
51. Neelakanta, P. S., *Handbook of Electromagnetic Materials: Monolithic and Composite Versions and Their Applications*. Taylor & Francis Group: **1995**.
52. Read, R. E. C.; Stow, C. D., An Experimental Investigation of Charge Transport through Rubber. *J Phys D Appl Phys* **1969**, 2, 567-&.
53. Zhu, J.; Shim, B. S.; Di Prima, M.; Kotov, N. A., Transparent Conductors from Carbon Nanotubes Lbl-Assembled with Polymer Dopant with Π−Π Electron Transfer. *J. Am. Chem. Soc.* **2011**, 133, 7450-7460.
54. Capadona, J. R.; Van Den Berg, O.; Capadona, L. A.; Schroeter, M.; Rowan, S. J.; Tyler, D. J.; Weder, C., A Versatile Approach for the Processing of Polymer

Nanocomposites with Self-Assembled Nanofibre Templates. *Nat. Nanotechnol.* **2007**, 2, 765-769.
55. Kim, K. K.; Bae, J. J.; Park, H. K.; Kim, S. M.; Geng, H.-Z.; Park, K. A.; Shin, H.-J.; Yoon, S.-M.; Benayad, A.; Choi, J.-Y.; Lee, Y. H., Fermi Level Engineering of Single-Walled Carbon Nanotubes by Aucl3 Doping. *J. Am. Chem. Soc.* **2008**, 130, 12757-12761.
56. Hellstrom, S. L.; Vosgueritchian, M.; Stoltenberg, R. M.; Irfan, I.; Hammock, M.; Wang, Y. B.; Jia, C.; Guo, X.; Gao, Y.; Bao, Z., Strong and Stable Doping of Carbon Nanotubes and Graphene by Moox for Transparent Electrodes. *Nano Lett.* **2012**, 12, 3574-3580.
57. Iler, R. K., Multilayers of Colloidal Particles. *J. Colloid Interface Sci.* **1966**, 21, 569-594.
58. Shimazaki, Y.; Mitsuishi, M.; Ito, S.; Yamamoto, M., Preparation of the Layer-by-Layer Deposited Ultrathin Film Based on the Charge-Transfer Interaction. *Langmuir* **1997**, 13, 1385-1387.
59. Schutte, M.; Kurth, D. G.; Linford, M. R.; Colfen, H.; Mohwald, H., Metallosupramolecular Thin Polyelectrolyte Films. *Angew. Chem., Int. Ed.* **1998**, 37, 2891-2893.
60. Stockton, W. B.; Rubner, M. F., Molecular-Level Processing of Conjugated Polymers. 4. Layer-by-Layer Manipulation of Polyaniline Via Hydrogen-Bonding Interactions. *Macromolecules* **1997**, 30, 2717-2725.
61. Lee, H.; Kepley, L. J.; Hong, H. G.; Mallouk, T. E., Inorganic Analogues of Langmuir-Blodgett Films: Adsorption of Ordered Zirconium 1,10-Decanebisphosphonate Multilayers on Silicon Surfaces. *J. Am. Chem. Soc.* **1988**, 110, 618-620.
62. Zhang, X.; Chen, H.; Zhang, H. Y., Layer-by-Layer Assembly: From Conventional to Unconventional Methods. *Chem. Commun. (Cambridge, U. K.)* **2007**, 1395-1405.
63. Ariga, K.; Hill, J. P.; Ji, Q. M., Layer-by-Layer Assembly as a Versatile Bottom-up Nanofabrication Technique for Exploratory Research and Realistic Application. *Phys. Chem. Chem. Phys.* **2007**, 9, 2319-2340.
64. Laugel, N.; Betscha, C.; Winterhalter, M.; Voegel, J. C.; Schaaf, P.; Ball, V., Relationship between the Growth Regime of Polyelectrolyte Multilayers and the Polyanion/Polycation Complexation Enthalpy. *J. Phys. Chem. B* **2006**, 110, 19443-19449.
65. Podsiadlo, P.; Michel, M.; Lee, J.; Verploegen, E.; Kam, N. W. S.; Ball, V.; Qi, Y.; Hart, A. J.; Hammond, P. T.; Kotov, N. A., Exponential Growth of Lbl Films with Incorporated Inorganic Sheets. *Nano Lett.* **2008**, 8, 1762-1770.
66. Lavalle, P.; Gergely, C.; Cuisinier, F. J. G.; Decher, G.; Schaaf, P.; Voegel, J. C.; Picart, C., Comparison of the Structure of Polyelectrolyte Multilayer Films Exhibiting a Linear and an Exponential Growth Regime: An in Situ Atomic Force Microscopy Study. *Macromolecules* **2002**, 35, 4458-4465.
67. Picart, C.; Mutterer, J.; Richert, L.; Luo, Y.; Prestwich, G. D.; Schaaf, P.; Voegel, J. C.; Lavalle, P., Molecular Basis for the Explanation of the Exponential Growth of Polyelectrolyte Multilayers. *Proc. Natl. Acad. Sci. U. S. A.* **2002**, 99, 12531-12535.

68. Podsiadlo, P.; Arruda, E. M.; Kheng, E.; Waas, A. M.; Lee, J.; Critchley, K.; Qin, M.; Chuang, E.; Kaushik, A. K.; Kim, H. S.; Qi, Y.; Noh, S. T.; Kotov, N. A., Lbl Assembled Laminates with Hierarchical Organization from Nano- to Microscale: High-Toughness Nanomaterials and Deformation Imaging. *ACS Nano* **2009**, 3, 1564-1572.
69. Lutkenhaus, J. L.; Hrabak, K. D.; McEnnis, K.; Hammond, P. T., Elastomeric Flexible Free-Standing Hydrogen-Bonded Nanoscale Assemblies. *J. Am. Chem. Soc.* **2005**, 127, 17228-17234.
70. Zhai, L.; Cebeci, F. C.; Cohen, R. E.; Rubner, M. F., Stable Superhydrophobic Coatings from Polyelectrolyte Multilayers. *Nano Lett.* **2004**, 4, 1349-1353.
71. Zhai, L.; Berg, M. C.; Cebeci, F. C.; Kim, Y.; Milwid, J. M.; Rubner, M. F.; Cohen, R. E., Patterned Superhydrophobic Surfaces:Toward a Synthetic Mimic of the Namib Desert Beetle. *Nano Lett.* **2006**, 6, 1213-1217.
72. Cebeci, F. C.; Wu, Z.; Zhai, L.; Cohen, R. E.; Rubner, M. F., Nanoporosity-Driven Superhydrophilicity: A Means to Create Multifunctional Antifogging Coatings. *Langmuir* **2006**, 22, 2856-2862.
73. Lee, D.; Rubner, M. F.; Cohen, R. E., All-Nanoparticle Thin-Film Coatings. *Nano Lett.* **2006**, 6, 2305-2312.
74. Shim, B. S.; Tang, Z. Y.; Morabito, M. P.; Agarwal, A.; Hong, H. P.; Kotov, N. A., Integration of Conductivity Transparency, and Mechanical Strength into Highly Homogeneous Layer-by-Layer Composites of Single-Walled Carbon Nanotubes for Optoelectronics. *Chem. Mater.* **2007**, 19, 5467-5474.
75. Shim, B. S.; Zhu, J.; Jan, E.; Critchley, K.; Kotov, N. A., Transparent Conductors from Layer-by-Layer Assembled SWNT Films: Importance of Mechanical Properties and a New Figure of Merit. *ACS Nano* **2010**, 4, 3725-34.
76. Podsiadlo, P.; Michel, M.; Critchley, K.; Srivastava, S.; Qin, M.; Lee, J. W.; Verploegen, E.; Hart, A. J.; Qi, Y.; Kotov, N. A., Diffusional Self-Organization in Exponential Layer-by-Layer Films with Micro- and Nanoscale Periodicity. *Angew. Chem., Int. Ed.* **2009**, 48, 7073-7077.
77. Shim, B. S.; Zhu, J.; Jan, E.; Critchley, K.; Ho, S. S.; Podsiadlo, P.; Sun, K.; Kotov, N. A., Multiparameter Structural Optimization of Single-Walled Carbon Nanotube Composites: Toward Record Strength, Stiffness, and Toughness. *ACS Nano* **2009**, 3, 1711-1722.
78. Podsiadlo, P.; Liu, Z. Q.; Paterson, D.; Messersmith, P. B.; Kotov, N. A., Fusion of Seashell Nacre and Marine Bioadhesive Analogs: High-Strength Nanocompoisite by Layer-by-Layer Assembly of Clay and L-3,4-Dihydroxyphenylaianine Polymer. *Adv. Mater.* **2007**, 19, 949-+.
79. Kenneth, J. L.; Junhee, K.; Jerome, P. L.; Nadine Wong Shi, K.; Nicholas, A. K., Multifunctional Layer-by-Layer Carbon Nanotube–Polyelectrolyte Thin Films for Strain and Corrosion Sensing. *Smart Materials and Structures* **2007**, 16, 429.
80. Michel, M.; Taylor, A.; Sekol, R.; Podsiadlo, P.; Ho, P.; Kotov, N.; Thompson, L., High-Performance Nanostructured Membrane Electrode, Assemblies for Fuel Cells Made by Layer-by-Layer Assembly of Carbon Nanocolloids. *Adv. Mater.* **2007**, 19, 3859-+.

81. Priolo, M. A.; Holder, K. M.; Gamboa, D.; Grunlan, J. C., Influence of Clay Concentration on the Gas Barrier of Clay–Polymer Nanobrick Wall Thin Film Assemblies. *Langmuir* **2011**, 27, 12106-12114.
82. Yang, Y.; Bolling, L.; Priolo, M. A.; Grunlan, J. C., Super Gas Barrier and Selectivity of Graphene Oxide-Polymer Multilayer Thin Films. *Adv. Mater.* **2013**, 25, 503-508.
83. Kaushik, A. K.; Podsiadlo, P.; Qin, M.; Shaw, C. M.; Waas, A. M.; Kotov, N. A.; Arruda, E. M., The Role of Nanoparticle Layer Separation in the Finite Deformation Response of Layered Polyurethane-Clay Nanocomposites. *Macromolecules* **2009**, 42, 6588-6595.
84. Hammond, P. T., Engineering Materials Layer-by-Layer: Challenges and Opportunities in Multilayer Assembly. *AIChE J.* **2011**, 57, 2928-2940.
85. Cho, J.; Char, K.; Hong, J. D.; Lee, K. B., Fabrication of Highly Ordered Multilayer Films Using a Spin Self-Assembly Method. *Adv. Mater.* **2001**, 13, 1076-1078.
86. Vozar, S.; Poh, Y. C.; Serbowicz, T.; Bachner, M.; Podsiadlo, P.; Qin, M.; Verploegen, E.; Kotov, N.; Hart, A. J., Automated Spin-Assisted Layer-by-Layer Assembly of Nanocomposites. *Rev. Sci. Instrum.* **2009**, 80.
87. Schlenoff, J. B.; Dubas, S. T.; Farhat, T., Sprayed Polyelectrolyte Multilayers. *Langmuir* **2000**, 16, 9968-9969.
88. Izquierdo, A.; Ono, S. S.; Voegel, J. C.; Schaaf, P.; Decher, G., Dipping Versus Spraying: Exploring the Deposition Conditions for Speeding up Layer-by-Layer Assembly. *Langmuir* **2005**, 21, 7558-7567.
89. Krogman, K. C.; Zacharia, N. S.; Schroeder, S.; Hammond, P. T., Automated Process for Improved Uniformity and Versatility of Layer-by-Layer Deposition. *Langmuir* **2007**, 23, 3137-3141.
90. Krogman, K. C.; Lowery, J. L.; Zacharia, N. S.; Rutledge, G. C.; Hammond, P. T., Spraying Asymmetry into Functional Membranes Layer-by-Layer. *Nat. Mater.* **2009**, 8, 512-518.
91. Izquierdo, A.; Ono, S. S.; Voegel, J. C.; Schaaf, P.; Decher, G., Dipping Versus Spraying: Exploring the Deposition Conditions for Speeding up Layer-by-Layer Assembly. *Langmuir* **2005**, 21, 7558-7567.

CHAPTER II

Transparent Conductors from Carbon Nanotubes LBL-Assembled with Polymer Dopant with π-π Electron Transfer

2.1 Introduction

. Simultaneous optimization of several critical properties at the same time is one of the most fundamental challenges of the materials science. Quite often the properties appear to be orthogonal, making this task very difficult and often haphazard. Examples of orthogonal properties and the difficulties of combining them can be encountered in virtually any area of both advanced and traditional materials. To give examples of such difficulties one can look into the development of materials for neuroprosthetic devices which require long-term biocompatibility, electrical conductivity, and flexibility,[1] materials for batteries and fuel cells, which require high ionic conductivity, high sheer modulus, and high temperature resilience,[2-4] or materials for aviation, which require high toughness, high electrical conductivity, and low density. Transparent conductors (TCs) can also be one of the best examples of materials with inherently orthogonal properties requiring high transparency and conductivity at the same time. Moreover, they also represent one of the most significant needs for several current technologies, drawing much attention to these materials.[5-10]

The most common TC is indium tin oxide (ITO), which is ubiquitous for information processing devices including the laptop computer on which this sentence was typed. ITO suffers from brittleness and scarcity of raw materials.[7, 8, 10-13] Ever increasing use of electronics, the need for flexible and potentially wearable devices, and new energy conversion technologies bring additional challenges for TCs. Considering different coatings as ITO replacements, they need to be comparable in conductivity and transparency to ITO, mechanically robust, thermally and environmentally stable, compatible with other processing stages, and easily available. Such multi-parameter optimization requires the development of new chemical approaches to structural tuning of potential TC candidates.

No optimum material has been found so far to replace ITO and completely satisfy the technological demands of, for instance, flexible electronics. Amorphous metal oxide semiconductors, such as In-Ga-Zn-O system, were developed to deposit on polymer substrate at low temperature, but their conductivity and mechanical flexibility are very limited.[14] Metal gratings and nanowire meshes have been demonstrated as one of possible solutions, which can be particularly useful for EMI shielding and some display applications.[12, 15-17] However, the approach suffers from formidable cost of complex nanoimprint technologies[15, 17] scale-up difficulties, and problems associated with light absorbance and scattering of nanowire materials.[16] In addition, the properties of thin coatings have limited reproducibility.[12]

Electroactive polymers, such as polythiophenes[18, 19] have also been examined as potential TCs; however, these materials are usually rather resistive and display intense coloration. Some of the more encouraging candidates are thin film from single-walled

carbon nanotubes (SWNTs) and graphene sheets.[20] Although absorptive in the visible range, individual SWNTs and graphene sheets have exceptional conductivity and mechanical properties, allowing them to be good candidates for low surface resistance and high strength TCs.

A nearly ideal SWNT- or graphene-based TC should have a sheet resistance of <50ohms/sq at 85% transparency,[10] or 100ohms/sq at 90%.[8] Considering strong absorption of carbon-based materials in visible range of spectrum, the bulk conductivity of the coatings should be at least 5.3×10^5S/m in order to meet these requirements.[8] Current state-of-the-art SWNT TCs have a sheet resistance of *ca* 300ohms/sq at 90% transmittance and 100ohms/sq at 80% transmittance with some variations depending on the methods used.[7-10] The conductivities of these coatings range from 1.6×10^5 to 2×10^5S/m,[7, 8] *i.e.* 2~3 times below the needed performance. Graphene (G) and chemically similar material often identified as reduced graphene oxide (rGO) generated a lot of excitement in the TCs field. However, one also need to admit that they often performed much worse than SWNT TCs with some G/rGO thin films having 1000ohms/sq at 70% transparency.[21] Materials from G and rGO typically showed conductivities below 5.5×10^4 S/m.[22] The pathway to improve TC performance was suggested to be *via* strong doping with electron acceptors but such doping detrimentally affects temperature resilience and compatibility with other electronic components.[23] Nevertheless, for G-based TCs surface resistance can be reduced further to 30ohms/sq at 90% transparency when high quality G sheets are produced by chemical vapor deposition (CVD) method combined with high doping.[24]

Despite the impressive efforts, the current SWNT and G-based TCs share several still-to-be-solved challenges:

1. Small molecules, such as acid,[25] $SOCl_2$[26] and $AuCl_3$[27] are often used to improve the conductivity through doping and reducing contact resistances between SWNTs or G.[24, 28] However, these dopants are mobile and known to spontaneously escape from the carbon-based matrices, thus resulting in the inevitable deterioration of electrical properties.[23, 28] Many electron acceptor (Lewis acid) dopants are becoming reduced or lost at even slightly elevated or even room temperatures by SWNTs, G, or rGO.[23] Additionally, the chemicals used for doping are corrosive; they can destroy contacts in electronic devices and poison surrounding materials, such as emissive layers in OLEDs.[8] Some non-volatile organic polymers can also induce doping.[29] However, up to now they were difficult to use and often caused high contact resistance between SWNTs,[29] or were relatively weak dopants aiming to reduce Schottky barriers in SWNT transistors.[30]

2. Uniformity of conductive pathways throughout the material and low surface roughness are needed to make efficient and long-living electronic devices.[8-10] Rough, porous, and non-uniform conductive networks of many SWNT and G/rGO polymer composites result in low conductivity. Traditional techniques in this area yielded, so far, composites with bulk conductivities only *ca.* 10 S/m.[8] SWNT- and G-based coating without polymers give much more conductive coatings but adhesion to glass/plastic substrates and flexural robustness suffer. Smooth, virtually nonporous, and uniform coatings for SWNT or G/rGO composite with polymer or otherwise are preferred from the perspective of device longevity as well.

3. Mechanical properties of SWNT- and G/rGO-based coatings are often insufficient for the long-term use under bending, stretching, and other stresses. Moreover, they are being studied much less than electrical properties,[8, 31] which could be attributed to the more traditional view of TCs as coatings for flat solid substrates, such as glass. TCs more compatible than ITO with bendable and stretchable substrates, for instance plastics, are much needed. Much better understanding of the fundamental relations between stress and strain on one side, transparency and conductivity on the other side, has to be established, which will require a series of systematic studies with well controlled model system(s).

These challenges, which must be addressed simultaneously, make it difficult to utilize the classical techniques for synthesis of composite materials and coatings. It is much easier to address one property at a time to gradually approach the optimal combination. But quite often it is discovered along the way that some of these properties are difficult to combine together. For instance, addition of some polymers makes possible the improvement of mechanical properties but drastically reduces the conductivity and thermal stability of TCs. In a nearly ideal case, a minimal amount of mechanically robust polymer should bind SWNTs to themselves and to the substrate while providing charge carrier doping. The dual function of the polymer limits the choice of processing/synthetic techniques and underscores the importance of the nanometer-scale control of the structure in the resulting coatings. Layer-by-layer (LBL) assembly is likely to be one of a few techniques that make possible fine control over materials structure and much simpler combination of multiple properties[32-34] including those important for TCs.[35] Easy-to-make conformal coatings with meticulously controlled thickness are characteristic for

LBL. Overall, LBL represents a method which is difficult to pass by when considering the fabrication of TC materials and the academic challenge of attaining multiple functional characteristics. Therefore, this paper endeavors to seek for new solutions to TC challenges by taking advantage of LBL engineering method. As such, we designed LBL multilayers (Figure 2.1A), which employ sulfonated polyetheretherketone (SPEEK, Figure 2.1C) as a new stabilizer for SWNTs and hydroxyethyl cellulose (HOCS, Figure 2.1.1B) as a new molecule glue. It was demonstrated that they could serve simultaneously as dopants. Moreover, these polymers were derived from macromolecules with outstanding mechanical properties (Figure 2.1C),[36] which would influence positively on the robustness of TCs. Both polymers are permanently locked in the coating through intricate interdigitation.[32] This structural feature was expected to impart both uniformity of conductive networks and thermal resilience. The prepared (HOCS/ SPEEK-SWNT)n composite coatings were found to have a conductivity of 1.1×105S/m, and ultimate strength of 360 ± 35MPa. A sheet resistance of 920ohms/sq with 86.7% transmittance was achieved. Although without record conductivity, we succeeded in complete elimination of mobile, volatile and corrosive dopants. Moreover, a new approach to SWNT doping was identified in this study. Unlike strong Brønsted and Lewis acids the doping is based on electron transfer from several valence bands of SWNTs to low lying unoccupied levels of SPEEK in the π-stacked electronic system. Due to substantially higher placement of lowest unoccupied molecular orbital (LUMO) of other structurally related compounds the doping was impossible or ineffective. Additionally, a cumulative electrical/optical/mechanical performance expressed as figure of merit, IITC,[35] substantially exceeding that of ITO was achieved. We also observed that the produced

TCs were thermally stable with little decomposition until 500°C, which is quite remarkable for polymer coatings. The findings of this study can potentially be applied to other carbon-based TCs and serve as a convenient model to establish structure-property relations with multiple coordinates and optimization targets.

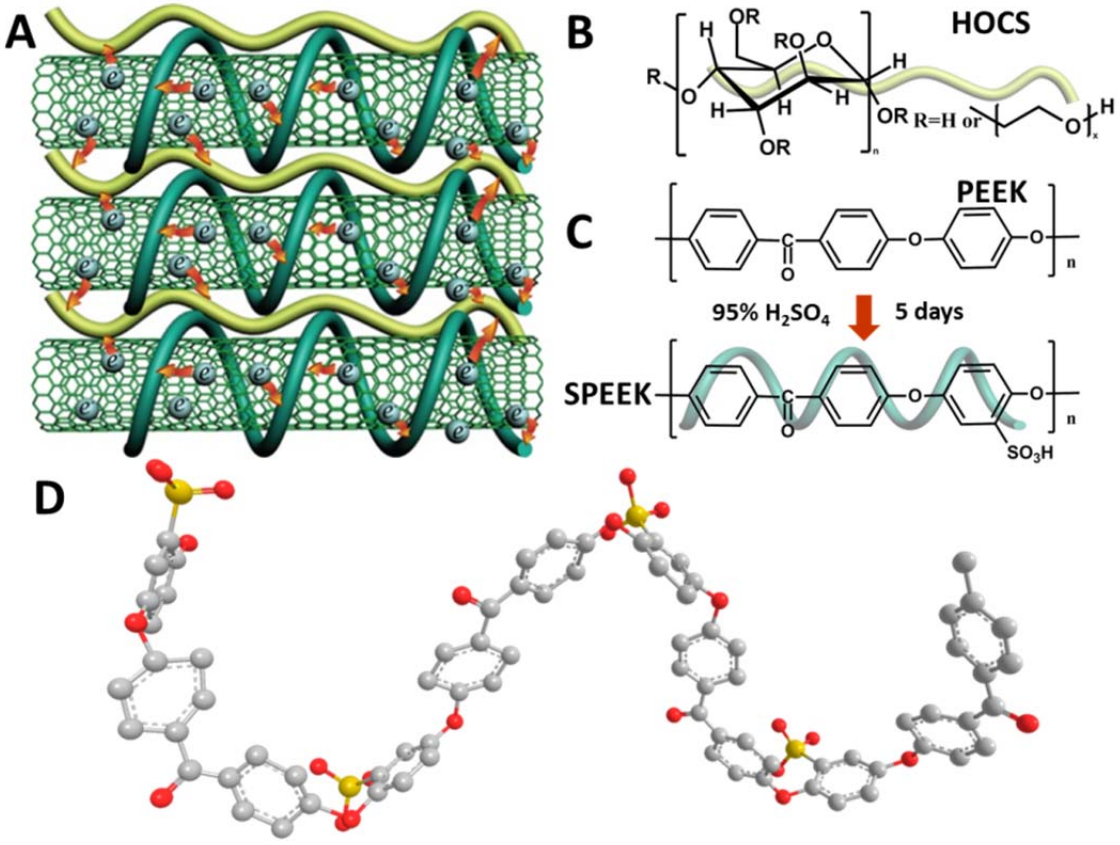

Figure 2.1 (A) Proposed ideal architecture for multi-parameter optimization of SWNT thin coatings. The arrows indicate hole-doping from the surrounding polymers. SPEEK is represented by the green tube, and HOCS is in yellow. Chemical structures of polymers used in this study (B) hydroxyethyl cellulose (HOCS) and (C) poly(etheretherketone) (PEEK), and sulfonated PEEK (SPEEK). (D) Ball-and-stick model of SPEEK in the minimal energy state calculated by Molecular Mechanics (MM2) algorithm. Grey spheres are assigned to carbon atoms, red to oxygen atoms, and yellow to sulfur atoms. Hydrogen atoms are omitted for greater clarity.

2.2 Experimental

Sulfonation of poly(etheretherketone) (PEEK). Fine powders of PEEK450P were purchased from Victrex and were gradually dissolved in 95%~98% sulfuric acid at a concentration of 2.5g/100ml. The mixture was stirred at room temperature for a period of 5 days. The sulfonated powders were then precipitated from solution with a five-fold excess of deionized (DI) water at 0^{o}C and thoroughly washed with water until neutral pH. Subsequently, the product, *i.e.* sulfonated PEEK (SPEEK), was dried at 50^{o}C under vacuum for 24 hours. The stock powder of SPEEK can be easily dissolved in boiling water.

Preparation of SWNT dispersions stabilized with SPEEK. SWNTs were bought from Carbon Solutions Inc. and carried product designations as P2 or P3. P2 and P3 SWNTs have similar purity (>90%), but P3 carried greater density of –COOH groups than P2 (see descriptions in website: http://www.carbonsolution.com). 0.5mg/ml of P2 or P3 SWNTs were dispersed by 2mg/ml and 1mg/ml SPEEK in DI water, respectively. Homogenous dispersions were obtained by sonication for 12 hours. The pH of the solution can be easily adjusted by NaOH.

Energy optimization and molecular orbital calculation of polymer. MM2 force field modeling with default parameters was used to roughly calculate the relaxed state of polymer in software of ChemBio3D 2010 from CambridgeSoft Corporation. The energy of molecular orbitals was calculated by UV-vis spectra simulator (version 1.5.3) from NanoHub.org. The tool uses the SCF-MO package ORCA to calculate molecular electronic structures. Excited states can be calculated via CI-singles (CIS) with the semiempirical Hamiltonian ZINDO.

Layer-by-layer assembly. In a typical LBL cycle, glass or silicon slides cleaned by piranha solution for 24 hours were immersed in 0.1wt% HOCS for 1 minute, rinsed in DI water, and then dried with compressed air. Subsequently, these slides were dipped into the SPEEK-stabilized SWNT solutions for 2 minutes, followed by similar rinsing and drying. The above cycle can be repeated *n* times to obtain desirable thickness. The resulting coating or free-standing film will be designated as $[HOCS/SPEEK\text{-}SWNT]_n$. The LBL film was generally assembled in pH10 SWNT dispersions unless specifically noted. In order to deposit LBL film onto polymer substrate, such as PET, the substrate was immersed into 1% polyethylenimine for 1min to make it hydrophilic, then similar deposition process to that on glass substrate can be followed. In order to ensure the good quality of films on PET, it is recommended to fix PET on glass to avoid bending during handling.

Characterization. UV-vis spectra throughout the study were obtained on a 8453 UV-vis ChemStation spectrophotometer (Agilent Technologies). The supernatants of SWNT dispersions after centrifugation at 10,000 rpm for 2 hours were used to obtain the UV-vis spectra.

The degree of sulfonation of PEEK was evaluated by attenuated total reflection Fourier transform infrared spectroscopy (ATR-FTIR) and X-ray photoelectron spectroscopy (XPS). ATR-FTIR spectroscopy was performed on a Nicolet 6700 spectrometer utilizing the grazing angle accessory (Smart SAGA) at a grazing angle of 85°. All the samples for IR were prepared by spin-coating of several drops of solutions onto gold-covered glass. PEEK was dissolved in methanesulphonic acid (MSA, Sigma-Aldrich), while SPEEK was dissolved in ethanol at room temperature. PEEK showed no

trace of sulfonation even after 8 days in MSA[37]. Powder samples were examined by a Kratos AXIS Ultra Imaging X-ray photoelectron spectrometer. All spectra were calibrated with the C1s photoemission peak for sp^2 hybridized carbons at 284.7 eV to compensate for the effect of charging. Component fitting of the photoemission spectra was performed with mixed Gaussian/Lorentzian model after a Shirley type background subtraction.

The transmittance of LBL films on glass substrate was measured by UV-vis spectroscopy with clean glass slide as background. In a typical LBL process, both sides of glass slide were coated with films. In order to get the transmittance for only one side, the other side had to be carefully removed with wet soft tissue. The transmittance of double sided film (T_2) and only one sided film (T_1) are usually related by the formula $T_1=T_2^{-0.5}$, which can be easily derived from Beer's law.

The thickness of films on silicon wafers were measured by a J.A.Woolham Co. VASE spectroscopic ellipsometer by fitting Cauchy model. Mass growth of films was investigated by quartz crystal microbalance (QCM) 200 from Stanford Research Systems. 5MHz quartz crystals were used in all the studies.

Tapping mode atomic force microscopy (AFM) images were obtained using a NanoScope IIIa atomic force microscope (AFM) from Veeco Instruments (Santa Barbara, CA). AFM tips are from MikroMasch with tip radius smaller than 10nm. Sheet resistance was measured for films deposited on glass substrates using a Lucas S-302-4 four point probe station with the Agilent 3440A multimeter. A series of 3-4 measurements were taken on each film and the measurements then were averaged to give the final reported value and errors. At least two different batches of films at the same experimental

conditions were measured to ensure the repeatability of the data. Scanning electron microscopy (SEM) images were obtained with an FEI Nova Nanolab dual-beam FIB and scanning electron microscope and energy dispersive X-ray spectroscopy (EDAX) was conducted in the SEM's EDAX mode. Perkin Elmer Pyris 1 TGA was used for thermal gravimetric analysis. Resonance Raman spectra were taken with a Dimension-P1 Raman system (Lambda Solutions, Inc.) with 532 nm excitation. Stress-strain curve of free standing films were analyzed by mechanical tester 100Q from TestResources Inc. at a constant rate of 0.01mm/s. The test samples were 1mm wide and 4-6mm long.

2.3 Results and Discussion

2.3.1 Preparation of the polymer dopant, SPEEK

SPEEK is obtained by an electrophilic aromatic substitution reaction toward poly(etheretherketone) (PEEK) (Figure 2.1C) with concentrated sulfuric acid at room temperature.[38] PEEK was selected as a parent polymer for this project due to (1) well-known mechanical properties, (2) large number of phenyl rings capable of π-π staking with chemically similar aromatic rings in graphene walls of SWNTs, and (3) transparency in the visible range of the electromagnetic spectrum. Chemical modification in PEEK can lead to adjustment of energy levels of the π-orbitals to effect efficient doping. As such, electron-withdrawing functional groups were introduced into PEEK to provide hole-doping of SWNTs. Incidentally, the same group(s) can also make PEEK easily soluble in polar solvents. Therefore, SPEEK with electronegative easy-to-ionize sulfonic acid groups ($-SO_3H$) was expected to be an effective dopant and stabilizer

to debundle SWNTs into individual nanotubes. Subsequent studies indicated that although the original premise was correct, the mechanism of doping turned out to be very different and interesting from both fundamental and practical points of views.

X-ray photoelectron spectroscopy (XPS) was performed to verify the identity of the SPEEK products (Figure 2.2). As expected, the 2p photoemission peaks from sulfur are clearly observed indicating the sulfonation of PEEK macromolecules. The atomic concentration of sulfur can be calculated to be 4.46% and agrees well with the suggested unit formula of SPEEK in Figure 2.1C with theoretical sulfur content of 4.00%. The C1s XPS band of PEEK (Figure 2.2B) has three components corresponding to C_1(-C=C), C_2(-C-O) and C_3(-C=O).[39] After successful sulfonation (Figure 2.2C) a new XPS component designated as C_4 appears between C_1(-C=C), C_2(-C-O) peaks and is attributed to –C-S groups. A new oxygen XPS peak appearing between O_1 (-O=C) and O_2 (-O-C) components is indicative of O=S groups (O_3) (Figure 2.2D and E).[40]

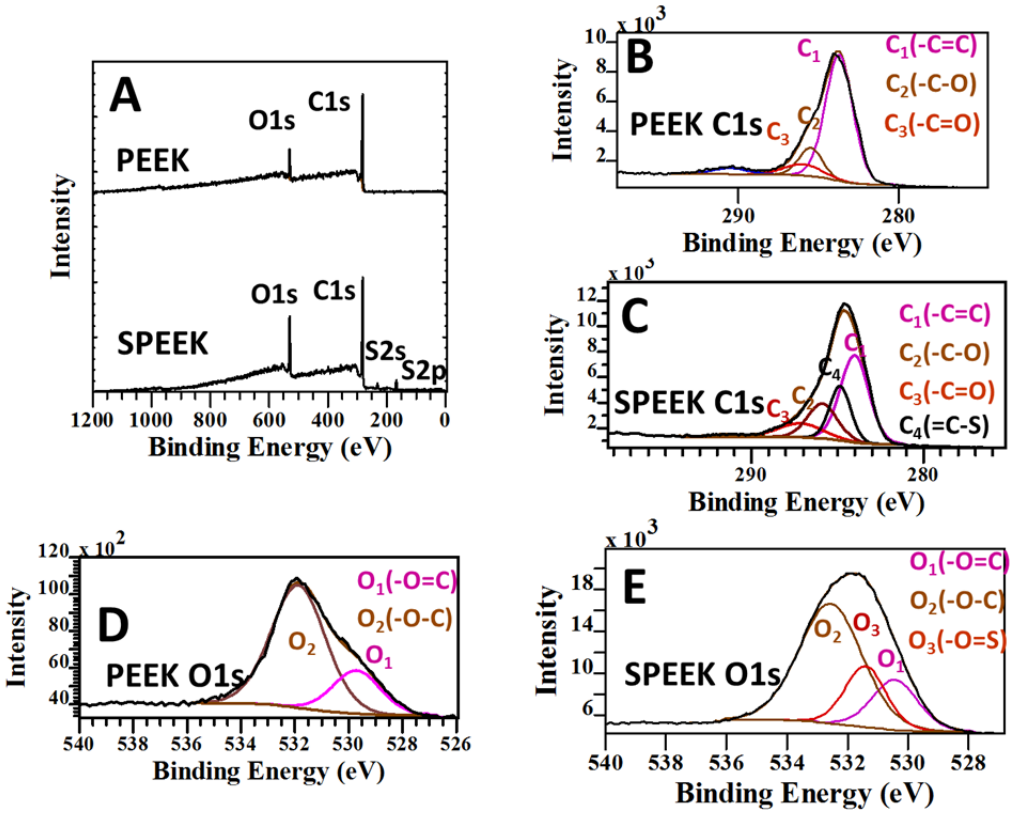

Figure 2.2 X-ray photoelectron spectroscopy (XPS) spectra of polyetheretherketone (PEEK) and sulfonated PEEK (SPEEK). (A) Wide scan survey spectrum. (B, C) C1s spectra of PEEK and SPEEK. (D, E) O1s spectra of PEEK and SPEEK.

The sulfonation of PEEK is also evident from FTIR spectra (Figure 2.10).[38] 1657cm^{-1} band is assigned to stretching vibrations of carbonyl functional group, while 1599cm^{-1} and 1497cm^{-1} are characteristic for stretching vibrations of aromatic rings; 1228cm^{-1} peak is typical for C-O stretching in the parent polymer. After sulfonation, the absorption band at 1497cm^{-1} is replaced by two new peaks at 1432cm^{-1} and 1477cm^{-1} characteristic of the phenyl rings vibration modes with $-SO_3H$ substitution. New absorption band occurred at 1255, 1138, 1083, and 1025 cm^{-1} indicates the sulfonic acid groups in SPEEK.[38, 41] The stretching vibration of S-O in the hydrosulfonate groups can be observed at the appropriate position at 1083cm^{-1}.[41] To be noted, physical adsorption

of sulfuric acid would not give changes in the phenyl ring characteristic region in FTIR and carbon emission peak in XPS.

2.3.2 SPEEK-stabilized dispersions of SWNTs

In the relaxed state of SPEEK through molecular mechanics calculations (Figure 2.1D), phenyl rings connected by carbonyl groups stay almost in-plane, while those connected by oxygen atoms tend to be perpendicular to each other. When interacting with SWNT, the flexible C-O-C bonds are expected to rotate and adjust to the shape of SWNT to maximize the overlap of π-orbitals between phenyl rings and graphene walls of SWNTs.[42, 43] These molecular adjustments do not prevent the charged sulfonated groups in polymers being accessible by water, thus facilitating the separation and stabilization of individual SWNTs through electrostatic repulsion.

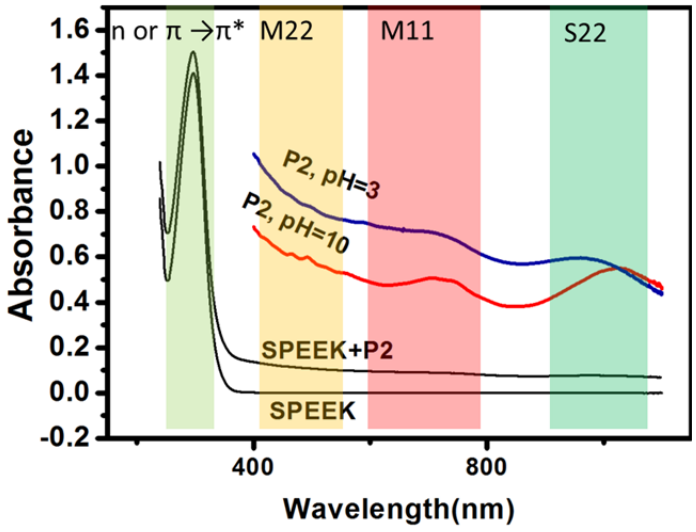

Figure 2.3 UV-vis spectroscopy of SPEEK aqueous solution and SPEEK-stabilized P2 SWNT dispersions under pH=3 and pH=10. The spectra at range of 400nm and above were shown to highlight the difference between different pH. The colored strips indicate the electron transitions contributing to the UV spectra. From left to right, lighter green: π-π* and n-π* transition in phenyl rings or C=O bond in SPEEK; yellow: M11 transition in SWNT; Red: M22 transition in SWNT; green: S11 transition in SWNT.

In UV-vis spectra of SPEEK, the absorption near 300nm in UV-vis spectra (Figure 2.3) can arise from both π-π* and n-π* transition in phenyl rings or C=O bond. In SPEEK-stabilized P2 SWNT dispersions a slight increase in the absorbance of this band is observed. The van Hove nanotubes bands in visible and NIR region (Figure 2.3) reveal interesting information about electronic interactions SPEEK and SWNT.[44-46,47] The bands[45] become sharper in basic dispersions compared to the acidic conditions under same preparation procedure, indicative of more exfoliated states of nanotubes due to increased ionization of SPEEK. One can also see a clear red shift in S22 (900nm-1100nm) bands around 1100 nm when pH is changed from pH3 to pH10. Unlike many previous cases of acid doping,[35] this suggests the increased doping of SWNTs in basic conditions, which usually causes the bleaching and reappearance of S22 band at the longer wavelength.[27] This is attributed to the larger surface area of more dispersed SWNT, which facilitates more efficient charge transfer between SPEEK and nanotubes, while the presence of acid groups in this system has less or no significance for doping process for SPEEK-SWNT pair.

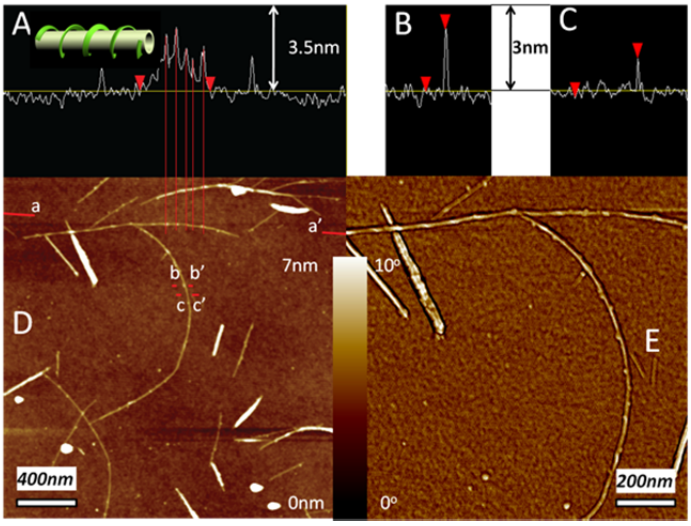

Figure 2.4 (A, B, C) Section analysis along a-a', b-b' and c-c' lines in AFM height image (D). a-a' line goes along the axis of an individual SWNT wrapped with SPEEK, while b-b' goes perpendicularly to the SPEEK-wrapped SWNT surface, while c-c' line is placed in the part where SWNT surface is bare. (E) A close-up phase image of nanotubes in (D). The cartoon in (A) inset demonstrates helical wrapping of SPEEK around SWNT.

Atomic force microscopy (AFM) images of SWNT dispersion at pH10 clearly display individual SWNTs with diameters around 1.4 ± 0.1 nm (Figure 2.4C), which agrees with their dimensions from the company specifications.[45] For macromolecules of interest for TC coatings, such as conductive polymers, both linear packing[48] and helical wrapping[43] were observed, dependent on the strength of interaction and rigidity of the polymeric chains.[49] In this system one can see that SPEEK wraps SWNTs in a helical manner (Figure 2.4 D and E), indicating the ability of the polymeric chains to coil around the nanotubes. The tight contact between SPEEK and SWNTs indirectly confirms the strong attractive interactions between SPEEK and SWNTs. The pitch of the SPEEK helix on SWNTs is 62nm (Figure 2.4A), which is similar to the pitch distance reported for DNA/SWNT hybrids.[50] At the same time, it is substantially longer than that for conductive polymer/SWNT hybrids with the pitch observed to be 14nm.[43]

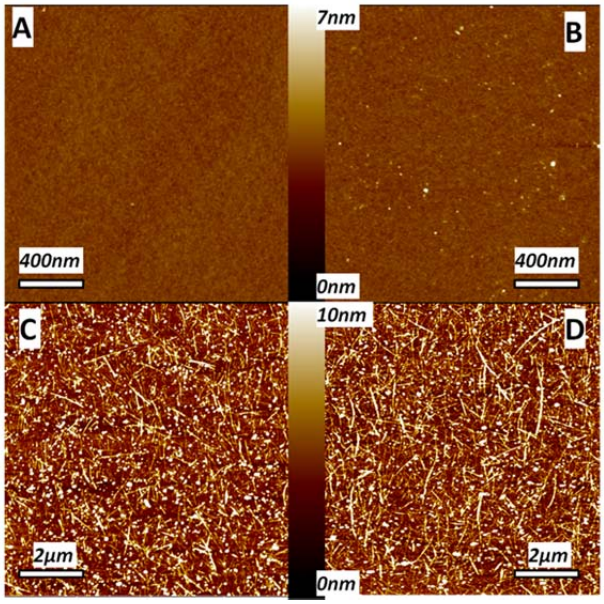

Figure 2.5 AFM height images of (A) HOCS layer on a silicon wafer, (B) $[HOCS/SPEEK]_1$without SWNT, (C) $[HOCS/SPEEK\text{-}P2]_1$ with SWNT on top and (D) $[HOCS/SPEEK\text{-}P2]_{1.5}$ with HOCS on top.

Unlike the continuous helixes shown for DNA/SWNT hybrids,[50] the periodicity of SPEEK/SWNT hybrids pitches are sometimes interrupted. The inconsistency of pitch distance arises from the relatively short chain of SPEEK,[50] estimated to be several hundred nanometers (for an average molecular weight of 50kDa),[51] while the length of the studied DNAs molecules was *ca*. 1.4μm.[50] Several molecular chains of SPEEK are needed to stabilize an individual SWNT, whose length is usually over 1μm. The AFM analysis of cross-sections along the *Z*-axis suggests that SPEEK "wrap" has a height of 2.2±0.1nm (Figure 2.4B). The thickness of polymer layer can thus be estimated to be (2.2-1.4)/2=0.4nm, which is consistent with a gap of 0.34nm characteristic for a stack of two aromatic rings bonded by π-π interaction.[52]

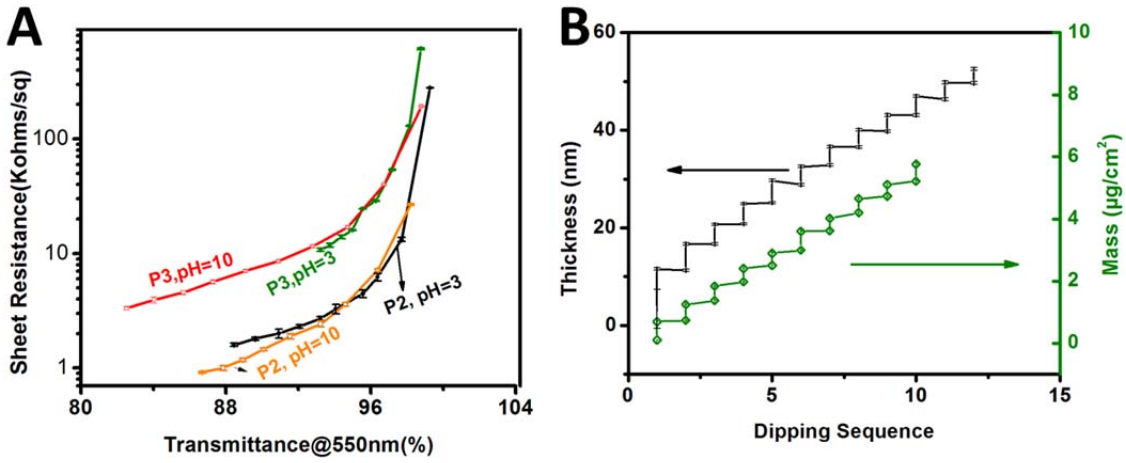

Figure 2.6 (A) Sheet resistance and transmittance@550nm of P2 and P3 SWNT LBL thin films under different pH values. Ten LBL deposition cycles were made for each set of conditions. (B) Dependence of thickness and mass of $[HOCS/SPEEK\text{-}P2]_n$ assembled at pH10 with the increasing number of LBL deposition cycles.

2.3.3 Layer-by-layer assembly

SPEEK-dispersed SWNTs were found to easily form multilayers with HOCS for both SWNT coatings and free-standing films. According to ellipsometry and quartz crystal microbalance (QCM) measurements (Figure 2.6B) the growth follows a linear fashion, with an average thickness of 3.7±0.5 nm and mass deposition of 0.47±0.08 $\mu g/cm^2$ for SWNT layers. Interestingly the average thickness increment for HOCS layers is negative and is equal to -0.2±0.4nm (large accidental errors are due to the very small thickness decrement, which can be smoothed by averaging 12 data to reveal the real trend. Examining each point in Figure6B can clearly see the decease of thickness) while mass increment is positive and equal to 0.10±0.05$\mu g/cm^2$. The overall density of the composite can be calculated to be $1.6 g/cm^3$, which is close to the average density of constituent materials, and much greater than that of buckypaper prepared from filtration method[53] (Table 2.1 and 2.2), which points to lower nanoscale porosity and excellent integration of polymers and nanotubes. The negative thickness increment with positive mass increment for each stage of HOCS adsorption stage is quite peculiar and indicates densification of the films. One can surmise that it occurs due to removal of a small amount of excessive SPEEK which is not tightly wrapped around SWNTs. A control experiment shows that a layer of free SPEEK adsorbed on glass is indeed washed off by HOCS being however unchanged after the DI water wash. Confirming the same point, LBL assembly of SPEEK (without SWNTs) and HOCS showed insignificant and erratic film growth pattern (Figure 2.10). One can also see here a manifestation of strong interaction between HOCS and SWNTs enabling the multilayer growth. These interactions are likely to include hydrophobic attraction, and van der Waals forces between the sugar cycle and curved graphene sheet.[33, 54] The presence of SWNTs in the

LBL films also delocalizes negative charge on SPEEK due to their high polarizability[55, 56] and axial anisotropy, which reduces localized electrostatic repulsion between adjacent SPEEK molecules that destabilizes the multilayers. This special assembly mechanism results in minimal incorporation of polymers in the coating while retaining highly accurate and predictable control over coating thickness. Due to the very thin polymer coatings, it is difficult to identify the layered structure in the composite even by TEM.[32]

AFM image in Figure 2.5A shows that HOCS forms a smooth layer on the substrate. A dense and strictly in-plane orientation of SWNTs layer can be subsequently adsorbed onto HOCS (Figure 2.5C). In addition to SWNTs, some nanoscale particles also appear on the surface. Initially, these particles were believed to be amorphous carbon present in small amount in SWNTs. However, a control experiment of direct adsorption of SPEEK onto HOCS also showed their presence (Figure 2.5B). Apparently, some of the molecular chains of SPEEK can be adsorbed onto the HOCS layers in a globular form. The number of SPEEK globules is reduced after depositing a layer of HOCS (Figure 2.5D). This is consistent with the negative thickness and positive mass increments observed in Figure 2.6B.

2.3.4 Optical and Electrical Properties

The transparency *vs.* conductivity curves are dependent on multiple factors including the pH and type of the nanotubes. P2 dispersions give noticeably better overall transparency and sheet resistance (920 ohms/sq with 86.7%@550nm) (Figure 2.6A) than P3 due to lower degree of oxidation. The opto-electrical properties of LBL coatings at different pH for P2 or P3 are quite similar, except that the deposition was faster in the basic condition, especially for the type of P3. Higher pH usually gives better exfoliation

of SWNT due to the more ionized state of sulfonic and carboxylic acid group. The more dispersed state of SWNT can generate a higher concentration of individual SWNT to expedite adsorption. In addition, electrostatic attraction for the assembly can be stronger when more charged groups are on SWNTs.

To be noticed, the sheet resistance of SWNT coatings decreases when depositing an extra insulating layer of HOCS on top (Figure 2.12). This observation may contradict the conventional notion and multiple data[29, 35] that addition of insulating matrix should decrease conductance, but is perfectly consistent with the mechanism of LBL deposition and expected changes in nanometer scale organization of the film. The improvement of conductivity results from the partial removal of SPEEK in HOCS solutions as discussed previously. Additionally, applying the HOCS layer could also result in densification of SWNT networks due to capillary effect and surface energy difference, thus in turn lowering the conducting barriers and causing the unusual decrease in resistance. Similar experimental results were also recently observed when applying an insulating layer of tetraorthosilicate sol on top of SWNT networks, which is essential for passivation of SWNT coatings without sacrificing conductivity.[57] The densification of coatings can be indeed seen as the negative growth characteristic of HOCS layers (Figure 2.6B). As we can see later addition of HOCS can also improve doping of SWNTs.

The conductivity of LBL assembled composites was evaluated by measuring the resistance and thickness of 200 bilayers to eliminate potential errors when working with thin hardly visible coatings. Robust freestanding films can be delaminated from glass substrate by HF (Figure 2.8A, B and C).[33, 58] The thickness across 200 bilayer films denoted as $[HOCS/SPEEK\text{-}P2]_{200}$ was 1000±40 nm, while $[HOCS/SPEEK\text{-}P3]_{200}$ was

620±20 nm. The average thickness per bilayer can accordingly be calculated to be 5.0±0.2nm and 3.1±0.1nm, agreeable with ellipsometry measurements. The conductivity of $[HOCS/SPEEK\text{-}P2]_{200}$ is 1.1×10^5S/m and turns lower when P3-SWNT are used, *i.e.* 7.2×10^4S/m. As a comparison, the P2 SWNT coatings made by filtration and subsequent PDMS transfer method had conductivity ranging from 1.6×10^5S/m to 2×10^5S/m,[7] while for P3 the conductivity was 7.3×10^4S/m.[9] Unlike these coatings which consist mostly of SWNTs, LBL assembled SWNT composites are quite remarkable in conductivity considering that they contained a lot of insulating matrix (34.38wt% or 44.03 vol%, supporting information) and demonstrate both the capabilities of LBL in materials engineering and importance of fine degree of structural control for these composites. The property is also superior to other SWNT/polymer composites made from other methods, for instance, SWNT/polystyrene composites with SWNT volume fraction as high as 50% were reported have a conductivity of 1×10^4S/m.[59] Even when the matrix was replaced by conductive polymers, conductivity only went up to 7×10^4S/m.[60]

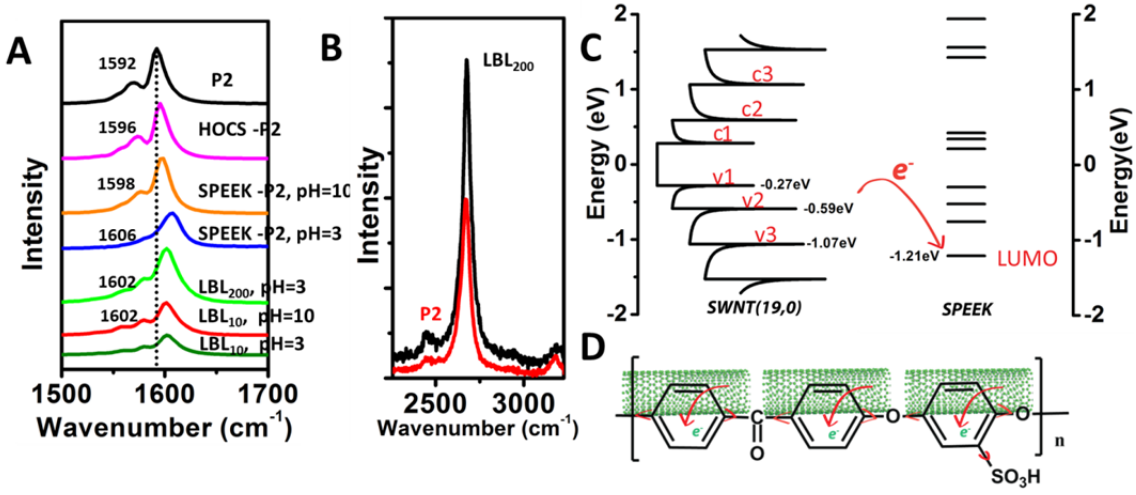

Figure 2.7 (A) *G* band in Raman spectra of as received P2 SWNT, P2 and HOCS half-half mixtures (P2-HOCS), P2 and SPEEK 1:4 mixtures (P2-SPEEK) at pH3 and pH10, $[HOCS/SPEEK\text{-}P2]_{200}$ free standing film at pH3 and $[HOCS/SPEEK\text{-}P2]_{10}$ coatings

assembled at pH3 and pH10. (B) *G*' band of P2 SWNT and $[HOCS/SPEEK\text{-}P2]_{200}$. Excitation wavelength for all Raman spectra is 532nm. (C) Density of states of SWNT(19,0) and energy band of SPEEK from quantum mechanical calculations. The HOMO level is at -9.28eV for SPEEK, which is not shown in the graph. (D) Diagram of charge transfer between SPEEK and SWNT.

2.3.5 Mechanism of Doping

The transparency *vs.* conductivity curve for $[HOCS/SPEEK\text{-}P2]_n$ indicates substantially higher conductivity for the same amount of deposited SWNT than for $[poly(vinyl\ alcohol)/poly(styrene\ sulfonate)\text{-}P2]_n$ or $[PVA/PSS\text{-}P2]_n$ which has a sheet resistance of 1790ohms/sq with a transmittance of 85%@550nm (Figure 2.13). This fact is indicative of possibly different mechanism of doping than from $-SO_3H$ groups and prompted us to look in greater details of electronic processes between SWNTs and SPEEK. The better overall performance of the studied film can be partially ascribed to the higher SWNT fraction obtained in the final film, which was estimated to be as high as 66wt% (Supplemental materials), as compared to 47wt%[34] or 10wt%[33] in previous studied SWNT LBL multilayer composites. However, this does not give a complete picture of the phenomenon. The *in-situ* doping of SPEEK does play the key role here, which can be verified by Raman spectroscopy. The *G* band in SWNT Raman spectrum undergoes a blue shift as a consequence of phonon stiffening induced by hole-doping.[27, 29] The *G* band of LBL assembled SWNT film shows a clear blue-shift by about 10 cm^{-1} *vs.* the original nanotubes (Figure 2.7A). Notably, this shift is comparable to that from such a strong dopant as $AuCl_3$[27] and is slightly larger than the shift from HNO_3 and H_2SO_4 doping,[29] which demonstrates that SWNTs in the film are indeed heavily doped. It is also known that the intensity of *G*'-band rises as metallicity of the sample increases.[27,

[61] The effect of enhanced hole-doping is also manifested in the increased intensity of *G*'-band near 2675cm^{-1} (Figure 2.7B). Similar shifts were also observed in P3 SWNT LBL films (Figure 2.15A).

The doping of SWNT in the LBL film can be contributed both by SPEEK and HOCS, as can be shown by Raman spectra of their mixtures with SWNT (Figure 2.7A). A blue shift of 4 cm^{-1} for HOCS and of 6 cm^{-1} for SPEEK (pH=10) were observed. The stronger shift (10 cm^{-1}) in the LBL film was a mutual and synergistic effect from both of the dopants. A much larger shift of 14cm^{-1} occurred for SPEEK-P2 SWNT mixtures at pH=3, which can be caused by residual traces of H_2SO_4 inside SPEEK. After drying, the traces of H_2SO_4 can be locally concentrated to form even stronger dopant. However, there is no difference between the *G* band shifts in LBL assembled films at different pH and even different thickness, which indicates that the impurities, such as H_2SO_4 are completely removed by the thorough rinsing in each of LBL cycles and are not relevant for doping.

Independence of *G*-band shift on pH and much greater conductivity observed for SPEEK than for PSS (Figure 2.15B) brings up the question about the chemical nature of the groups responsible for doping. The above observations are inconsistent with the mechanism based on hole-doping of SWNTs by -SO_3H groups. Let's recall the fact that *p*-doping is the partial transfer of electrons from SWNTs to a dopant. For this reason, Brönsted and Lewis acids, such as concentrated H_2SO_4, HNO_3, or $AuCl_3$, are so effective when intercalated into SWNT bundles.[27, 62] We also considered possibilities those other groups besides -SO_3H, for instance –SO_3^-, -C=O, and multiple oxygen atoms in HOCS and SPEEK, could potentially act as local electron acceptors or donors (electron-doping).

But none of these assumptions can consistently explain experimental data in this study. For example, $-SO_3^-$ group alone, cannot cause a significant shift in the *G* band of SWNTs neither as a hole- or electron-dopant, based on the previous data for SWNT dispersions stabilized with sodium dodecyl sulfate.[63]

It is thus suggested that that the charge transfer process is mediated by the phenyl rings of SPEEK rather than the direct doping from $-SO_3H$ functional groups. In order to evaluate the possibility of this mechanism, molecule orbital calculations were performed to establish the relative energies of HOMO and LUMO orbitals in SPEEK. For comparative purposes the same calculations were also performed for structurally related PSS (Figure 2.16A and C). The corresponding energy densities of state were also calculated[27] for a semiconducting SWNT (19, 0) with diameter of 1.48nm, and energy gap of S22 of 1.2eV, representative of the SWNTs in this study. It was found that SPEEK has a much lower LUMO energy of -1.21eV than LUMO of PSS (-0.70eV, Figure 2.16C and E) being at the same time substantially lower than the top of valence band of SWNT (Figure 2.7C) located at -0.27eV and even two other valence bands located at -0.59 and -1.07 eV. The correctness of the quantum mechanical calculation was confirmed by the excellent agreement of calculated and experimental UV spectra of SPEEK (Figure 2.16B). The low energy of LUMO in SPEEK, the presence of other unoccupied orbital above it, and tight wrapping of the polymer around the nanotubes (Figure 2.4) provide all the necessary conditions for effective electron transfer from SWNT to SPEEK (Figure 2.7D). Due to the higher position of LUMO of PSS, the hole-doping by this polymer is much less effective. It is also likely that unfavorable geometry of phenyl rings of PSS around SWNT allow less extensive π-stacking.

The charge transfer effects are also indicated by significant downshift of carbon[64] and change of oxygen photoemission peaks in the XPS spectra in the SWNT nanocomposite (Figure 2.17). A downshift of -2.4eV is much larger than what's reported for hole doping of small molecules,[29] which is usually around -0.2eV to -0.5eV, suggesting significant Fermi level shift due to the charge transfer. Through doping, the conductivities of semiconducting SWNT can be increased and the Schottky barrier between metallic and semiconducting SWNT can be reduced,[27] which would contribute to the improvement of overall conductivities of composite.

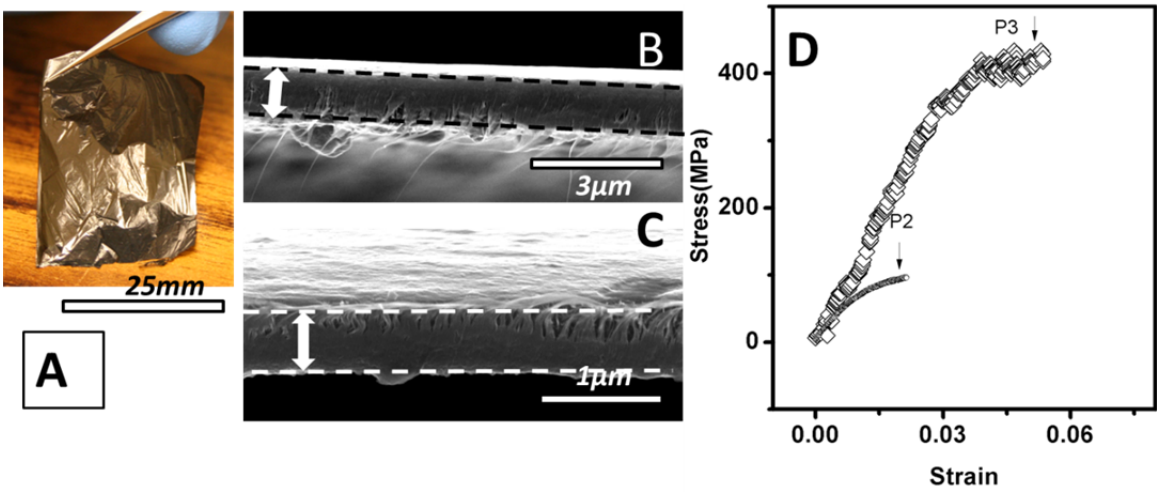

Figure 2.8 (A) Free-standing film of $[HOCS/SPEEK-P2]_{200}$. Cross-section images of (B) $[HOCS/SPEEK-P2]_{200}$ and (C) $[HOCS/SPEEK-P3]_{200}$. The arrows show the cross-sections of films. (D) Representative stress-strain curve of $[HOCS/SPEEK-P3]_{200}$ and $[HOCS/SPEEK-P2]_{200}$

2.3.6 Mechanical Properties

Although LBL coatings from P2-SWNT have higher conductivity than those with P3-SWNT, their ultimate strength is only 90±10MPa, which is much lower than P3-SWNTmultilayers with tensile strength of 360±35MPa (Figure 2.8D). Stiffness and

toughness followed similar trend: 13±2.4GPa, 7.5±3 kJ/m^3 compared with 7±0.4 GPa, and 0.9±0.3 kJ/m^3. The mechanical properties of the P2-SWNT LBL films are superior to those of bucky paper, with ultimate strength distributed from 10MPa to 76MPa in ultimate strength and stiffness from 0.2GPa to 2GPa.[65] More carboxylic acid groups in P3 SWNTs facilitate stronger interactions with HOCS matrix. As was reported recently that the degree of oxidation of SWNTs can be optimized to confer the highest mechanical properties achieved so far for LBL assembled SWNT composite.[34]

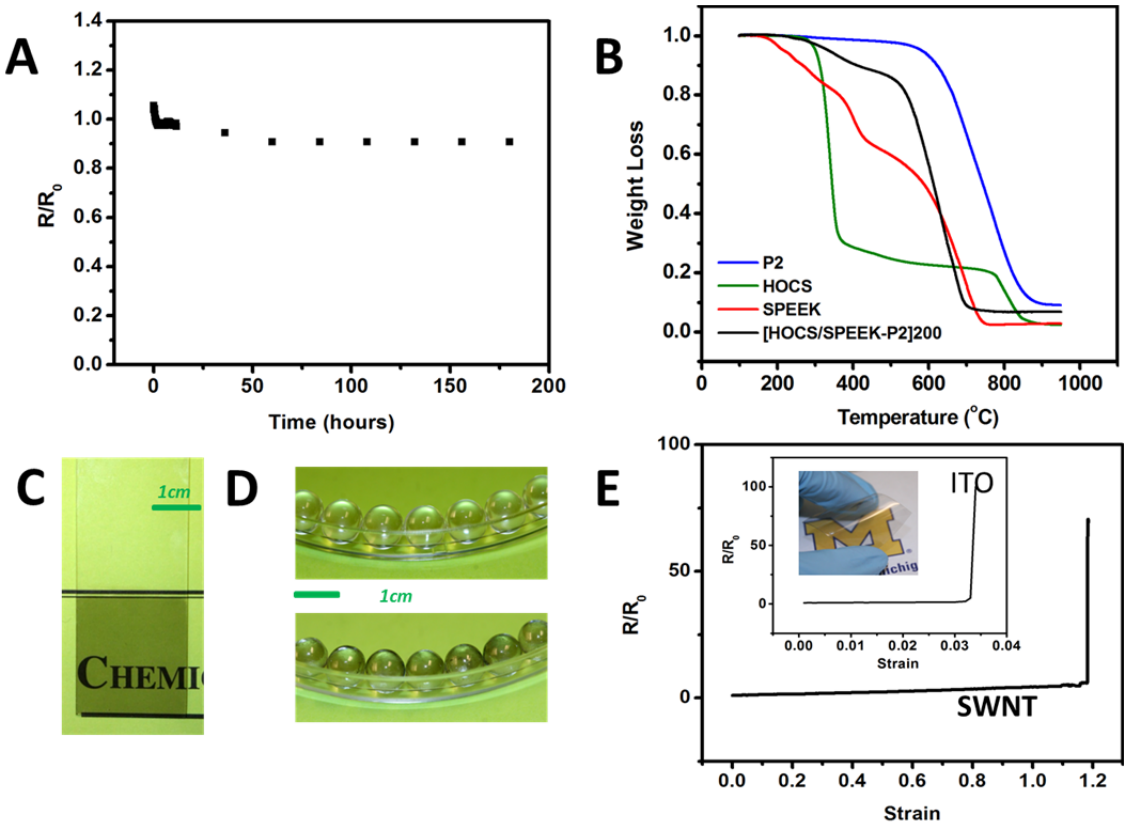

Figure 2.9 (A) Electrical stability of SWNT thin films at 100°C. (B) TGA analysis of P2 SWNT, HOCS, SPEEK and [HOCS/SPEEK-P2]$_{200}$. Flexibility of LBL method demonstrated on glass slide (C) and glass beads (D), plastic substrate (E, inset) for transparent coatings. (E) Dependence of surface resistance on stretching strain for LBL SWNT coatings and ITO on PET substrates.

It needs to be pointed out that the mechanical strength of free-standing film can only partially reflect mechanical behavior of coatings.[66] Mechanical performance of the coatings tends to be even better on the substrate as the separation process is likely to introduce some amount of defects onto free-standing films.

2.3.7 Environmental Stability

Environmental stability of TCs is desirable in most of the practical applications. For example, in actual device fabrications, active layer deposition or module encapsulation usually involve moderate temperature processes[23] and the actual device operation can also cause elevated temperatures. The electrical stability of SWNT thin films here was evaluated by exposing the film in air at 100^{o}C for a week, which may be one of the harshest environments TCs can be involved in reality (Figure 2.9A). Transparency of the film was not affected through this process (Figure 2.18). The resistance increased by 4% when the temperature was raised due to the metallic nature of the film, and then dropped quickly within one hour as a result of thermal annealing and kept almost unchanged after 60 hours. The incredible "shelf life" of the film originates from the involatility of the polymer dopant and placid nature of SWNTs. In addition, only 10% of mass loss was observed after burning in air at 500^{o}C, which is quite remarkable for organic coatings (Figure 2.9B).

The surface of coatings with few layers deposited had roughness of 3.5nm which was comparable to 2.4nm of typical ITO surface or 3.1nm for PEDOT passivated SWNT surface.[9] Additionally, these coatings could be uniformly deposited not only on planar glass slides and but easily on spherical glass beads and flexible polymer substrate (Figure

2.9 C, D and E). To the best of the authors' knowledge, this is the first report to demonstrate SWNT transparent coatings on curved surfaces. LBL technique could be more competitive and advantageous over available methods when uniform, transparent and conductive spherical surfaces are needed. The process is also amenable to scaled-up versions of TC deposition.[35]

2.3.8 Comparison with ITO

ITO thin films undergo catastrophic failure when the strain is over 0.03 which leads drastic decrease of conductivity.[11, 31] On the contrary, TCs from SWNT only show a gradual increase in resistivity upon stretching; the catastrophic conduction failure only occurs when the substrate is physically pulled apart.[35] The traditional TC figure of merit (TCFM) is defined as TCFM=σ/α, where σ is electrical conductance and α is visible absorption coefficient.[67] ITO has a high TCFM, close to 4 ohms^{-1}, [67] and in these terms is better than most of reported SWNT transparent conductors. However, the traditional TCFM fails to take into account other properties highly relevant for TCs. Mechanical properties are one of the most valuable properties for the state-of-art TC; other properties could also be included in the consideration. Therefore, it would be logical to introduce a parameter of critical strain ε_c of TC into the currently used figure of merit.[35] The new TCFM can be expressed as $\Pi_{TC}=\sigma\varepsilon_c/\alpha$ with the new parameter in the nominator because the larger the critical strain the better it is for most of TC applications and in particularly for flexible electronics. ITO on polyethylene terephthalate (PET) substrate (Sigma-Aldrich) displays a sheet resistance of 60ohms/sq at 80% (550nm) and critical strain of 0.032 (Figure 2.9E),[11] which corresponds to Π_{TC} of 0.006 ohms^{-1}(Supporting

information). And one of the best ITOs on PET reported so far was 14.19ohms/sq at 80% (550nm),[68] and had Π_{TC} of 0.023 $ohms^{-1}$, assuming same critical strain. For the appropriate comparison, we made SWNT LBL films on identical PET substrates. Due to the self-organizing/assembling characteristics of LBL method, the performance of coatings is independent of substrate. The sheet resistance can be kept around 960 ohms/sq and transmittance of 86.7% at 550nm on PET substrate using the same recipe on glass substrate (Figure 2.6A). The strain for catastrophic conductivity failure for them was observed at ε_c= 120% (Figure 2.9E).[35] Π_{TC} of the LBL assembled transparent conductor thus can be estimated to be 0.022$ohms^{-1}$, which is clearly higher than that of commercial ITO, and comparable to the best ITO reported. Another interesting point to note is that experimentally elongation for catastrophic conductivity failure of thin SWNT coatings on elastic substrates is much higher than maximum mechanical extensibility of corresponding free-standing film of SWNT (Figure 2.8D). Unlike free-standing films, the coatings are stretched uniformly over both "weak" and "strong" points and can undergo, therefore, even greater extensions.

2.4 Conclusion

In this chapter, SPEEK has been introduced as an effective stabilizer and hole-dopant for SWNTs. It helically wraps the nanotubes making possible effective π-π stacking interactions. The alignment and effective hybridization of the unoccupied electronic levels of SPEEK and valence bands of SWNTs facilitates charge transfer comparable or better in effectiveness to other dopants. The use of SPEEK combined with ability of LBL technique to produce highly uniform composites with characteristically

strong intermolecular interactions between the components allow for improvement of multiple parameters in SWNT-based TCs.

The cumulative hole-doping of SWNTs from SPEEK and its LBL partner, HOCS, allow one to get rid of volatile and corrosive doping agents, such as acids. Smooth and acid-free SWNT TCs with competitive transparency conductance curves were demonstrated on both planar and curved substrates. The overall performance of the fabricated TCs is better than commercially available ITO on PET taking into account the critical strain of the coating material. In addition, these thin coatings demonstrate record thermal stability.

With their current performance parameters LBL-made TCs with π-doping are suitable for many applications.[69] However, the most demanding applications, such as solar cells and LEDs, will require further reduction of the sheet resistance. Properties of SWNT TCs can be further optimized by introduction of stronger electron-withdrawing functional groups such as nitro-groups (-NO_2) in phenyl rings capable of π-π stacking interactions with SWNTs. Calculation shows that introduction of –NO_2 into phenyl rings in the SPEEK unit can significantly lower the LUMO level to -4.20eV (Figure 2.16D and F). In addition, selective deposition of metallic SWNT on substrate, and proper control over the alignment of SWNTs inside the composite would be beneficial for improving the electrical conductivity of composites. It will be interesting as well to establish the detailed mechanism of doping of SWNTs by HOCS, however, it is apparently less effective than π-doping observed for SPEEK.

π-doping with polymer can be further extended to graphene TCs. Moreover, freestanding and flexible films with high conductivity, thermal stability, and robustness obtained by LBL steps can be vital in other applications, such as neural interface[1, 70] and actuators.[71]

2.5 Supplementary Information

The material in this Chapter has been adapted with minor modifications from the following peer-reviewed, published article:

Zhu, J.; Shim, B. S.; Di Prima, M.; Kotov, N. A., Transparent Conductors from Carbon Nanotubes Lbl-Assembled with Polymer Dopant with Π−Π Electron Transfer. J. Am. Chem. Soc. 2011, 133, 7450—7460.

Quantification of SWNT fraction in the LBL assembled composites. Thermal gravimetric analysis (TGA) is commonly used to determine the nanoparticle content inside a LBL assembled film. In the SWNT nanocomposite with SPEEK, the TGA analysis is complicated due to the multiple components and high temperature resilience of several of them. We had to use a different quantification procedure based on a combination of QCM and EDAX results.

According to QCM results (Figure 2.6B), HOCS has a mass deposition increment of 0.100±0.047μg/cm^2 in comparison to 0.476±0.082μg/cm^2 for SPEEK stabilized P2 SWNT per layer. HOCS can thus to be determined to have a mass fraction of 17.36%, which can be slightly underestimated due to the dissolution of SPEEK during the deposition process. EDAX is a useful technique to quantify elements, and penetration

depth is 1.2μm on bulky carbon under 10kV electron beam. An EDAX analysis (Figure 2.14A) on SPEEK shows the element atomic ratio C:O:S= 16.93:7.05:1, which correlates well with the assumed SPEEK unit of [$C_{19}O_6SH_{12}$] shown in Figure 1. Elements of the LBL assembled film can also be easily determined accordingly, with C:O:S=142.32:20.61:1. SPEEK is the only component inside film with sulfur element, so that its content can be easily determined to be as 17.02%. The last component SWNT can thus be calculated to be 65.62%.

Unlike the previously studied systems, mass fraction can be easily estimated from TGA curves (Figure 2.14B). Only SWNT leaves traces of residue after burning until 950^0C, so the content of SWNT can be determined by analyzing the residue of the film after burning. Estimated from this method, the fraction of SWNT is 73.91%, quite agreeable with the previous analysis.

In the P3 composite, C:O:S has an atomic ratio of 222:54:1, corresponding to a weight percentage of 0.91% of S. Weight fraction of SPEEK can thus be determined to be 10.05%.

Complete reference of (24): Bae, S.; Kim, H.; Lee, Y.; Xu, X. F.; Park, J. S.; Zheng, Y.; Balakrishnan, J.; Lei, T.; Kim, H. R.; Song, Y. I.; Kim, Y. J.; Kim, K. S.; Ozyilmaz, B.; Ahn, J. H.; Hong, B. H.; Iijima, S. Nat. Nanotechnol. 2010, 5, 574.

Cumulative Figure of Merit (Π_{TC}) calculation of ITO: In our previous publication, we estimated Π_{TC} of ITO is 0.07 ohms-1 by using the best property of ITO reported on **glass**: **6 ohms/sq at 90%** [Ref: Gordon, R.G. Mrs Bulletin 25, 52 (2000)], and critical strain of **1.7%** [Ref: Chen, Z., et al. Thin Solid Films 394, 201-205 (2001).] . (The transmittance T and visible absorption coefficient α can be converted by α=*-lgT*.) When drafting this

paper, we realized that the performance of ITO on plastic substrate, such as PET, can be much worse due to the low processing temperature required for polymer substrate. Thus in this paper, we quoted the best results of ITO on PET substrate, and tested the commercially available ITO in our lab. We believe this data can more accurately reflect the real performance of ITO on PET.

Table 2.1 Density of materials.

	Density(g/cm^3)
HOCS	1.5
PEEK	1.32
SWNT	2.11
Buckypaper	0.28~0.42

Table 2.2 Intrinsic density of an individual SWNT(19, 0).

Diameter	**1.48**	**nm**
Length	2.5	nm
Number of atoms	456	
Mass	9.09×10^{-21}	g
Volume	4.30	nm^3
Density	2.11	g/cm^3

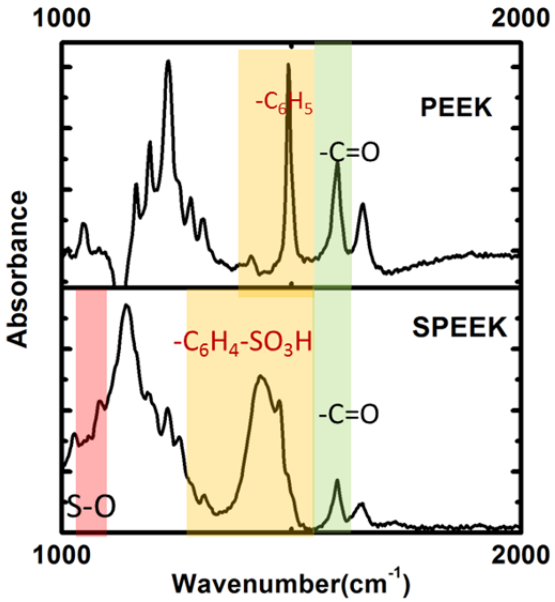

Figure 2.10. Fourier transform infrared (FTIR) spectra of PEEK and SPEEK.

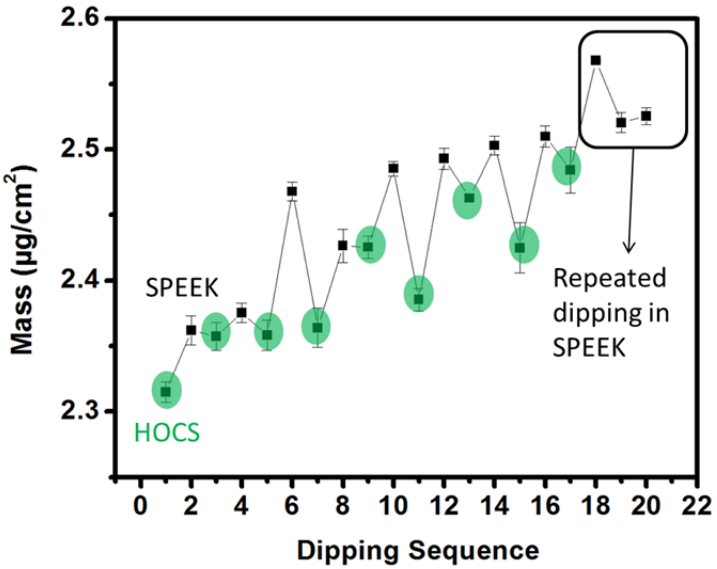

Figure 2.11. Mass deposition with the increasing dipping sequence for $[HOCS/SPEEK]_n$ multilayers. A layer of [polyethyleneimine/polystyrene sulfonate] was initially deposited onto the quartz crystal.

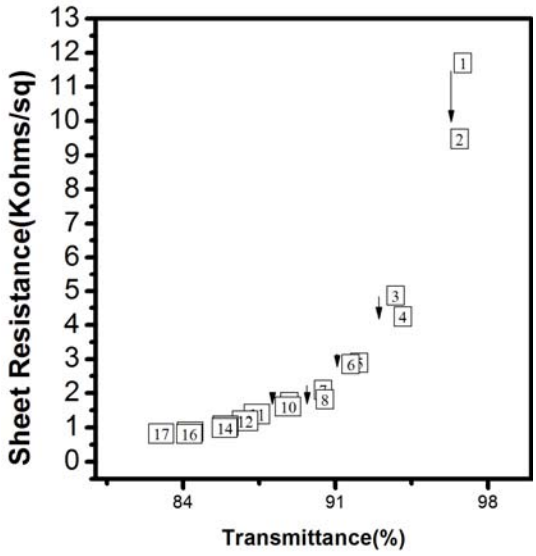

Figure 2.12. Sheet resistance vs. transmittance@550nm for $[HOCS/SPEEK\text{-}P2]_n$. The number marked on each point indicates the LBL deposition cycle, with odd number for SWNT layer and even number for HOCS adsorption layers. The enumeration starts from the first SWNT layer.

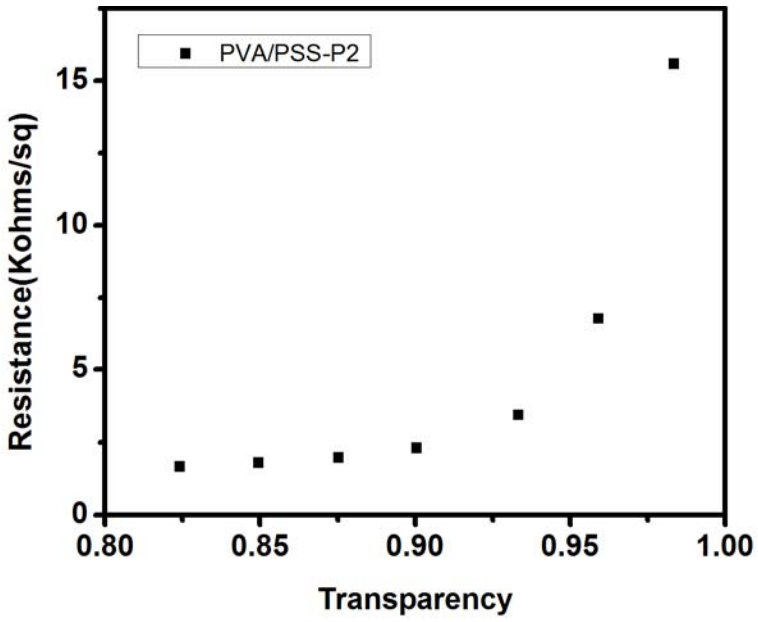

Figure 2.13. Sheet resistance vs. transmittance@550nm for [PVA/PSS-P2]. The preparation of the film follows the optimized recipe and procedure in Reference 5.

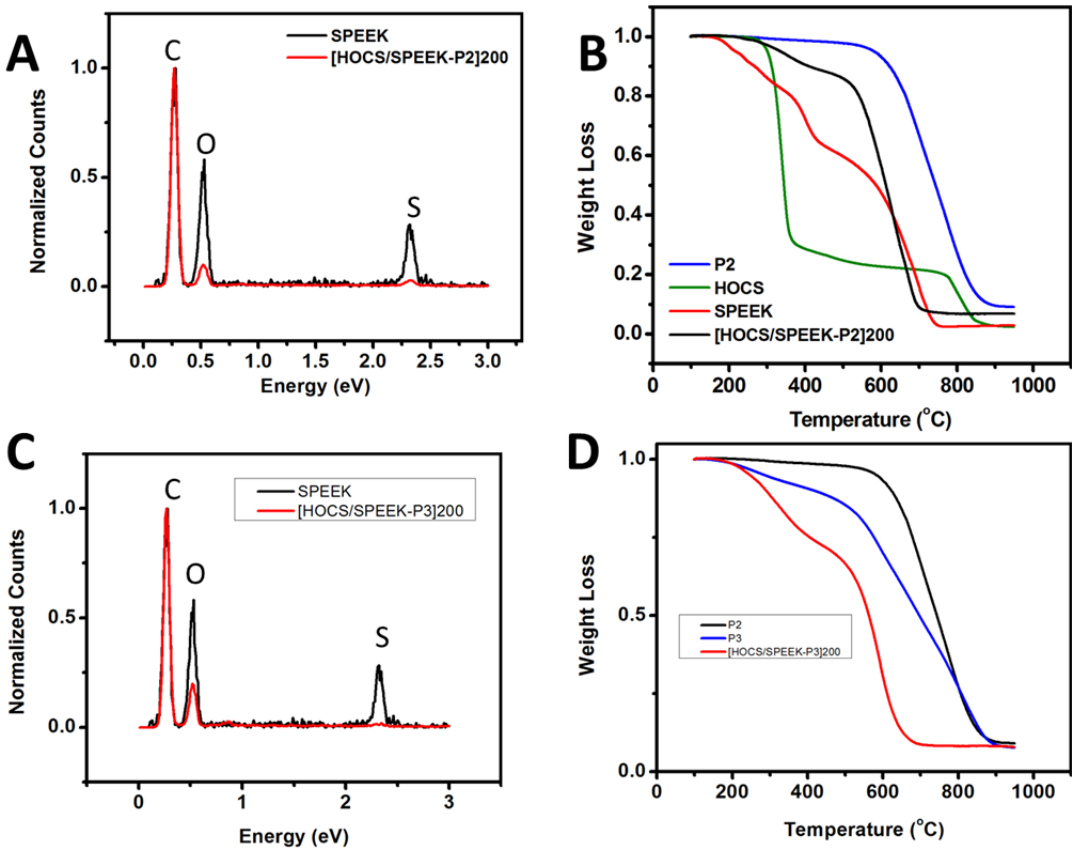

Figure 2.14. (A) EDAX analysis of SPEEK and $[HOCS/SPEEK\text{-}P2]_{200}$ (B) TGA analysis of P2 SWNT, HOCS, SPEEK and $[HOCS/SPEEK\text{-}P2]_{200}$ (C) EDAX analysis of SPEEK and $[HOCS/SPEEK\text{-}P3]_{200}$ (D) TGA analysis of P2 SWNT, HOCS, SPEEK and $[HOCS/SPEEK\text{-}P3]_{200}$.

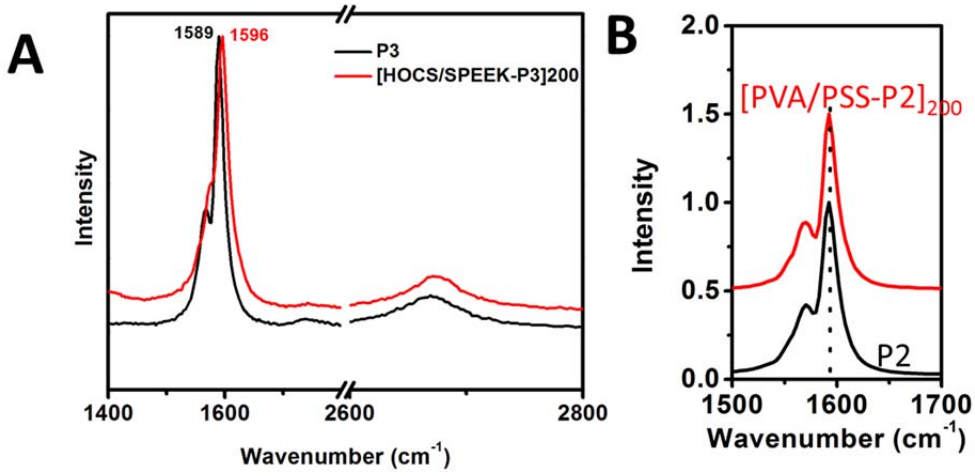

Figure 2.15. (A) Raman spectra of P3 SWNT and $[HOCS/SPEEK\text{-}P3]_{200}$. (B) *G* band in Raman spectra of P2 SWNT and $[PVA/PSS\text{-}P2]_{200}$. No significant shift can be seen.

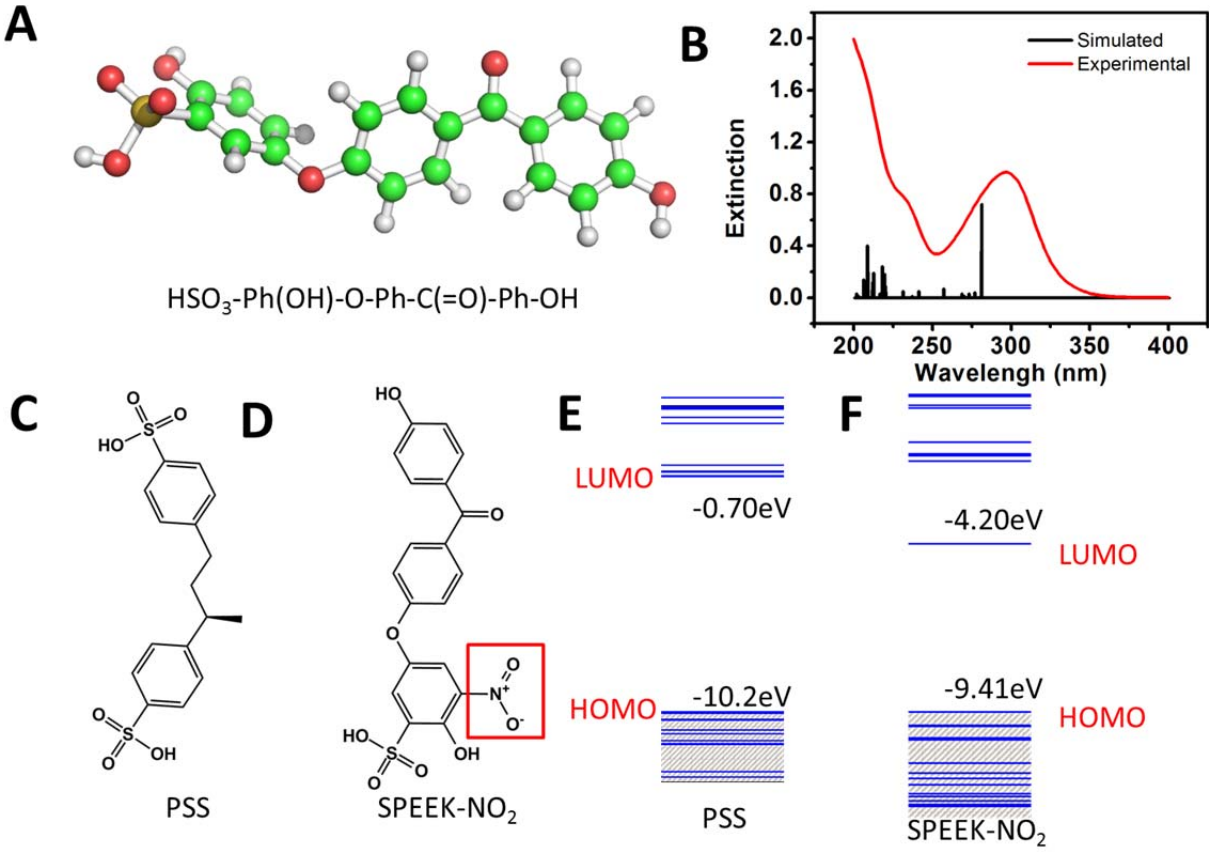

Figure 2.16. (A) 3D model of SPEEK unit used for calculation of energy levels. (B) Comparison between simulated and experimental UV spectra of SPEEK. (C) PSS unit used for calculation of energy levels. (D) SPEEK unit with $-NO_2$ substituting into phenyl ring. (E, F) Energy levels of PSS and SPEEK-NO_2.

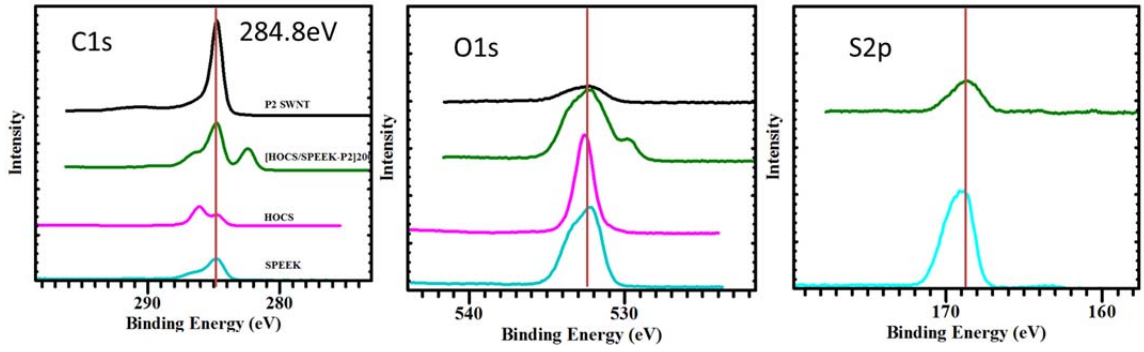

Figure 2.17. XPS spectra of $[HOCS/SPEEK\text{-}P2]_{200}$, HOCS, P2 SWNT and SPEEK.

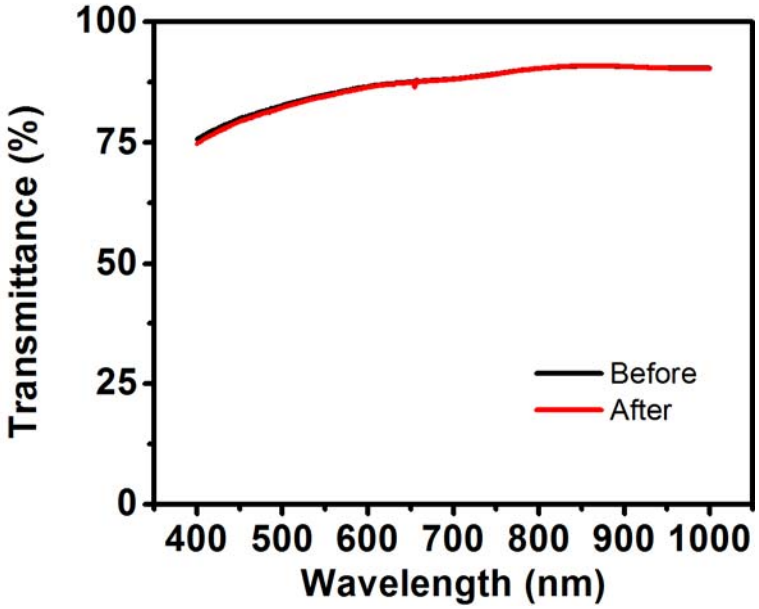

Figure 2.18. Transmittance of $[HOCS/SPEEK\text{-}P2]_{10}$ across visible wavelength range before and after keeping the film in the air at 100^{o}C for a week.

2.6 References

1. Kotov, N. A.; Winter, J. O.; Clements, I. P.; Jan, E.; Timko, B. P.; Campidelli, S.; Pathak, S.; Mazzatenta, A.; Lieber, C. M.; Prato, M.; Bellamkonda, R. V.; Silva, G. A.; Kam, N. W. S.; Patolsky, F.; Ballerini, L., Nanomaterials for Neural Interfaces. *Adv. Mater.* **2009**, 21, 3970—4004.
2. Meyer, W. H., Polymer Electrolytes for Lithium-Ion Batteries. *Adv. Mater.* **1998**, 10, 439-448.
3. Endo, M.; Kim, Y. A.; Hayashi, T.; Nishimura, K.; Matusita, T.; Miyashita, K.; Dresselhaus, M. S., Vapor-Grown Carbon Fibers (Vgcfs): Basic Properties and Their Battery Applications. *Carbon* **2001**, 39, 1287-1297.
4. Monroe, C.; Newman, J., The Impact of Elastic Deformation on Deposition Kinetics at Lithium/Polymer Interfaces. *J. Electrochem. Soc.* **2005**, 152, A396—A404.
5. Granqvist, C. G., Transparent Conductors as Solar Energy Materials: A Panoramic Review. *Sol. Energy Mater. Sol. Cells* **2007**, 91, 1529-1598.
6. Ou, E. C. W.; Hu, L. B.; Raymond, G. C. R.; Soo, O. K.; Pan, J. S.; Zheng, Z.; Park, Y.; Hecht, D.; Irvin, G.; Drzaic, P.; Gruner, G., Surface-Modified Nanotube Anodes for High Performance Organic Light-Emitting Diode. *ACS Nano* **2009**, 3, 2258-2264.
7. Zhou, Y. X.; Hu, L. B.; Gruner, G., A Method of Printing Carbon Nanotube Thin Films. *Appl. Phys. Lett.* **2006**, 88.
8. De, S.; Lyons, P. E.; Sorel, S.; Doherty, E. M.; King, P. J.; Blau, W. J.; Nirmalraj, P. N.; Boland, J. J.; Scardaci, V.; Joimel, J.; Coleman, J. N., Transparent, Flexible, and Highly Conductive Thin Films Based on Polymer,Nanotube Composites. *ACS Nano* **2009**, 3, 714-720.
9. Zhang, D. H.; Ryu, K.; Liu, X. L.; Polikarpov, E.; Ly, J.; Tompson, M. E.; Zhou, C. W., Transparent, Conductive, and Flexible Carbon Nanotube Films and Their Application in Organic Light-Emitting Diodes. *Nano Lett.* **2006**, 6, 1880-1886.
10. Hellstrom, S. L.; Lee, H. W.; Bao, Z., Polymer-Assisted Direct Deposition of Uniform Carbon Nanotube Bundle Networks for High Performance Transparent Electrodes. *ACS Nano* **2009**, 3, 1423-1430.
11. Cairns, D. R.; Witte, R. P.; Sparacin, D. K.; Sachsman, S. M.; Paine, D. C.; Crawford, G. P.; Newton, R. R., Strain-Dependent Electrical Resistance of Tin-Doped Indium Oxide on Polymer Substrates. *Appl. Phys. Lett.* **2000**, 76, 1425-1427.
12. Azulai, D.; Belenkova, T.; Gilon, H.; Barkay, Z.; Markovich, G., Transparent Metal Nanowire Thin Films Prepared in Mesostructured Templates. *Nano Lett.* **2009**, 9, 4246-4249.
13. Hecht, D.; Hu, L. B.; Gruner, G., Conductivity Scaling with Bundle Length and Diameter in Single Walled Carbon Nanotube Networks. *Appl. Phys. Lett.* **2006**, 89.
14. Nomura, K.; Ohta, H.; Takagi, A.; Kamiya, T.; Hirano, M.; Hosono, H., Room-Temperature Fabrication of Transparent Flexible Thin-Film Transistors Using Amorphous Oxide Semiconductors. *Nature* **2004**, 432, 488-492.

15. Myung-Gyu, K.; Myung-Su, K.; Jinsang, K.; Guo, L. J., Organic Solar Cells Using Nanoimprinted Transparent Metal Electrodes. *Adv. Mater.* **2008**, 20, 4408-4413.
16. Lee, J.-Y.; Connor, S. T.; Cui, Y.; Peumans, P., Solution-Processed Metal Nanowire Mesh Transparent Electrodes. *Nano Lett.* **2008**, 8, 689-692.
17. Kang, M. G.; Guo, L. J., Nanoimprinted Semitransparent Metal Electrodes and Their Application in Organic Light-Emitting Diodes. *Adv. Mater.* **2007**, 19, 1391-1396.
18. Kao, C. Y.; Lee, B.; Wielunski, L. S.; Heeney, M.; McCulloch, I.; Garfunkel, E.; Feldman, L. C.; Podzorov, V., Doping of Conjugated Polythiophenes with Alky Silanes. *Adv. Funct. Mater.* **2009**, 19, 1906-1911.
19. Ha, Y. H.; Nikolov, N.; Pollack, S. K.; Mastrangelo, J.; Martin, B. D.; Shashidhar, R., Towards a Transparent, Highly Conductive Poly(3,4-Ethylenedioxythiophene). *Adv. Funct. Mater.* **2004**, 14, 615-622.
20. Roth, S.; Park, H. J., Nanocarbonic Transparent Conductive Films. *Chem. Soc. Rev.* **2010**, 39, 2477—2483.
21. Yamaguchi, H.; Eda, G.; Mattevi, C.; Kim, H.; Chhowalla, M., Highly Uniform 300 Mm Wafer-Scale Deposition of Single and Multilayered Chemically Derived Graphene Thin Films. *ACS Nano* **2010**, 4, 524—528.
22. Wang, X.; Zhi, L.; Mullen, K., Transparent, Conductive Graphene Electrodes for Dye-Sensitized Solar Cells. *Nano Lett.* **2007**, 8, 323—327.
23. Roderick, J.; Benoit, D.; Rishabh, J.; Bernard, K.; Samuel, G., Stability of Doped Transparent Carbon Nanotube Electrodes. *Adv. Funct. Mater.* **2008**, 18, 2548-2554.
24. Bae, S.; Kim, H.; Lee, Y.; Xu, X. F.; Park, J. S.; Zheng, Y.; Balakrishnan, J.; Lei, T.; Kim, H. R.; Song, Y. I.; Kim, Y. J.; Kim, K. S.; Ozyilmaz, B.; Ahn, J. H.; Hong, B. H.; Iijima, S., Roll-to-Roll Production of 30-Inch Graphene Films for Transparent Electrodes. *Nature Nanotech.* **2010**, 5, 574—578.
25. Geng, H. Z.; Kim, K. K.; So, K. P.; Lee, Y. S.; Chang, Y.; Lee, Y. H., Effect of Acid Treatment on Carbon Nanotube-Based Flexible Transparent Conducting Films. *J. Am. Chem. Soc.* **2007**, 129, 7758-+.
26. Hellstrom, S. L.; Lee, H. W.; Bao, Z. N., Polymer-Assisted Direct Deposition of Uniform Carbon Nanotube Bundle Networks for High Performance Transparent Electrodes. *ACS Nano* **2009**, 3, 1423-1430.
27. Kim, K. K.; Bae, J. J.; Park, H. K.; Kim, S. M.; Geng, H.-Z.; Park, K. A.; Shin, H.-J.; Yoon, S.-M.; Benayad, A.; Choi, J.-Y.; Lee, Y. H., Fermi Level Engineering of Single-Walled Carbon Nanotubes by Aucl3 Doping. *J. Am. Chem. Soc.* **2008**, 130, 12757-12761.
28. Nirmalraj, P. N.; Lyons, P. E.; De, S.; Coleman, J. N.; Boland, J. J., Electrical Connectivity in Single-Walled Carbon Nanotube Networks. *Nano Lett.* **2009**, 9, 3890-3895.
29. Geng, H. Z.; Kim, K. K.; Song, C.; Xuyen, N. T.; Kim, S. M.; Park, K. A.; Lee, D. S.; An, K. H.; Lee, Y. S.; Chang, Y.; Lee, Y. J.; Choi, J. Y.; Benayad, A.; Lee, Y. H., Doping and De-Doping of Carbon Nanotube Transparent Conducting Films by Dispersant and Chemical Treatment. *J. Mater. Chem.* **2008**, 18, 1261-1266.

30. Siddons, G. P.; Merchin, D.; Back, J. H.; Jeong, J. K.; Shim, M., Highly Efficient Gating and Doping of Carbon Nanotubes with Polymer Electrolytes. *Nano Lett.* **2004**, 4, 927-931.
31. Doherty, E. M.; De, S.; Lyons, P. E.; Shmeliov, A.; Nirmalraj, P. N.; Scardaci, V.; Joimel, J.; Blau, W. J.; Boland, J. J.; Coleman, J. N., The Spatial Uniformity and Electromechanical Stability of Transparent, Conductive Films of Single Walled Nanotubes. *Carbon* **2009**, 47, 2466-2473.
32. Mamedov, A. A.; Kotov, N. A.; Prato, M.; Guldi, D. M.; Wicksted, J. P.; Hirsch, A., Molecular Design of Strong Single-Wall Carbon Nanotube/Polyelectrolyte Multilayer Composites. *Nat. Mater.* **2002**, 1, 190—194.
33. Shim, B. S.; Tang, Z. Y.; Morabito, M. P.; Agarwal, A.; Hong, H. P.; Kotov, N. A., Integration of Conductivity Transparency, and Mechanical Strength into Highly Homogeneous Layer-by-Layer Composites of Single-Walled Carbon Nanotubes for Optoelectronics. *Chem. Mater.* **2007**, 19, 5467—5474.
34. Shim, B. S.; Zhu, J.; Jan, E.; Critchley, K.; Ho, S. S.; Podsiadlo, P.; Sun, K.; Kotov, N. A., Multiparameter Structural Optimization of Single-Walled Carbon Nanotube Composites: Toward Record Strength, Stiffness, and Toughness. *ACS Nano* **2009**, 3, 1711—1722.
35. Shim, B. S.; Zhu, J.; Jan, E.; Critchley, K.; Kotov, N. A., Transparent Conductors from Layer-by-Layer Assembled SWNT Films: Importance of Mechanical Properties and a New Figure of Merit. *ACS Nano* **2010**, 4, 3725—3734.
36. Reyna-Valencia, A.; Kaliaguine, S.; Bousmina, M., Tensile Mechanical Properties of Sulfonated Poly(Ether Ether Ketone) (Speek) and Bpo4/Speek Membranes. *J. Appl. Polym. Sci.* **2005**, 98, 2380—2393.
37. Bailly, C.; Williams, D. J.; Karasz, F. E.; MacKnight, W. J., The Sodium Salts of Sulphonated Poly(Aryl-Ether-Ether-Ketone) (Peek): Preparation and Characterization. *Polymer* **1987**, 28.
38. Devaux, J.; Delimoy, D.; Daoust, D.; Legras, R.; Mercier, J. P.; Strazielle, C.; Nield, E., On the Molecular Weight Determination of a Poly(Aryl-Ether-Ether-Ketone) (Peek). *Polymer* **1985**, 26, 1994—2000.
39. Louette, P.; Bodino, F.; Pireaux, J.-J., Poly(Ether Ether Ketone) (Peek) Xps Reference Core Level and Energy Loss Spectra. *Surface Science Spectra* **2005**, 12, 149.
40. Wagner, C. D.; Muilenberg, G. E., *Handbook of X-Ray Photoelectron Spectroscopy: A Reference Book of Standard Data for Use in X-Ray Photoelectron Spectroscopy*. Perkin-Elmer Corp., Physical Electronics Division: Eden Prairie, Minn, **1979**; pp 190 p.
41. Ismail, A. F.; Othman, N. H.; Mustafa, A., Sulfonated Polyether Ether Ketone Composite Membrane Using Tungstosilicic Acid Supported on Silica-Aluminium Oxide for Direct Methanol Fuel Cell (Dmfc). *J. Membr. Sci.* **2009**, 329, 18—29.
42. Brownstein, S.; Roovers, J., Calculation of Barriers to Rotation in Peek and Some of Its Substituted Derivatives. *Canadian Journal of Chemistry-Revue Canadienne De Chimie* **1997**, 75, 1225—1228.
43. Kang, Y. K.; Lee, O.-S.; Deria, P.; Kim, S. H.; Park, T.-H.; Bonnell, D. A.; Saven, J. G.; Therien, M. J., Helical Wrapping of Single-Walled Carbon Nanotubes by Water Soluble Poly(P-Phenyleneethynylene). *Nano Lett.* **2009**, 9, 1414-1418.

44. Tanaka, T.; Jin, H.; Miyata, Y.; Fujii, S.; Suga, H.; Naitoh, Y.; Minari, T.; Miyadera, T.; Tsukagoshi, K.; Kataura, H., Simple and Scalable Gel-Based Separation of Metallic and Semiconducting Carbon Nanotubes. *Nano Lett.* **2009**, 9, 1497-1500.
45. Green, A. A.; Hersam, M. C., Colored Semitransparent Conductive Coatings Consisting of Monodisperse Metallic Single-Walled Carbon Nanotubes. *Nano Lett.* **2008**, 8, 1417-1422.
46. Arnold, M. S.; Green, A. A.; Hulvat, J. F.; Stupp, S. I.; Hersam, M. C., Sorting Carbon Nanotubes by Electronic Structure Using Density Differentiation. *Nat Nano* **2006**, 1, 60-65.
47. Weisman, R. B.; Bachilo, S. M., Dependence of Optical Transition Energies on Structure for Single-Walled Carbon Nanotubes in Aqueous Suspension: An Empirical Kataura Plot. *Nano Lett.* **2003**, 3, 1235-1238.
48. Chen, J.; Liu, H.; Weimer, W. A.; Halls, M. D.; Waldeck, D. H.; Walker, G. C., Noncovalent Engineering of Carbon Nanotube Surfaces by Rigid, Functional Conjugated Polymers. *J. Am. Chem. Soc.* **2002**, 124, 9034-9035.
49. Naito, M.; Nobusawa, K.; Onouchi, H.; Nakamura, M.; Yasui, K.-i.; Ikeda, A.; Fujiki, M., Stiffness- and Conformation-Dependent Polymer Wrapping onto Single-Walled Carbon Nanotubes. *J. Am. Chem. Soc.* **2008**, 130, 16697-16703.
50. Gigliotti, B.; Sakizzie, B.; Bethune, D. S.; Shelby, R. M.; Cha, J. N., Sequence-Independent Helical Wrapping of Single-Walled Carbon Nanotubes by Long Genomic DNA. *Nano Lett.* **2006**, 6, 159-64.
51. Wu, G.-M.; Schultz, J. M., Lamellar Morphology of High Molecular Weight Poly(Ether Ether Ketone) after Rolltrusion. *Die Angewandte Makromolekulare Chemie* **1998**, 257, 53—57.
52. McAllister, M. J.; Li, J.-L.; Adamson, D. H.; Schniepp, H. C.; Abdala, A. A.; Liu, J.; Herrera-Alonso, M.; Milius, D. L.; Car, R.; Prud'homme, R. K.; Aksay, I. A., Single Sheet Functionalized Graphene by Oxidation and Thermal Expansion of Graphite. *Chem. Mater.* **2007**, 19, 4396—4404.
53. Whitby, R. L. D.; Fukuda, T.; Maekawa, T.; James, S. L.; Mikhalovsky, S. V., Geometric Control and Tuneable Pore Size Distribution of Buckypaper and Buckydiscs. *Carbon* **2008**, 46, 949-956.
54. Kotov, N. A., Layer-by-Layer Self-Assembly: The Contribution of Hydrophobic Interactions. *Nanostructured Materials* **1999**, 12, 789—796.
55. Brothers, E. N.; Izmaylov, A. F.; Scuseria, G. E.; Kudin, K. N., Analytically Calculated Polarizability of Carbon Nanotubes: Single Wall, Coaxial, and Bundled Systems. *J. Phys. Chem. C* **2008**, 112, 1396-1400.
56. Brothers, E. N.; Scuseria, G. E.; Kudin, K. N., Longitudinal Polarizability of Carbon Nanotubes. *J. Phys. Chem. B* **2006**, 110, 12860-12864.
57. Han, J. T.; Kim, J. S.; Jeong, H. D.; Jeong, H. J.; Jeong, S. Y.; Lee, G.-W., Modulating Conductivity, Environmental Stability of Transparent Conducting Nanotube Films on Flexible Substrates by Interfacial Engineering. *ACS Nano* **2010**, 4, 4551-4558.
58. Podsiadlo, P.; Sui, L.; Elkasabi, Y.; Burgardt, P.; Lee, J.; Miryala, A.; Kusumaatmaja, W.; Carman, M. R.; Shtein, M.; Kieffer, J.; Lahann, J.; Kotov, N.

A., Layer-by-Layer Assembled Films of Cellulose Nanowires with Antireflective Properties. *Langmuir* **2007**, 23, 7901—7906.
59. Blighe, F. M.; Hernandez, Y. R.; Blau, W. J.; Coleman, J. N., Observation of Percolation-Like Scaling - Far from the Percolation Threshold - in High Volume Fraction, High Conductivity Polymer-Nanotube Composite Films. *Adv. Mater.* **2007**, 19, 4443-4447.
60. Wang, G.-F.; Tao, X.-M.; Wang, R.-X., Flexible Organic Light-Emitting Diodes with a Polymeric Nanocomposite Anode. *Nanotechnology* **2008**, 19, 145201.
61. Kim, K. K.; Park, J. S.; Kim, S. J.; Geng, H. Z.; An, K. H.; Yang, C.-M.; Sato, K.; Saito, R.; Lee, Y. H., Dependence of Raman Spectra G^{'} Band Intensity on Metallicity of Single-Wall Carbon Nanotubes. *Phys Rev B* **2007**, 76, 205426.
62. Duclaux, L., Review of the Doping of Carbon Nanotubes (Multiwalled and Single-Walled). *Carbon* **2002**, 40, 1751-1764.
63. Moonoosawmy, K. R.; Kruse, P., Cause and Consequence of Carbon Nanotube Doping in Water and Aqueous Media. *J. Am. Chem. Soc.* **2010**, 132, 1572-1577.
64. Graupner, R.; Abraham, J.; Vencelova, A.; Seyller, T.; Hennrich, F.; Kappes, M. M.; Hirsch, A.; Ley, L., Doping of Single-Walled Carbon Nanotube Bundles by Bronsted Acids. *Phys. Chem. Chem. Phys.* **2003**, 5, 5472-5476.
65. Xu, G. H.; Zhang, Q.; Zhou, W. P.; Huang, J. Q.; Wei, F., The Feasibility of Producing Mwcnt Paper and Strong Mwcnt Film from Vacnt Array. *Appl. Phys. A: Mater. Sci. Process.* **2008**, 92, 531—539.
66. Chen, J.; Bull, S. J., Indentation Fracture and Toughness Assessment for Thin Optical Coatings on Glass. *Journal of physics. D, Applied physics* **2007**, 40, 5401.
67. Gordon, R. G., Criteria for Choosing Transparent Conductors. *Mrs Bulletin* **2000**, 25, 52.
68. Sandoval-Paz, M. G.; Ramírez-Bon, R., Indium Tin Oxide Films Deposited on Polyethylene Naphthalate Substrates by Radio Frequency Magnetron Sputtering. *Thin Solid Films* **2009**, 517, 2596-2601.
69. Kaempgen, M.; Duesberg, G. S.; Roth, S., Transparent Carbon Nanotube Coatings. *Appl. Surf. Sci.* **2005**, 252, 425-429.
70. Jan, E.; Kotov, N. A., Successful Differentiation of Mouse Neural Stem Cells on Layer-by-Layer Assembled Single-Walled Carbon Nanotube Composite. *Nano Lett.* **2007**, 7, 1123—1128.
71. Shim, B. S.; Chen, W.; Doty, C.; Xu, C. L.; Kotov, N. A., Smart Electronic Yarns and Wearable Fabrics for Human Biomonitoring Made by Carbon Nanotube Coating with Polyelectrolytes. *Nano Lett.* **2008**, 8, 4151—4157.

CHAPTER III

Vacuum Assisted Flocculation for Multifunctional Graphene Layered Composites

3.1 Introduction

Water removal is a time and labor consuming step in the LBL assembly technique. Using proper environment to quickly eliminate water in the assembly would definitely accelerate the process. Vacuum filtration is a commonly known operation for the separation of solids from fluids. The layer-by-layer deposition process of solids in the filtration process simulates the nature's formation of layered sedimentary rocks over ages. It is thus interesting to take advantage of this technique to formulate layered nanocomposites. Here, chemically derived graphene oxide and reduced graphene will be demonstrated to fabricate multifunctional composites via this vacuum assisted flocculation technique. The high-aspect-ratio graphene nanomaterials tend to be easily aligned on top of porous membrane under the pressure difference. In addition, the high surface area of those nanosheets and easily engineered functional groups enable the attachment of polymers of interest. A combination of high strength and toughness is demonstrated in the reduced graphene composites. The layered architecture also induced a unique phenomenon of negative thermal expansion in the stiff graphene oxide

composites. The union of tunable thermal expansion within a wide range plus the high mechanical strength is a special advantage of layered graphene composites. A structure and performance comparison between the layered composites assembled with this technique and the conventional LBL assembly is also discussed in the following sections.

3.2 Engineering Multifunctional Graphene Composites by Vacuum Assisted Flocculation and its Comparison with Layer-by-layer Assembly

3.2.1 Introduction

High-performance nanocomposites require high concentrations of nanomaterial phase (inorganic component or filler) with carefully engineered interface with the polymer matrix. Tight control over the structure at different scales is the key to ensure materials' uniformity and to minimize the contribution of defects of different nature. At the same time, the influence of structural features found at different scales – atomic, nanometer, submicron, micron, *etc.* – on different properties is only partially understood. Greater clarity in the multiscale structure-property relationships is needed in order to conceptualize engineering of these and other materials. In particularly, multiscale materials engineering is needed to identification unusual combination of dissimilar properties. Many technological bottlenecks[1-3] require a set of properties that can be described as "mechanics+" combinations that define the targets for materials performance as parameter pairs, triplets, *etc.* linking mechanical, electrical, optical, and other properties into figures of merit or graphing them as target high-performance materials.[4]

Among new methods developed for such materials are layer-by-layer (LBL) assembly and vacuum assisted flocculation (VAF). They stand out among others by the demonstrated success with reaching unusual 'mechanics+' combinations for a variety of nanoscale components including clay,[1, 5] cellulose,[6, 7] carbon nanotubes (CNTs),[4, 8] and lately with graphene and its derivatives.[9-13] Materials produced by LBL and VAF have apparent similarities and can potentially be used for the same applications. A systematic study of their advantages and disadvantages is missing, however, despite being much needed when selecting one or the other technique for high-performance materials.

Based on the large body of literature data[4, 10, 14, 15], one could expect that LBL composites should have better nanoscale organization and uniformity than VAF-made materials due to the higher accuracy of the step-by-step deposition one nanoscale layer at a time typical for LBL.[16, 17] VAF-made materials are expected to have virtually the same functional properties, while the time needed to assemble similar laminated structures[10, 18-20] should be much shorter. There are little or no *a priori* expectations regarding the comparison of their properties. The objective of this work is to make such comparison in respect to properties and correlated it with differences in structure. The VAF *vs.* LBL comparison will not only make conclusions regarding this particular composite, but also advance materials engineering as a research field because it will be able to make a framework for the correlation between specific properties and structural features and guide future materials preparation with justifiable *a priori* expectations of properties.

The choice of components to obtain an adequate LBL *vs.* VAF comparison needs to be carefully contemplated. One should consider the possibility (1) to investigate multiple 'mechanics+' performance characteristics and (2) to prepare both LBL and VAF

composites from identical components under identical conditions. It was, in fact, more difficult than one could expect. Reduced graphene (RG) and polyvinyl alcohol (PVA) provide a model system suitable for this study. LBL *vs.* VAF comparison for PVA/RG composites is made in respect to their structure, mechanical, electrical, and some thermal properties as the most representative characteristics essential for most materials. In addition to the systematic evaluation of these assembly techniques and materials engineering concept, our study also leads to materials with record high toughness among other layered composites and better understanding the structural reasons behind it. It also demonstrates that electrical properties in these composites are primarily determined by atomic and nanoscale structural parameters that are markedly different in these composites. Mechanical properties are, nevertheless, nearly identical especially for high RG content LBL and VAF composites except the case of covalent cross-linking. All aspects of mechanical performance can be rationalized considering thermodynamic state of polymer at RG interface.

3.2.2 Experimental

Preparation of graphene oxide (GO). GO can be made by modified Hummers method from graphite powders (Bay carbon, SP-1).[21] In a typical reaction, 1 g of graphite, 1g of $NaNO_3$, and 50 mL of H_2SO_4 were stirred together in an ice bath, and 6 g of $KMnO_4$ was then slowly added. The solution was then transferred to a 35°C water bath and stirred for about 1 h. 80 mL of water was subsequently added, and the solution was stirred for 30 min at a temperature of 90°C. Finally, 200 mL of water was used to dilute the mixtures, followed by addition of 6 mL of H_2O_2 (30%). The warm solution was then filtered. The GO slurry collected from membrane was then washed with 300ml 2M HCl,

and purified GO can be collected at the tube bottom after centrifugation. The GO was further purified by dialysis for one week, and GO powder was made by lyophilization. Typical Raman spectra are shown in Figure 3.15. The element analysis shows the mass ratio of C: O: N is 43:54:3 in GO.

Preparation of chemically reduced graphene (RG) dispersions. The RG dispersion was made according to report by Li et al.[22] 62.5mg GO was dispersed by tip-sonication in 100ml DI water for 20mins. Additional 150ml DI water, 75µl 50 wt% hydrazine, 875µl ammonia solutions were then added. The mixtures were then heated to 90°C for 3 hours and homogenous graphene dispersion was obtained. The concentration of the RG solution was calibrated by weighing the RG paper formed by filtration, and was around 0.14mg/ml. The element analysis shows the mass ratio of C: O: N: H is 82:13.5:3.5:1 in RG. The comparison of GO and RG Raman spectra were shown in Figure 3.15.

Layer-by-layer (LBL) assembly of polyvinyl alcohol (PVA) and RG. In a typical LBL cycle, glass slides cleaned by piranha solution for 24 hours were immersed in 1 or 0.2wt% PVA (Aldrich, Mowiol® 56-98, Mw ~195000) for 2-5 min, rinsed with DI water, and then dried with compressed air. Subsequently, these slides were dipped into the 0.05-0.14 mg/ml RG dispersions for 2-5 min, followed by rinsing and drying. 300 bilayer films were deposited on a glass substrate by NanoStrata robot. Modified deposition conditions for preparations of LBL composites with different RG content could be described as [PVA(*a*)-*m*/RG(*b*)-*n*], where *a* and *b* are the concentration of PVA and RG in mg/ml; *m* and *n* are the dipping time in the unit of min for each solution. The RG fractions for films under conditions of [PVA(10)-15/RG(0.05)-2], [PVA(10)-5/RG(0.14)-

5], and [PVA(1)-2/RG(0.14)-5] were 34 wt%, 50 wt% and 72 wt%, and the corresponding films were labeled as LBL34, LBL50 and LBL72 for simple discussions.

Vacuum Assisted Flocculation (VAF) of PVA and RG. 100ml of 0.14 mg/ml RG dispersion were mixed with 2ml, 3ml, 4ml, 6ml of 10mg/ml PVA, briefly sonicated, and then filtrated through a 0.1μm pore size nylon membrane under vacuum in the course of 2 days. The film was peeled off from the filter, and dried in the vacuum oven. The films were labeled as VAF85, VAF60, VAF50, VAF46, VAF27 according to RG fractions in the films.

Characterization. LBL process was monitored by an 8453 UV-vis ChemStation spectrophotometer from Agilent Technologies. The growth of film was also investigated by quartz crystal microbalance (QCM) 200 from Stanford Research Systems. 5MHz quartz crystals were used in all the studies. Cross-section of the films was examined by FEI NOVA Nanolab Scanning electron microscopy (SEM). Transmission Electron Microscopy (TEM) images were collected by JEOL 3011 HRTEM. Samples were sliced into ~70nm thick by an ultramicrotome, followed by deposition on a copper grid.

Differential scanning calorimetry (DSC) was carried out on TA instrument Q2000 DSC under nitrogen atmosphere at a temperate ramp rate of 20°C/min. The glass transition and melting temperature were determined according to the protocol in ASTM D3418–08. Tapping mode atomic force microscopy (AFM) images were obtained using a NanoScope IIIa Atomic force microscope from Veeco Instruments. Perkin Elmer Pyris 1 TGA was used for thermal gravimetrical analysis. X-ray diffraction (XRD) patterns of GO paper were collected at ambient temperature using a Rigaku R-AXIS SPIDER diffractometer with an imaging plate detector using graphite monochromated Cu-Kα

radiation (1.5406 Å). Samples were glued to the tip of a glass capillary. Images were collected sequentially with collection time of 2 minutes and the face of the films was oriented parallel or normal to the beam. Images were integrated from 2.0° to 50° 2θ with a 0.1° step size with the AreaMax software package. Powder patterns were processed in Jade 6.5 to calculate peak positions.

The mixing enthalpy between PVA and water, RG and water, and PVA and RG was determined by NANO ITC from TA instruments. In a typical experiment, 50μL PVA was placed in the top syringe and 350μL 0.14mg/ml RG was put in the bottom sample cell. After stabilization at 25°C for about 20mins, 48μL PVA was injected into RG within 1min. The released energy was obtained from integration of the exothermal peak.

The resistance of films was measured by the 4-point probe method with the Agilent 3440A multimeter. The 4 electrodes were made on a 3mm by 30mm sample strip with silver epoxy, and further annealed at 70°C for 1 h. The silver epoxy can ensure the good contacts for all layers of RG.

Uniaxial tensile testing and dynamic mechanical analysis (DMA) were done on RSAIII Rheometrics Systems Analyzer from TA instruments. The tensile tests confirm to the ASM standard ASTM D882. In a typical measurement, 1mm wide and 6mm long sample strip was fixed on the steel grips either by gripping or double tape (thin films) and tested at a speed of 0.01mm/s. In order to correctly measure the specimen extension, gage marks were put onto sample surface by white marker, and recorded with high speed camera during the testing (Figure 3.14a). The specimen images were then analyzed by the software to track the marks' movement to obtain the extension. Each sample was measured at least 5 times. In a DMA test, the sample was pre-stretched by 0.5%, and the

experiment was run at a dynamic strain of 0.2% with static force larger than dynamic force by 25% from room temperature to 200°C at a rate of 5°C/min in air. The agreement between storage modulus measured by DMA and Young's modulus determined by this uniaxial tensile test further validate the method in use for correctly reflecting the failure strain of samples (Table 3-1).

Table 3-1. Mechanical Properties of PVA/RG composites made by LBL and VAF assemblies

		Storage Modulus	Stiffness	Strain	Tensile Strength
	RG	19.02±1.34	19.87±2.55	0.01±0.002	193±30
	PVA	3.01±0.25	3.52±0.18	2.5±0.5	90±5
VAF	VAF85	13.1±1.26	11.41±2.68	0.022±0.00	137.5±4.5
	VAF60	9.13±1.13	7.8±0.2	0.031±0.00	138±12
	VAF50	8.42±0.58	7.8±1	0.051±0.01	143.1±11.2
	VAF46	9.51±2.47	7.8±0.7	0.046±0.00	143.7±8.1
	VAF27	4.00±0.34	3.97±0.20	0.48±0.08	95±7
LBL	LBL72	10.2±0.75	9.8±0.5	0.017±0.00	148±20
	LBL50	8.1±0.28	8.3±0.1	0.056±0.00	157±3
	LBL34	7.6±0.83	7±0.5	0.044±0.01	160±11
	LBL50(G	13±0.52	13±2	0.041±0.00	222±18

3.2.3 Results and Discussion

3.2.3.1 PVA and RG interactions

RG and PVA were chosen as the basic components for LBL *vs.* VAF evaluation considering the following reasons:

(1) Both VAF and LBL composites can be made from RG and PVA. Moreover, the fractions of polymer and nanoscale component in RG/PVA system could be nearly identical for both methods [1, 10, 18, 23] allowing adequate comparison of the two techniques.

(2) Each component of the RG/PVA composites has important contributions to the properties of the resulting material. RG is well-known for its mechanical,[24] electrical,[25] and thermal[26] characteristics. PVA is a common viscoelastic polymer that becomes a valuable tool in evaluation of nanostructure of the composites. Combination of all these properties makes the comparison comprehensive. It also opens the possibility of finding the structure-property relationships for hard-to-reach multiparameter combinations. Note also that RG is a better alternative than graphene oxide (GO), clays, or other wide-band gap nanomaterials despite passing the criterion (1) because of the multiple functional properties available for comparison.

(3) Systematic evaluation of LBL *vs.* VAF materials assembly methods also enables us to improve performance characteristics of RG composites reducing, for instance, brittleness and increasing toughness. This study provides an opportunity to evaluate VAF and LBL as tools for this common problem.[11]

The atomic and nanoscale engineering of the interface in layered nanocomposite assemblies relies on specific interactions between polymers and inorganic components. Noteworthy is the fact that such high strength of such interactions is problematic for VAF as they could become a cause for coagulation prior to the successful assembly process.

On the other hand, strong specific interactions of macromolecules represent the foundation of the LBL assembly. They are also essential for high mechanical performance. Adequate VAF *vs.* LBL comparison requires these interactions to be strong enough to afford LBL but not too strong to cause premature coagulation of components in VAF technique.

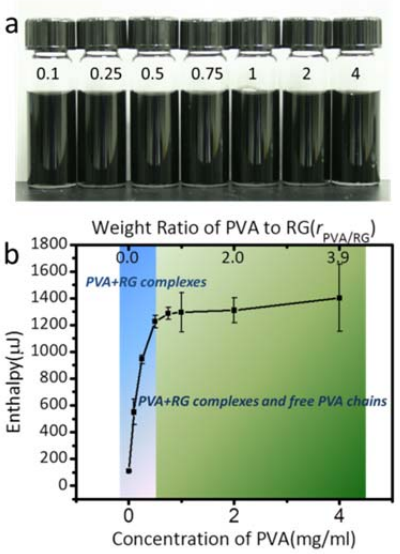

Figure 3.2.1. (a) Photograph of dispersions from PVA and RG at different weight ratios. (b) Mixing enthalpies of PVA and RG for different PVA/RG ratios.

A series of PVA and RG mixtures display no agglomeration in a wide range of PVA/RG weight ratios, $r_{PVA/RG}$ (Figure 3.1a). At the same time, isothermal titration calorimetry (ITC) indicates generally attractive interactions between the components. Mixing of PVA and RG is an invariably exothermic process with enthalpy initially increasing linearly and then reaching a plateau for $r_{PVA/RG} > 0.55$ (Figure 3.1b). The total enthalpy is measured by integrating heat rate and time curve after the mixing reaching a thermally equilibrium process (Figure 3.9a). Note that dilution enthalpy of PVA plays a very minor role in the total mixing enthalpy as it varies little with PVA concentration (Figure 3.9b). Such behavior suggests that specific interactions between PVA and RG reach their maximum at $r_{PVA/RG} = 0.55$, which will be reflected in mechanical and other properties of RG/LBL composites.

The primary contributors to the interactions between RG and PVA are believed to be hydrogen bonds between abundant –OH groups on PVA chains and –OH/–COOH groups on RG sheets. Van der Waals (vdW) forces, hydrophobic attractions, and charge transfer between polar functionalities in PVA and π-conjugated domains[4] in RG can also

bind PVA to RG. Mixing enthalpy increases with PVA concentration until all possible adsorption sites on RG surface are occupied, which explains the plateau for $r_{PVA/RG} > 0.55$. Beyond this threshold, addition of additional PVA increases the concentration of 'free' polymeric chains in solution.

3.2.3.2 Preparation of LBL and VAF Composites

LBL Assembly was realized using the classical approach by alternatively dipping a glass substrate in PVA solutions and RG dispersion with intermittent rinsing with water (Figure 3.2a). The assembly process was monitored by the absorbance change at 550nm (Figure 3.2b) and quartz crystal microbalance (QCM, Figure 3.2c). Both techniques indicate that the RG+PVA LBL system has a linear and uniform multilayer growth with an increment of 1-2 nanometers in thickness or 0.2-0.4 $\mu g/cm^2$ of mass per layer (Figure 3.2c). As indicated by QCM, the concentrations of PVA, RG, and corresponding immersion time affect the growth pattern of the multilayers, which allows us to control RG fractions in the resulting LBL composites. In this study a series of 300-bilayer films with different $r_{PVA/RG}$ are prepared. These composite samples contained 34 wt.%, 50 wt.% and 72 wt.% of RG; they are denoted as LBL34, LBL50, LBL72 respectively.

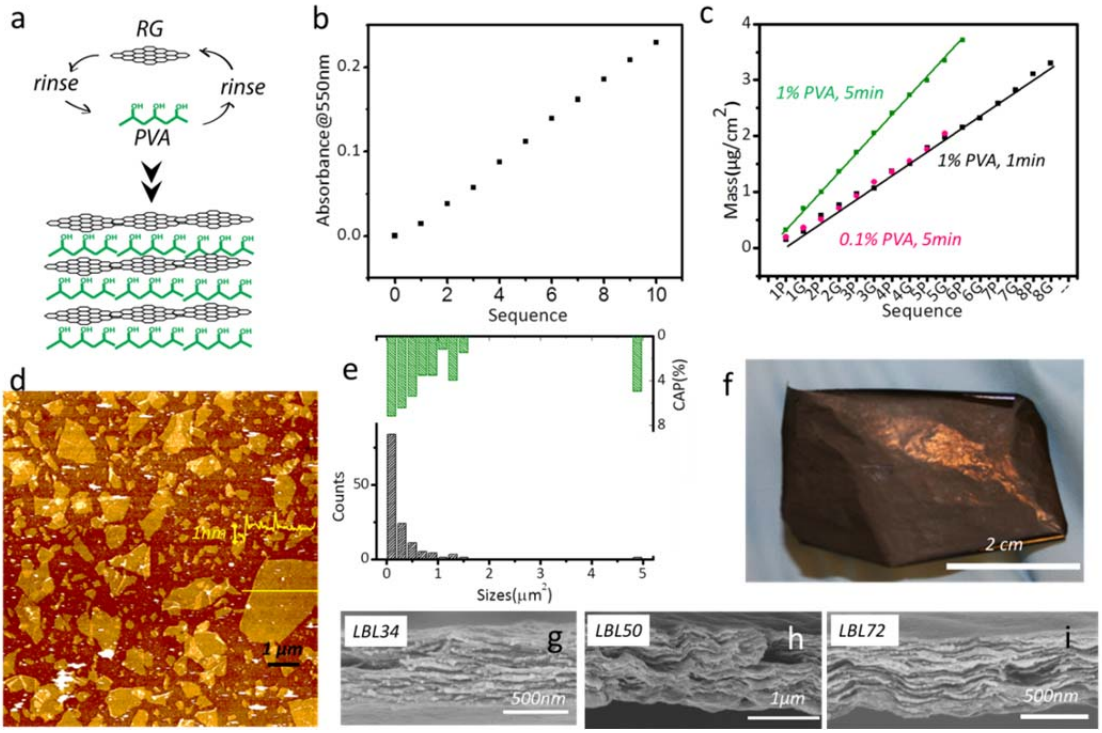

Figure 3.2. Layer-by-layer (LBL) assembled PVA/RG composites. (a) A schematic drawing of LBL assembly. (b) UV-vis absorbance of PVA/RG LBL film grown on a glass substrate at 550nm for different number of deposition cycles. (c) QCM weight per area data for different number of deposition cycles and LBL deposition conditions. (d) AFM image of one bilayer of PVA and RG deposited on a silicon substrate. (e) Number and cumulative area percentage (CAP) of RG nanosheets of different sizes calculated from AFM images. (f) A photograph of a piece of freestanding LBL50 film. (g-i) Scanning electron microscopy images for the cross-sectional areas of LBL34, LBL50, LBL72.

Approximately 1 nm thick film of RG sheets adsorb on a smooth and uniform layer of PVA with dominantly flat orientation in each dipping cycle (Figure 3.2d). RG sheets with an area of <0.2 μm^2, 0.2—0.6 μm^2, and >0.6 μm^2 cover 7%, 12%, 19% of the total area of the substrate surface (Figure 3.2e), respectively. More than 50% of the nanosheets are smaller than 0.2 μm^2 (Figure 3.2e). Although a belief that bigger sheets can give rise to better mechanical performance exists,[3] current studies on graphene do not support this idea.[27]

The layered structures for LBL composites (Figure 3.2e) can be seen in the cross-sectional SEM image (Figure 3.2g-i). The total thickness of LBL50 after 300 dipping cycles is 1000±10 nm (Figure 3.2h), which is almost two times greater than that of LBL34 (575±25 nm) and LBL72 (500±7 nm) obtained after the same number of cycles (Figure 3.2g and i) but either enhanced concentration of PVA or the RG accordingly. In the preparation of LBL50, longer immersion times in each LBL cycle stimulate the adsorption of both species producing the nearly thermodynamically equilibrium state (see Fig. 1), while in the LBL34 and LBL72 one or the other component produces incompletely adsorbed layers although the packing mode of each PVA macromolecule is likely to be similar to those in LBL50. The more balanced adsorption of PVA and RG leads to thicker films, which also accelerates the deposition. The time needed to make 1 μm thick LBL50 including solution preparation and delamination from substrate is *ca.* 115 h in comparison to the *ca.* 195 h for 1 μm thick LBL34 and LBL72.

VAF Assembly was carried out by mixing 10mg/ml PVA and 0.14mg/ml RG aqueous solutions together at different volume ratios. PVA and RG slowly assembled on top of each other as the film settles down on a nylon filter under vacuum and transitions from a semi-ordered gel to the layered structure (4a).[28, 29] Typically, it takes 48 hours to assemble a piece of 20μm film. The overall rate of assembly is 2.4 h/μm, much can be compared to 115 h/μm for the LBL process.

The fraction of RG can be adjusted by altering $r_{PVA/RG}$ (Figure 3.1a). The RG content in VAF composites was determined by TGA (Figure 3.10) to be 85%, 60%, 50%, 46%, 27%; the corresponding samples were labeled as VAF85, VAF60, VAF50, VAF46, and VAF27 correspondingly. Note that if $r_{PVA/RG} > 0.55$, PVA is present in the

dispersion with RG as free chains and as a complex with the nanosheets. Most of free PVA is retained in the material during the vacuum filtration process otherwise we would not be able to have RG content below 45%. The presence of these free chains and mode of their packing among RG sheets makes, as we shall see below, a significant effect on the properties.

The stability of both LBL and VAF assembled films were tested in boiling water for 20 min, under which pure PVA was easily dissolved. Both type of films shows no sign of material loss except for VAF27, whose thickness decreased from 56μm to 40μm. The excessive free PVA chains can easily escape from the confined nanochannels in VAF27. For other VAF films, however, strong interactions between PVA and RG plus the geometrical confinement prevent the loss of polymers. Films made by LBL assembly, however, can survive the intense conditions even for LBL34 due to the rinsing/drying steps for removing the loosely bonded polymers.

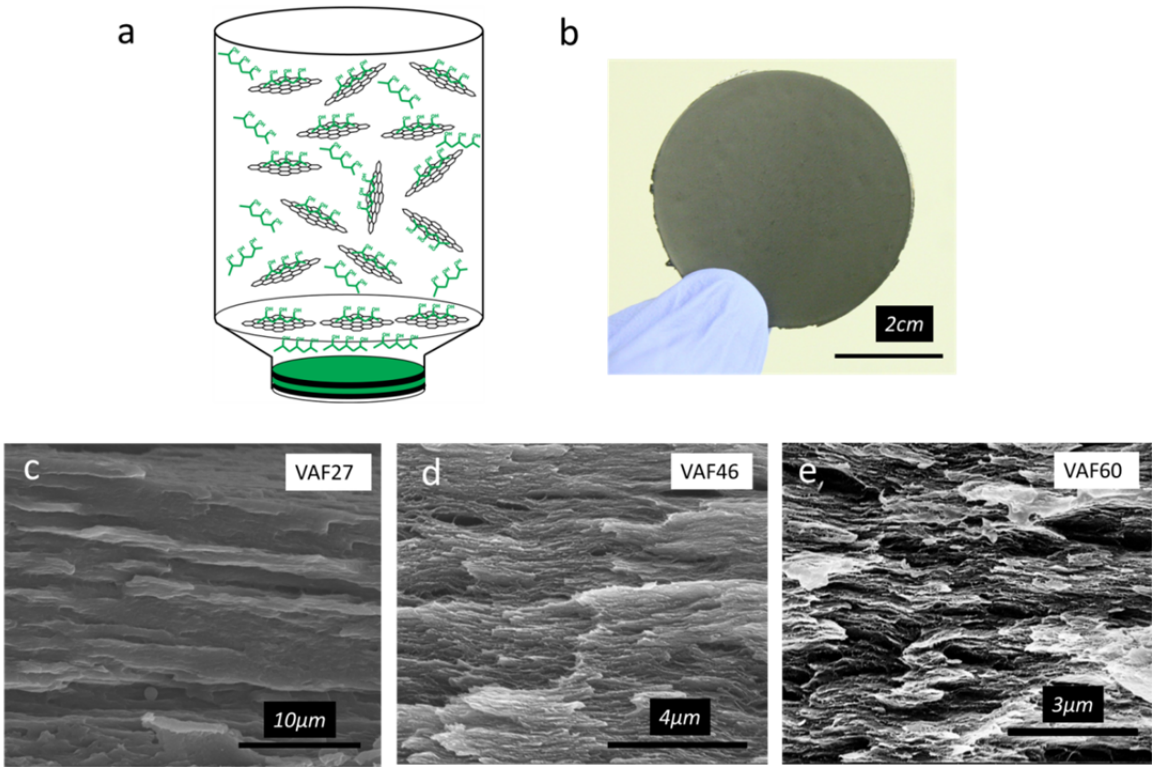

Figure 3.3. Vacuum assisted flocculation (VAF) of PVA/RG composites. (a) Schematics of VAF assembly. (b) A photograph of a piece of freestanding VAF60 film. (c, d, e) Scanning electron microscopy images for the cross-sectional areas of VAF27, VAF46, and VAF60.

3.2.3.3 Structural Comparison

Both LBL and VAF assembly produce materials with well-defined layered structures (Figure 3.2 and 3.2.3). The alignment of RG sheets appears to be more pronounced for the LBL than VAF composites. The anisotropy of LBL- and VAF-made stacks of nanosheets can be quantified by X-ray diffraction (XRD) patterns especially when X-ray beam is directed from their side/edge (Figure 3.4a and b). The films appear to be mostly isotropic when X-ray beam is directed normal to the surface of the films (Figure 3.4c and d). Two characteristic repeating distances of ≈0.4 nm ($2\theta \approx 20°$) and ≈1.75nm ($2\theta \approx 5°$) are evident in the XRD profiles for both LBL and VAF materials

(Figures 4e, f, g, h). Previously published XRD studies of similar composites[10, 14, 18] indicate that the Bragg diffraction peaks and shoulders at $2\theta \approx 5°$ should be attributed to the diffraction from adjacent RG sheets. The repetitive distance between sheets in layered materials is also known as basal spacing. The peaks $2\theta \approx 20°$ correspond to the diffraction from $[10\bar{1}]$ plane of PVA crystallites, which was previously observed in neat PVA (Figure 3.4e).[30, 31]

In VAF composites, the consistent shift of the ≈5° shoulder/peak towards lower 2θ values with increasing PVA content (Figure 3.4e) indicates enhanced intercalation of the polymer between RG sheets, which confirms the assignment of the peak as its disappearance in the X-ray diffractograms obtained with perpendicular orientation of the beam (Figure 3.4g). VAF46 displays a spacing of 1.9 nm as compared to 0.36 nm for the RG paper that does not contain PVA at all (Figure 3.11a). VAF27 shows no such peak possibly due to shift of the peak beyond the lower 2θ limit of XRD instrument or complete lack of regularity (Figure 3.3).

It is worthwhile to make a brief sideline comparison to VAF-assembled composites from GO. The interlayer spacing of PVA/RG composites is larger at similar weight fraction of the nanosheets than in PVA/GO composites (Figure 3.11b). This observation suggests that the larger number of functional groups of GO lead to a stronger intermolecular interactions and more proximate positioning of PVA chains to the sheets of GO than to RG.

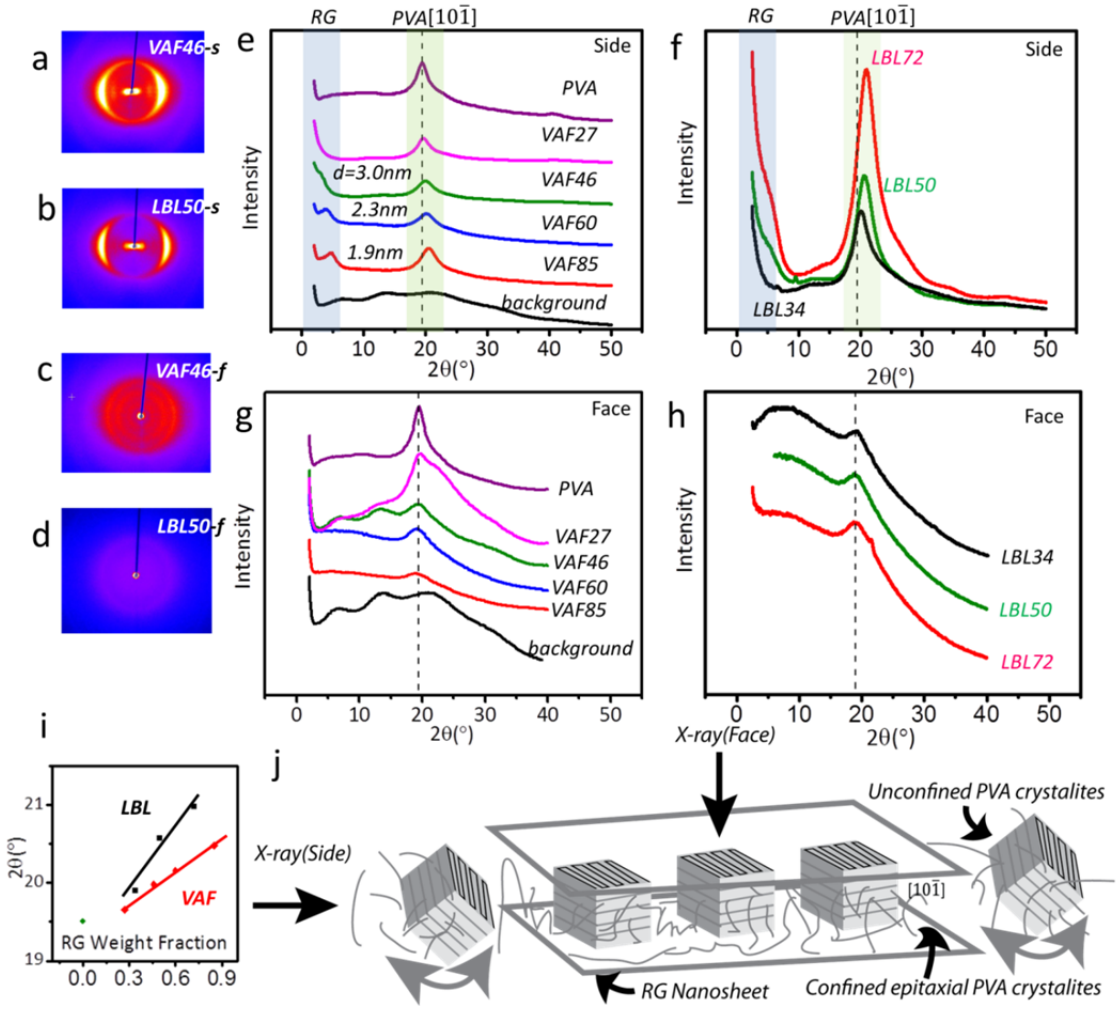

Figure 3.4. X-ray diffraction spectra for PVA/RG composites. (a, b, c, d) XRD images for VAF (a, c) and LBL (b, d) composites with X-ray beam directed at the side (a, b) and through the face (c, d) of the samples. (e, f, g, h) XRD profiles for VAF (e, f) and LBL (f, h) composites with X-ray beam directed at the side (e, f) and through the face (g, h) of the samples. The intensity of XRS profile is shown in the linear scale. (i) Dependence of the X-ray scattering angle for PVA crystallites on the RG content for VAF and LBL composites. (j) Schematics of confined epitaxial and peripheral PVA crystallites.

Continuing with VAF composites, PVA [10$\bar{1}$] XRD peaks at $2\theta \approx 20^{o}$ change with RG content. However, this change is different for PVA crystallites aligned along the RG surfaces and those formed beside the RG, which are presumably from free PVA chains present in solution (Figure 3.4j). They can be denoted as peripheral crystallites. The anisotropy of the PVA crystallites is obvious in the XRD diffraction patterns (Figure

3.4a) when the X-ray is directed through the side of the film. This behavior indicates the epitaxial effect of RG surface in respect to the growth of PVA crystallites,[32] which are aligned along the RG sheets (Figure 3.4j). Similar behavior was observed for TiO_2 crystallites confined between the adjacent polymer layers.[33] These crystallites lead to the anisotropic patterns (Figure 3.4a) diffracting from $[10\bar{1}]$ planes parallel to the RG surface. For composites with higher RG content, $[10\bar{1}]$ peak shifts to higher 2θ region, indicating decreased spacing from 0.45 to 0.43 nm (Figure 3.4e). It was once observed that the introduction of clay nanosheets can promote new phase formation of PVA.[30] The precise control over organic crystallites' spacing was only reported recently through lattice straining effect via shearing,[34] while in our case the mechanism to introduce lattice strains is clearly different. It is likely that the capillary effect of different sized RG nanochannel causes varied compressive stress thus strain on the PVA crystallites during their formation with removal of water. The smaller the basal spacing, the stronger the effect is. In comparison, randomly distributed peripheral PVA crystallites (Figure 3.4j), demonstrate isotropic diffraction rings in the XRD images when X-ray beam is perpendicular to the surface (Figure 3.4c). The $[10\bar{1}]$ peak in the random PVA crystallites show no dependence on the RG content (Figure 3.4f). Interestingly, in the PVA/GO composites, PVA crystallites are absent according to XRD spectra obtained under similar conditions, and only reappears after the reduction of GO.[14, 18] This fact suggests that the strong interaction with GO prevents PVA crystallization. In contrast, RG sheets with milder interactions with the polymer allow for additional degrees of freedom for the PVA chains on the surface of RG, and therefore facilitate their crystallization.

The XRD profiles of LBL-assembled composites also display a shoulder peak at ≈5° (Figure 3.4f). The signal for RG basal spacing is less defined for LBL than for VAF assemblies because LBL films are thinner, however it is clearly located at $2\theta > 5^{o}$ while the same peak corresponding to the basal spacing of VAF composites is located at $2\theta < 5^{o}$ at any RG content (Figure 3.4 e, f). A clear case comparison is LBL50 ($2\theta = 5.0^{o}$ shoulder) *vs.* VAF46 ($2\theta = 3.6^{o}$ shoulder) and VAF60 ($2\theta = 4.0^{o}$ peak). We conclude that for the same RG content the basal spacing in LBL composites is generally smaller than for VAF composites. Similarly to VAF-made materials, the signal from RG basal spacing shifts towards larger 2θ values with increasing the RG content (Figure 3.4f).

The LBL composites also reveal the presence of 'epitaxial' and peripheral PVA crystallites similarly to the VAF composites. The anisotropy of PVA crystallites for PVA $[10\bar{1}]$ peak at $2\theta \approx 20°$ in LBL-made materials is visibly greater (Figure 3.4b *vs*. 4d and Figure 3.4f *vs.* 4h), which is indicative of the lower contribution of the peripheral than from epitaxial PVA crystallites. The position of the corresponding XRD peak shifts with different RG contents and shows similar differences of face- and side-directions of the X-ray beams as in VAF composites although greater. As the content of RG increases, the PVA $[10\bar{1}]$ plane spacing decreases from 0.454 nm ($2\theta = 21.0°$) in pure PVA to 0.423nm ($2\theta = 19.5°$) (Figure 3.4f).

PVA crystallites in LBL and VAF assembled composites (Figure 3.4i) display distinct structural differences as well. At similar RG content, the LBL assembled composites tend to have higher 2θ or smaller PVA $[10\bar{1}]$ plane spacing than VAF composites. This fact suggests that in LBL composites PVA interacts with larger area of RG than in VAF composites. By other words, LBL process is more effective in epitaxial

templating of PVA crystallites due to greater degrees of freedom available to the PVA chains at the substrate-solution interface when it has to adapt its conformation to the substrate.[35]

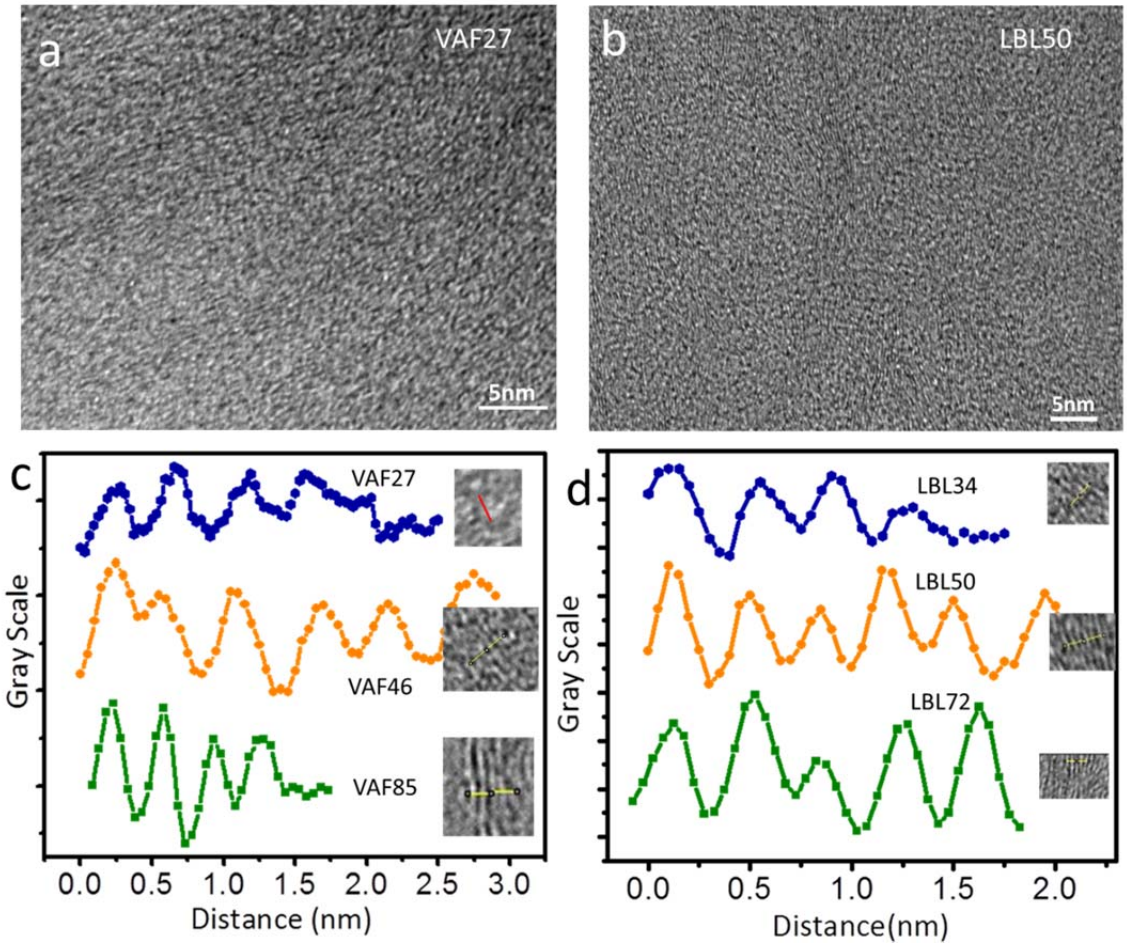

Figure 3.5. High resolution TEM images of (a) VAF27 and (b) LBL50 cross-sections. The variation of gray scale along the scan for (c) VAF- and (d) LBL-made composites.

The nanoscale stacking patterns in the VAF and LBL composites were further confirmed by high resolution transmission electron microscopy (HR-TEM) and selected area electron diffraction (SAED, Figure 3.5 and S4). All VAF and LBL made films show similar length scale of 0.4nm for the layer spacing with VAF27 and LBL34 slightly larger in their own categories. This observation complies with the basal spacing of PVA

crystallites in the XRD results (Figure 3.4). It is difficult, however, to observe the longer range periodicity corrresponding to the arrragement of RG, which is possibly due to the poor imaging contrast between RG and PVA crystallites. Overall, LBL films shows more uniform layer distribution in comparison with VAF ones (Figure5 and S4).

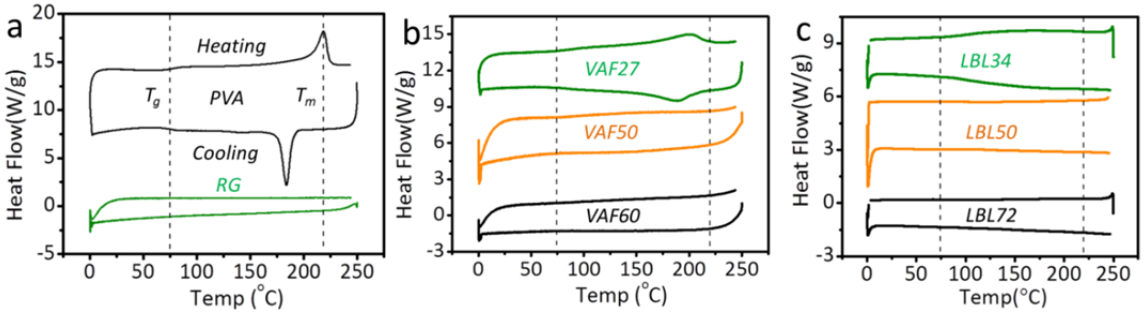

Figure 3.6. DSC curves for (a) neat PVA and RG VAF assembly without a polymer, (b) VAF composites, and (c) LBL composites. Zoomed-in curve for VAF27 demonstrating the glass transition point of the composite can be found in Figure 3.13.

3.2.3.4 Thermal Properties

A great advantage of combining nanoscale components and polymers is enhanced thermal stability associated with profound changes in chain dynamics and reduced gas permeability to avoid oxidation.[13, 36] According to differential scanning calorimetry (DSC), both LBL and VAF composites show marked suppression of glass transition of the matrix material (Figure 3.6a, b). Glass transition temperature can be identified as a DSC 'step' corresponding to a second order endothermic phase transition, while melting shows up as a first order phase transition appearing as a peak.[37] Neat PVA (Figure 3.6a black trace) demonstrates the glass transition temperature (T_g) of 75°C and pronounced

melting temperature (T_m) of 218°C in the heating curve (Figure 3.6a)[30] followed by crystallization upon cooling at 165^0C.

The T_g of VAF27 is increased by 10°C while T_m is reduced by 20 °C compared to pure PVA (Figure 3.6a *vs.* b). Concurrently, LBL34 displays an increased T_g by 25 °C without defined T_m (Figure 3.6c). The changes in T_g and T_m are more pronounced for LBL than for VAF assembled materials. This finding supports the conclusion that polymer chains are constrained between RG sheets in LBL composites stronger than in VAF composites.[38] The further increase of RG fraction leads to the complete suppression of the glass transition point in both LBL and VAF assembled films (Figure 3.6b and c). Such thermal behavior is quite similar to many "neatly intercalated" clay composites.[30] Note also that the effect of clay on the T_m is different in other layered materials, such as PVA/clay composites. It was reported that the composites exhibited dual melting point as compared to a single melting point of neat PVA due to phase separation of syndiotactic and atactic PVA.[30]

3.2.3.5 Mechanical Properties

We then systematically investigated and compared mechanical properties of LBL- and VAF-made PVA/RG composites, namely, their Young's modulus (E), storage modulus (E'), ultimate strength (σ_{ult}), ultimate strain (ε_{ult}) and toughness (K). PVA/RG composites made by both methods display progressively higher E and E' with increasing RG content (Figure 3.7a) and demonstrate overall high mechanical performance (Table 3-1). The properties of LBL and VAF differ greatly when RG volume fraction is low while becoming more similar for high RG contents. Neat PVA shows E=3.5±0.2 GPa, and σ_{ult} =90±5 MPa. With addition of 27 wt% RG, the VAF27 shows slightly higher

E=4±0.3 GPa, and σ_{ult} =95±7 MPa. In contrast, the addition of 34 wt% RG via LBL makes the film improve both properties by almost two times to E=7±0.5 GPa, and σ_{ult} =160±11 MPa. This result is attributed to the better plane-oriented RG sheets via the bottom-up alternative stacking of PVA and RG in LBL (Figure 3.4). At higher RG content, the mechanical performance difference shown in LBL72, LBL50, and VAF85, VAF60, VAF50 is minor (Figure 3.7a and b). The differences at atomic and nanometer scales observed in XRD between these composites are apparently less influential for these materials; the reasons behind this similarity and apparent inconsequentiality of atomic and nanoscale features are discussed below. It is not entirely unexpected that the existing theoretical models such as Voigt,[39] Reuss,[39] Padawer&Beecher,[39, 40] Riley,[39, 40] Mori-Tanaka,[41] and Halpin-Tsai[42] equations give poor predictions of the Young's modulus of our composites (Figure 3.7c and 3.14g) either overestimating (Voigt, Padawer&Beecher, Riley, Mori-Tanaka and Halpin-Tsai) or underestimating (Reuss) the experimental values. The reasons for failure of these models to predict correctly the mechanical properties are multiple. The most essential problem of these models appears to be in the assumption of the ideal stress transfer at the RG-polymer interface. Uncertainty about the atomic, molecular, and nanometer, and submicron scale mechanics at these interfaces does not allow researchers to develop better models. It is also unclear whether the Reuss model with the 'serial' coupling of matrix and the filer would be applicable to layered composites with parallel orientation of both soft and hard components.

The RG-PVA interaction and the interface between them are *de facto* described empirically from the perspective of thermodynamics in Figure 3.1. Therefore, one can

raise the question whether there would be some correlation between the mechanics and thermodynamics of the composites. In this respect one can see that the point of inflection of the curve in Figure 3.1b describing the enthalpy of RG-PVA system occurs for volume fraction of 53.5%. The inflection point on the tensile strength curve occurs at *ca.* 40% for both VAF and LBL composites in Figure 3.6d. At the same time, we do not see any particularly inflections on the dependence of Young's modulus vs. volume fraction in Fig. 3.6c.

Thermodynamics of RG-PVA interactions should have strong influence of the energy expenditures required for composite deformation. Therefore, it would be meaningful to look at the toughness of the prepared composites. As one can see in Figure 3.7, the volume fractions of *ca.* 50% RG corresponding to the case when all the polymer chains are interacting with the RG surface also leads to increased K. Moreover, we observed that in both VAF and LBL cases this composition gives the unique combination of ultimate tensile strength and toughness with $\sigma_{ult} \sim 150$MPa, and $K \sim 6.1$ MJ/m^3. One could also point out that This RG content of 50% is close to the brittle to ductile transition point, which makes sense since the excess of easily deformed PVA will compromise mechanical strength. Therefore, the hypothesis about the correlation between the thermodynamics of polymer-filler interactions and its mechanical performance appears to us plausible. At the same time, its thorough evaluation will need a more extensive investigation than a single paper.

Continuing with mechanical properties, we cannot help but notice that this combination of σ_{ult} and K is best among various layered GO, clay, or RG composites

previously studied (Figure 3.7c). In general, strength and toughness are the two mutually exclusive properties, which usually require a reduction of one to improve the other.[43, 44]

Glutaldehyde (GA) capable of aldehyde-hydroxyl crosslinking was reported to increase the strength and/or toughness of the layered composites. The samples of LBL50 and VAF46 were treated by 10 wt. % GA overnight to understand the effect of potential crosslinking on the mechanical properties of PVA/RG composites. The GA treatment increases E to 13 GPa and σ_{ult} to 222 MPa for LBL50 (Figure 3.7b, Table 3-1), while it has no effect on VAF-assembled composites. The fact can be attributed to the difference in nanoscale structure between the two different types of composites. Both VAF and LBL films have excellent barrier properties, thus the amount of GA that penetrates into the bulk of the films is small. In case of LBL the polymer exists primarily at the interface with RG where the crosslinking occurs. In case of VAF composites, PVA chains have smaller area of contact with RG sheets. We believe that GA preferentially crosslinks PVA molecules themselves rather than creating covalent bonds between the polymer and RG. Since PVA is already stiffened due to constrained volume (see Figure 3.6), the net effect on mechanical properties is negligible. Despite the dramatic decrease or increase of toughness reported for PVA/clay[1] or PVA/CNT[2] composites, GA crosslinking does not affect toughness of LBL50 material (Figure 3.7c).

Comparison of the structural data, mechanical and thermal properties warrants additional discussion. Layered architecture typical for aligned RG sheets established by SEM imaging is associated with micron and submicron levels of organization. At this structural level VAF and LBL composites display clear similarities. On the other hand, their atomic and nanometer scale features revealed in AFM, XRD and TGA data are

different. In this respect, the findings about *mechanical properties of VAF and LBL composites are surprising because the differences in atomic and nanoscale structure have unexpectedly little influence on the mechanical properties of VAF and LBL composites especially with high RG contents* (compare LBL50 and LBL72 *vs.* VAF46, VAF50, VAF60, and VAF85) (Figure 3.7a and b, Table 3-1). One might conclude that the similarities of mechanical properties at high RG content are associated with similarities at the micron and submicron scale. However, such conclusion is not valid. The evidence that atomic scale and nanoscale structures are still influential for the layered composites can be found in the results obtained after the GA treatment that improves Young's modulus and tensile strength for LBL composites but does not change the mechanical properties of VAF composites due to covalent crosslinking at the RG-PVA interface.

Considering (a) the inability of the existing models (Fig. 3.7c,d) to describe the mechanics of the composites adequately and (b) our expectations how strongly the atomic/nanoscale morphology should affect the mechanical performance, the hypothesis about the correlation between thermodynamics of RG-PVA interaction and mechanics of resulting composites can help us explain the experimental observations. Conceptually, the mechanical properties of the composites could be rationalized from the standpoint of the thermodynamic state of the polymer at the RG-PVA interface. Reaching a thermodynamic minimum of PVA chains on the surface of nanosheets leads to stronger, stiffer, and tougher materials than those formed with suboptimal packing polymer at this boundary. By other words, minimization of the energy of macromolecule in contact with the RG surface improves stress transfer and energy dissipation. As a consequence, we

see the highest toughness for LBL50 and VAF46 composites (Figure 3.4c) among all other filler contents. The weight composition for the high toughness material is identical to that of the RG-PVA complex observed in solution (Figure 3.1). The role of the adsorption state thermodynamics can also be traced in the similarities and differences of mechanical properties of LBL and VAF composites. In case VAF composites with high RG content, the relative amount of the epitaxial *vs.* peripheral PVA crystallites is different and alignment nanosheets is less regular than in LBL (Figure 3.4) but the most of PVA at the RG interface is in the optimal conformation corresponding to the thermodynamic minimum, which is the same for LBL and VAF materials. Thus the mechanical properties are similar as well.

At the moment we cannot identify the reasons why the dependence of Young's modulus on RG content in Fig. 3.7c does not have appear to have an inflection point for RG content ~ 50%. A part of the reason can be different mechanisms of elastic deformations for small strains compared to large strains responsible for ultimate tensile strength and toughness.

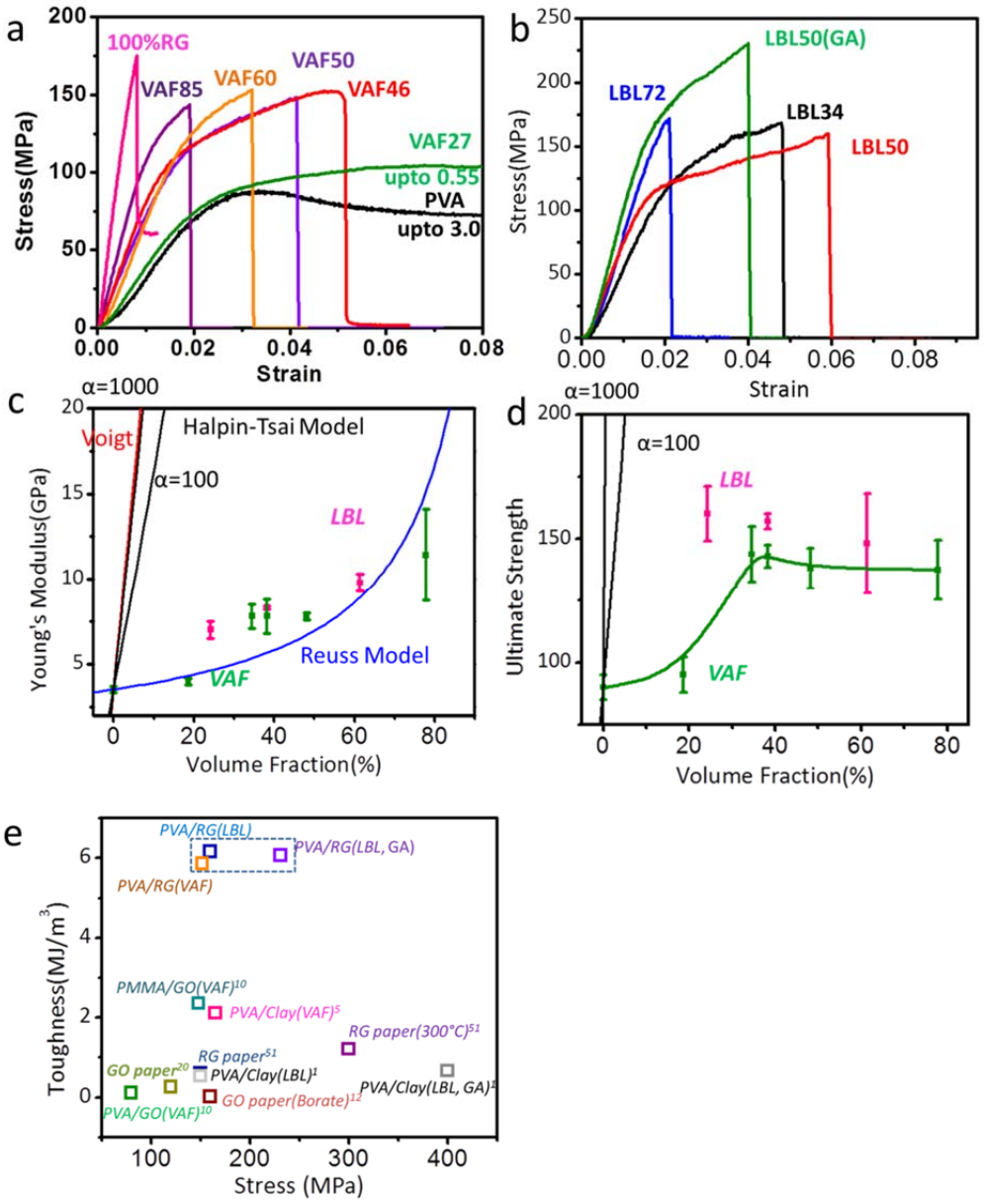

Figure 3.7. Mechanical properties of PVA/RG composites. (a, b) Stress-strain curves for VAF (a) and LBL (b) composites. The full range for VAF27 and PVA is shown in Figure 3.14b. c) Young's modulus prediction based on the Voigt (red), Reuss (blue) and Halpin-Tsai (black) for different aspect ratios of the filler (α). (d) Comparison of calculated and experimental data for ultimate strength of RG composites. (e) A comparison of PVA/RG composites with other GO, RG and clay composites in the toughness-strength chart.

3.2.3.6 Electrical Properties

The conductivity of the as-made PVA/RG LBL composites is more than one order of magnitude higher than that of VAF-made composites at similar RG content (Figure 3.8). Thermal treatment and related chemical changes in RG improve the conductivity while reducing the difference in charge transport performance between the two types of materials. After incubation at 220°C causing further restoration of graphitic network of sp^2 hybridized carbon in RG,[45] the conductivity reaches 46 S/m and 12 S/m for LBL and VAF composites, respectively. These electrical properties are better than most of reported RG composites.[46]

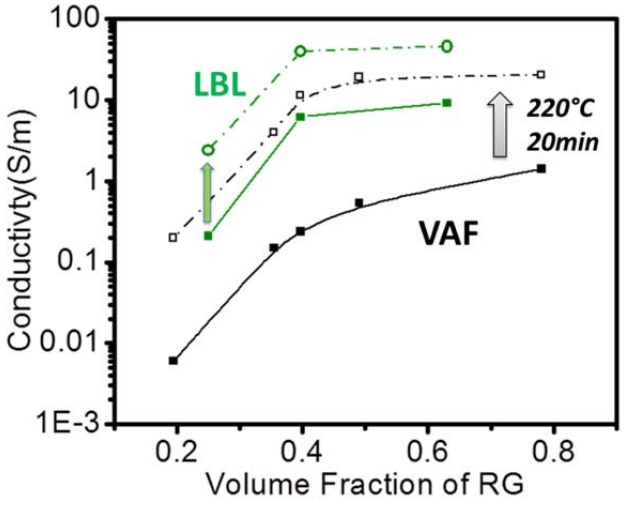

Figure 3.8. Electrical properties of LBL (green) and VAF (black) composites before (solid lines) and after (dashed lines) incubation at 220°C for different RG fractions.

The large disparity in electrical conductivity is a clear representation of their structural differences at atomic and nanoscale level of organization. The greater contents of randomly oriented peripheral PVA crystallites and larger basal spacing observed for VAF composites in XRD studies (Figure 3.4) lead to the conclusion that the average

separation between the conductive RG sheets in LBL composites is smaller than in VAF composites. In respect to micron- and submicron scales, the improved alignment of RG sheets in LBL assembly as compared to their organization in VAF composites (Figure 3.4) enhances their overlap. It is common to observe several pieces of RG overlapping each other in the AFM image of LBL bilayers (Figure 3.2d). In contrast, most of individual RG sheets in the VAF assembly are surrounded by PVA, which serve as an insulating interface.

3.2.4 Conclusion

LBL and VAF are the widely used methods for making advanced composites. From the previous works we could infer that LBL assembly can be favored in terms of better control of nanoscale organization and applications toward microscale devices,[47-50] while VAF composites as well as exponential LBL[51] can be more advantageous for applications where large volume of the material is needed. The novelty of the study carried out here is that comparison of LBL- and VAF-made materials creates a conceptual framework for property-oriented materials engineering of layered composites. Multiple structural factors at different RG contents were correlated with thermal, electrical, and mechanical properties. Molecular processes, such as epitaxial crystallization of PVA on RG that were not identified before to take place in RG-polymer systems and were clearly demonstrated. They are essential for understanding of composite properties. The structural effects on electrical conductivity were consistent with *a priory* expectations favoring LBL assembly that minimizes tunneling barriers between conducting sheets. Unexpected lack of correlation between nano- and microscale structural features and mechanical properties was also observed. The findings

about mechanical properties were rationalized based on enthalpic effects at the organic-inorganic interface. We believe that reaching energy minimum for polymer chains adsorbed to nanosheets plays the critical role in the improvement of mechanical properties, while the other structural parameters are secondary. Notably we made for LBL and VAF composites with toughness of 6.1 MJ/m^3. It is the highest than for any layered composites from RG, cellulose, clay, and similar materials. Optimization of the mechanical properties from the perspective of thermodynamics rather than purely morphological perspective appears to us to be a universal and quantifiable approach that could be extended to a variety of other composites. Application of the thermodynamic approach to the design of organic-inorganic materials will may simplify the process of materials engineering.

3.2.5 Supplementary Information

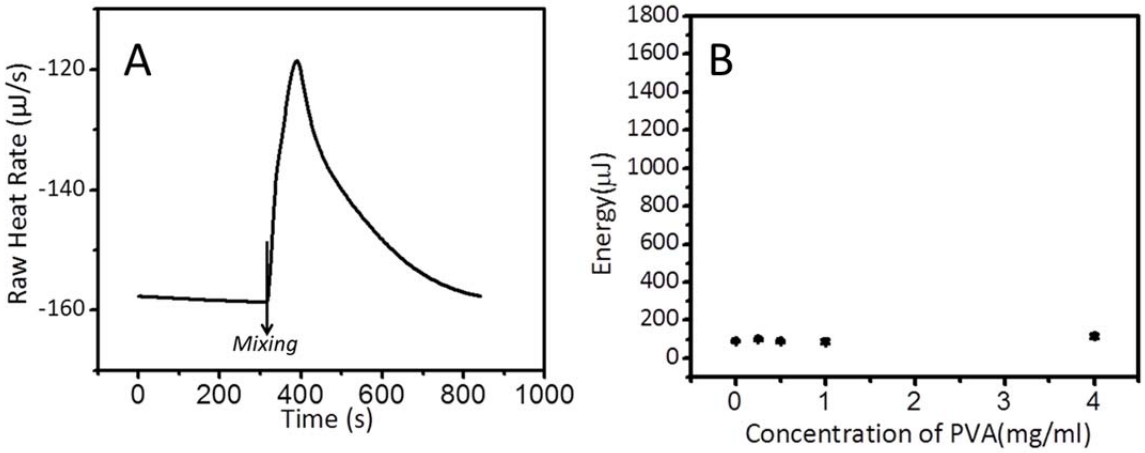

Figure 3.9. (a) Typical raw heat rate vs. time when mixing PVA and RG solutions. (b) Mixing enthalpies for PVA and DI water for different concentrations of PVA.

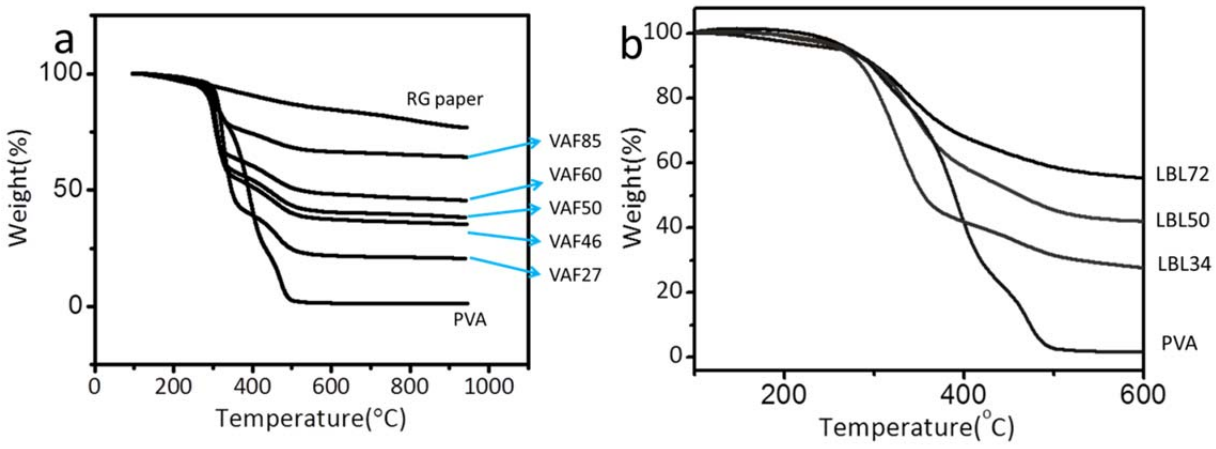

Figure 3.10. TGA curves for (a) VAF and (b) LBL composites from PVA and RG, pure PVA and RG paper. RG fractions are calculated from the residual weights at 600°C.

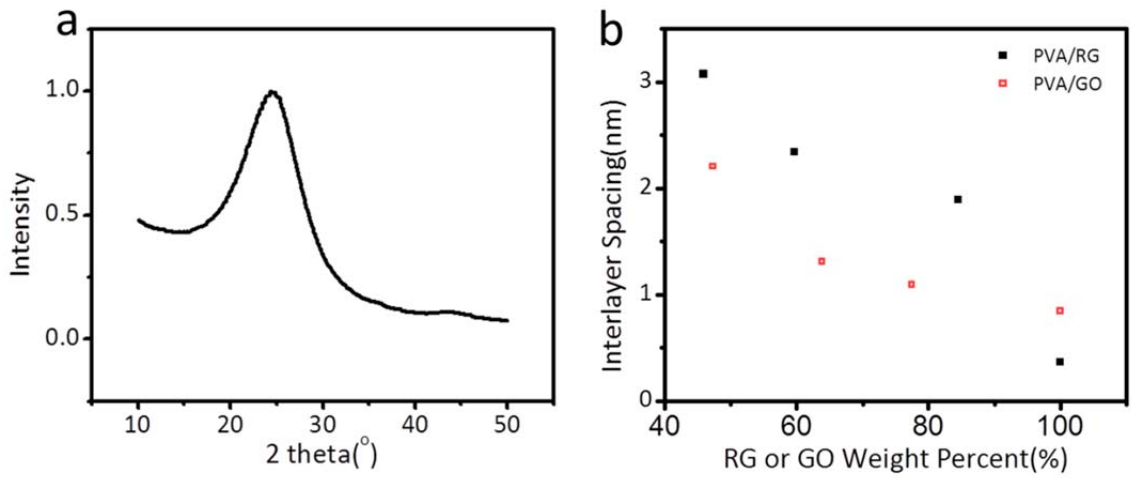

Figure 3.11. (a) XRD scattering of VAF-made RG paper without any polymer. (b) Comparison of interlayer spacing of PVA/RG and PVA/GO composites made by VAF at different RG weight fractions. The data for PVA/GO composites are taken from Ref.[10]

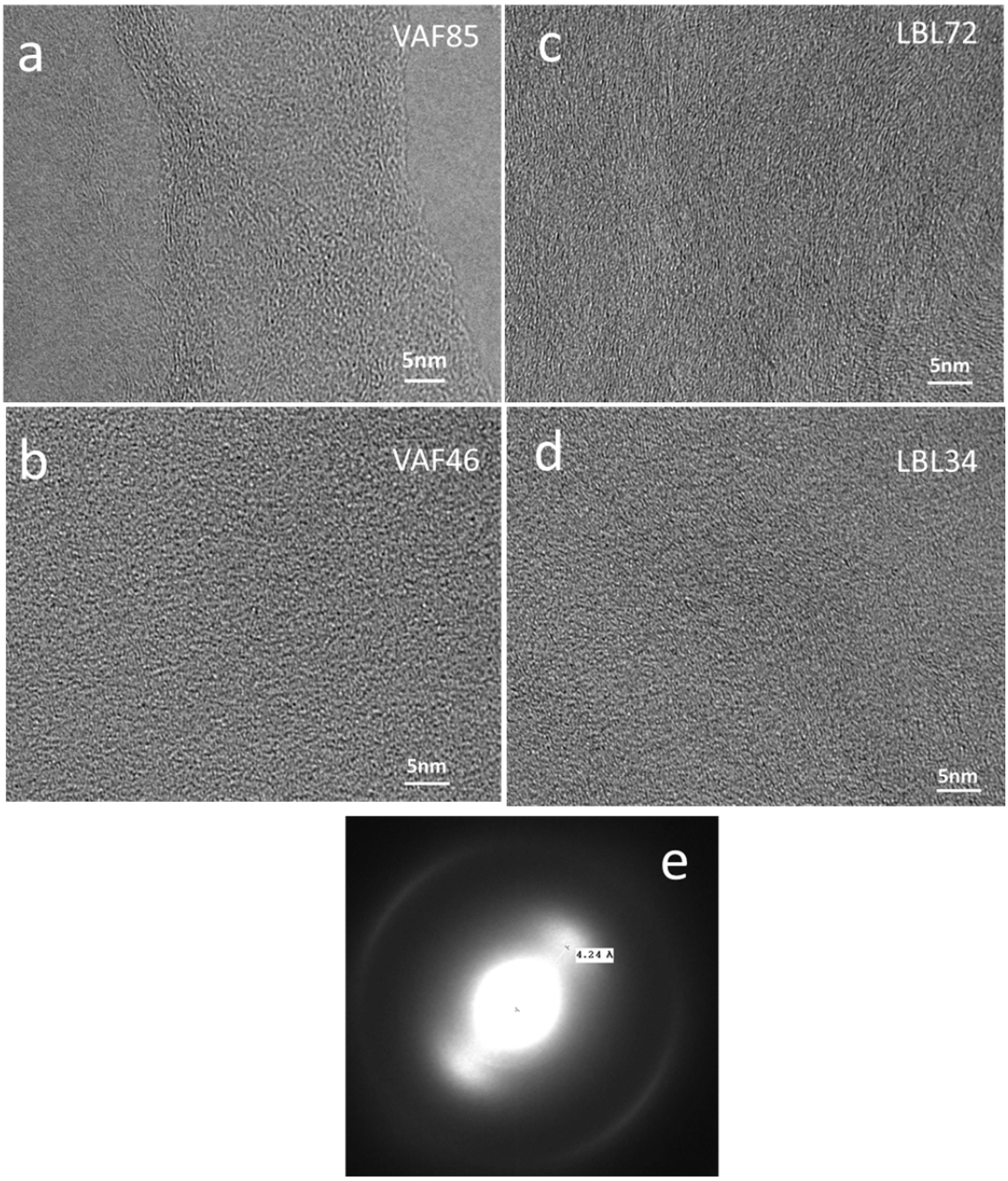

Figure 3.12. High resolution TEM images of (a) VAF85, (b) VAF46, (c) LBL72, and (d) LBL34 cross-sections. (e) The selected area electron diffraction of LBL34.

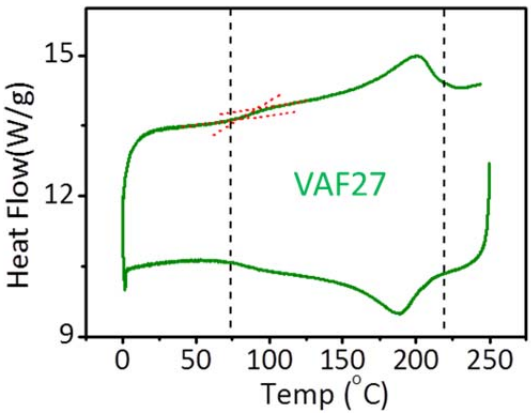

Figure 3.13. DSC curve for VAF27 showing the glass transition.

Theoretical Predictions of Mechanical Properties of Layered PVA/RG Composites.

A. Known Parameters used in Calculations:

For calculations of Young's moduli of composites:

Young's Modulus of RG:[52, 53] E_f=250GPa

Poisson ratio of RG: ν_f=0.41

Aspect ratio of *RG* sheets: $\alpha = \frac{L}{d} = 100\sim1000$, where *L* and *d* are the average diameter and thickness of the sheet respectively. (Figure 3.14e)

Young's Modulus of PVA: E_m=3.52GPa

Poisson ratio of PVA: ν_m=0.45

Shear Modulus of PVA: $G_m=E_m/[2\times(1+\nu_m)]=1.21GPa$

For calculations of ultimate tensile strength of composites:

Strength of RG:[54] σ_f = 42GPa

Shear strength of PVA: τ_y = 45 MPa

Critical aspect ratio:[3, 39] $\alpha_c = \sigma_f/\tau_y$=1000

Tensile strength of polymer: σ_m = 90 MPa

B. Theoretical Calculations of Young's Modulus:

1. **Voigt Model**[39] (Figure 3.14c)

   $E=V_fE_f+(1-V_f)E_m$ **(Eq.1)**

2. ***Reuss Model***[39] (Figure 3.14d)

   $1/E=V_f/E_f+(1-V_f)/E_m$ **(Eq.2)**

3. ***Padawer&Beecher Model***[39, 40] (Figure 3.14e)

   $E=V_fE_f(MRF)+(1-V_f)E_m$, where $MRF=1-\tanh(u)/u$, and $u=\alpha\{G_mV_f/[E_f*(1-V_f)]\}^{0.5}$ **(Eq.3)**

4. ***Riley Model***[39, 55] (Figure 3.14e)

   $E=V_fE_f(MRF)+(1-V_f)E_m$, where $MRF=1-\ln(1+u)/u$, and $u=\alpha\{G_mV_f/[E_f*(1-V_f)]\}^{0.5}$ **(Eq.4)**

5. ***Mori-Tanaka Model***[41] (Figure 3.14f)

   $E=E_{11}=1/S_{11}$, where S11 is the element in compliance tensor S of the composite. **(Eq.5)**

   $S=(V_mS_m+V_fS_fB)(VmI+V_fB)^{-1}$,

   $B=C_fA(C_m)^{-1}$,

   $A=[P_mC_m^{-1}(C_f-C_m)+I]^{-1}$

   C_m, S_m and C_f, S_f are the modulus and compliance tensors of the matrix and the filler respectively. I is identity tensor, A and B are referred to as stress and stress concentration tensor respectively. P_m is the well-known Eshelby's tensor, and depends on the elastic properties of the matrix and the shape of the fillers.

6. ***Halpin-Tsai Model***[42] (Figure 3.14e)

   $$E = E_m\left[\frac{1+\eta\xi V_f}{1-\eta V_f}\right],\ \eta = \frac{\frac{E_f}{E_m}-1}{\frac{E_f}{E_m}+\xi},\ \xi = 2\alpha/3 \qquad \textbf{(Eq.6)}$$

Comment: The Young's modulus (E) of PVA/RG layered composites could be predicted by relating the matrix and filler elements using two different approaches. In the Voigt model, the elements are in parallel with each other and experience the same strain (Figure 3.14c). The value of Young's modulus E is then given by Eq. 1. The other approach is represented by the Ruess model where all the elements are in series and

undergo the same stress (Figure 3.14d). The value of Young's modulus *E* is then given by Eq. 2. The Voigt and Reuss models predict the upper and lower bounds of *E*, respectively.

Figure 3.14e depicts the model of the layered PVA/RG composites, where discontinuous sheets are parallel to each other in a matrix. The sheets are embedded in the matrix and load is transferred from matrix to the sheet by shear force at the interface. A "shear lag" analysis was developed in Padawer and Beecher model (Eq.3) taking into account the shear modulus of the matrix and aspect ratio of the filler. The Riley model (Eq. 4) considers the interactions between adjacent sheets while the others do not.

Another approach of predicting the *E* of layered composites is through the Mori-Tanaka model (Eq. 5).[41, 42] It takes into account the overlapping stress field of neighboring fillers. This model can effectively predict the reinforcing effects of fibers, spheres and sheets by using either prolate or oblate spheroids (Figure 3.14f). Remember that when the filler has geometry of sheets, the aspect ratio in this model is defined as 1/α, where α= *L/d* (Figure 3.14e). This model is based on the Eshelby's equivalent inclusion method and the Mori-Tanaka's average stress theory.

The *E* of this structure (Figure 3.14e) can also be predicted by a semi-empirical Halpin-Tsai model (Eq. 6). Since the empirical parameter ξ is usually calculated by the Mori-Tanaka model,[41] the curves based on those models usually overlap.

When the aspect ratio α of sheets is high enough (>1000), the predictions for *E* based on models 3–6 are close to that those obtained from the Voigt model or the rule of mixtures (Figure 3.14g). *To be noted here, all those models presume that matrix is firmly bonded to the RG (i.e. stress transfer at the interface is ideal.*

The values of Young's moduli measured in this study are close to those predicted by the Reuss model (Figure 3.7) while all the other models greatly overestimate their mechanical properties. Considering the assumptions and the directionality of the hard and soft segments in the Reuss model (Figure 3.14d), the approximate coincidence is likely to be fortuitous. The strong discrepancy with predictions by other models describing the directionality of the sheets much closer to the actual structure of LBL and VAF composites should be attributed to the non-ideal stress transfer at the RG-PVA interface. The reasons behind non-ideality of the stress transfer even for small deformations can be multiple and need more extensive experimental studies.

C. Theoretical Calculations of Ultimate Strength:

The aspect ratio of RG is typically smaller than critical aspect ratio, so that the RG composites should rupture under the sheets pull-out mode. [3, 39]

Thus the strength of composites (σ_{ult}) can be calculated in the structure similar to Figure 3.14e using the Rule of Mixtures:[3, 39]

$$\sigma_{ult}=0.5V_p\tau_i\alpha+(1-V_p)\sigma_m$$

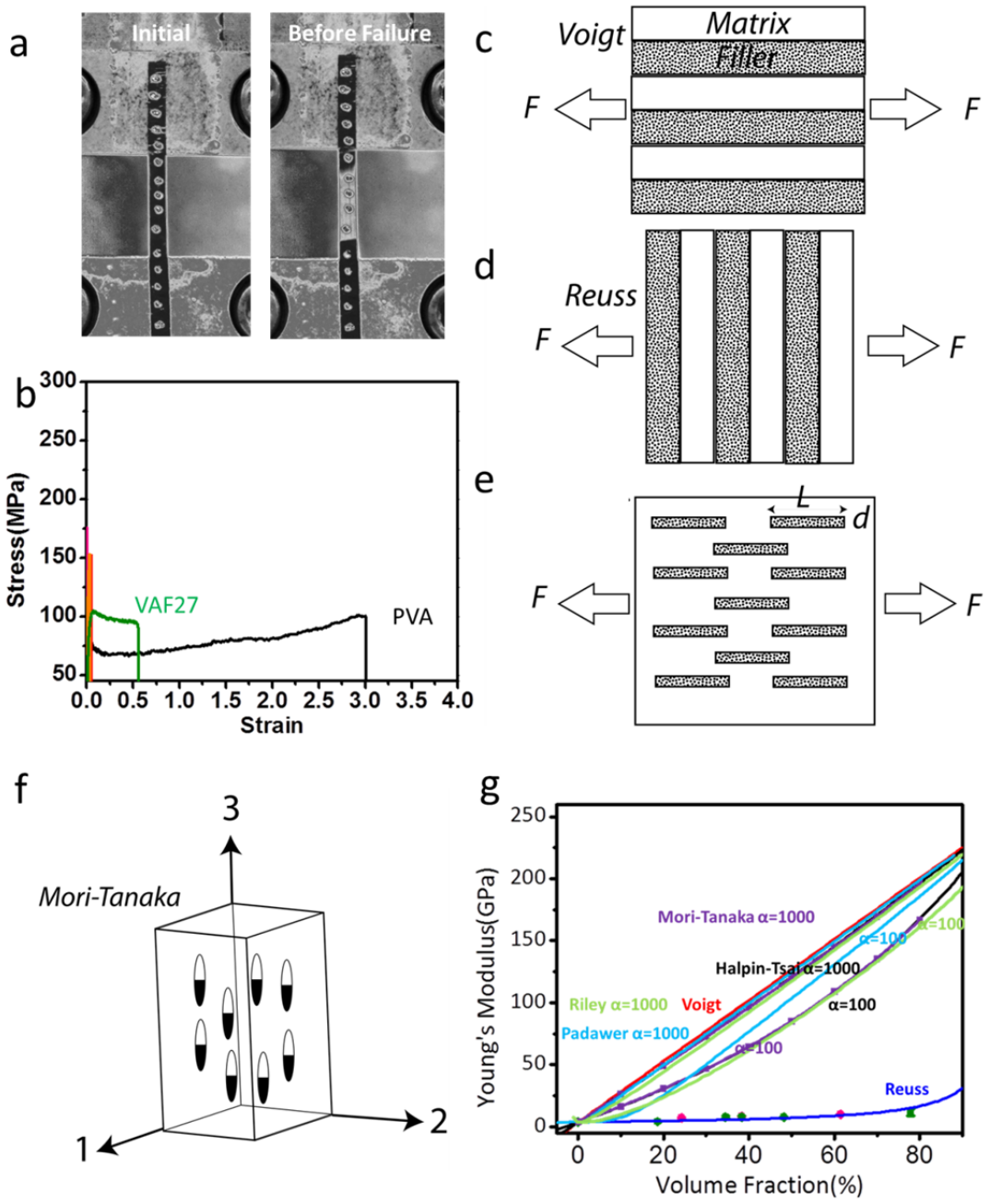

Figure 3.14. (a) A photograph of LBL50 sample strip with gauge marks stretched between two grips at the initial and before-failure states. (b) Stress-strain curves for VAF27 and PVA. c, d, e, f) Different configurations of layered structures theoretical models are based on. g) Predictions of Young's moduli of LBL/VAF composites with specific volume fractions based on Voigt (red), Reuss (blue), Padawer (light blue), Riley(light green), Mori-Tanaka (Purple) and Halpin-Tsai (black) for different aspect ratios of the filler (α).

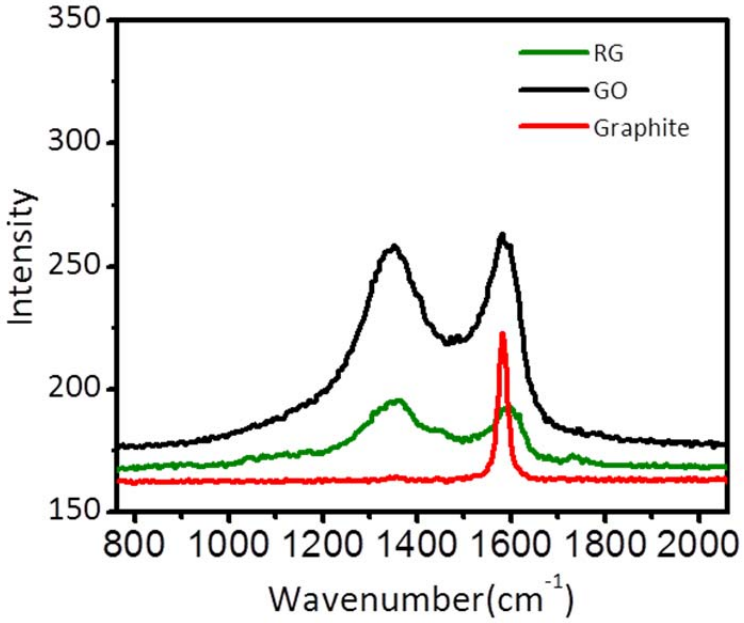

Figure 3.15. Raman spectra of GO, RG and graphite.

3.3 Engineering Stiff Graphene Oxide Composites with Psedonegative and Tunable Thermal Expansion by Vacuum Assisted Flocculation

3.3.1 Introduction

Typically materials expand on heating and have a positive coefficient of thermal expansion (CTE). The material expansion is associated with the general asymmetry of interatomic potential when the energy penalty for bringing bonded atoms closer together is steeper than for pulling them apart.[56] In some solids, however, other factors, such as phase transitions,[57] electronic valence transitions,[58] magnetoresticton,[59] transverse vibrations,[60, 61] or topology[62, 63] may yield the overall contraction at higher temperature resulting in a phenomenon of negative thermal expansion (NTE). Such NTE materials are fundamentally interesting, however, their applications especially in zero-CTE composites[58, 63] are limited due to poor scalability and toxicity (for instance, metal oxide- and cyanide-framework materials).[57,60,61] Also, the NTE effects are often very small and anisotropic as in Kevlar,[64] polyethylene fibers,[65] and carbon nanotubes[66] showing CTE below -5ppm K^{-1}. Graphene was also found to display negative yet small CTE of -6 or -8 ppm K^{-1} at 300 K[67, 68] with theoretically predicted value[69] of -3.8ppm K^{-1}. Dense packing of graphene sheets reduces their out-of-plane deformation and solid graphite shows even smaller NTE of -1.5ppm K^{-1} for 273—423K.[70] Alternatively, liquid crystal phase of nanographene with large inter-gallery spacing has shown highly anisotropic NTE equal to -121, 91.2 and -59.6 ppm K^{-1} along the *a, b* and *c* axes.[71] Large NTE materials with high mechanical properties are needed as a starting point for preparation of zero-CTE composites,[58, 63] actuators, sensors and memory materials.

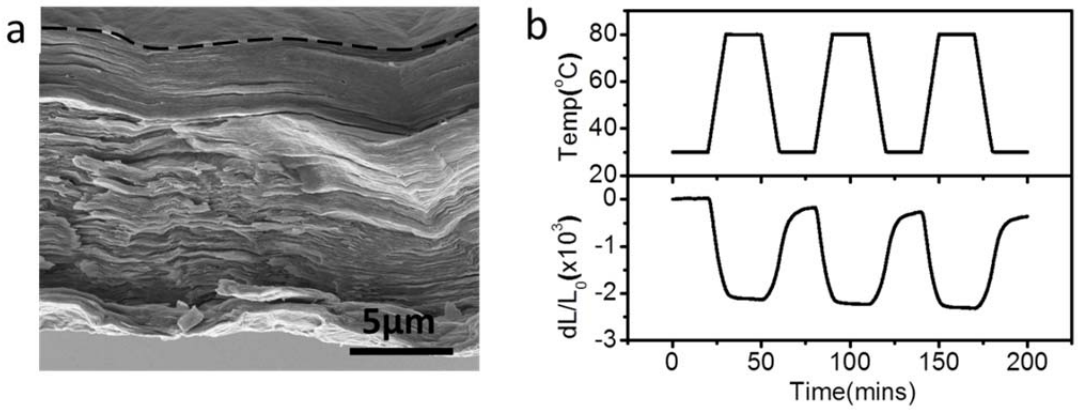

Figure 3.16 Properties of GO paper. (a) SEM image showing the cross-section of GO paper. (b) Thermal behavior of GO paper for repeated cooling and heating cycles at relative humidity of 2.0% with label dL standing for absolute length change and L_0 initial length at 30°C.

In this section we investigate the thermal behavior of stiff graphene oxide (GO, Figure 3.16a) that demonstrates highly negative apparent CTE associated with temperature-induced removal/insertion of interstitial water (thermohydration). The observed thermohydration effects can be described as pseudonegative thermal expansion (PNTE) and are more complex and surprising than might be expected from any previous studies.[20, 72] As such, PNTE reveals a lot of similarities to classic NTE exemplified by the reversibility of expansion-contraction cycles (Figure 3.16b) and retention of high mechanical characteristics of the material (Figure 3.22c). Simultaneously, GO displays a number of unusual thermal expansion properties including the strong hysteresis of expansion/contraction rates. It is also quite surprising to see how low levels of humidity are needed for PNTE to take place. At present, the interplay between thermal properties and solvent/water incorporation cannot be easily predicted based on the current conceptual basis of soft matter and should be treated as poorly understood property for such materials with GO being just one of them. The recent findings about remarkable

water permeation through GO[73] give strong indication that there are potentially many unexpected phenomena related to water transport in GO and other materials.

The need for understanding of the thermohydration effects is further underscored by many developing applications[20, 74] in energy storage, MEMS, actuators, and essential for the design of new memory materials. PNTE can be potentially useful for the rapidly evolving area of laser patterning of GO.[75, 76] Importantly, while displaying large PNTE coefficients, GO is also associated with traits such as biocompatibility, scalability, and 2D isotropy, which are not shared by many other classic NTE materials.

3.3.2 Experimental

Preparation of GO paper and GO coating: GO was prepared by the Hummers and Offeman's method from graphite (Bay carbon, SP-1).[20] Element analysis shows C: O: H = 43.26: 53.41: 3.33 in GO with 20.58 wt % mobile water and 8.76 wt% bound water included, which were determined by Karl Fischer titration when the sample was burnt at 100°C and 200°C respectively. 3mg/ml GO dispersions were prepared by sonication of GO in DI water for 30mins. GO paper was made by pouring the dispersion onto a 0.1μm Nylon filter under vacuum followed by thorough drying in vacuum oven for 48 hours.[20] GO coating was made by spraying 0.5mg/ml GO dispersion on a heated silicon surface at a temperature lower than 80°C.

Preparation of thermally and chemically reduced graphene paper: Thermally reduced graphene paper was prepared by heating the as-prepared GO paper at 300°C for 1 hour. In order to make chemically reduced graphene paper, 100μl hydrazine solution (50wt%, Aldrich), and 700 μl of ammonia solution (28wt%, Aldrich) were added into 200ml 0.25mg/ml GO dispersion, and the mixture was put into the 80^{o}C oven for 1

hour.[22] The mixture was filtered through 0.1μm Nylon filter under vacuum to make chemically reduced graphene paper.

Coefficient of thermal expansion (CTE) measurement: 1) *In-plane* CTE measurement: CTE of films was measured in extension mode by Perkin Elmer TMA7 following ASTM *Test Method for Linear Thermal Expansion of Solid Materials by Thermomechanical Analysis* (E 831) and slightly modified to measure thin films.[77, 78] The extension probe and grips were customized by RT instruments, Inc. to minimize the expansion of grips during the measurement (Figure 3.30). Ultrapure helium was used as purge gas to give an inert atmosphere and facilitate heat transfer. Cooling of the chamber was accomplished by circulating water at 8°C provided by a chiller. The TMA instrument was calibrated using Aluminum standard; the experimental error for CTE of Aluminum was 7.6% for temperature as high as 300°C. CTE of Kevlar fibers from DuPont was also measured as additional calibration for negative expansion yielding a value of -4.58ppm K^{-1}, which agreed with the data reported in literature.[64] 2 mm wide and 15mm long GO paper strips were used for CTE measurements; the strips were stretched under 30mN and the length changes were recorded by monitoring probe displacement for temperature ramps of 5°C/min and 1°C/min. The sample was initially heated from 30 up to 80°C and then stabilized for 2 hours to remove free water and residual stress. The length change for both cooling and heating segments was used to calculate CTE represented by the slope of the curve normalized by the initial length at 30°C. This parameter can be mathematically defined as CTE=$d(\frac{\Delta L}{L_0})/dT$. The thermal curve was non-linear, thus average CTEs were calculated for every 10°C interval. More than 3 samples were measured for each data point. 2) CTEs were also measured for transversal (through-thickness) direction of GO

assemblies. In order to achieve that, the thickness of GO coating on silicon wafers was measured by a J.A.Woolham Co. VASE spectroscopic ellipsometer through fitting Cauchy model with homemade temperature controlled stage. 3) Modulated Temperature TMA was performed on GO paper samples by Q400 Thermomechanical Analyzer in a lab of TA instruments, Inc. The samples were cut into thin strips approximately 16mm in length and 2.8mm in width. Modulated TMA was used with amplitude of ±5°C, a period of 300 seconds, and heating/cooling rate of 1°C/min. The data from 30 to 80 °C in the second heating step were used in this paper.

Material characterization: *Element analysis and Karl Fischer Titration* were conducted by Galbraith Lab Inc. *Differential scanning calorimetry (DSC)* was carried out on a TA instrument Q2000 DSC under nitrogen atmosphere at a rate of 5^{o}C/min. Cross-section of the films was examined by *FEI NOVA Nanolab Scanning electron microscopy* (SEM). *ATR-FTIR spectroscopy* was performed on a Nicolet 6700 spectrometer utilizing the grazing angle accessory (Smart SAGA) at a grazing angle of 85°. A drop of GO dispersion was put on a gold coated silicon substrate, and let dry for 24 hours. This sample was then attached onto a heat strip with temperature controller for *in-situ* FTIR measurement. Similar setup was used for Raman measurement. *Solid NMR experiments* were performed on 400 MHz NMR spectrometer with spinning rate of 7 KHz on a 5mm MAS probe. C^{13} 1D NMR spectra were recorded using Ramp CP pulse sequence with CP time 1 ms, and a decoupling of 70 kHz was applied. A 3s recycle delay and 2048 scans were used for all experiments. *Powder x-ray diffraction (XRD) patterns* of GO paper were collected at ambient temperature using a Rigaku R-AXIS SPIDER diffractometer with an imaging plate detector and graphite monochromated Cu-Kα radiation (1.5406 Å).

Samples were glued to the tips of glass capillaries. Images were collected sequentially with collection time of 2 minutes and χ was set at 0° with the face of the film oriented parallel to the beam. 20 liter/min room-temperature ultrapure nitrogen was controlled on and off to flow onto the sample. Images were integrated from 2.0° to 50° (2θ) with a 0.1° step size with the AreaMax (2.0.0.4 ed., Rigaku, 2005) software package. Powder patterns were processed in Jade 6.5 to calculate peak positions.

3.3.3 Results and Discussion

GO with sheet thickness of 1nm (Figure 3.22a) was prepared by the Hummer's method.[21] The layered GO assemblies (Figure 3.16a) were made through vacuum assisted filtration leading to *ca.* 18μm thick free-standing film (GO paper)[20] or by spraying to obtain a GO coating with a thickness of *ca.* 100nm.[73] Thermal expansion of a freestanding GO paper was studied by thermal mechanical analyzer (TMA). The TMA can eliminate grips related errors, which can hardly be circumvented by other tool used in previous studies.[20, 79] It is found that the length of GO paper shows reversible contraction/expansion upon heating/cooling (Figure 3.16b). Considering the facts that (1) the samples were exhaustively dried in vacuum for at least 48 hours prior to the measurements; (2) exceptional care was taken to control the humidity of sample environment including using ultrapure helium (99.9995%) as purging gas, (3) temperature window between 30°C and 80°C was purposefully selected to avoid any temperature-induced chemical changes in GO (see SI), the NTE of GO is initially attributed to deformation of the out-of-plane bonds (*i.e.* the well-known membrane effect[80]). The dominance of out-of-plane over in-plane vibrational modes is hypothesized to significantly enhance the similar effects in graphene,[71] which can be a plausible NTE

mechanism for GO. However, the exhaustive evaluation of the data reveals inconsistencies of this seemingly realistic hypothesis.[24] As such, if NTE occurs due to the deformation of out-of-plane bonds, this effect should be visible in NMR,[81] Raman or FTIR[82] spectroscopy, but the intensity and positions of the characteristic bands change insignificantly (Figure 3.18). In addition, the membrane effect would lead to a positive CTE in the transversal direction to the packing of GO sheets as a result of "bending" of sheets. In contrast, the thermal behavior of GO paper still shows negative expansion in this direction (Figure 3.26a).

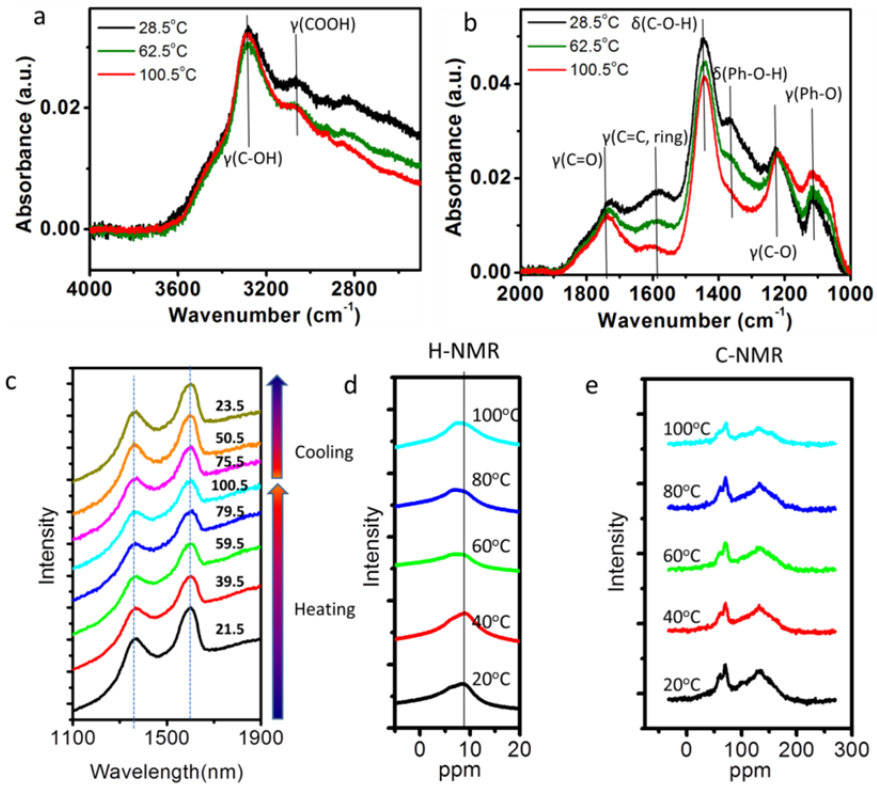

Figure 3.18 |Thermal spectral analyses of GO paper. (a,b) *In-situ* FTIR of GO sample at 28.5°C, 62.5°C, and 100.5°C. The FTIR spectra[27] show vibration modes of various functional groups on the GO, including –OH stretching from C–OH (3289.1cm^{-1}), and COOH (3094.8 cm^{-1}), C=O stretching (1736.1 cm^{-1}), aromatic ring (Ph) stretching (1610.3 cm^{-1}), –OH bending from COOH (1441.1 cm^{-1}) and Ph–OH (1368.8 cm^{-1}), C–O stretching from Ph–O (1216.9 cm^{-1}) and C–O–C or C–OH (1109.4 cm^{-1}). All displayed

FTIR spectral changes are reversible for cooling-heating cycles. (c) Raman spectra of GO at different temperatures. In the spectra, D band (1368.8cm $^{-1}$) and G band (1601.8 cm^{-1}) were shown. No significant shift was observed. (d) ^{1}H-NMR and ^{13}C-NMR spectra of GO at different temperatures. The peak in ^{1}H NMR spectra mainly comes from C–OH and water. ^{13}C NMR spectra of GO consists of three resonance lines at ca. 60, 70 and 130ppm.[26] The first two peaks originate from tertiary C–OH and C–O–C groups and the third from C=C bond.

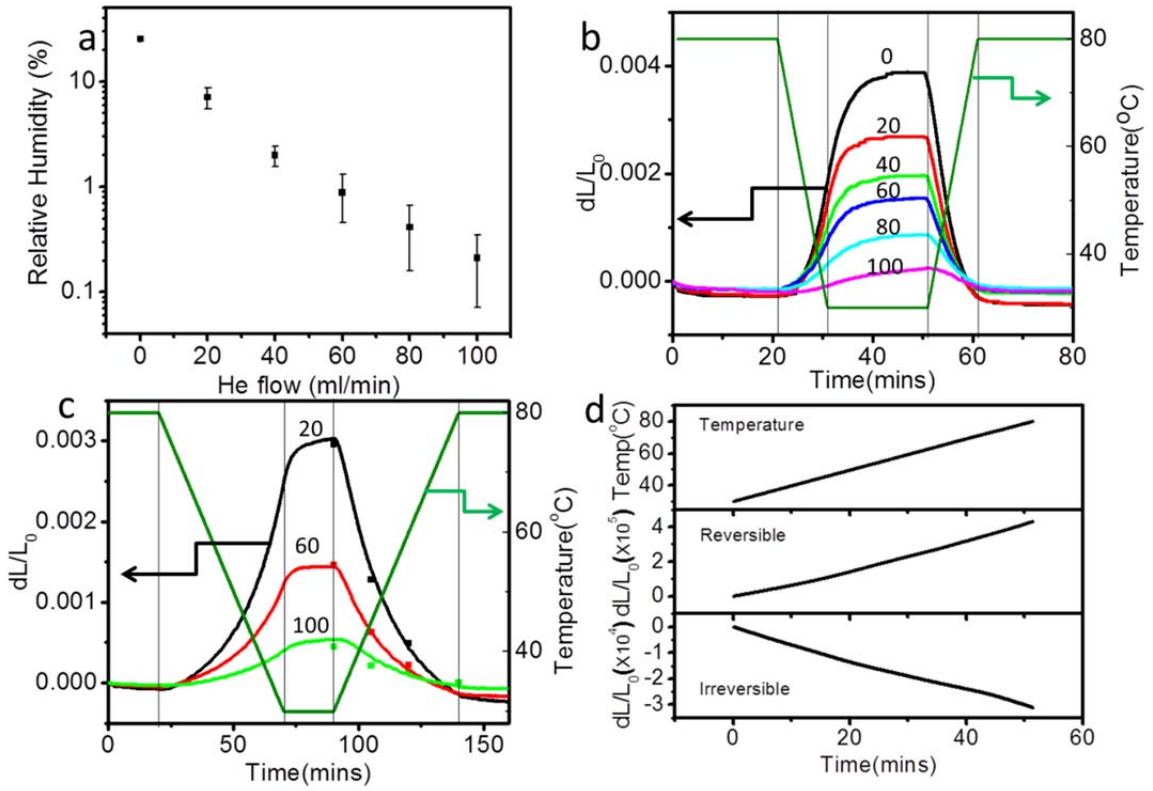

Figure 3.18 |Thermal Properties of thoroughly dried GO paper. (a) Dependence of the relative humidity of the TMA sample chamber on the helium flow rates. (b and c) Thermal behaviors of GO paper at different relative humidity (helium flow rates) with temperature ramp rates of (b) 5°C and (c) 1°C/min. Solid points in (c) are in conditions of long-term equilibration at corresponding temperatures and relative humidity (helium flow rates). (d) Modulated thermal mechanical analysis of GO paper, showing temporal change of temperature, reversible normalized length and irreversible normalized length changes.

We find that despite all the precautions and additional external isolation of TMA probe in a specially-made enclosure flooded with 99.9995% nitrogen, the continuous flux of ultrapure 99.9995% helium at 40ml/min for as long as 24 hours in the testing chamber

cannot reduce the relative humidity to zero related probably to the state of water in the sample and in the testing chamber. The humidity of environment around the sample is found to depend on helium flow rate (Figure 3.18a-c), which becomes an important experimental parameter to consider. We also observe that the expansion of GO during cooling stage continues after reaching the temperature plateau, *i.e.* the isothermal stage at 30°C. In contrast, the contraction of sample during the heating is virtually in-sync with the temperature ramp. All these observations in aggregate indicate to us that thermohydration effects can potentially be the reason for apparent NTE behavior. For instance, the difference in expansion and contraction dynamics during cooling/heating ramps could be due to unequal rates of water adsorption/removal, which is agreeable with water sorption studies on freeze-dried food[83] and polyelectrolytes.[84, 85] The difference is reduced when d*T*/d*t* is lowered from 5°C/min to 1°C/min without affecting the overall length changes as long as humidity remains the same (Figure 3.18b *vs.* 3c). In addition, since relative humidity is exponentially increased upon cooling (Figure 3.24a), the increase of length speeds with decreasing temperatures before reaching a steady state.

The changes of sample length after long-term equilibration at a specific temperature (Figure 3.26b) are similar to those at faster temperature ramps, *i.e*. 5°C/min to 1°C/min, and closely followed the T(*t)* trace (Figure 3.18c). This finding indicates the presence of equilibrium state in the thermal trajectory, consistent with the thermodynamically reversible water adsorption/removal. Therefore, water-related thermal behavior of GO can be characterized by means of the CTE. Since thermal behavior is always nonlinear for GO, CTE is calculated by linearizing the data in a set of 10°C intervals (Figure 3.25). As expected, CTE of GO is more negative at higher humidity, and

less negative at higher temperatures. The most negative CTE values for 25%, 7.1%, 2.0%, 0.88%, 0.41% and 0.21% humidity levels are -130.14, -94.17, -67.80, -51.4, -25.88, -11.7 ppm K^{-1}, respectively (Figure 3.25). Notably, CTE of GO are much larger in magnitude than that of reported NTE materials such as graphene,[67, 68] carbon nanotubes,[66] Kevlar,[64] ZrW_2O_8,[60] $Zn(CN)_2$,[86] and $Cd(CN)_2$[86] even at very low relative humidity of 0.21%.

Solid materials with large PNTE associated with thermohydration effects have never been carefully studied or even observed. Hydrogels (although not always solid materials) were reported to have irreversible shrinkage during drying.[87] Wood, a solid material with high equilibrium moisture content at high relative humidity, only shows -3ppm K^{-1} at temperature below 50°C[88] and its reversibility is questionable as a result of sorption hysteresis[89] attributed to changes in the complicated and irregular nanopore structures.[90] Other hygroscopic material, such as cement paste,[91] shows only positive CTE with a delayed response to temperature as a result of water transport. It can be argued that the presence of basal spacing between the GO sheets coupled with strong water uptake/desorption abilities leads to the manifestation of PNTE.

In order to study thermohydration effects in GO, powder x-ray diffraction (XRD) was applied (Figure 3.19a) to observe structural variations at room temperature under conditions allowing fast switching between "wet" and "dry" states. We changed the environment between (1) ambient air with relative humidity of 35% and (2) ultrapure nitrogen environment with untraceable humidity levels. In addition to the typical strong diffraction peak within 2θ of 10—15°, which are usually assigned to stacks of hydrophilic regions with oxygenated functional groups on GO sheets, the sensitive XRD

analyzer can also pick up weak signals for stacks of non-oxidized and hydrophobic graphitic region in GO sheets (Figure 3.19c) with typical spacing of 0.342nm, which matches well with 0.344nm spacing of multilayer turbostratic graphene and is larger than *d*-spacing of 0.335nm in graphite.[92] The position of weak "hydrophobic" peak is unaffected during the wet-dry switching, while the strong peak "hydrophilic" peak shifts almost immediately (<1min) from 0.78nm to 0.66nm upon drying and quickly moves back at higher humidity (Figure 3.19b). Its intensity also increases from wet to dry state as a result of better ordering. Therefore water molecule can indeed be easily and reversibly inserted and removed from the GO layered assemblies in response to the humidity change. Due to close correlation between relative humidity and temperature (Figure 3.24a), this XRD experiment analysis also sheds light on what occurs in the material in response to temperature changes.

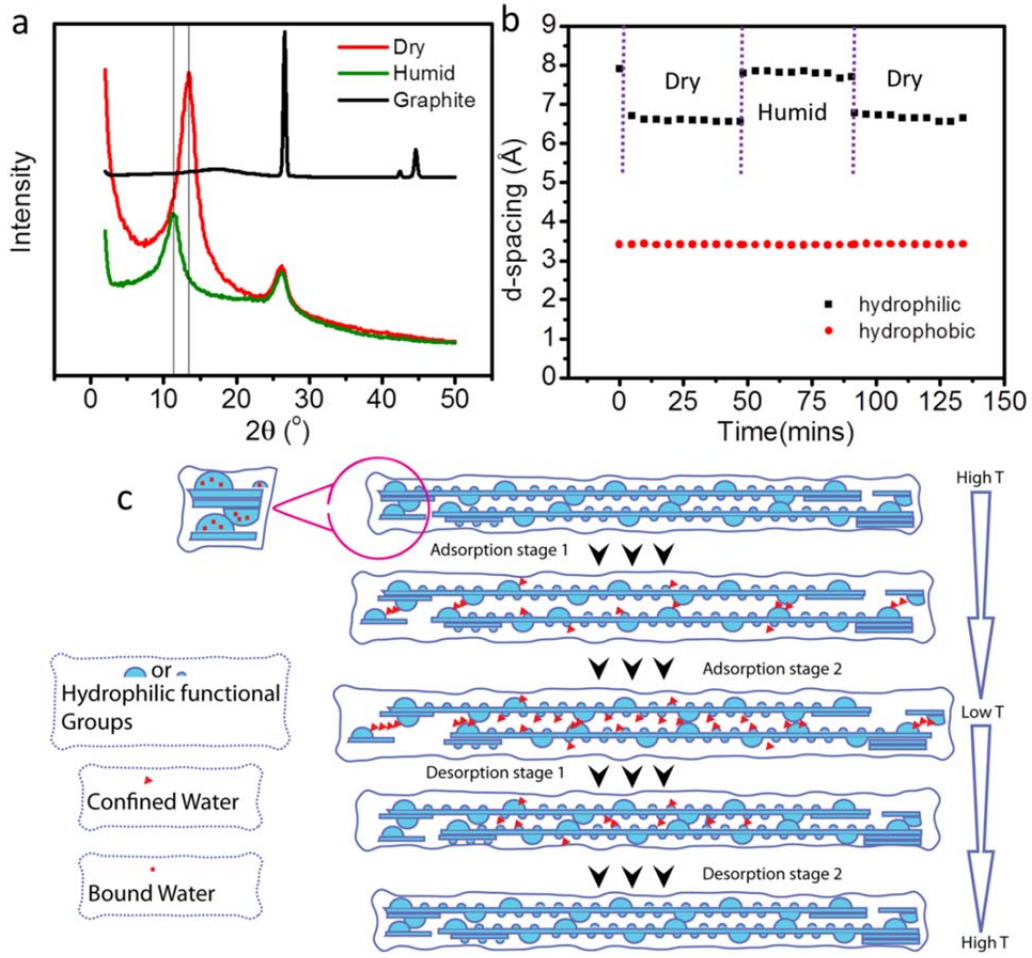

Figure 3.19 |XRD analysis of GO paper. (a) Powder x-ray diffraction (XRD) pattern of GO paper for the dry and humid states. (b) Temporal trace of d-spacing for characteristic peaks in (a) with label "hydrophilic" for the peak at 2θ between 10–15°, and "hydrophobic" for the peak at 2θ between 25–30°. (c) Schematic drawing of water adsorption/desorption process in GO paper.

There are likely to be three types of water[93] in GO: "free water", which behaves like normal water without any confinement; "confined water", which encounters arbitrary constraints (GO sheets) while retaining translational mobility; and "bound water", which is tightly bound to GO by different bonds allowing only local motions. Standard Karl Fischer titration shows that "free water" and "confined water" in total constitute 21wt%

for a partially dried GO paper while "bound water" constituted 8.8% of the sample (see experimental section). The "free water" can be completely removed from GO sample by the vacuum drying, as evidenced by the absence of the corresponding peak in the DSC analysis (Figure 3.24b). Such water is certainly removed in the initial drying process in all the studies. As can be seen from XRD data in Figure 3.19, the GO water involved in PNTE is likely to be the "confined water". The "bound water" of GO cannot be removed without causing the irreversible reduction of the GO, but may be likely to completely eliminated by drying the powdered GO.[94] The obtained anhydrous GO has a "hydrophilic" XRD peak of 0.57nm,[94] which is obviously smaller than 0.66nm *d*-spacing after removing the "free" and "confined" water" in this study. Compared to the initial *d*-spacing of 0.78nm, the change is 0.12nm, which is much smaller than the van der Waals diameter of water 0.282nm.[95] Apparently, after the removal of water, the vacated space does not completely collapse being supported by functional groups protruding in the basal spacing from the carbon grid. This unique structure makes tremendous contribution to reversibility and high rate of the diffusion process as the basal spaces vacated remain accessible and ready for the re-insertion of water molecules.

The process of adsorption and desorption of water molecules is further examined through NMR[81] and FTIR[82] spectroscopy (Figure 3.18a, b, d and e). While features of ^{13}C NMR spectra remain unchanged during the temperature sweep, ^{1}H NMR spectra (Figure 3.18d) show strong peak shifts from 9.1ppm at 20–40°C to 7.5ppm at 40-100°C, which are attributed to the loss of "confined water" (9.1ppm) leaving behind the "bounded water" (7.5ppm) as temperature increases.[96] In the FTIR spectra (Figure 3.18a), intensity and position of OH stretching mode are almost identical despite the desorption of water at

higher temperatures, indicating that hydrogen-bonding environment around hydroxyl functional groups are barely disturbed due to the retained "bound water". The obvious change in FTIR spectra is the weakening of O–H bending mode from phenol (Ph–OH) at 1368.8cm^{-1} at higher temperature, suggestive of the loss of hydrogen bonds with removed "confined water" molecules. Two points need to be made about this observation: (1) Inductive and resonance effect from phenyl rings lead to weaker hydrogen bonds between water and phenol groups, and therefore, these water molecules are easier to be removed. (2) Phenyl rings are to be present at edges of hydrophobic regions made of fused aromatic rings, which is one of the likely locations of the "confined water". The strongly "bound water" is instead localized at the most hydrophilic regions with multiple –COOH, –OH and epoxy functional groups.

The temperature-induced process of water desorption is monitored by thermal gravimetrical analysis (TGA). At 22°C, 9% of weight is lost within 30 minutes in GO placed in 100ml/min flow of 99.9995% N_2. 50% of change occurs within 4 minutes, which are much longer than the period of <1min for structure change/recovery in *in-situ* XRD experiments (Figure 3.19). In addition, TMA analysis shows that 9-10 minutes are needed to reach a steady state (Figure 3.18b) upon cooling when water is re-adsorbed. Those results indicate that timing of water desorption/adsorption process and structural changes observed by XRD are markedly different. This finding and other experimental data can be explained by the model presented in Figure 3.19c. GO sheets are pillared by multiple islands constituted of protruding out-of-plane oxygenated functional groups and bound water between adjacent layers. In this case, the interlayer spacing is determined by islands from vertically adjacent sheets that touch each other. During adsorption (cooling)

stage, water molecules penetrate predominantly to the protruding islands in the hydrophilic regions, attach there and lift the overall interlayer spacing. Here, GO in hydrophilic areas behaves as stiff nanoscale sheets which correlates well with the data on their bending stiffness.[24] Fast saturation of these "elevated" hydrophilic regions gives fast shifts in XRD 2θ peak in Figure 3.18 from 13.5° (0.66 nm) to 11.2° (0.78 nm). There are plenty of other areas on GO sheets where water can be adsorbed. Then water saturates many other isolated islands and edges of the GO sheets. Concomitantly, GO sheets slide apart from each other due to water insertion, resulting in the increase of length of GO paper. During this stage many islands that produced the shift in "hydrophilic" XRD peak, become misaligned but the sheets remain supported by many other water "pillars". The desorption (heating) process reverses the structural changes but with the *d*-spacing collapsed more rapidly as a result of this misalignment and larger spacing. The interlayer spacing after that is 0.66nm (Figure 3.19b), which is far larger than the van der Waals diameter of water 0.282nm,[95] allowing for completion of the desorption process and reversibility of the PNTE behavior.

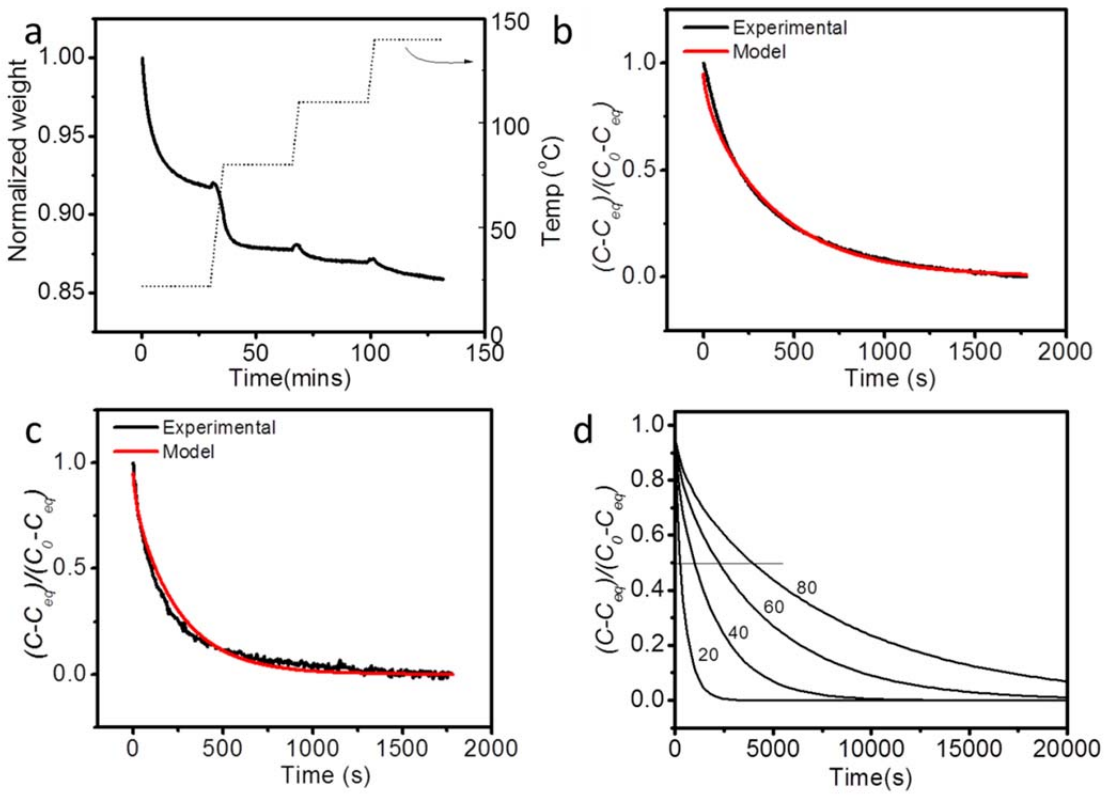

Figure 3.20 |Water dynamic analyses in GO paper. (a) Water loss of GO measured by TGA. (b) The fitting of the Crank equation to the water loss data at 22°C. (c) The fitting of the Crank equation to the water loss data at 80°C. (d) Water diffusion prediction using the Crank equation for thickness of 20, 40, 60 and 80 μm at 22°C.

The diffusivity of water in GO can be analytically described by the Crank equations.[97] Fitting TGA curve at specific temperatures with the Crank equations yields the diffusion coefficient, D_{H2O}, of water in GO. At 22°C it is estimated to be 8×10^{-14}m^2/s, and at 80°C is 1.3×10^{-13}m^2/s (Figure 3.20a, b, c). This is larger than diffusivity of water in some other hydrophilic polymers,[98] such as polyvinyl alcohol,[99] but smaller than in nylon and cellulose.[99] Note that D_{H2O} depends on humidity. The ultrafast diffusion and permeation of water is observed when GO is exposed to water vapor,[73] while lower

humidity results in much slower water diffusion. This result is not surprising and agrees with the model in Figure 3.19c: the narrowing of 2D capillaries with the decreasing relative humidity block the flux of water,[73] and the diffusivity of water is impeded by the electrostatic drag exerted by protruding functional groups.

Knowing D_{H2O} allows us to analytically calculate the time scale of PNTE and compare it with the dL/L in curves in Figure 3.18b. Under assumption that thickness of the sample (18μm) is much smaller than its width and length (2×15 mm), the calculated time to reach half-equilibrium is 4 min which correlates fairly well with ca. 8 min found from Figure 3.18. The characteristic response time for thermohydration should increase with increasing thickness. Indeed, the characteristic time for 50% change quadruples when the thickness of GO doubles (Figure 3.20d).

A logical question then one can ask at this point is: "What is the intrinsic CTE (ICTE) of GO paper if one disregards thermohydration effects?" This question can be answered using state-of-the-art modulated temperature TMA, which uses a sinusoidal temperature profile (300s period; amplitude ±5°C) overlaid on a linear underlying heating, cooling or isothermal profile. In this way, one can separate thermal expansion by the characteristic timescale which is much faster for intrinsic (molecular) CTE compared to PNTE. For fast cycling of temperature, water molecules are too slow to respond and cause irreversible size change under these modulated conditions, while the intrinsic expansion owing to vibrations of atoms in GO is in-sync with the temperature modulations. The sample length change due to water removal is a magnitude higher than that from intrinsic thermal expansion. The magnitude of the overall change is similar to that in conventional TMA (100ml/min helium flow rate, ramp rate of 1°C/min,

temperature window 30 °C to 80 °C). The averaged ICTE for 30—80°C range was 0.85ppm (Figure 3.18d) and can be confirmed by the minimal changes of layer spacing at different temperatures in the ultrapure N_2 environment (Figure 3.27a). The very small ICTE of GO layered assemblies makes thermohydration effects more apparent. The ICTE of GO paper is also similar to the apparent CTE of chemically or thermally reduced graphene paper, which has smaller number of hydrophilic groups in the nanochannels to interact with water molecules (Figure 3.27 b and c). Also note that the ICTE of GO paper is positive and larger than that of graphite. It means that the larger basal spacing and crumpled morphology does not necessarily lead to more negative ICTE. The membrane effect causing NTE of graphene may be counteracted by hydrogen bonding and van der Waal forces holding the GO sheets together. Furthermore, the notion that the chemical groups protruding between the GO sheets are relatively free is erroneous; most of them are to be strongly confined by water molecules. The large NTE obtained for the crystal phase of nanographene assemblies[71] are due to the more accessible space in the gallery when the water adsorption is minimized.

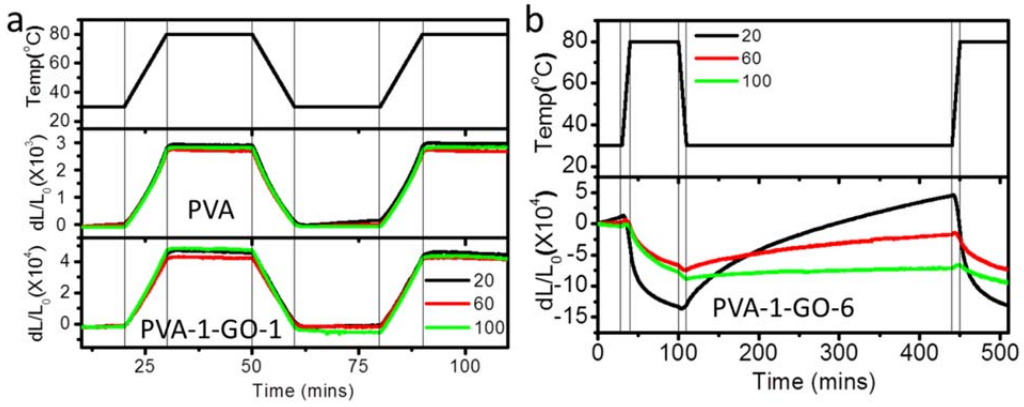

Figure 3.21 |Thermal mechanical analysis of polyvinyl alcohol (PVA)/GO composites. The changes of dL/L_0 with temperature at different helium flow rate of 20, 60 and 100ml/min for (a) PVA and PVA-1-GO-1 and (b) PVA-1-GO-6

It is also possible to combine GO with other materials with positive CTE resulting in a variety of composites being investigated for many applications.[100, 101] Such materials can be excellent examples of complexity of thermohydration effects. PVA/GO composites were made by filtration after mixing PVA and GO at different ratios (Figure 3.28, Table 3-2). XRD analysis shows an increase of layer spacing after inclusion of PVA (Table 3-2) while neat PVA has an overall positive CTE of 56.8 ppm K^{-1} from 30°C to 80°C with a glass transition point at 70°C (Figure 3.21a).[102] The incorporation of 81.1 wt% of GO into PVA (labeled as PVA-1-GO-1) reduces the CTE to 9.14 ppm K^{-1} (Figure 3.21b), which suggests GO sheets immobilize PVA chains. In addition, both PVA and PVA-1-GO-1 show perfect reversibility and independence on humidity and no continuing deformation in the isothermal region despite being tested at a fast ramp rate of 5°C/min. Further increase of GO content to 93.6 wt% (PVA-1-GO-6), however, does not result in reversible PNTE. Instead, PVA-1-GO-6 shows long saturation times during the isothermal stage and is highly influenced by the relative humidity. The instability and non-equilibrium nature of the expansion/contraction process make estimates of CTE ambiguous (Figure 3.21b). The slow equilibration rate indicates a slower diffusion process of water than that in original GO layered assemblies. The inclusion of PVA leads to more crowded space between GO sheets and higher drag exerted on diffusing water molecules. The diffusion completely stops for PVA-1-GO-1, making the CTE of composite less dependent on relative humidity and more related with ICTE of GO and PVA.

3.3.4 Conclusion

In summary, the fast water transport in response to the temperature and the close-to-zero intrinsic thermal expansion are responsible for PNTE in GO. The presence of multiple types of water and amphiphilic sites in GO makes its thermohydration behavior quite distinctive. The magnitude of PNTE displays obvious dependence on humidity, and so do the classic NTE materials. High mechanical strength, non-toxic nature, relative robustness and variety of established methods for nanoscale materials engineering make PNTE materials an asset for a variety of applications.[103, 104] Thermohydration effects in GO can also shed light on the fundamental issues in its use in charge storage, actuation, laser/heat patterning, and MEMS devices.

3.3.5 Supplementary Information

The material in this Section has been adapted with minor modifications from the following peer-reviewed, published article:

Zhu, J.; Andres, C. M.; Xu, J.; Ramamoorthy, A.; Tsotsis, T.; Kotov, N. A., Pseudonegative Thermal Expansion and the State of Water in Graphene Oxide Layered Assemblies. ACS Nano 2012, 6, 8357—836

Selection of temperature range for TMA testing: In order to examine the CTE of GO, careful selection of experimental temperature range is necessary to eliminate the possible reduction of GO.[105] Considerable exothermic energy release, mass loss, and length contraction were observed between 130°C and 205°C (Figure 3.23). However, slow thermal reduction may occur at lower temperature, and GO is likely to start degradation from 80°C.[106] Actually, in-situ FTIR (Figure 3.24), Raman (Figure 3.25), and NMR

(Figure 3.26) spectra on GO indicates reversible changes in 30~100°C cycles, but we notice that the weight and length of GO may slightly decrease over the time when GO was stabilized at 100°C (Figure 3.23b), which may be related to permanent structure change.

Calculation of diffusion coefficient of water in GO paper:

A complete drying profile consists of the first stage of drying, a constant-rate period and a falling-rate period. In most occasions, the third period is the dominating stage. It is frequently agreed that the mechanisms of moisture movement within hydroscopic solid during the third stage could be represented by the second Fick's law of diffusion. In the desorption stage, the time-dependent water flux from GO paper can be expressed as:

$$\frac{\partial C}{\partial t} = \frac{\partial y}{\partial x}\left(D\,\frac{\partial C}{\partial x}\right) \qquad (1)$$

In order to solve this partial differential equation, it is assumed that: (1) The initial water content is uniform through the GO paper (2) The surface water concentration of GO paper is at equilibrium with the dry air throughout the experiment. (3)The shape of the solid remains constant during the period considered. (4) The diffusivity is constant for the entire experiment.

The initial and the boundary condition for GO paper with thickness of 2d with the Y-Z plane located at in parallel to its surface and the center of coordinate located in the center of mass of the material. X axis in this case describes the principle direction of diffusion mass transfer and x=0 is located

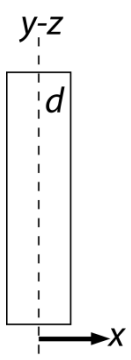

in the middle of the film.

t=0 and 0<x<d, C=C_0

t>0 and x=0, $\frac{\partial C}{\partial x} = 0$

t>0 and x=d, C=C_{eq}

The solution to the differential equation with the above boundary conditions has been solved by Crank (1975),[97] and is expressed by:

$$E = \frac{C-C_{eq}}{C_0-C_{eq}} = \frac{8}{\pi^2}\sum_{n=0}^{\infty}\frac{1}{(2n+1)^2}exp(-\frac{2n+1}{4}\pi^2\frac{Dt}{d^2})$$

According to the TGA results the variable in this equation are the following.

C_0=0.15 g H_20/ g in dry GO; and C_{eq}=0.05 gH_20/ g in dry GO for 22°C.

C_0=0.04 g H_20/ g in dry GO; C_{eq}=0.01 gH_20/ g dry GO at 80°C;

d=9μm=0.0009cm.

By using the first 4 terms (n=0, 1, 2, 3) in the Crank solution, the desorption curve of water in GO paper can be well presented with the fitting parameter of diffusivity (See Figure 3.20)

D=8×10^{-10}cm^2/s at 22°C; and D= 1.3×10^{-9}cm^2/s. at 80°C.

Table 3-2. Physical properties of various films tested in this study. The water content was estimated by comparing the difference of sample weight at room temperature and at 100°C. The GO weight fraction was calculated using the residue after 500°C based on the fact that PVA leaves no residue after 500°C (See TGA results in Figure 3.29).

FIlm	Thickness (µm)	Water/dry sample	GO fraction/dry sample	d-spacing by XRD (nm)
PVA	4.8±0.2	1%	0	-
PVA-1/GO-1	34.7±0.3	2.5%	81.07%	1.50
PVA-1/GO-6	18.7±0.5	1.7%	93.64%	0.95
GO	17.2±0.5	15%	100%	0.78

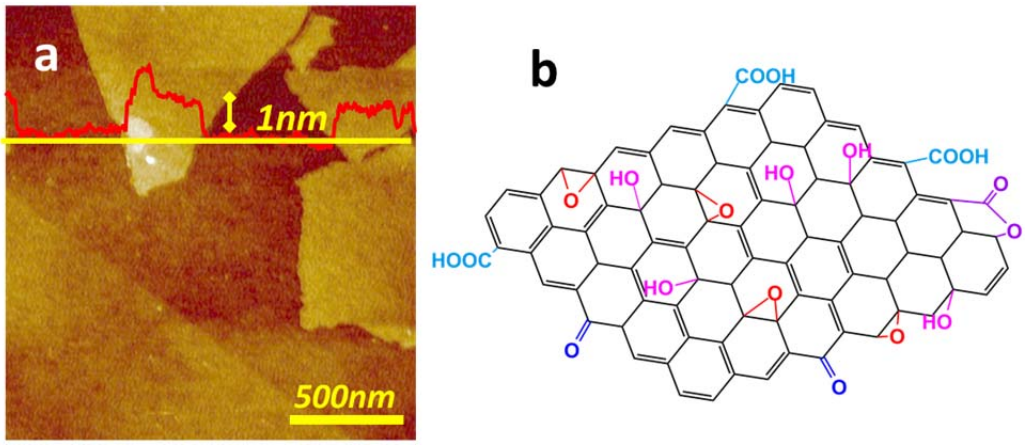

Figure 3.22. (a) AFM image of exfoliated GO sheets with height profile (b) GO chemical structure.

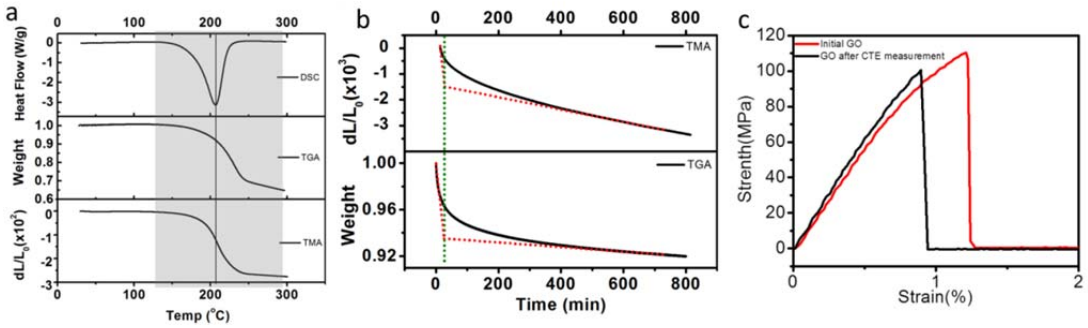

Figure 3.23. (a) Energy, weight, and normalized length change of GO paper when heated up to 300°C measured by DSC, TGA, and TMA respectively. The shaded area shows the temperature range where the GO thermal reduction reaction occurs. (b) Normalized length change and weight change of GO sample at 100°C determined by TMA and TGA. (c) Stress-strain curve for GO paper before and after CTE measurement.

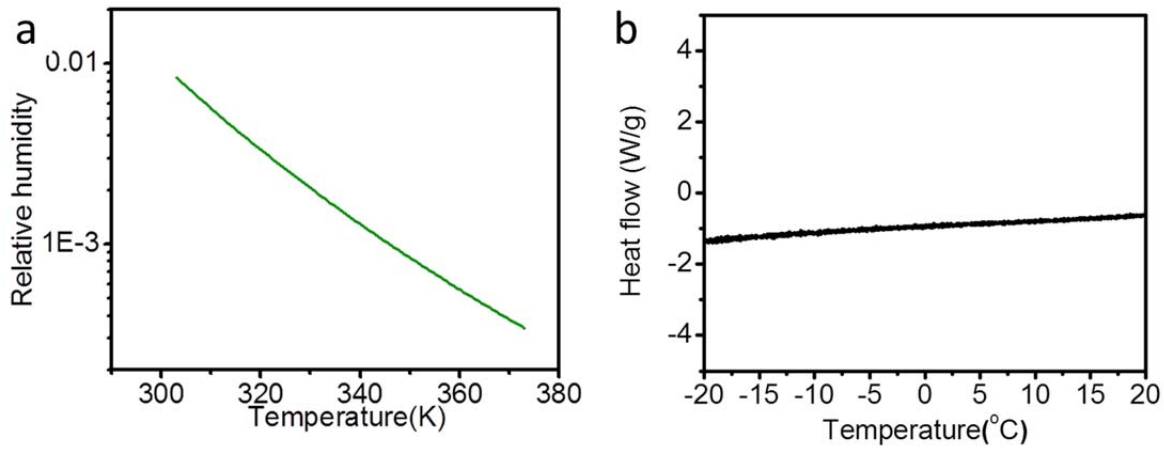

Figure 3.24. (a) Theoretical prediction of relative humidity change with temperature assuming constant water content. The initial water partial pressure at 303K is 3533kPa. The vapor pressure of water at each temperature point is calculated using Antoine equation with parameters obtained from NIST Chemistry web-book: A=5.4, B=1838.7, and C=-31.7. Relative humidity is defined by the partial pressure of water, which is unchanged with temperature, divided by the vapor pressure of water. (b) Heat flow of GO paper tested at low temperature by DSC.

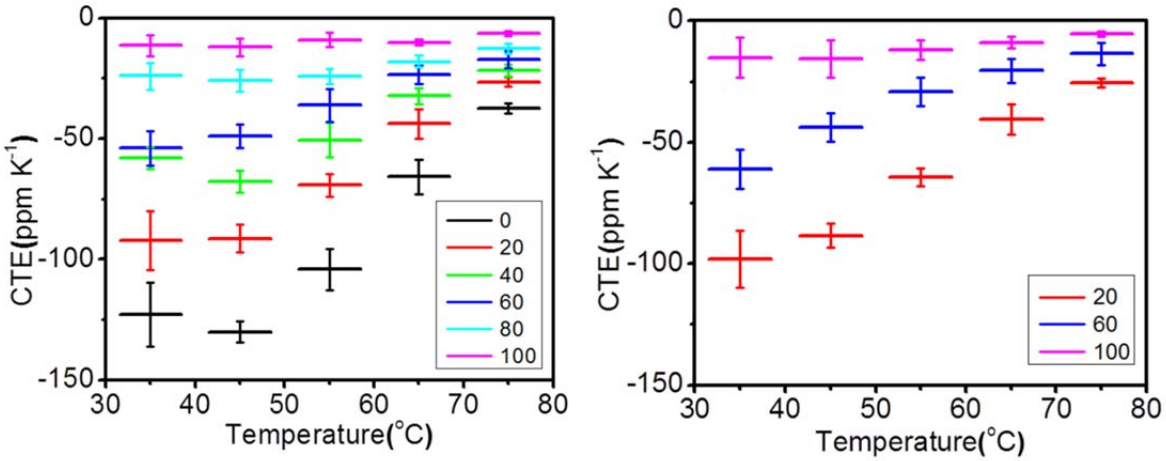

Figure 3.25. Coefficient of thermal expansion (CTE) calculated from heating section in Figure 3.18 for (a) 5 °C/min and (b) 1 °C/min.

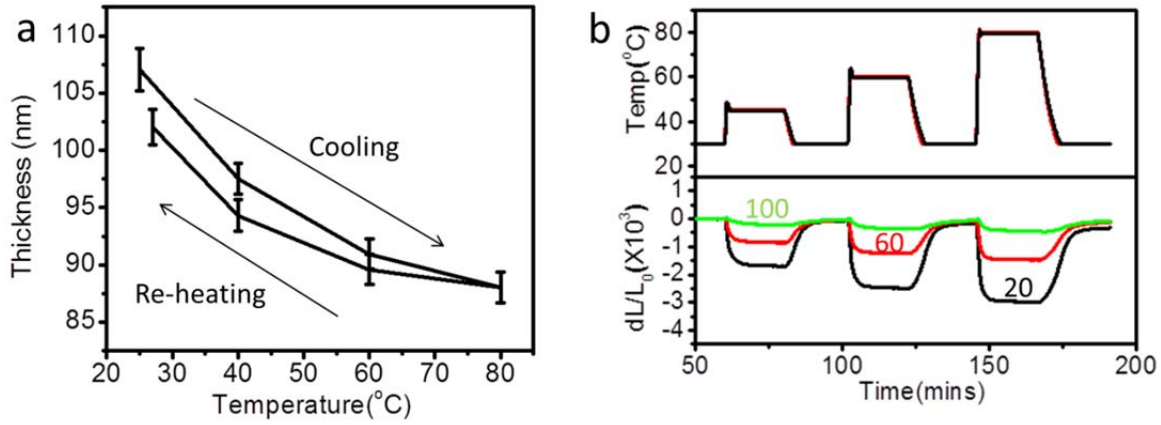

Figure 3.26. (a) Change of thickness of GO coating during cooling and reheating. The thickness of GO layered coating is also non-linearly changed with temperature with sharper changes at low temperatures. CTE at 30 °C in the transversal (through-thickness) direction in an ambient environment with humidity around 40% is -5931ppm K^{-1}, which is related with the *d*-spacing changes owing to the removal and insertion of water molecules. (b) dL/L_0 at 45, 60, 80°C with helium flow rate of 20, 60, and 100ml/min.

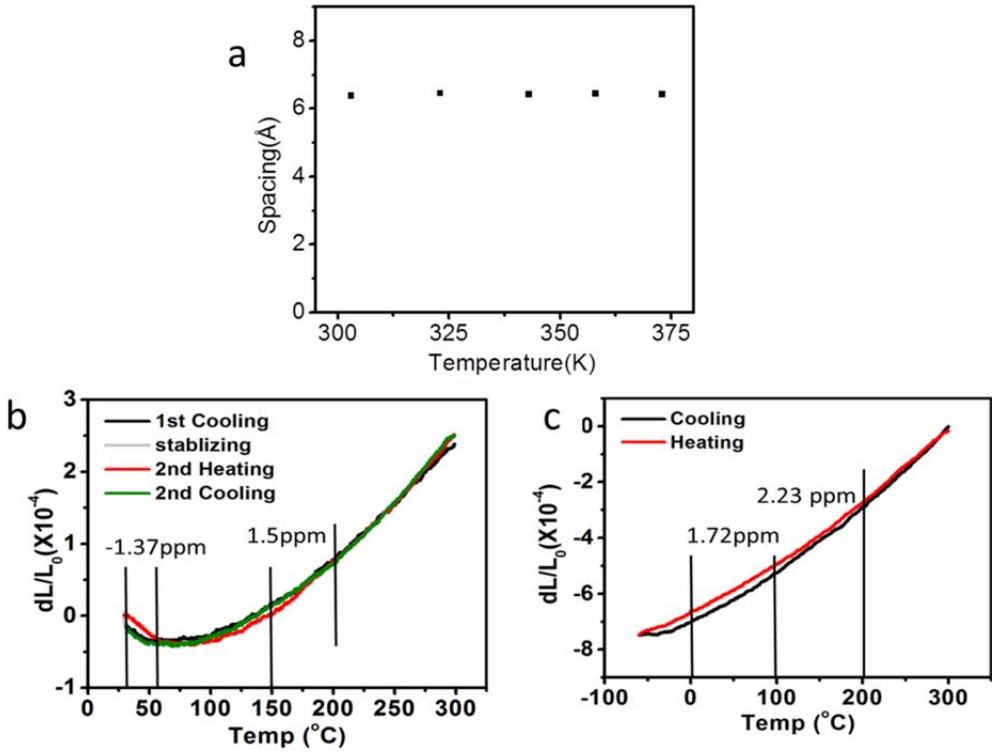

Figure 3.27. (a) Interlayer spacing of GO paper in 99.9995% N_2 environment at different temperatures. (b) Thermal behavior of chemically reduced GO paper for repeated cooling and heating cycles at relative humidity of 2.0%. (c) Thermal behavior of thermally reduced GO paper for a cooling and heating cycle at relative humidity of 2.0%.

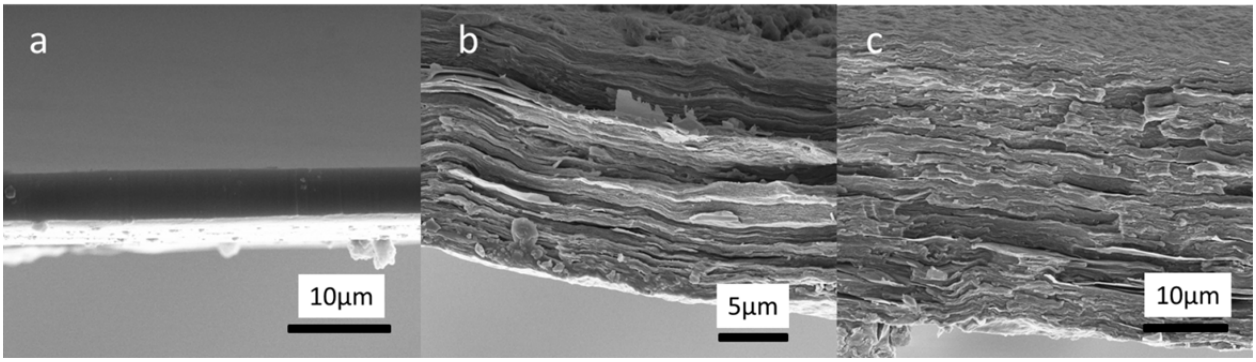

Figure 3.28. Cross-sectional SEM images of (a) PVA (b) PVA-1/GO-6 (c) PVA-1/GO-1.

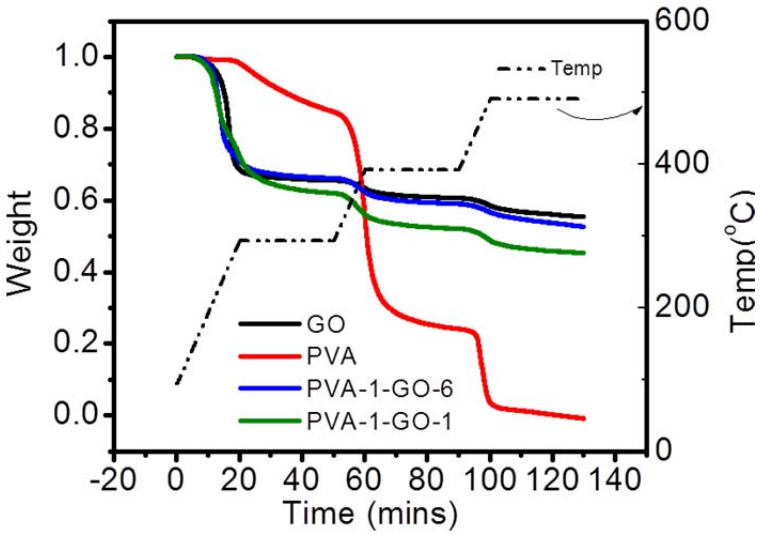

Figure 3.29. Thermal gravimetrical analyses for PVA, PVA-1/GO-6, PVA-1/GO-1, and GO films.

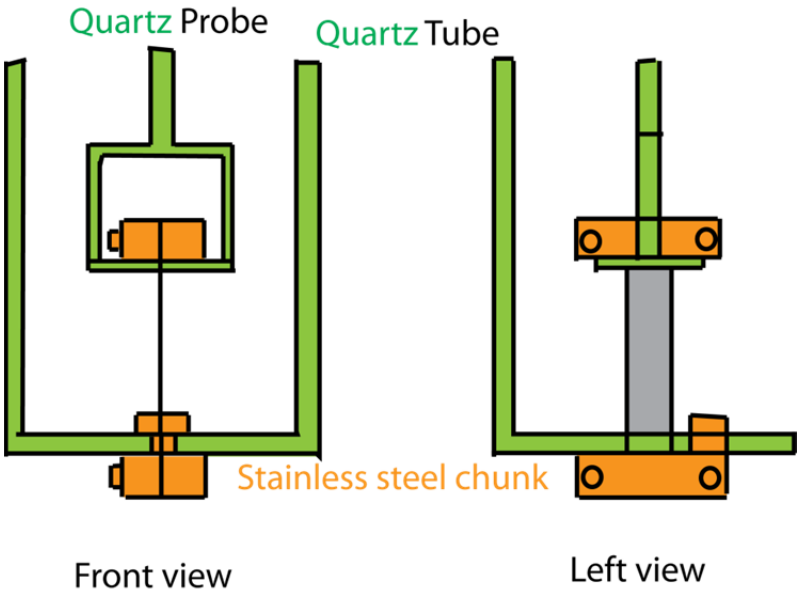

Figure 3.30. TMA probes and grips (chuck) customized by RT instruments, Inc.

3.4 References

1. Podsiadlo, P.; Kaushik, A. K.; Arruda, E. M.; Waas, A. M.; Shim, B. S.; Xu, J. D.; Nandivada, H.; Pumplin, B. G.; Lahann, J.; Ramamoorthy, A.; Kotov, N. A., Ultrastrong and Stiff Layered Polymer Nanocomposites. *Science* **2007**, 318, 80-83.
2. Shim, B. S.; Zhu, J.; Jan, E.; Critchley, K.; Ho, S. S.; Podsiadlo, P.; Sun, K.; Kotov, N. A., Multiparameter Structural Optimization of Single-Walled Carbon Nanotube Composites: Toward Record Strength, Stiffness, and Toughness. *ACS Nano* **2009**, 3, 1711-1722.
3. Bonderer, L. J.; Studart, A. R.; Gauckler, L. J., Bioinspired Design and Assembly of Platelet Reinforced Polymer Films. *Science* **2008**, 319, 1069-1073.
4. Zhu, J.; Shim, B. S.; Di Prima, M.; Kotov, N. A., Transparent Conductors from Carbon Nanotubes Lbl-Assembled with Polymer Dopant with Π−Π Electron Transfer. *J. Am. Chem. Soc.* **2011**, 133, 7450-7460.
5. Walther, A.; Bjurhager, I.; Malho, J.-M.; Pere, J.; Ruokolainen, J.; Berglund, L. A.; Ikkala, O., Large-Area, Lightweight and Thick Biomimetic Composites with Superior Material Properties Via Fast, Economic, and Green Pathways. *Nano Lett.* **2010**, 10, 2742-2748.
6. Podsiadlo, P.; Sui, L.; Elkasabi, Y.; Burgardt, P.; Lee, J.; Miryala, A.; Kusumaatmaja, W.; Carman, M. R.; Shtein, M.; Kieffer, J.; Lahann, J.; Kotov, N. A., Layer-by-Layer Assembled Films of Cellulose Nanowires with Antireflective Properties. *Langmuir* **2007**, 23, 7901-7906.
7. Nogi, M.; Iwamoto, S.; Nakagaito, A. N.; Yano, H., Optically Transparent Nanofiber Paper. *Adv. Mater.* **2009**, 21, 1595-1598.
8. Wu, Z. C.; Chen, Z. H.; Du, X.; Logan, J. M.; Sippel, J.; Nikolou, M.; Kamaras, K.; Reynolds, J. R.; Tanner, D. B.; Hebard, A. F.; Rinzler, A. G., Transparent, Conductive Carbon Nanotube Films. *Science* **2004**, 305, 1273—1276.
9. Zhao, X.; Zhang, Q.; Hao, Y.; Li, Y.; Fang, Y.; Chen, D., Alternate Multilayer Films of Poly(Vinyl Alcohol) and Exfoliated Graphene Oxide Fabricated Via a Facial Layer-by-Layer Assembly. *Macromolecules* **2010**, 43, 9411-9416.
10. Putz, K. W.; Compton, O. C.; Palmeri, M. J.; Nguyen, S. T.; Brinson, L. C., High-Nanofiller-Content Graphene Oxide–Polymer Nanocomposites Via Vacuum-Assisted Self-Assembly. *Adv. Funct. Mater.* **2010**, 20, 3322-3329.
11. Shin, M. K.; Lee, B.; Kim, S. H.; Lee, J. A.; Spinks, G. M.; Gambhir, S.; Wallace, G. G.; Kozlov, M. E.; Baughman, R. H.; Kim, S. J., Synergistic Toughening of Composite Fibres by Self-Alignment of Reduced Graphene Oxide and Carbon Nanotubes. *Nat Commun* **2012**, 3, 650.
12. An, Z.; Compton, O. C.; Putz, K. W.; Brinson, L. C.; Nguyen, S. T., Bio-Inspired Borate Cross-Linking in Ultra-Stiff Graphene Oxide Thin Films. *Adv. Mater.* **2011**, 23, 3842–3846.
13. Yang, Y.; Bolling, L.; Priolo, M. A.; Grunlan, J. C., Super Gas Barrier and Selectivity of Graphene Oxide-Polymer Multilayer Thin Films. *Adv. Mater.* **2013**, 25, 503-508.
14. Zhu, J.; Andres, C. M.; Xu, J.; Ramamoorthy, A.; Tsotsis, T.; Kotov, N. A., Pseudonegative Thermal Expansion and the State of Water in Graphene Oxide Layered Assemblies. *ACS Nano* **2012**, 6, 8357-8365.
15. Decher, G., Fuzzy Nanoassemblies: Toward Layered Polymeric Multicomposites. *Science* **1997**, 277, 1232-1237.

16. Ariga, K.; Hill, J. P.; Ji, Q., Layer-by-Layer Assembly as a Versatile Bottom-up Nanofabrication Technique for Exploratory Research and Realistic Application. *Phys. Chem. Chem. Phys.* **2007**, 9, 2319-2340.
17. Hammond, P. T., Engineering Materials Layer-by-Layer: Challenges and Opportunities in Multilayer Assembly. *AIChE J.* **2011**, 57, 2928-2940.
18. Li, Y.-Q.; Yu, T.; Yang, T.-Y.; Zheng, L.-X.; Liao, K., Bio-Inspired Nacre-Like Composite Films Based on Graphene with Superior Mechanical, Electrical, and Biocompatible Properties. *Adv. Mater.* **2012**, 24, 3426-3431.
19. Sen, D.; Buehler, M. J., Structural Hierarchies Define Toughness and Defect-Tolerance Despite Simple and Mechanically Inferior Brittle Building Blocks. *Sci. Rep.* **2011**, 1, 1-9.
20. Dikin, D. A.; Stankovich, S.; Zimney, E. J.; Piner, R. D.; Dommett, G. H. B.; Evmenenko, G.; Nguyen, S. T.; Ruoff, R. S., Preparation and Characterization of Graphene Oxide Paper. *Nature* **2007**, 448, 457-460.
21. Hummers, W. S.; Offeman, R. E., Preparation of Graphitic Oxide. *J. Am. Chem. Soc.* **1958**, 80, 1339-1339.
22. Li, D.; Muller, M. B.; Gilje, S.; Kaner, R. B.; Wallace, G. G., Processable Aqueous Dispersions of Graphene Nanosheets. *Nature Nanotech.* **2008**, 3, 101-105.
23. Sriupayo, J.; Supaphol, P.; Blackwell, J.; Rujiravanit, R., Preparation and Characterization of A-Chitin Whisker-Reinforced Poly(Vinyl Alcohol) Nanocomposite Films with or without Heat Treatment. *Polymer* **2005**, 46, 5637-5644.
24. Lee, C.; Wei, X. D.; Kysar, J. W.; Hone, J., Measurement of the Elastic Properties and Intrinsic Strength of Monolayer Graphene. *Science* **2008**, 321, 385-388.
25. Bae, S.; Kim, H.; Lee, Y.; Xu, X. F.; Park, J. S.; Zheng, Y.; Balakrishnan, J.; Lei, T.; Kim, H. R.; Song, Y. I.; Kim, Y. J.; Kim, K. S.; Ozyilmaz, B.; Ahn, J. H.; Hong, B. H.; Iijima, S., Roll-to-Roll Production of 30-Inch Graphene Films for Transparent Electrodes. *Nature Nanotech.* **2010**, 5, 574-578.
26. Balandin, A. A.; Ghosh, S.; Bao, W. Z.; Calizo, I.; Teweldebrhan, D.; Miao, F.; Lau, C. N., Superior Thermal Conductivity of Single-Layer Graphene. *Nano Lett.* **2008**, 8, 902-907.
27. Kulkarni, D. D.; Choi, I.; Singamaneni, S. S.; Tsukruk, V. V., Graphene Oxide−Polyelectrolyte Nanomembranes. *ACS Nano* **2010**, 4, 4667-4676.
28. Yang, X.; Qiu, L.; Cheng, C.; Wu, Y.; Ma, Z.-F.; Li, D., Ordered Gelation of Chemically Converted Graphene for Next-Generation Electroconductive Hydrogel Films. *Angew. Chem.* **2011**, 50, 7325-7328.
29. Putz, K. W.; Compton, O. C.; Segar, C.; An, Z.; Nguyen, S. T.; Brinson, L. C., Evolution of Order During Vacuum-Assisted Self-Assembly of Graphene Oxide Paper and Associated Polymer Nanocomposites. *ACS Nano* **2011**, 5, 6601-6609.
30. Strawhecker, K. E.; Manias, E., Structure and Properties of Poly(Vinyl Alcohol)/Na+ Montmorillonite Nanocomposites. *Chem. Mater.* **2000**, 12, 2943-2949.
31. Ricciardi, R.; Auriemma, F.; De Rosa, C.; Lauprêtre, F., X-Ray Diffraction Analysis of Poly(Vinyl Alcohol) Hydrogels, Obtained by Freezing and Thawing Techniques. *Macromolecules* **2004**, 37, 1921-1927.

32. Strawhecker, K. E.; Manias, E., Afm of Poly(Vinyl Alcohol) Crystals Next to an Inorganic Surface. *Macromolecules* **2001**, 34, 8475-8482.
33. Lee, C.; Kim, I.; Shin, H.; Kim, S.; Cho, J., Nonvolatile Resistive Switching Memory Properties of Thermally Annealed Titania Precursor/Polyelectrolyte Multilayers. *Langmuir* **2009**, 25, 11276-11281.
34. Giri, G.; Verploegen, E.; Mannsfeld, S. C. B.; Atahan-Evrenk, S.; Kim, D. H.; Lee, S. Y.; Becerril, H. A.; Aspuru-Guzik, A.; Toney, M. F.; Bao, Z., Tuning Charge Transport in Solution-Sheared Organic Semiconductors Using Lattice Strain. *Nature* **2011**, 480, 504-508.
35. Podsiadlo, P.; Tang, Z.; Shim, B. S.; Kotov, N. A., Counterintuitive Effect of Molecular Strength and Role of Molecular Rigidity on Mechanical Properties of Layer-by-Layer Assembled Nanocomposites. *Nano Lett.* **2007**, 7, 1224-1231.
36. Ramanathan, T.; Abdala, A. A.; Stankovich, S.; Dikin, D. A.; Herrera Alonso, M.; Piner, R. D.; Adamson, D. H.; Schniepp, H. C.; Chen, X.; Ruoff, R. S.; Nguyen, S. T.; Aksay, I. A.; Prud'Homme, R. K.; Brinson, L. C., Functionalized Graphene Sheets for Polymer Nanocomposites. *Nature Nanotech.* **2008**, 3, 327-331.
37. Debenedetti, P. G.; Stillinger, F. H., Supercooled Liquids and the Glass Transition. *Nature* **2001**, 410, 259-267.
38. Anastasiadis, S. H.; Karatasos, K.; Vlachos, G.; Manias, E.; Giannelis, E. P., Nanoscopic-Confinement Effects on Local Dynamics. *Phys. Rev. Lett.* **2000**, 84, 915-918.
39. Jackson, A. P.; Vincent, J. F. V.; Turner, R. M., The Mechanical Design of Nacre. *Proceedings of the Royal Society of London. Series B. Biological Sciences* **1988**, 234, 415-440.
40. Padawer, G. E.; Beecher, N., On the Strength and Stiffness of Planar Reinforced Plastic Resins. *Polym. Eng. Sci.* **1970**, 10, 185-192.
41. van Es, M. A., *Polymer-Clay Nanocomposites: The Importance of Particle Dimensions*. **2001**.
42. Liang, J.; Huang, Y.; Zhang, L.; Wang, Y.; Ma, Y.; Guo, T.; Chen, Y., Molecular-Level Dispersion of Graphene into Poly(Vinyl Alcohol) and Effective Reinforcement of Their Nanocomposites. *Adv. Funct. Mater.* **2009**, 19, 2297-2302.
43. Ritchie, R. O., The Conflicts between Strength and Toughness. *Nat. Mater.* **2011**, 10, 817-822.
44. Launey, M. E.; Ritchie, R. O., On the Fracture Toughness of Advanced Materials. *Adv. Mater.* **2009**, 21, 2103-2110.
45. Chen, H.; Muller, M. B.; Gilmore, K. J.; Wallace, G. G.; Li, D., Mechanically Strong, Electrically Conductive, and Biocompatible Graphene Paper. *Adv. Mater.* **2008**, 20, 3557-3561.
46. Stankovich, S.; Dikin, D. A.; Dommett, G. H. B.; Kohlhaas, K. M.; Zimney, E. J.; Stach, E. A.; Piner, R. D.; Nguyen, S. T.; Ruoff, R. S., Graphene-Based Composite Materials. *Nature* **2006**, 442, 282-286.
47. Bai, Y.; Ho, S.; Kotov, N. A., Direct-Write Maskless Lithography of Lbl Nanocomposite Films and Its Prospects for Mems Technologies. *Nanoscale* **2012**, 4, 4393-4398.

48. Jiang, C. Y.; Markutsya, S.; Pikus, Y.; Tsukruk, V. V., Freely Suspended Nanocomposite Membranes as Highly Sensitive Sensors. *Nat. Mater.* **2004**, 3, 721-728.
49. Shutava, T. G.; Balkundi, S. S.; Vangala, P.; Steffan, J. J.; Bigelow, R. L.; Cardelli, J. A.; O'Neal, D. P.; Lvov, Y. M., Layer-by-Layer-Coated Gelatin Nanoparticles as a Vehicle for Delivery of Natural Polyphenols. *ACS Nano* **2009**, 3, 1877-1885.
50. Zhang, H.; Shih, J.; Zhu, J.; Kotov, N. A., Layered Nanocomposites from Gold Nanoparticles for Neural Prosthetic Devices. *Nano Lett.* **2012**, 12, 3391-3398.
51. Schaaf, P.; Voegel, J.-C.; Jierry, L.; Boulmedais, F., Spray-Assisted Polyelectrolyte Multilayer Buildup: From Step-by-Step to Single-Step Polyelectrolyte Film Constructions. *Adv. Mater.* **2012**, 24, 1001-1016.
52. Gomez-Navarro, C.; Burghard, M.; Kern, K., Elastic Properties of Chemically Derived Single Graphene Sheets. *Nano Lett.* **2008**, 8, 2045-2049.
53. Suk, J. W.; Piner, R. D.; An, J.; Ruoff, R. S., Mechanical Properties of Monolayer Graphene Oxide. *ACS Nano* **2010**, 4, 6557-6564.
54. Paci, J. T.; Belytschko, T.; Schatz, G. C., Computational Studies of the Structure, Behavior Upon Heating, and Mechanical Properties of Graphite Oxide. *J. Phys. Chem. C* **2007**, 111, 18099-18111.
55. Lusis, J.; Woodhams, R. T.; Xanthos, M., The Effect of Flake Aspect Ratio on the Flexural Properties of Mica Reinforced Plastics. *Polym. Eng. Sci.* **1973**, 13, 139-145.
56. S. O. Evans, J., Negative Thermal Expansion Materials. *J. Chem. Soc. Dalton* **1999**, 3317—3326.
57. Rossetti, G. A.; Cline, J. P.; Navrotsky, A., Phase Transition Energetics and Thermodynamic Properties of Ferroelectric $PbTiO_3$. *J. Mater. Res.* **1998**, 13, 3197—3206.
58. Salvador, J. R.; Guo, F.; Hogan, T.; Kanatzidis, M. G., Zero Thermal Expansion in Ybgage Due to an Electronic Valence Transition. *Nature* **2003**, 425, 702—705.
59. Takenaka, K.; Takagi, H., Giant Negative Thermal Expansion in Ge-Doped Anti-Perovskite Manganese Nitrides. *Appl. Phys. Lett.* **2005**, 87, 261902.
60. Mary, T. A.; Evans, J. S. O.; Vogt, T.; Sleight, A. W., Negative Thermal Expansion from 0.3 to 1050 Kelvin in ZrW_2O_8. *Science* **1996**, 272, 90—92.
61. Goodwin, A. L.; Calleja, M.; Conterio, M. J.; Dove, M. T.; Evans, J. S. O.; Keen, D. A.; Peters, L.; Tucker, M. G., Colossal Positive and Negative Thermal Expansion in the Framework Material $Ag_3[Co(CN)_6]$. *Science* **2008**, 319, 794—797.
62. Sigmund, O.; Torquato, S., Composites with Extremal Thermal Expansion Coefficients. *Appl. Phys. Lett.* **1996**, 69, 3203.
63. Lakes, R., Cellular Solids with Tunable Positive or Negative Thermal Expansion of Unbounded Magnitude. *Appl. Phys. Lett.* **2007**, 90, 221905.
64. Jain, A.; Vijayan, K., Kevlar 49 Fibres: Thermal Expansion Coefficients from High Temperature X-Ray Data. *Curr. Sci.* **2000**, 78, 331—335.
65. Kobayash.Y; Keller, A., Temperature Coefficient of C Lattice Parameter of Polyethylene - an Example of Thermal Shrinkage Along Chain Direction. *Polymer* **1970**, 11, 114—117.

66. Maniwa, Y.; Fujiwara, R.; Kira, H.; Tou, H.; Kataura, H.; Suzuki, S.; Achiba, Y.; Nishibori, E.; Takata, M.; Sakata, M.; Fujiwara, A.; Suematsu, H., Thermal Expansion of Single-Walled Carbon Nanotube (SWNT) Bundles: X-Ray Diffraction Studies. *Phys. Rev. B* **2001**, 64, 241402.
67. Bao, W. Z.; Miao, F.; Chen, Z.; Zhang, H.; Jang, W. Y.; Dames, C.; Lau, C. N., Controlled Ripple Texturing of Suspended Graphene and Ultrathin Graphite Membranes. *Nature Nanotech.* **2009**, 4, 562—566.
68. Yoon, D.; Son, Y. W.; Cheong, H., Negative Thermal Expansion Coefficient of Graphene Measured by Raman Spectroscopy. *Nano Lett.* **2011**, 11, 3227-3231.
69. Mounet, N.; Marzari, N., First-Principles Determination of the Structural, Vibrational and Thermodynamic Properties of Diamond, Graphite, and Derivatives. *Phys. Rev. B* **2005**, 71, 205214.
70. Nelson, J. B.; Riley, D. P., The Thermal Expansion of Graphite from 15°C to 800°C. *Proc. Phys. Soc.* **1945**, 57, 477—486.
71. Grigoriadis, C.; Haase, N.; Butt, H. J.; Mullen, K.; Floudas, G., Negative Thermal Expansion in Discotic Liquid Crystals of Nanographenes. *Adv. Mater.* **2010**, 22, 1403—1406.
72. Lerf, A.; Buchsteiner, A.; Pieper, J.; Schottl, S.; Dekany, I.; Szabo, T.; Boehm, H. P., Hydration Behavior and Dynamics of Water Molecules in Graphite Oxide. *J. Phys. Chem. Solids* **2006**, 67, 1106-1110.
73. Nair, R. R.; Wu, H. A.; Jayaram, P. N.; Grigorieva, I. V.; Geim, A. K., Unimpeded Permeation of Water through Helium-Leak–Tight Graphene-Based Membranes. *Science* **2012**, 335, 442-444.
74. Park, S.; Ruoff, R. S., Chemical Methods for the Production of Graphenes. *Nature Nanotech.* **2009**, 4, 217-224.
75. El-Kady, M. F.; Strong, V.; Dubin, S.; Kaner, R. B., Laser Scribing of High-Performance and Flexible Graphene-Based Electrochemical Capacitors. *Science* **2012**, 335, 1326-1330.
76. Gao, W.; Singh, N.; Song, L.; Liu, Z.; Reddy, A. L. M.; Ci, L. J.; Vajtai, R.; Zhang, Q.; Wei, B. Q.; Ajayan, P. M., Direct Laser Writing of Micro-Supercapacitors on Hydrated Graphite Oxide Films. *Nature Nanotech.* **2011**, 6, 496-500.
77. Nogi, M.; Iwamoto, S.; Nakagaito, A. N.; Yano, H., Optically Transparent Nanofiber Paper. *Adv. Mater.* **2009**, 21, 1595—1598.
78. Nishino, T.; Matsuda, I.; Hirao, K., All-Cellulose Composite. *Macromolecules* **2004**, 37, 7683—7687.
79. Su, Y.; Wei, H.; Gao, R.; Yang, Z.; Zhang, J.; Zhong, Z.; Zhang, Y., Exceptional Negative Thermal Expansion and Viscoelastic Properties of Graphene Oxide Paper. *Carbon* **2012**, 50, 2804—2809.
80. Lifshitz, I., Thermal Properties of Chain and Layered Structures at Low Temperatures. *Zh. Eksp. Teor. Fiz.* **1952**, 22, 475—486.
81. He, H.; Riedl, T.; Lerf, A.; Klinowski, J., Solid-State NMR Studies of the Structure of Graphite Oxide. *J. Phys. Chem.* **1996**, 100, 19954-19958.
82. Acik, M.; Lee, G.; Mattevi, C.; Chhowalla, M.; Cho, K.; Chabal, Y. J., Unusual Infrared-Absorption Mechanism in Thermally Reduced Graphene Oxide. *Nature Mater.* **2010**, 9, 840-845.

83. Saravacos, G. D.; Stinchfield, R. M., Effect of Temperature and Pressure on the Sorption of Water Vapor by Freeze-Dried Food Materials. *J. Food Sci.* **1965**, 30, 779—786.
84. Ge, S.; Li, X.; Yi, B.; Hsing, I. M., Absorption, Desorption, and Transport of Water in Polymer Electrolyte Membranes for Fuel Cells. *J. Electrochem. Soc.* **2005**, 152, A1149—A1157.
85. Tosto, S.; Knauth, P.; Di Vona, M. L., Water Adsorption/Desorption in Proton-Conducting Ionomer Membranes: The Model Case of Sulfonated and Silylated Poly-Ether-Ether-Ketone. *Solid State Ionics* **2012**, 209, 9—14.
86. Goodwin, A. L.; Kepert, C. J., Negative Thermal Expansion and Low-Frequency Modes in Cyanide-Bridged Framework Materials. *Phys. Rev. B* **2005**, 71, 140301.
87. Bar, A.; Ramon, O.; Cohen, Y.; Mizrahi, S., Shrinkage Behaviour of Hydrophobic Hydrogel During Dehydration. *J. Food Eng.* **2002**, 55, 193—199.
88. Salmen, L., Thermal Expansion of Water Saturated Wood. *Holzforschung* **1990**, 44, 17—19.
89. Glass, S. V.; Zelinka, S. L., *Wood Handbook, Chapter 04: Moisture Relations and Physical Properties of Wood*. U.S. Department of Agriculture, Forest Service: Madison, **2010**; pp 1—19.
90. Bazant, Z. P.; Bazant, M. Z., Theory of Soprtion Hysteresis in Nanoporous Solids: I. Snap-through Instablilities. *Arxiv preprint arXiv11084949* **2011**, 1—22.
91. Bazabt, Z. P., Delayed Thermal Dilatation of Cement Paste and Concrete Due to Mass Transport. *Nucl. Eng. Des.* **1970**, 14, 308—318.
92. Li, Z. Q.; Lu, C. J.; Xia, Z. P.; Zhou, Y.; Luo, Z., X-Ray Diffraction Patterns of Graphite and Turbostratic Carbon. *Carbon* **2007**, 45, 1686-1695.
93. Buchsteiner, A.; Lerf, A.; Pieper, J., Water Dynamics in Graphite Oxide Investigated with Neutron Scattering. *J. Phys. Chem.B* **2006**, 110, 22328-22338.
94. Cerveny, S.; Barroso-Bujans, F.; Alegria, A.; Colmenero, J., Dynamics of Water Intercalated in Graphite Oxide. *J. Phys. Chem. C* **2010**, 114, 2604-2612.
95. Franks, F., *Water: A Matrix of Life*. Royal Society of Chemistry: Cambridge, **2000**; pp 43-44.
96. Lerf, A.; He, H.; Forster, M.; Klinowski, J., Structure of Graphite Oxide Revisited. *J. Phys. Chem.B* **1998**, 102, 4477-4482.
97. Crank, J., *The Mathematics of Diffusion*. Clarendon Press: Oxford, **1975**; pp 1—414.
98. Marcovich, N. E.; Reboredo, M. M.; Aranguren, M. I., Moisture Diffusion in Polyester–Woodflour Composites. *Polymer* **1999**, 40, 7313—7320.
99. Long, F. A.; Thompson, L. J., Diffusion of Water Vapor in Polymers. *Journal of Polymer Science* **1955**, 15, 413—426.
100. Wang, S.; Tambraparni, M.; Qiu, J.; Tipton, J.; Dean, D., Thermal Expansion of Graphene Composites. *Macromolecules* **2009**, 42, 5251-5255.
101. Balandin, A. A., Thermal Properties of Graphene and Nanostructured Carbon Materials. *Nature Mater.* **2011**, 10, 569-581.
102. Xu, J. Y.; Hu, Y.; Song, L.; Wang, Q. G.; Fan, W. C.; Liao, G. X.; Chen, Z. Y., Thermal Analysis of Poly(Vinyl Alcohol)/Graphite Oxide Intercalated Composites. *Polym. Degrad. Stab.* **2001**, 73, 29-31.

103. Park, S.; An, J.; Suk, J. W.; Ruoff, R. S., Graphene-Based Actuators. *Small* **2010**, 6, 210-212.
104. Ma, Y.; Zhang, Y.; Wu, B.; Sun, W.; Li, Z.; Sun, J., Polyelectrolyte Multilayer Films for Building Energetic Walking Devices. *Angew. Chem.* **2011**, 50, 6254-6257.
105. Kim, F.; Luo, J.; Cruz-Silva, R.; Cote, L. J.; Sohn, K.; Huang, J., Self-Propagating Domino-Like Reactions in Oxidized Graphite. *Adv. Funct. Mater.* **2010**, 20, 2867-2873.
106. Rourke, J. P.; Pandey, P. A.; Moore, J. J.; Bates, M.; Kinloch, I. A.; Young, R. J.; Wilson, N. R., The Real Graphene Oxide Revealed: Stripping the Oxidative Debris from the Graphene-Like Sheets. *Angew. Chem.* **2011**, 50, 3173-3177.

CHAPTER IV

Aramid Nanofiber Network: Discovery and Assistance for Layer-by-layer Deposition of Multifunctional Composites

4.1 Introduction

In Chapter II and III, I discussed the methods of conventional layer-by-layer assembly (LBL) and vacuum assisted flocculation (VAF) for fabricating high performance multifunctional nanocomposites. The common feature of those composites is the inclusion of large content highly dispersed nanomaterials with tailored interfacial interactions. Despite all the successes, both methods are stringent in the possible combination of materials. The LBL is usually restricted for aqueous components with strong complementary interactions, while the VAF has to rely on the high-aspect-ratio nanoparticles and their appropriate interactions with the polymers. On the other hand, previous chapters make use of extremely expensive carbon nanotube and graphene nanomaterials. The search for cheaper alternatives is an attractive and important topic, especially for industrial applications. This chapter endeavors to address these two issues with the discovery of robust aramid nanofiber (ANF) percolation network. Any polymer of choices can be easily incorporated into the network without agglomerating the ANFs. A subsequent drying step can give rise to automatic layering of the composites. The rest

part of this chapter introduces a gelation-assisted layer-by-layer deposition technique, which is an important step towards efficient use of ANF network for high quality nanocomposites. The ANF/PVA and ANF/Epoxy composites are demonstrated here to show their interesting combination of properties.

4.2 Aramid Nanofiber Network

4.2.1 Introduction

Percolated nanoscale networks (PNNs) are typically built from nanoscale polymeric and/or inorganic components capable of self-assembly into three-dimensional 3D superstructures.[1] The connectivity of segments and simplicity of their formation attract a lot of attention as a method for optimization of optical and electronic devices[2, 3] utilizing metallic or semiconductive nanoparticles, nanotubes, and nanowires. The porous structures are also promising for the preparation of materials with high mechanical performance and ultralow density.[4, 5] When coupled with matrix, the networks can give rise to advanced mechanical, electrical and thermal properties through synergistic effects by virtue of interfacial interactions.[6-9] Particularly interesting here is to tune the content of functional fillers in composites especially to the high end which is difficult to achieve by traditional composite preparation techniques. Percolated high-filled composites can maximize different functionalities and lead to record mechanical, optical, electrical, and combinations thereof.[10-12] However, the preparation of 3D PNNs in respect to the components and their content in composites is greatly restricted by the solubility and stability of mixed liquid/solid phases of specific composition as well as significant viscosity of mixtures associated with traditional processes.[13] Greater choice of the polymeric and nanoscale components as well as much wider range of their compositions

is afforded by methods such as layer-by-layer assembly (LBL)[14, 15] or vacuum assisted flocculation (VAF) for making clay,[12, 16] graphene,[15, 17] carbon nanotube (CNT)[10, 18] or cellulose nanofiber (CelluNF) composites.[19, 20]

The greater applicability of 3D PNNs in composite materials could be afforded by using a "base" porous network to be filled with any variety of polymers.[21] Examining available network materials, one can see that various conventional aerogels and hydrogels – the most common examples of self-assembled 3D PNNs - often consist of irregular and weak molecular chains, thus unable to be served as reinforcing/functional skeletons needed for composites.[22] Silica aerogel with interconnected colloidal silica is lauded for its high compressive stress, but is intrinsically brittle and cannot be easily processed into a composite by filling a polymer.[23, 24] Graphene 3D networks made by hydrothermal process from graphene oxide[25] or chemical vapor deposition (CVD) process[26] draw a lot of attention recently. Unfortunately, they also have low toughness and can be easily shattered[15] despite the possibility to incorporate polymers into the pores.[21,22] 3D PNNs from fibrous nanoscale components perform better. Aerogels in original and filled form made from CelluNFs and CNTs[21, 27] might eventually lead to composites with record mechanical properties, although it is not the case at the moment due to the challenges both with stress transfer/distribution and impregnation process for CelluNFs and CNTs. The exfoliation and dispersion of highly concentrated CNTs can be difficult even with the assistance of special surfactants, which have to be removed to produce 'clean' networks.[28] The production of CelluNF-based PNNs is not trivial also and includes mechanical homogenization, acid hydrolysis, or bacterial synthesis.[29] Hydrogels and organogels formed by CNT or CelluNFs[21] represent a material bordering with fluids and

have low mechanical properties.[21, 30, 31] 3D PNNs from CelluNFs can also be generated through coagulating the cellulose dissolved in some special non-aqueous solvents, but the cellulose is present as fibers of large diameter. The uniformly of the network is also compromised by the inclusions of amorphous cellulose.[32, 33]

Here, we turn to a new type nanomaterial: aramid nanofibers (ANFs) derived from Kevlar™ macrofibers. The latter can be dissolved in KOH-saturated DMSO.[34] High stiffness E = 90GPa and strength σ = 6GPa of the parent polymer Kevlar™,[35] cooperative hydrogen bonds between aramid chains, negative coefficient of thermal expansion, and low light scattering associated with the nanometer scale diameter of ANFs create unique possibilities for the preparation of versatile 'base' percolating network and make possible a variety of subsequent modifications.

In the present study, we achieve the fabrication of ANF networks by re-protonating ANFs in DMSO through a simple solvent exchange process leading to aerogels and hydrogels. Having considerable robustness ANF PNNs can be impregnated with polyvinyl alcohol (PVA) to create a composite with exceptional strength and toughness. ANFs are also effective in depressing thermal expansion of PVA, and overall coefficient of thermal expansion (CTE) of composite is smaller than most of ceramics in the glassy state.

4.2.2 Experimental

Preparation of ANF gel with cylindrical shape:

1% aramid nanofiber (ANF) dispersion was prepared by stirring Kevlar 69 (from Thread Exchange, right twist) in dimethyl sulfoxide (DMSO) for two weeks at the presence of over saturated KOH (1g/100ml DMSO). 4ml of the as-prepared solution was

put into a cylindrical tube, and 10ml water was slowly dropped on top of Kevlar solution to minimize disturbance. The phase separation started immediately and completed within 12 hours. Fresh water was added two times a day for four days to completely replace DMSO in the Kevlar hydrogel. In order to prepare ANF aerogel, the water in hydrogel was exchanged with ethanol, and then extracted with supercritical CO_2.

Preparation of thin sheets from ANF networks:

The 1% ANF dispersion was confined within two pieces of 2" by 3" clean glass slides in a controlled distance, and then put into water. The thickness of a gel film can be controlled by a spacer between glass slides or adapted to the weight placed on top glass slide balanced by the viscosity of ANF dispersion (Figure 4.6a). Within 12 hours, ANF thin sheet gel can be peeled off from glass slides under water. The gel was then transferred into fresh water for storage.

Preparation of PVA/ANF composite:

The ANF thin sheet hydrogel was immersed in 1wt% PVA (Aldrich, Mowiol® 56-98, Mw ~195000) for 12 hours, and then rinsed in fresh water for 5mins. The thin sheet was then carefully transferred onto Teflon sheet and dried in 60°C oven for 30mins.

Characterization:

The transparency of film was determined by an 8453 UV-vis ChemStation spectrophotometer from Agilent Technologies. Cross-section and morphology of the film were examined by FEI NOVA Nanolab Scanning electron microscopy (SEM). Tapping mode atomic force microscopy (AFM) images were obtained using a NanoScope IIIa Atomic force microscope (AFM) from Veeco Instruments.

Differential scanning calorimetry (DSC) was carried out on TA instrument Discovery DSC under nitrogen atmosphere at a temperature ramp rate of 20°C/min. To eliminate thermal history, the samples went through steps of heating-cooling-heating according to the protocol in ASTM D3418–08. The second heating step was used for analysis. PVA content can then be estimated by comparing the PVA melt enthalpy in the composite with that in pure PVA. Thermal gravimetrical analysis (TGA) was run on a TA instrument Discovery TGA with a heating rate of 10°C/min in nitrogen. Coefficient of thermal expansion (CTE) of films was measured using extension mode in Perkin Elmer TMA7 following ASTM *Test Method for Linear Thermal Expansion of Solid Materials by Thermomechanical Analysis* (E 831) and slightly modified to measure the thin film. The extension probe and grips were customized by RT instruments, Inc. to minimize the expansion of grips during the measurement. A ramp rate of 5°C/min was used and the second heating step was used for analysis.

Uniaxial tensile testing was done on RSAIII Rheometrics Systems Analyzer from TA instruments. The tensile tests confirm to the ASTM standard ASTM D882. In a typical measurement, 1mm wide and 6mm long sample strip was fixed onto the steel grips. The Kevlar microfiber was fixed by super-gluing the ends onto two pieces of stainless steel metal sheets separated by a distance of 6mm. The metal sheets were then put between the grips for measurement. The test speed is 0.01mm/s. A total of 6 measurements were made for 2 batches of PVA/ANF composite. A total of 3 measurements were made for the Kevlar microfiber.

4.2.3 Results and Discussion

Kevlar^{TM} macrofibers (KMF) consist of well-aligned polymeric chains held closely by hydrogen bonds (Figure 4.1a). Kevlar microfibers display structural hierarchy at different length scales with an poly(p-phenylene terephthalamide) (PPTA) being the basic building block assembled, in turn, into nanofibers (Figure 4.1c).[36] The multilevel structure is visualized in SEM images of KMFs after tensile failure (Figure 4.1b). Recently we demonstrated that KMF can also be split chemically into stable nanofiber dispersions by deprotonation with saturated KOH in DMSO.[34] With some similarity to CelluNF hydrolysis, the abstraction of protons from PPTA leads to the dissociation of some weaker hydrogen bonds while the remaining chains form nanofibers. The colloidal stability of ANFs is made possible by negative charges resulting after deprotonation. Atomic force microscopy (AFM) images of ANFs indicate that they have a diameter of 4.5nm (Figure 4.1e) and have high aspect ratio with a total length of several micrometers long when ANF is fully extended (Figure 4.1d and e). Importantly, the bifurcation and branching of ANFs is a direct representation of KNF hierarchical organization and differentiate ANFs from both CNTs and CelluNFs. Besides, the high aspect ratio, such unique morphology especially in comparison with other nanowire/nanorod/nanotube components make them nearly ideal for the formation of 3D PNNs.

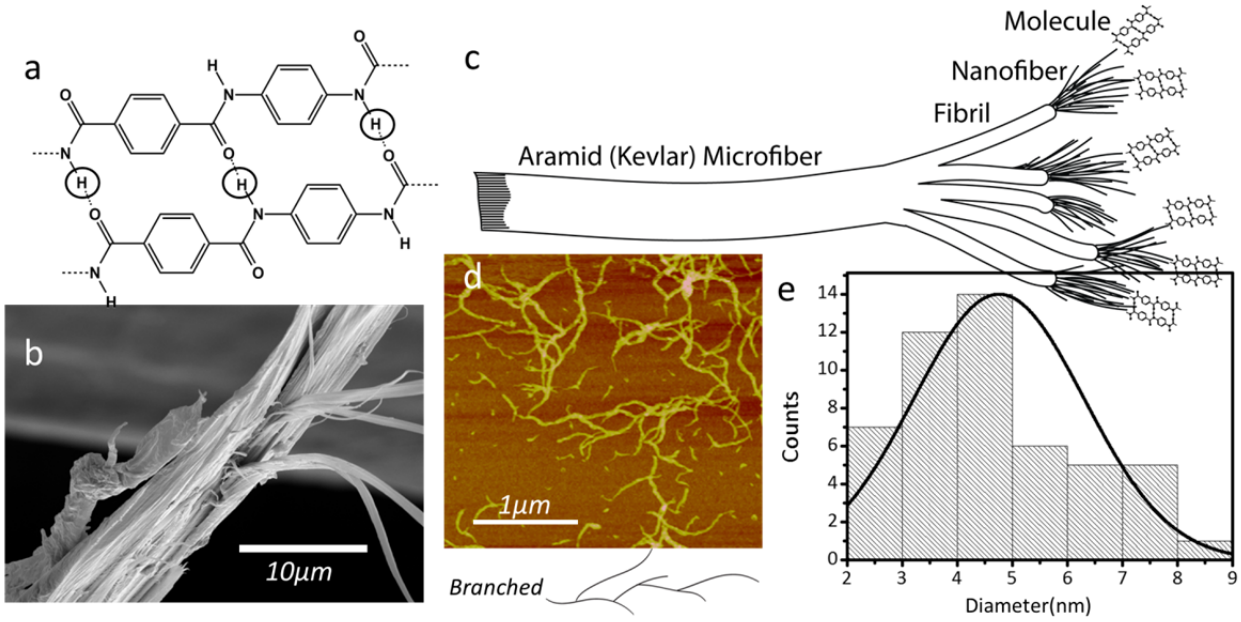

Figure 4.1. (a) Molecular structure in the Kevlar microfibers (KMS). (b) A fractured KMF showing the fibrils and aligned structure. (c) A schematic drawing of the hierarchical structure of KMF. (d) AFM image of ANFs deposited on a silicon substrate by drying off DMSO. (e) Statistical distribution of ANF diameters.

A dispersion of ANFs in DMSO in a concentration of 1wt% can be solidified by a slow solvent exchange process into a solid hydrogel (Figure 4.2 a, b and c). In a typical process, deionized water is gently placed on top of ANF dispersions in DMSO, leading to immediate phase separation taking place at the interface and slowly penetrating into the DMSO phase. In this process, the deprotonated PPTA, a strong Brønsted base, can be easily restored into its initial chemical structure using protons from water. This acid-base reaction is accompanied by color change from the dark red into light yellow (Figure 4.2a *vs.* 2c). The generated hydrogel made of the entangled phase-separated ANFs have structural integrity even after shear cause by cutting with a razor blade (Figure 4.2d). Its 3D PNN is revealed by converting it into aerogel with 99.3% porosity through supercritical CO_2 extraction. The density of ANF aerogel (0.024 g/cm^3) is only 20 times

higher than air (0.00129 g/cm^3), and can be easily trapped by electrostatic attraction around the opening of a glass vial (Figure 4.2e). The aerogel consist of intertwined and uniform ANFs shown in the scanning electron microcopy (SEM) image (Figure 4.2f and g). It also has large surface area of 275m^2/g determined by the Brunauer–Emmet–Teller (BET) method. CelluNF PNN has 5-10 times smaller BET area ranging between 20 and 66 m^2/g.[37]

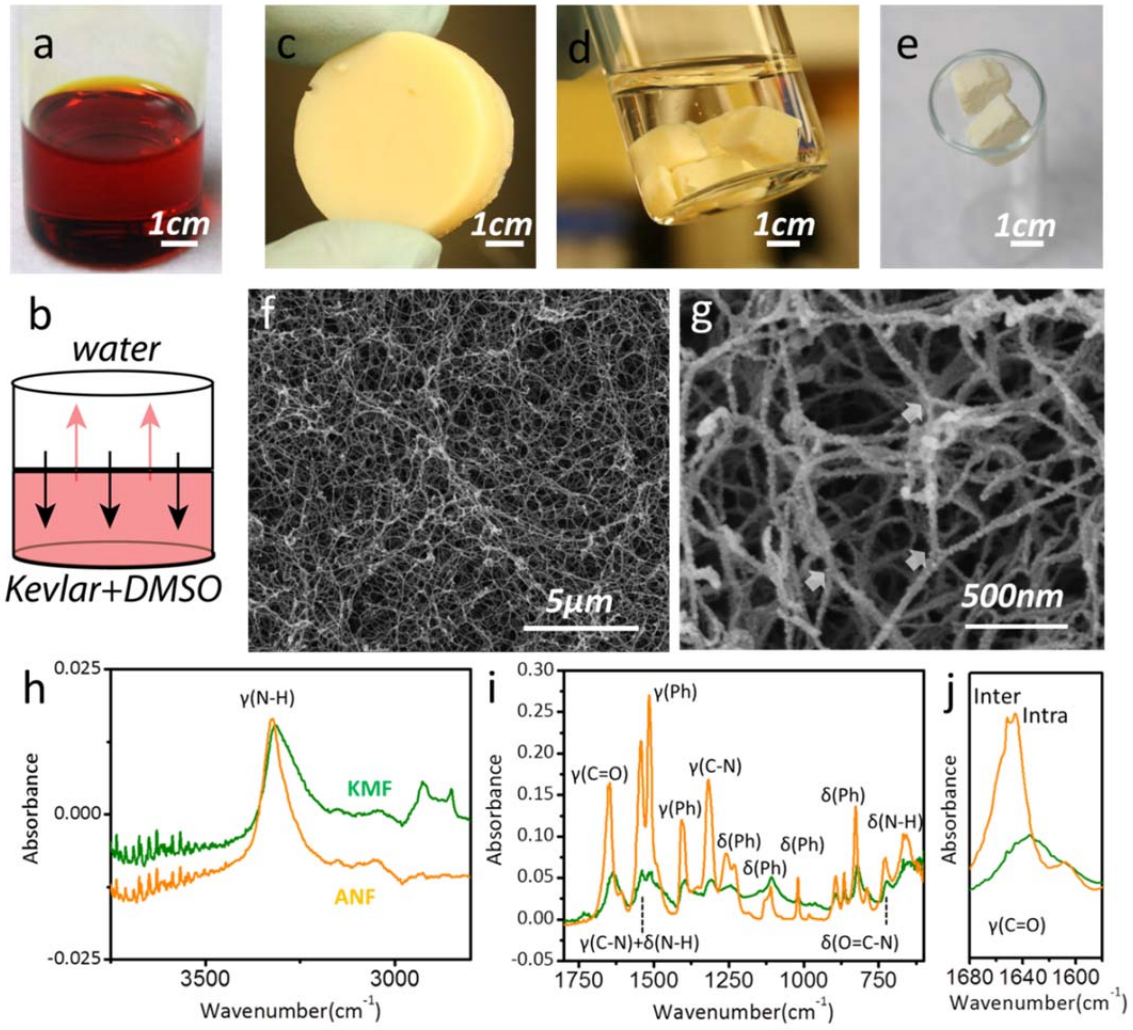

Figure 4.2. (a) ANF dispersion in DMSO. (b) A schematic drawing of solvent exchange process. (c) Photograph of ANF hydrogel. (d) Pieces of hydrogels cut and stored in fresh deionized water. (e) ANF aerogels wedged in an opening of a beaker. (f, g) SEM images of ANF aerogel in different magnifications. (h, i, j) A comparison of FTIR spectra for

KMF and ANF. The stretching and bending modes of different functional groups were indicated by γ and δ respectively.

The 3D PNN of ANFs is held together by inter-nanofiber hydrogen bonds at contacts as well as stronger intra-nanofiber hydrogen bonds. Overall, the hydrogen bonds are weaker than in KNFs which is revealed by the upshift of stretching vibration of N-H (γ(N-H)) from 3313 to 3323 cm^{-1} and that of C=O (γ(C=O)) from 1633 to 1649 cm^{-1} in FTIR spectra (Figure 4.2h and i).[34, 38] A careful examination of γ(C=O) band reveals more detailed information of hydrogen bonding environment (Figure 4.2j): the peak splits into two: 1646 and 1652 cm^{-1}, which can be attributed to the stretching vibrations of carbonyl group affected by the intra-nanofiber (interior PPTA) and inter-nanofiber (exterior PPTA) hydrogen bonds respectively. Recalling the fact that the total absence of hydrogen bonds in the amide group in the gas phase causes the shift of γ(N-H) and γ(C=O) vibration to 3480 cm^{-1} and to 1720cm^{-1},[39] respectively, hydrogen bonds holding the ANF network together are still abundant.

The integrity of the ANF network in the hydro- and aero-gel form can be demonstrated even more vividly by its mechanical properties in uniaxial compression and tension. Hydrogel and aerogel show three stages in compressive strain-stress curve typical for porous materials (Figure 4.3a).[40] The linear elastic stage was observed initially and then, the material reached its elastic limit at which point PNN started to yield at a nearly constant stress. This plateau stage is followed by a densification region where the porous network starts to collapse. Both gels can be compressed into 1/10 of their initial volume or less (compressive strain>90%) without any cracks at macro, micro-, or nanoscale (Figure 4.3b, c and d). In contrast, other reinforcing PNNs exhibit substantially

higher brittleness during the compression. For example, graphene hydrogel show microcracks and stress discontinuity at a strain of 42%[25] and cellulose aerogel can be totally fractured at 68%.[37] As expected in similarity to CNT or CelluNF PNN,[37, 41] ANF aerogel is not elastic and cannot recover after compression. It is likely that the hydrogen-bonding interactions can re-form in new deformation states after bending and slippage of individual ANFs. This property can be especially useful in making polymer composites.

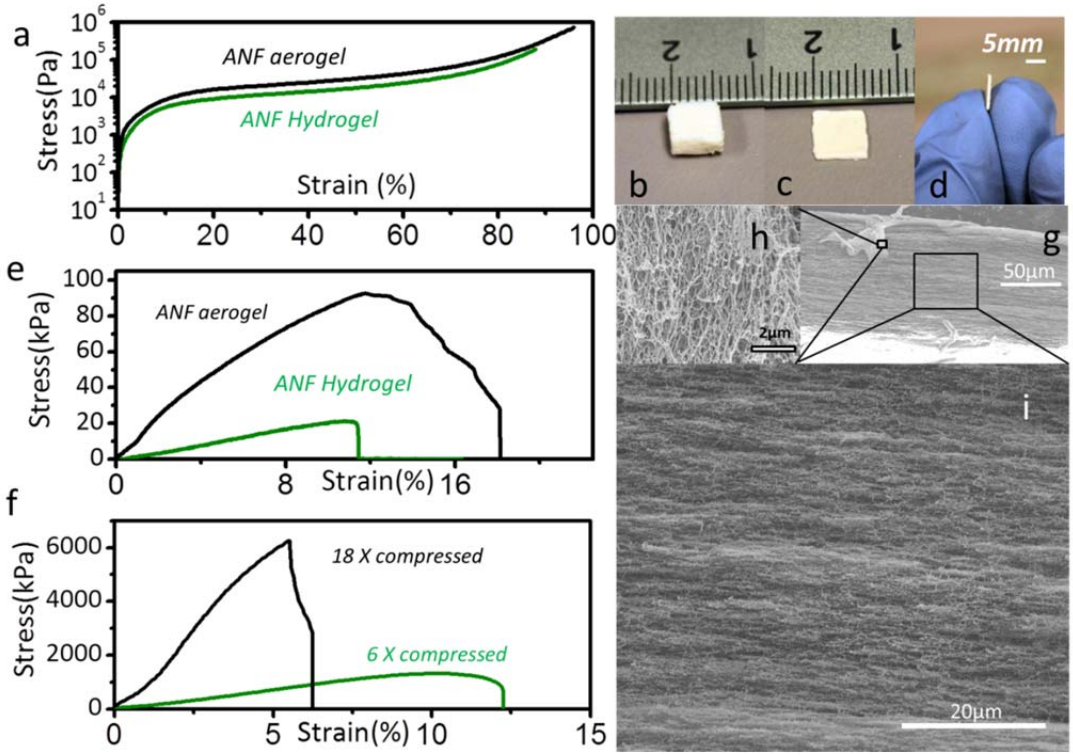

Figure 4.3. (a) Compressive stress-strain curves for ANF hydrogel and aerogel. (b) ANF aerogel before compression. (c) The same aerogel after compression. (d) Cross-sectional view of the aerogel in (c). (e) Tensile stress-strain curves for ANF hydrogel and aerogel. (f) Tensile stress-strain curves for ANF aerogel after being compressed into 1/6 and 1/18 of the initial height. (g-i) SEM images of the edge of fractured compressed ANF aerogel at different magnifications.

The compressive modulus E and yield stress σ_y are 8±1 kPa and 57±3 kPa for the ANF hydrogel. The same parameters for ANF aerogel are about two times higher

reaching 18±1 kPa and 90±5 kPa, respectively (Figure 4.3a). It is believed that the presence of water can have a plasticization effect on ANF PNN and its hydrogen-bonding interaction can compete with ANF's intra and inter hydrogen bonds in the networks, thus lowering the stress bearing properties of the hydrogel. Note, however, water has much less effect on the ANF than other 3D PNNs and gels. For example, it is known that high porosity (>99%) CelluNF and CNT hydrogel can be so compliant that they are reminiscent of a viscous fluid that cannot retain its shape.[28, 31, 37, 42] Except bio-made CelluNF hydrogels,[30] they are destroyed after swelling. Instead, the ANF hydrogel can be surprisingly stable in water for over a year without any degradation, and cannot be re-dispersed in water even with the assistance of sonication.

The compressive E and σ_y of ANF PNN can be remarkably similar to those made of much stiffer CNT and graphene sheets (Table 4-1). Graphene hydrogel with 99.56% porosity has a lower E and σ_y of 3 and 29 kPa respectively.[25] And CNT aerogel with 99.73% porosity has an E and σ_y of 20 and 100 kPa, quite similar to those of ANF aerogel.[41] The E and σ_y for CelluNF aerogel with 98% porosity can have a higher E and σ_y of 75 and 188 kPa,[37] which can be attributed to the higher CelluNF content and larger nanofiber diameter. The E and σ_y of ANF network can be attributed to the abundant hydrogen-bonding interactions and minimal amount of defects during the employed solvent exchange process.

The tensile properties of ANF PNNs are also impressive. The Young's modulus E_y, ultimate strain ε_u, ultimate stress σ_u are 230±18 kPa, 13±2%, 24±4 kPa for ANF hydrogel, respectively. ANF aerogel reveals E_y = 750±10 kPa, ε_u = 12±3%, and σ_u = 90±7 kPa (Figure 4.3e). The Young's modulus of ANF PNN measured in extension is

much higher than that obtained in compression. Similarly to the energies of atomic oscillations (and corresponding bands in IR spectra), the energy needed for stretching of ANF during tension test can be much higher than that for bending of ANF during compression test. Similar behavior can be observed for KMF and its composites.[43, 44] Notably, the tensile properties of ANF network are better than those of CNT, graphene, cellulose network at similar porosity (>99%), as it is usually difficult to obtain those properties for them due to the poor stability of the hydrogel and the fragility of the aerogel.[25, 37, 41]

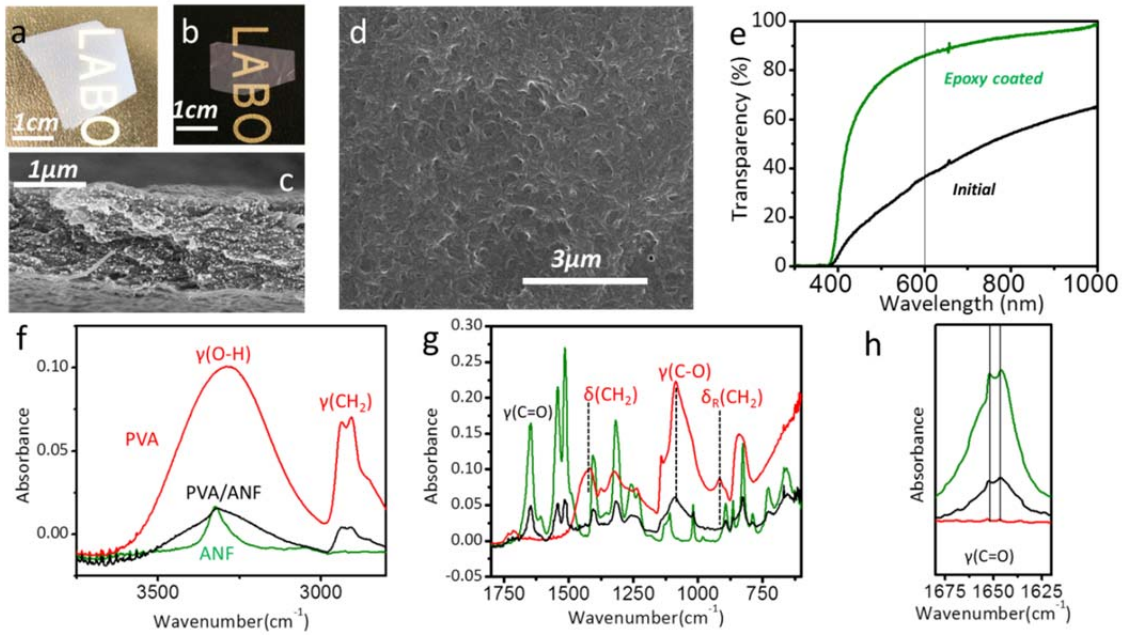

Figure 4.4. (a) A piece of thin film hydrogel in water. (b) PVA/ANF composite film. (c) The cross-section of a PVA/ANF composite film. (d) The surface morphology of a PVA/ANF composite film. (e) Transparency of PVA/ANF composite film with and without epoxy coating. (f-h) A comparison of FTIR spectra for PVA, ANF and PVA/ANF composite. The stretching and bending modes of different functional groups were indicated by γ and δ respectively.

The tensile properties of ANF network are much enhanced after densification. The ANF aerogel compacted into 1/6 of its initial volume displays E_y, ε_u, σ_u of 16±2 MPa,

11±2%, 1.3±0.7 MPa, respectively. These properties can be further improved to 136±11MPa, 7±2%, 6.2±0.5 MPa, respectively, when the aerogel is further compressed down to 1/18 of the initial volume (Figure 4.3f). Such enhancement certainly originates from the increased density of hydrogen-bonding crosslinks and better alignment of fibers transverse to the compression direction. At the fractured cross-section of the compressed aerogel (Figure 4.3g), the alignment of pulled ANFs and layered architecture demonstrate the effectiveness of load transfer in these compressed PNNs. The densified ANF networks can have comparable ultimate stress to the CNT bulky paper[45] made from filtration but with seven times higher ultimate strain.

The robust ANF 3D PNNs, even in the form of flexible ultrathin gel film (Figure 4.4a), can be further exploited as reinforcing skeleton towards composites with high stiffness, extensibility, strength, and toughness. Flexible polymers can be filled inside densified ANF PNNs to facilitate stress transfer and improve the defect-tolerance. Such integration can be easily implemented for ANF PNNs by immersing the aero/hydrogel into liquid various liquid solutions of required components without causing disintegration. Polyvinyl alcohol (PVA) was selected as the right matrix component due to its abundant –OH groups capable of interacting with ANFs through hydrogen-bonding interaction. The same polymer was also used in composites including a variety of nanoinorganic components, such as clays,[12] CNT,[11] graphene,[15] or nanoorganic fillers such as chitin whiskers[46] and CelluNF,[47] so that it would be convenient for comparative studies. When the ANF gel was soaked into 1wt % PVA solution, the polymer chains adsorbed onto the exposed surface of ANFs. The adsorbed PVA interact strongly with ANF as the intense rinsing in long term period had little influence on the PVA content.

This behavior can be comparable to the LBL assembly process[10, 12] in the sense that PVA chains are deposited onto interconnected 3D ANF PNNs instead of a flat glass substrate in a LBL cycle.

The gel film after saturating with PVA was dried at 70 °C into a solid translucent film (Figure 4.4b). A 332 nm absorbance band of ANFs[34] led to complete adsorption of the UV region. The morphology of the resulting film can be described as entangled thickened ANFs wrapped by PVA collapsed from the capillary force during the removal of solvents (Figure 4.4c and d). The irregular micro/nano pores (Figure 4.4d) in the structure left by the drying process can be scattering interfaces to prevent the transmission of light.[48] The light scattering can be reduced by applying a transparent epoxy coating to further reduce the roughness of the surface,[20] which greatly enhance the transparency of the 1.25μm thick film up to 86% at 600 nm (Figure 4.4f).

ANFs constitute 35wt% in the composite as determined by DSC (Figure 4.6b), which agrees with 40wt% estimated by TGA analysis (Figure 4.6c). ANFs in the composite can be easily observed in the fracture cross-section image of composite (Figure 4.4d). FTIR spectra further confirm the interactions between ANF and PVA (Figure 4.4i, j, k). A broad peak between 3000 and 3500 cm^{-1} for the composite is the overlap of characteristic peaks of γ(N–H) from ANF and γ(O–H) from PVA. The hydrogen-bonding interaction can be revealed in the change of γ(C=O) position. The band at 1646 cm^{-1} for intra-ANF hydrogen bonds influenced C=O does not change appreciably, but the other C=O band for inter-hydrogen bonds is upshifted by 0.8 cm^{-1} (Figure 4.4k). This observation suggests that extra –OH groups from PVA compete with C=O as hydrogen acceptors, thus increasing the electron density in the C=O. In addition,

it is also interesting to notice the fingerprint of bending ($\delta(CH_2)$) and rocking mode ($\delta_R(CH_2)$) of $-CH_2$ disappears in the composite spectra.[49] It is likely that the strong van der Waal interactions from phenyl groups in ANF limit the movement of $-CH_2$ in PVA.

PVA/ANF composite has high σ_u = 257±9 MPa with ε_u = 27±5% (Figure 4.5a). Although the KMFs usually display higher σ_u, the toughness of the PVA/ANF composite is 46±3 MJ/m^3, almost two times higher (SI, Figure 4.6). Such an optimum combination is usually difficult to achieve in composites.[50, 51] For example, laminated PVA/clay composite[12] had σ_u of 400±40MPa with ε_u of only 0.33±0.04%, too brittle to be useful for structural material. Graphene composites are also generally brittle with both smaller σ_u and ε_u.[8, 15, 52] The σ_u of chitin whiskers or CelluNFs composite can barely reach 150MPa, and ε_u is less than 7%. [46, 47] Such high σ_u and ε_u was only attained through more time/labor intensive bottom-up method in the past, such as the laminated chitosan/alumina platelet composites[53] with σ_u of 315±95MPa and ε_u of 21±5%, and LBL assembled PVA and CNT composite[11] with σ_u 225±25 MPa and ε_u of 19±7%. In addition to the expensive procedures to make composites, those nanofillers also had to be surface-modified to disperse in solvent or improve the interaction with matrix materials. The PVA/ANF films here made through simple impregnation process can almost surpass or be comparable to the properties of those composites.

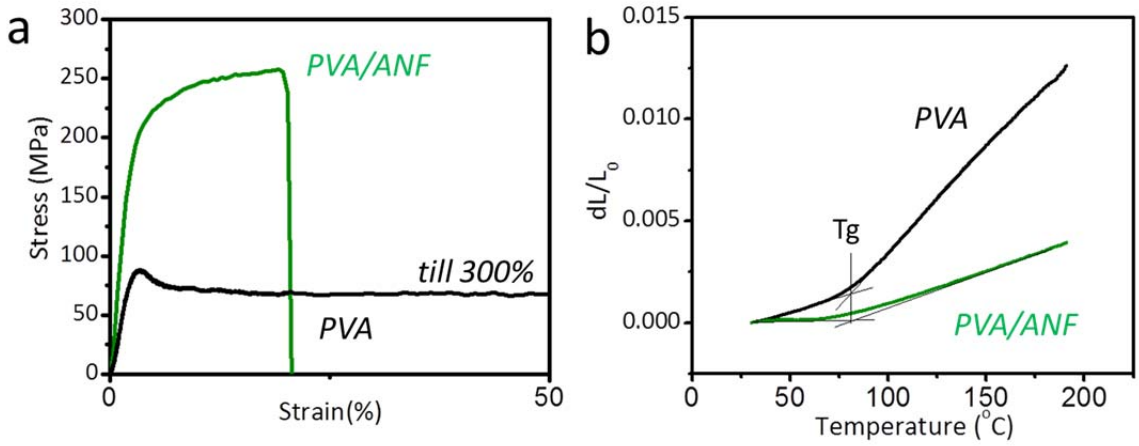

Figure 4.5. (a) Stress-strain curve for PVA and PVA/ANF film. (b) Relative length change dL/L_0 for PVA and PVA/ANF composite for a temperature scan from 30°C to 190°C. dL is the absolute length change while L_0 is the initial length at 30°C.

ANFs can not only boost the mechanical performance of matrix material but the thermal stability as well. The fluidity of thermoplastic polymers after glass transition temperature (T_g) is usually a major factor limiting its use.[54] For example, at temperature lower than T_g, PVA has a coefficient of thermal expansion (CTE) of 30 ppm K^{-1} (Figure 4.5b). When the temperature is above T_g, CTE of PVA is tripled to 102 ppm K^{-1} (Figure 4.5b). The inclusion of ANF, which has an unusual negative CTE in the axial direction,[55] can greatly reduce the overall CTE of composite. Below T_g, The PVA/ANF composite can have a CTE of 1.9 ppm K^{-1}, which is smaller than most of the ceramics, such as glass, silicon and boron carbide;[40] Above T_g, the composite has a CTE of 32 ppm K^{-1} close to that of the neat PVA in the glassy state (Figure 4.5b).

4.2.4 Conclusion

In summary, this work demonstrates a 3D PNN made of bifurcating ANFs, into which polymers can be impregnated to create PNN composites. The unique strength and

toughness combination of PVA/ANF composite is comparable to the record set by CNTs[11] or alumina[53] composites so far. PVA/ANF composites also exhibit low thermal expansion thanks to the axial negative thermal expansion of ANF.[55] Not limited by what is achieved here, ANF PNNs the high compatibility of ANF with various solvents can make it compatible with almost any polymers which presents a considerable advantage for loading various functional nanoparticles onto the network.[56] As a biocompatible material,[57] ANF network can also find medical applications as durable scaffold to replace silk[58] or collagen[59] networks to address challenges in tissue engineering.

4.2.5 Supporting Information

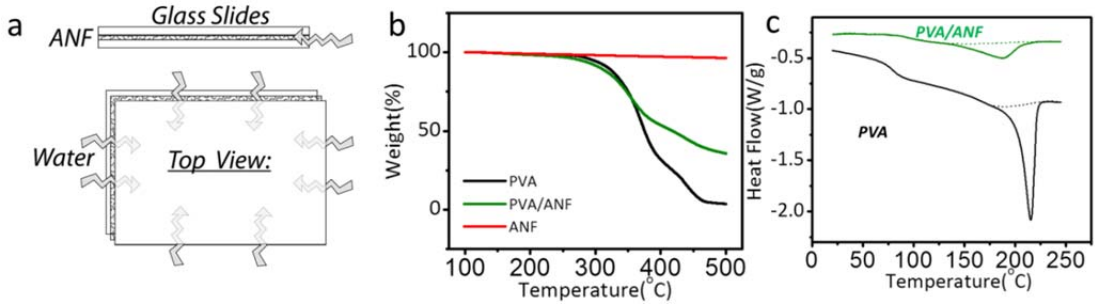

Figure 4.6. (a) A schematic drawing showing the preparation of ~~Kevlar~~ ANF thin film hydrogel. (b) TGA of PVA, ANF and PVA/ANF composite. (c) DSC analysis of PVA and PVA/ANF composite.

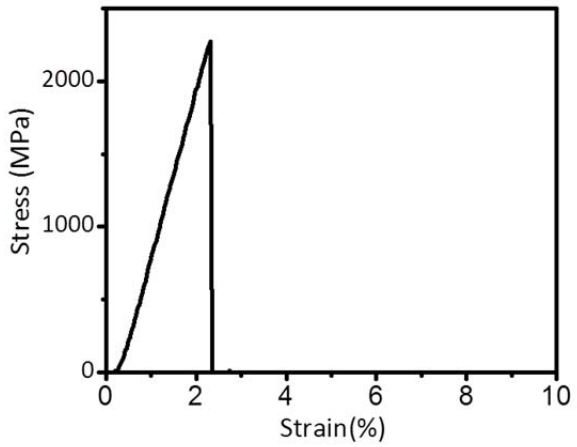

Figure 4.7. Tensile property of Kevlar 69 microfiber

Table 4-1 Comparison of Mechanical Properties of Various Networks.

		Compression		Tension		
	Porosity	Yield Strength(kPa)	Modulus (kPa)	Young's Modulus(kPa)	Strain (%)	Stress (kPa)
Graphene[25] Hydrogel	99.56%	3	29	NA	NA	NA
Graphene[25] Aerogel	99.56%	NA	NA	NA	NA	NA
SWNT Hydrogel[28, 41]	99.73%	NA	NA	NA	NA	NA
SWNT Aerogel[28, 41]	99.73%	20	100	NA	NA	NA
Cellulose Aerogel[37, 42]	98.00%	75	187.5	NA	NA	NA
Cellulose Hydrogel[37, 42]	98.00%	NA	NA	NA	NA	NA
BC cellulose Hydrogel[30]	93.30%	NA	7	2900	21	2200
Kevlar Hydrogel	99.30%	8±1	57±3	230±18	13±2	24±4
Kevlar Aerogel	99.30%	18±1	90±5	750±10	12±3	90±7
Kevlar Aerogel(6X)	95.94%	NA	NA	$(16\pm2)\times10^3$	11±2	$(1.3\pm0.7)\times10^3$
Kevlar Aerogel(18X)	88.71%	NA	NA	$(136\pm11)\times10^3$	7±2	$(6.2\pm0.5)\times10^3$

4.3 Gelation-Assisted Layer-by-Layer Deposition of High Performance Aramid Nanocomposites

4.3.1 Introduction

Nanocomposites have been under intense R&D since the discovery of remarkable mechanical enhancement by addition of only a small amount of nanoclay into nylon.[60] A variety of available nanomaterials[61] further fuel the interest of the application of nanocomposites in the fields of electronics,[62] photonics,[63] biomedical implants,[64] and energy storage and conversion devices.[65, 66] The exceptional multifunctionality associated with those nanomaterials, such as carbon nanotube[67, 68] and graphene,[69, 70] drives high expectation on the potential achievements of nanocomposites in the future. Currently, however, the prospect of making mechanically-super nanocomposites is remote considering lots of efforts spent but with limited success[53, 71-73] in this area. The mechanical performance of nanocomposites is not satisfactory particularly in comparison to the conventional composites reinforced with continuous carbon or aramid microfibers.[74] The inadequate dispersion, alignment, and volume fraction of the nanoreinforcement in addition to its poor interface with the matrix may be the major hurdles contributing to the disappointing performance of nanocomposites.[75]

Nanocomposites with proper material processing to tackle those deficient compositional/structural factors can finally overtake the performance and/or market of the microfiber reinforced composites (or micro-composites). In addition, the development of nanocomposites can address several challenging issues of the micro-composites. For example, those composites lack the intrinsic homogeneity of structure, thus perform

poorly in the direction perpendicular to the fiber alignment. The quasi-isotropic micro-composites have to rely on the expensive lamination of prepregs with different fiber orientations.[74] The laminated carbon fiber/epoxy composites can have ultimate tensile strength of 303 MPa, almost only 1/6 of that of unidirectional composites.[74, 76] Moreover, the carbon and aramid micro-composites are usually brittle with the fracture strain determined by the microfibers, which are usually 1.4-2.8%.[74] The nanoscale reinforcements, however, can be intrinsically homogenous with more energy dissipation interfaces to make strong, tough and even transparent composites with other advanced quantum-related functionalities.

Such high-performance nanocomposites with the inclusion of high volume content well-dispersed nanomaterials have been successfully managed by the techniques of layer-by-layer assembly (LBL),[10, 12] vacuum assisted flocculation (VAF)[15, 77] as well as the preformed nanoscale network infiltration (PNI).[21, 27, 71] LBL is a versatile bottom-up assembly approach, which makes use of the alternate nanoscale layering of polymers and nanomaterials based on the complementary interactions.[14] The strong interface obtained by selective adsorption can lead to a stiff film but with quite high brittleness.[12] A major challenge of this technique is the slow assembly process. A 1μm thick film can typically take 3-4 days to create. The stringent requirement for water dispersible components in LBL can be another roadblock for high performance materials. VAF is capable of fast assembly of nanocomposites even in the organic solvents.[15] However, the two phases need optimum interaction to stay dispersed in the solvent, otherwise, agglomeration can occur to affect the distribution and alignment of nanomaterials in the composites. In addition, the use of expensive size-limited porous membrane and dead-end filtration can

directly affect the dimension and thickness of films plus their use as coatings. PNI uses the back diffusion of polymers into the preformed percolation nanoscale network (PNN) in the form of hydrogel or aerogel.[21, 27, 71] It can thus allow the combination of any polymer with the network to tune the functionality of the composites. The creation of thick nanocomposite samples, however, needs a rather thick gel and also quite long time to allow the polymers to diffuse it in.[21, 27] Besides, the defects created during the gel management, the incomplete polymer diffusion into nanopores, and the compression induced voids might deteriorate the mechanical performance of the composites.

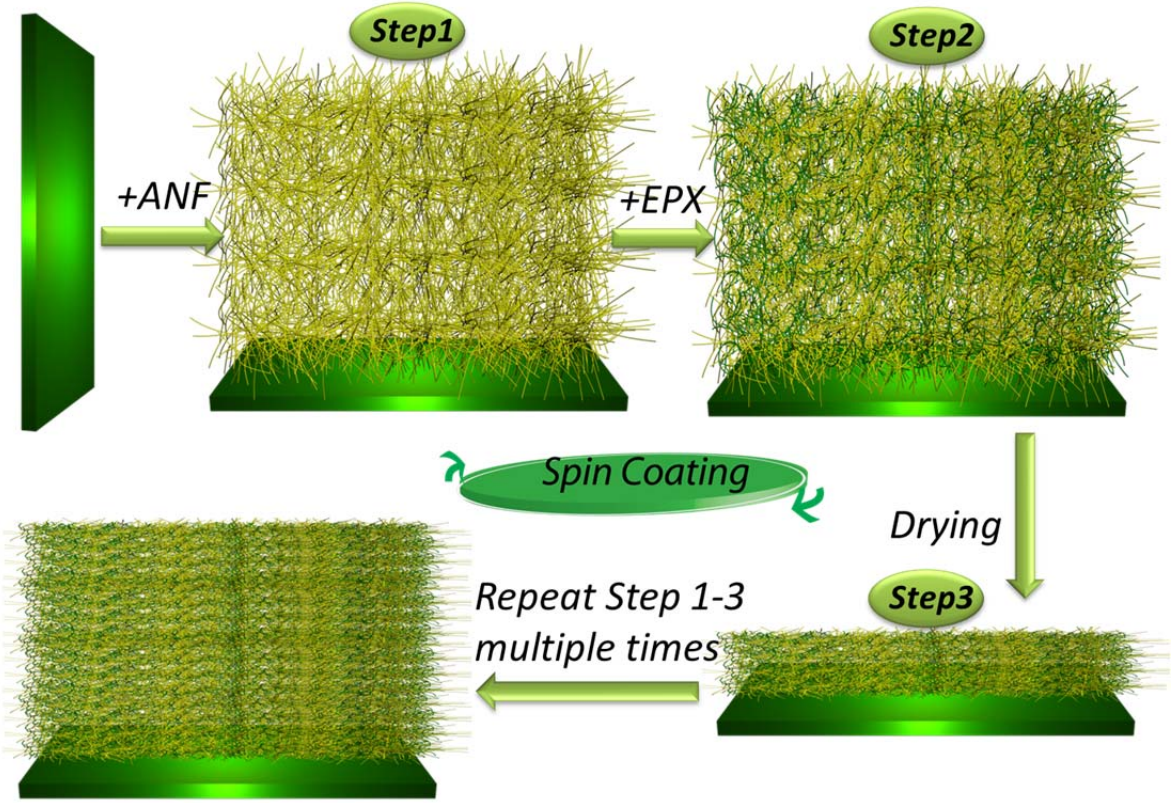

Figure 4.8. The schematic of gelation-assisted layer-by-layer deposition process

Here we introduce a gel-assisted layer-by-layer deposition (GLBL) technique. GLBL is a fast assembly approach with a combination of the merits from both LBL and PNI. In this method (Figure 4.8), a thin layer of PNN gel instead of a monolayer of nanoparticles is deposited on a substrate by spin or spray coating. Polymer of choice is then allowed to diffuse into the PNN with ease due to the relatively thinness of PNN. Subsequent removal of solvent makes the thin PNN collapse evenly as a result of capillary force. This cycle can then be repeated as needed to get the desired thickness. This technique is less resourceful than LBL with advantages of hundreds of nanometers thick deposition each cycle and less dependence on the thermodynamics of adsorption. It is also more easily executable than PNI due to the relatively thinness of PNN.

The aramid nanofiber (ANF) PNN is used here for the GLBL process. ANF PNN is chosen due to the simplicity and low cost of preparation, purity and robustness of the network, as well as the high surface area. Epoxy (EPX) is selected to infiltrate into the ANF PNN. EPX is a widely used thermosetting polymer for microfiber reinforced composites with the edge of strength, adhesion, process versatility, and environmental stability. Its combination with nanomaterials,[78-81] however, has not yet achieved the high performance matchable with those microcomposites. In this work, quasi-isotropic ANF/EPX composite made by GLBL shows comparable ultimate strength but with 4~5 times toughness than the conventional micro-composites. The ANF and EPX combination also renders close-to-zero thermal expansion and high transparency in the visible spectrum.

4.3.2 Experimental

Material:

1% aramid nanofiber (ANF) dispersion was prepared by stirring Kevlar 69 (from Thread Exchange, right twist) in dimethyl sulfoxide (DMSO) for two weeks at the presence of over saturated KOH (1g/100ml DMSO). System 2000 epoxy resin and 2020 epoxy hardener were bought from Fibre Glast. The two parts were mixed together in the ratio of 3:1, and then diluted with acetone (Aldrich) to the needed concentration.

Typical procedures for gelation assisted layer-by-layer deposition:

2" by 2" glass slides were cleaned by immersion in Piranha solution (3:1 H_2SO_4/H_2O_2) for 12 h, then thoroughly rinsed with DI water prior to use. 1ml 1% ANF dispersion was poured onto the substrate, and then spread uniformly all over the surface by spinning with a rate of 1000 rpm and an acl of 45 for 30 s. Then DI water was quickly dropped onto the surface, the color of the coating was immediately changed from orange to white, indicating the formation of thin layer hydrogel. The substrate then went through another spin at the same settings for 30 s to remove extra water. 1ml 0.1~1% EPX in acetone was subsequently put on the hydrogel layer to allow infiltration, and a 30 s spin removed the extra EPX solution. After that, the glass slide was taken from the spin coater and put in the 100°C oven for 2 min to allow pre-annealing. This complete cycle usually takes 4 min. The above procedures could be repeated to put another ANF/EPX layer on top. Typically, films made after 6 cycles of deposition were used for property measurements. The samples finally went through an overnight annealing at 70°C to completely cure the EPX and remove the solvent. The freestanding films were

delaminated from glass substrate with the aid of 1% HF. For thickness measurement by ellipsometry, silicon rather than glass was used, and other procedures were kept the same.

Characterization:

The transparency of film was determined by an 8453 UV-vis ChemStation spectrophotometer from Agilent Technologies. Cross-section and morphology of the film were examined by FEI NOVA Nanolab Scanning electron microscopy (SEM). Tapping mode atomic force microscopy (AFM) images were obtained using a NanoScope IIIa Atomic force microscope (AFM) from Veeco Instruments. Thicknesses of thin films were measured by a BASE-160 spectroscopic ellipsometer produced by J.A.Woolam Co., Inc.

Thermal gravimetrical analysis (TGA) was run on a TA instrument Discovery TGA with a heating rate of 10°C/min in nitrogen. Coefficient of thermal expansion (CTE) of films was measured using extension mode in Perkin Elmer TMA7 following ASTM *Test Method for Linear Thermal Expansion of Solid Materials by Thermomechanical Analysis* (E 831) and slightly modified to measure the thin film. The extension probe and grips were customized by RT instruments, Inc. to minimize the expansion of grips during the measurement. A ramp rate of 5°C/min was used and the second heating step was used for analysis.

Uniaxial tensile testing was done on RSAIII Rheometrics Systems Analyzer from TA instruments. The tensile tests confirm to the ASTM standard ASTM D882. In a typical measurement, 1mm wide and 6mm long sample strip was fixed onto two pieces of stainless steel metal sheets. The metal sheets were then put between the grips for measurement. The test speed is 0.01mm/s. A total of 10 measurements were made for 2 batches of ANF/EPX composite.

4.3.3 Results and Discussion

ANF dispersion can be easily prepared by dissolving aramid microfiber (or commonly known as Kevlar) into dimethyl sulfoxide (DMSO). A subsequent solvent exchange with water leads to the formation of ANF hydrogel. In order to make a thin ANF hydrogel PNN to, a thin liquid layer of ANF in DMSO is spin-coated on a glass substrate before the solvent exchange. This thin ANF hydrogel can be carefully peeled off from the substrate (Figure 4.9a) and dried by supercritical CO_2 to examine the structure (Figure 4.9b). The obtained ANF aerogel is 57µm thick with a wide range of pores defined by interconnected ANFs (Figure 4.9c).

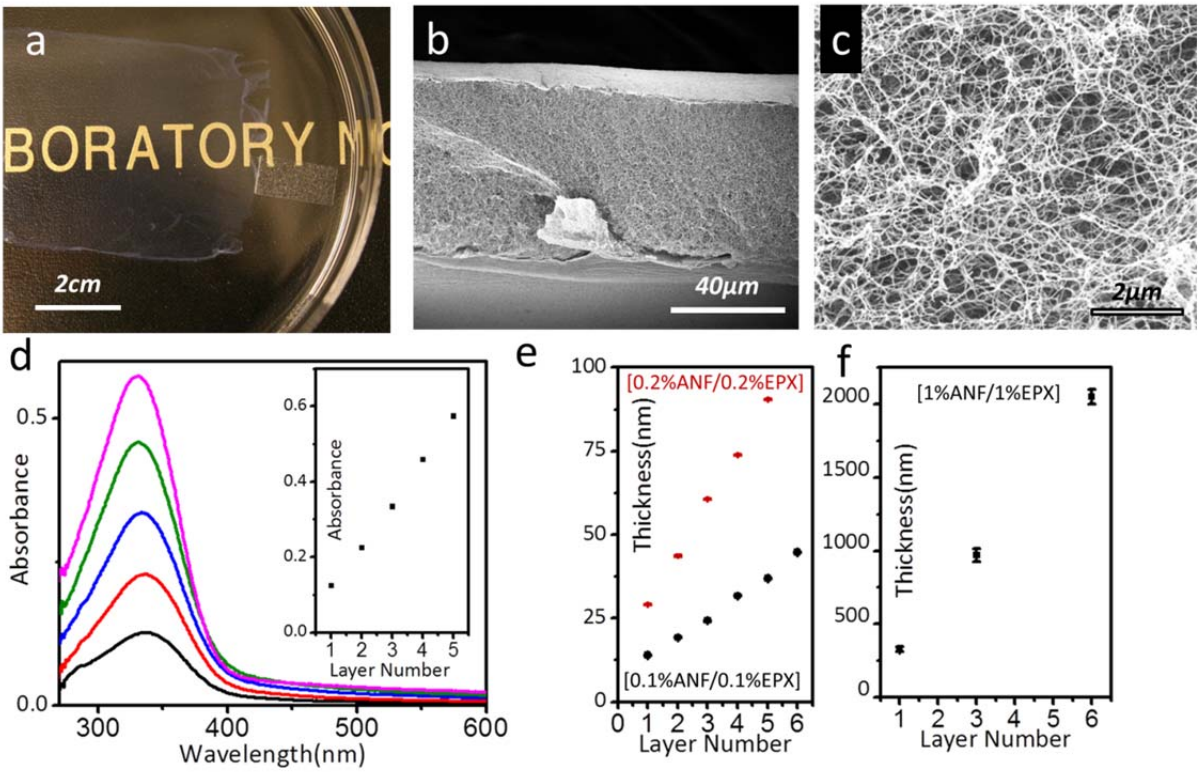

Figure 4.9. a) A thin layer of hydrogel peeled off from the glass slide in water. b) The cross-section of a thin layer of aerogel obtained by CO_2 supercritical drying. c) A zoomed region in b) showing the porous nanofiber network. d) Linear growth of the film examined by UV-vis spectroscopy. The inset shows the absorbance at 330nm. e) A linear

increase of thickness at the concentrations of 0.1% and 0.2%. f) A linear increase of thickness at the concentration of 1%.

To make the ANF/EPX composites, the ANF hydrogel layer is left on the substrate to allow the diffusion of EPX. The hydrogel is adhesive enough to the substrate to allow EPX to diffuse into PNN without causing wrinkles. 0.1—2% EPX in acetone is used here due to acetone's full miscibility with water. Extra EPX solution can be removed by spinning off the substrate. After coating, the substrate is put in the 100 °C oven for 2 min to pre-anneal the film by removing the solvent. Then, another cycle can take place with ANF hydrogel deposited on the solidified coating. The cycle can be repeated continuously to obtain the needed thickness, which is similar to the conventional LBL assembly.[14] The film made after nth cycle is denoted as $[ANF/EPX]_n$.

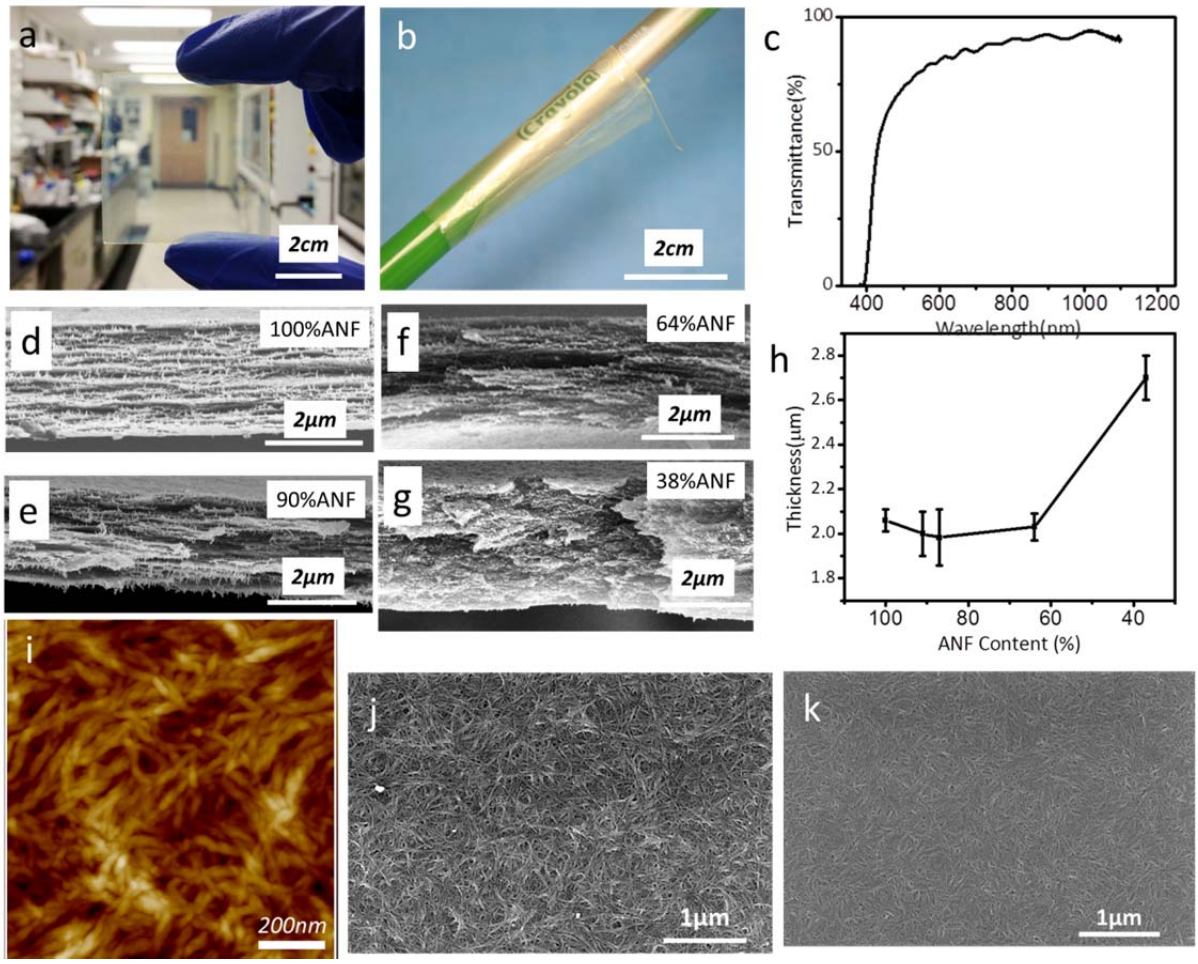

Figure 4.10. a) The transparent $[1\%ANF/1\%EPX]_6$ on glass slide. b) The freestanding $[1\%ANF/1\%EPX]_6$ wrapped on a pen. c) UV-vis spectrum of $[1\%ANF/1\%EPX]_6$. d) Cross-section of $[1\%ANF]_6$. e) Cross-section of $[1\%ANF/0.1\%EPX]_6$. f) Cross-section of $[1\%ANF/1\%EPX]_6$. g) Cross-section of $[1\%ANF/2\%EPX]_6$. h) Thickness of the film with different ANF fractions. i) AFM image of $[1\%ANF]_1$. j) $[1\%ANF]_1$ surface morphology by SEM. h) $[1\%ANF/2\%EPX]_1$ surface morphology by SEM.

The linear growth of the film is confirmed by absorbance and thickness change (Figure 4.9d, e, and f). An absorbance band centered at 330nm is shown for ANF/EPX film, and its intensity increases linearly with cycle number. Similar linear trend can be observed for thickness, which can be finely tuned by the concentration of ANF and EPX. When concentrations are 0.1%, 0.2% or 1% for each component at the same spin rate of

1000 rpm, the average thickness per cycle is 7.5, 18, 342 nm. This result demonstrates GLBL technique has remarkable thickness control from several to hundreds of nanometers per layer.

The 1% ANF solution is then focused on for the following investigations for the thick layer formed each cycle. EPX concentration is changed from 0.1 to 2% to control the ANF volume fraction in the composites. As is determined by thermal gravimetrical analysis (TGA, Figure 4.14), ANF weight fraction is 90%, 87%, 64% and 38% when EPX varies at 0.1%, 0.5%, 1% and 2%. TGA also demonstrates a high decomposition temperature of 250°C.

The ANF/EPX composite is typically transparent (Figure 4.10a). The transparency of $[1\%ANF/1\%EPX]_6$ is 88% at 700nm (Figure 4.10c). High uniformity in the film is indicated by Fabry-Perot patterns[12, 82] displayed in the absorbance spectrum. The ANF/EPX composite films can also be easily delaminated from glass substrate using dilute HF.[10, 11] The obtained transparent freestanding film is flexible enough to be wrapped around a pen (Figure 4.10b). Fourier transform infrared spectroscopy (FTIR) confirms the chemical features of both ANF and EPX in the composite (Figure 4.15).

Further examination of the composite structure led some interesting discoveries. We observed a stratification of ANFs (Figure 4.10d, e and f) in the composite, which is likely owing to the compression induced alignment during the collapse of PNN. With the increase of EPX in the composite, the layered structure becomes less distinct (Figure 4.10g). This configuration of nanofibers is similar to nanosheets reinforced composites, such as clay[12] or graphene,[15] and quite different from other 1D nanoreinforcement, such as carbon nanotube,[10, 11] or cellulose nanocrystal.[83] This observation indicates strong

ANF-ANF interactions in the composites as a result of abundant hydrogen-bonds-abled amide functional groups. With such strong interactions, the strand of ANF under stress can easily transfer to other strands so that the whole neighboring network can be pulled out under load and then fractured. EPX here serves as crosslinks to ANF contacts when filling into the nanopores formed during the drying (Figure 4.10i). However, when EPX content is above a threshold, individual ANF can be completely surrounded by EPX. The strong ANF-ANF interaction is replaced by ANF-EPX-ANF interaction. The fracture then occurs at each individual ANF rather than the layered collective mode (Figure 4.10g). The overfilling of EPX is also evident in the abrupt jump of the film thickness from approximately 2 μm to 2.7 μm when 2% EPX is used for infiltration. The surface of overfilled EPX composites is also less porous by appearance (Figure 4.10j vs. k). Those structural differences can influence on the mechanical and thermal expansion properties of the composites.

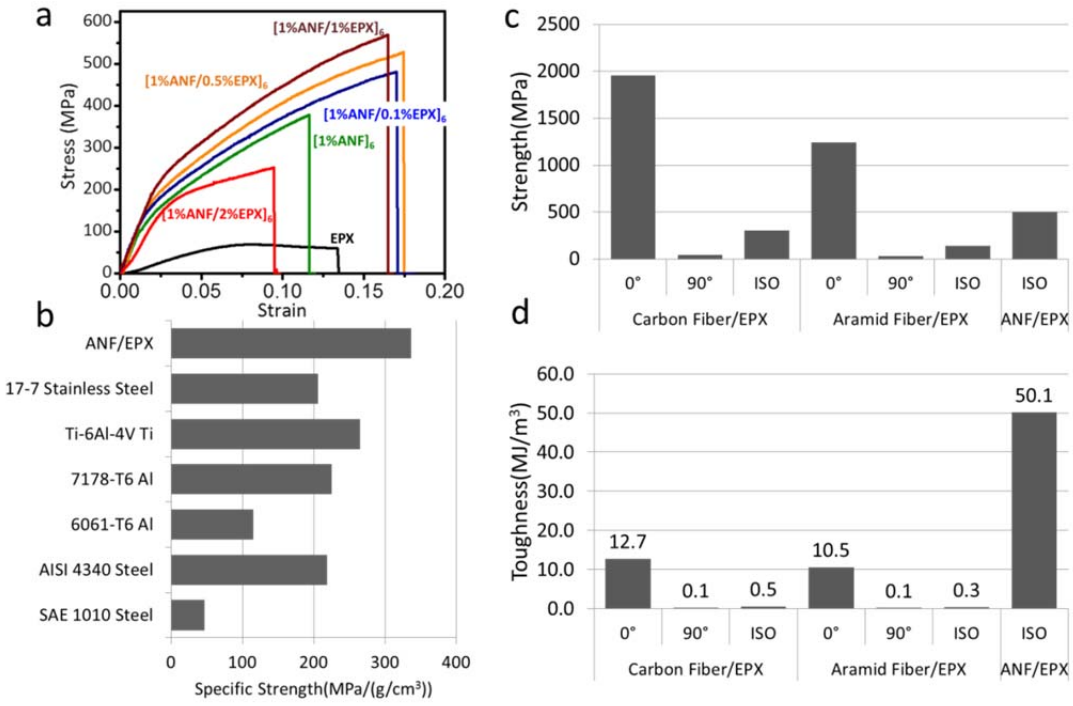

Figure 4.11. a) Stress-strain curves for the composites in this work. b) The specific strength comparison of $[1\%ANF/1\%EPX]_6$ with various metal alloys. c) $[1\%ANF/1\%EPX]_6$ in comparison with various carbon and aramid microfiber reinforced composites[76] in terms of ultimate strength. ISO stands for quasi-isotropic here. d) Toughness comparison.

Rather than the brittle behavior of micro-composites, the ANF/EPX composites are rather ductile, demonstrating a plastic deformation after the initial elastic region (Figure 4.11a). This characteristic is similar to those high performance aerospace alloys, such as titanium, steel or aluminum.[84] In particular, $[1\%ANF/1\%EPX]_6$ shows an ultimate strength (σ_u) of 505±47 MPa, an ultimate strain (ε_u) of 0.16±0.03 with only a density (ρ) of 1.5±0.1 g/cm^3. The calculated toughness (K) by integrating the area under the stress/strain curve is 50.1± 9.8 MJ/m^3. Similar to the micro-composites, the specific strength (σ_u / ρ) of this ANF/EPX composite is significantly larger than that of titanium, steel or aluminum alloys[74] (Figure 4.11b). The absolute strength σ_u is much higher than those of SAE 1010 steel (365 MPa) and 6061-T6 aluminum alloy (310 MPa).[74] Although σ_u of $[1\%ANF/1\%EPX]_6$ is not comparable to the σ_u of unidirectional micro-composites in the alignment (0°) direction, it is 10 times and 16 times higher than the σ_u in the 90°direction in those micro-composites respectively[76] (Figure 4.11c). In addition, both the quasi-isotropic laminas of carbon and aramid fiber micro-composites are inferior in σ_u (303 MPa and 141 MPa, respectively)[76] to the ANF/EPX examined in this work (Figure 4.11c), which is more intrinsically isotropic with the nanofiber reinforcement.

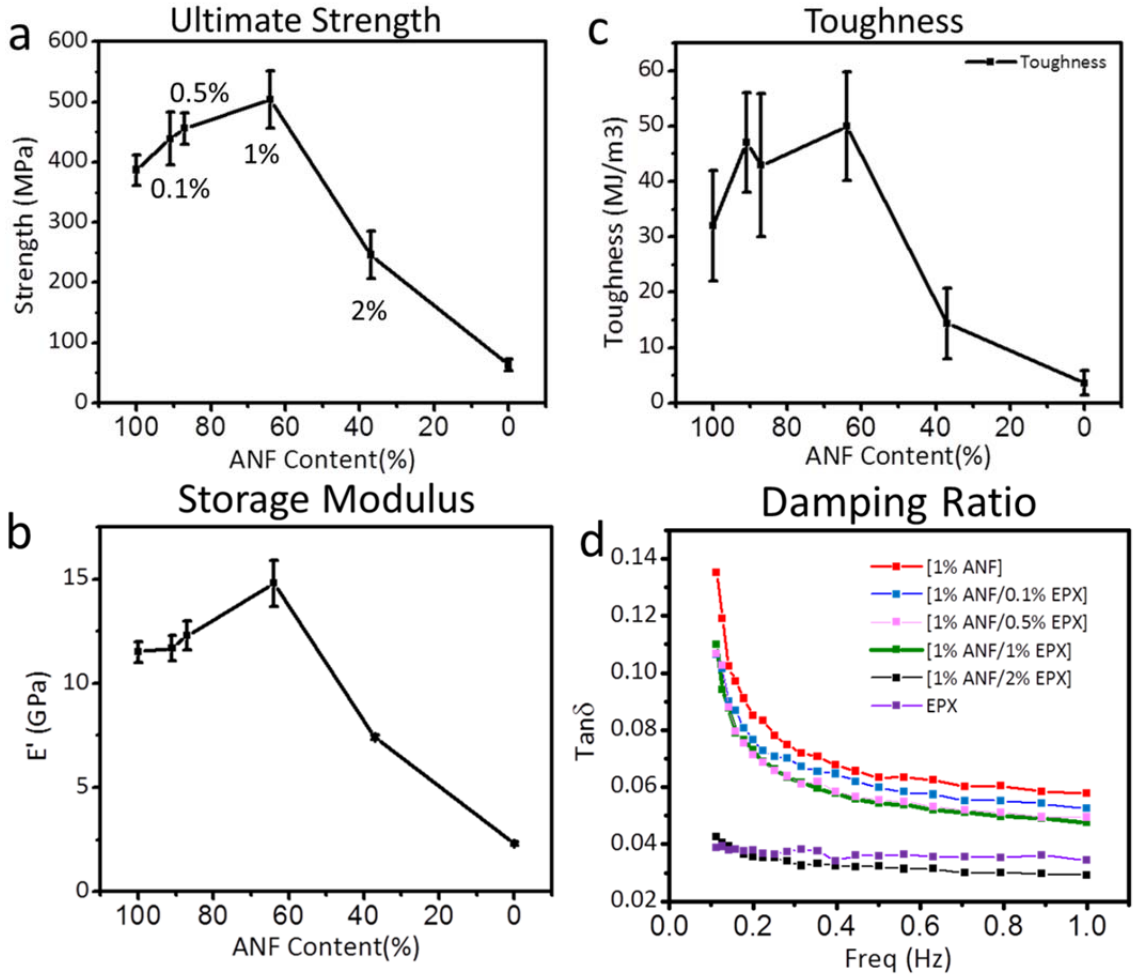

Figure 4.12. A comparison of various properties for ANF/EPX composites made in this work: a) Ultimate strength. b) Storage Modulus. c) Toughness. d) Damping ratio.

Such a high σ_u for ANF/EPX composite, however, is not connected with the brittleness or low toughness that many composite materials have encountered.[51, 73] The toughness (K) of the ANF/EPX is **4~5 times** higher than that of the unidirectional microcomposites measured in the 0° direction. The K is also much higher than the layered composites made by alumina nanoplatelets[53] or carbon nanotube[11] with greater or comparable σ_u. It is believed that σ_u and K are mutually exclusive properties in many cases.[50, 51] An optimum combination of both properties, however, is important for

structural materials to avoid catastrophic failure under load. The solution to this dilemma relies on the design of hierarchical composite architecture similar to that in many natural materials.[51, 85] Here, the layered configuration of ANF, their strong interactions, and crosslinks formed by EPX lead to strong load-bearing ability. The collective layered failure mode plus the "stick-slip" interactions afforded by the hydrogen bonds[52] also facilitate energy dissipation during the stretching and thus high toughness.

More EPX or less in the composite leads to poorer mechanical performance than the $[1\%ANF/1\%EPX]_6$ (Figure 4.12). As is discussed above, this condition is a transition point at which nanopores start to get overfilled. This structural evolvement directly affects the σ_u and K, plus the storage modulus E', which is an indication of elastic stiffness of the material. All those properties show maxima for the film of $[1\%ANF/1\%EPX]_6$ (Figure 4.12).

To be noted here, pure ANF film without EPX shows σ_u of 387±25 MPa, ε_u of 0.16±0.03, E' of 11.5±0.5 GPa, which are much higher than those from VAF made ANF film (σ_u~160MPa, ε_u~0.1, E~7.1).[86] The mechanical performance enhancement can result from this elegant GLBL processing technique. In VAF, the long filtration step can lead to the deterioration of solution qualities, and thus the generation of defects in the final film. Additionally, hand-peeling the ANF film from the porous membrane can also break some film microstructures. In GLBL, all those defects-introduction steps are avoided. Besides, some mechanical factors in the spin coating process, such as the centrifugal and air shear force can usually lead to some degree of lateral chain orientation and stratification.[87, 88] These factors can lead to an improved mechanical performance for the GLBL made film with the same chemical composition, but with the different microarchitecture.

Another interesting property in dynamic mechanical properties measurement (Figure 4.16) is the damping ratio or tan δ, which is the ratio between the loss modulus and storage modulus. Tan δ measures the degree to which a material dissipates the vibration energy into heat. High damping capacity is useful in many automotive and sporting goods applications.[74] The carbon and aramid micro-composites typically have very low tan δ of 0.0024 and 0.018 respectively.[76] The ANF/EPX composites show higher tan δ (Figure 4.12d). Interestingly, pure ANF film displays the largest tanδ over the range of 0.1-1Hz. At 0.1 Hz, the tan δ of ANF film can be as high as 0.14, and is decreased to 0.06 at 1 Hz. With the addition of EPX, the tan δ gradually declines. The highest tan δ of pure ANF film can be related with the more freedom of ANFs in the periphery of abundant unfilled nanopores. The strong but unlocked ANF-ANF interfaces cause the high mechanical damping.[79] With the introduction of EPX into the PNN, the touching interface is gradually locked by the poor-damping EPX to result in a lower tan δ. $[1\%ANF/1\%EPX]_6$ has slightly lower tan δ of 0.11 at 0.1 Hz and 0.5 at 1 Hz. An significant drop of tan δ occurs for $[1\%ANF/2\%EPX]_6$, which has even smaller tan δ than EPX (Figure). This finding actually agrees with the previously discussed structure transition. In this film, ANF is surrounded by EPX with the interface of ANF-EPX-ANF. The dissipating mechanism relying on the ANF-ANF friction disappears here, while the ANF serves as reinforcing agent for EPX to make its chain even less mobile.

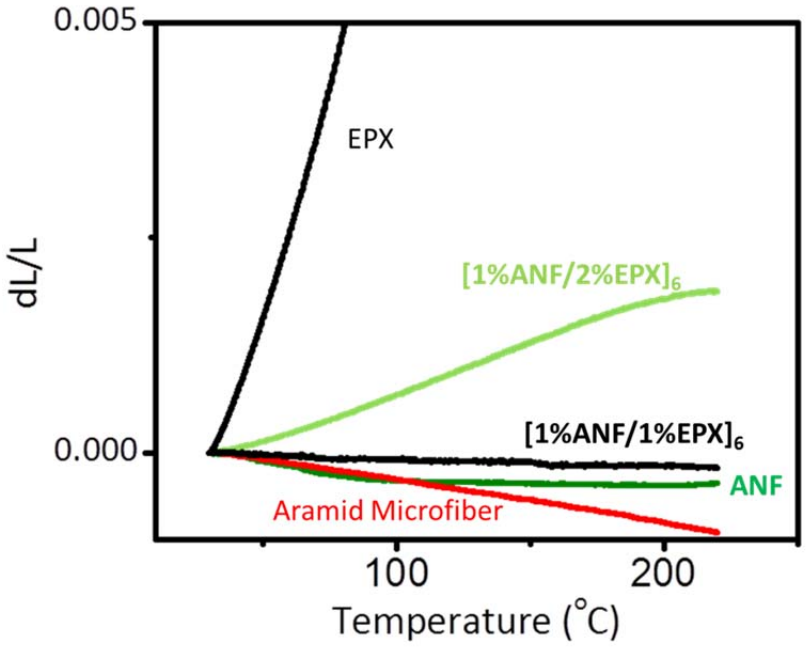

Figure 4.13. Normalized length change dL/L_0 *vs.* temperature for several ANF/EPX composites, ANF film, EPX and aramid microfiber.

Low coefficient of thermal expansion (CTE) is another key feature for conventional carbon or aramid micro-composites.[74] The low CTE can exhibit a better dimensional stability over a wide temperature range. Unidirectional carbon micro-composites have CTE of -0.44~0.16 ppm K^{-1}in 0° direction, and 0.36~4.02 ppm K^{-1} in 90° direction, while the quasi-isotropic ones have CTE of 0.36~4.02 ppm K^{-1}.[76] On the other hand, unidirectional aramid micro-composites have CTE of -2.57~-1.74 ppm K^{-1} in 0° direction, and 21.4~27.5 ppm K^{-1} in 90° direction, while the quasi-isotropic ones have CTE of 9.5~12.9 ppm K^{-1}.[76] Amazingly here, $[1\%ANF/1\%EPX]_6$ can have the quasi-isotropic close-to-zero CTE of -0.9 ppm K^{-1} till 220 °C (Figure 4.13). With finer tuning, a real zero expansion could be achieved. It is interesting to notice that the aramid micro-composites have high positive CTE at 90° to the fiber direction, and this property

contributes to the slightly lower but still positive CTE for quasi-isotropic composites. However, material made with ANF with the same chemical composition but much smaller diameter gives overall negative and even zero CTE.

This phenomenon is related with the existence of nanopores. Aramid microfiber is proved to have CTE of -4.9 ppm, agreeing with the previous studies.[55] Pure ANF film shows two regimes of thermal expansion: one with CTE of -6 ppm K^{-1} till 75 °C, and the other one with CTE of -0.5 ppm K^{-1}. Similar to graphene,[89, 90] the negative CTE in ANF is contributed by the transversal acoustic bending modes along the axis,[91, 92] or commonly known as the "membrane effect".[93] The nanopores formed by the overlapping of ANFs give rise to more free space to enhance this bending effect, thus more negative CTE.[92] With the increase of temperature, however, other phonon modes contributing to the positive CTE might take effect.[91] The nanopores can also accommodate the positive radial expansion of ANF. In addition, since the mechanical load is carried mainly by the axial direction of the ANF, the overall CTE shows more axial behavior of ANF. With EPX in the composite, the thermal behavior is a combined effect of both components. When the nanopores are underfilled, the CTE increases a bit even with 36% EPX in the composites. When the nanopores are overfilled, such as in the film of $[1\%ANF/2\%EPX]_6$, the CTE has increased by a lot to 11 ppm. In this film, no enough space exists to accommodate the positive radial expansion, and EPX as a matrix can uniformly distribute the load to various directions in ANF. Accordingly, the radial expansion can contribute more to the overall CTE.

4.3.4 Conclusion

In summary, this work demonstrates a novel gelation-assisted layer-by-layer deposition (GLBL) approach to efficiently fabricate transparent, strong and tough aramid nanofiber/epoxy (ANF/EPX) composites with high damping and zero-expansion. The ultimate fracture strength is much higher than that of quasi-intrinsic carbon or aramid microfiber reinforced composites (micro-composites). The toughness is even better than that of the unidirectional micro-composites. ANF/EPX composites with such combined functionalities can be used for bio-implants, packaging materials, electronic boards, bullet-proof windows and many more. This GLBL approach can also be adopted for other gel-forming networks, such as cellulose nanofibers, carbon nanotube, and graphene to produce other functional materials for fields in need.

4.3.5 Supplementary Information

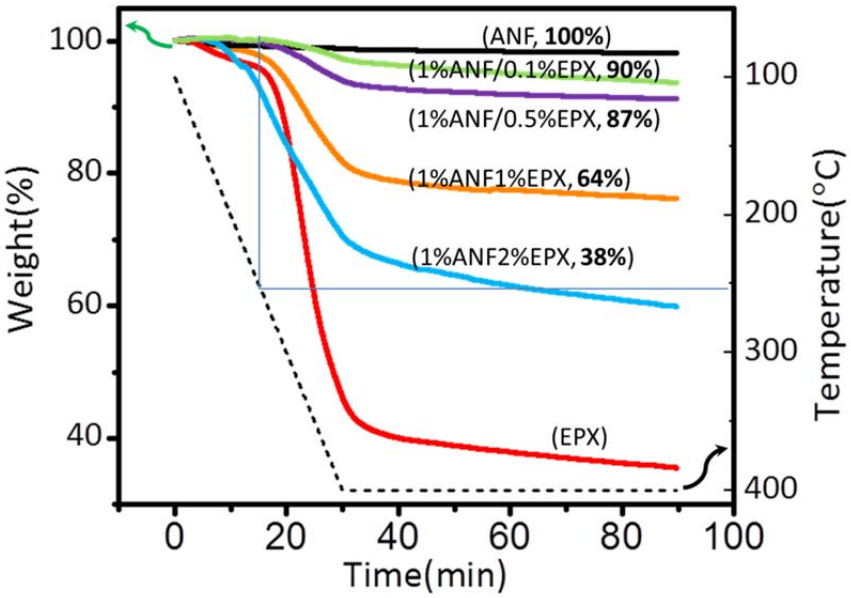

Figure 4.14. TGA analysis of the composites, ANF, and EPX.

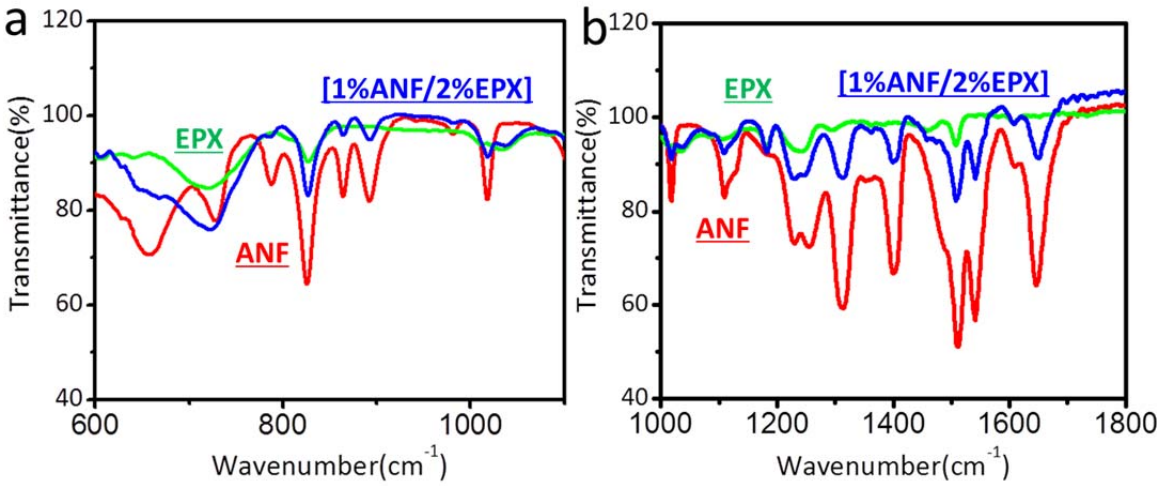

Figure 4.15. FTIR of [1%ANF/2%EPX], ANF and EPX.

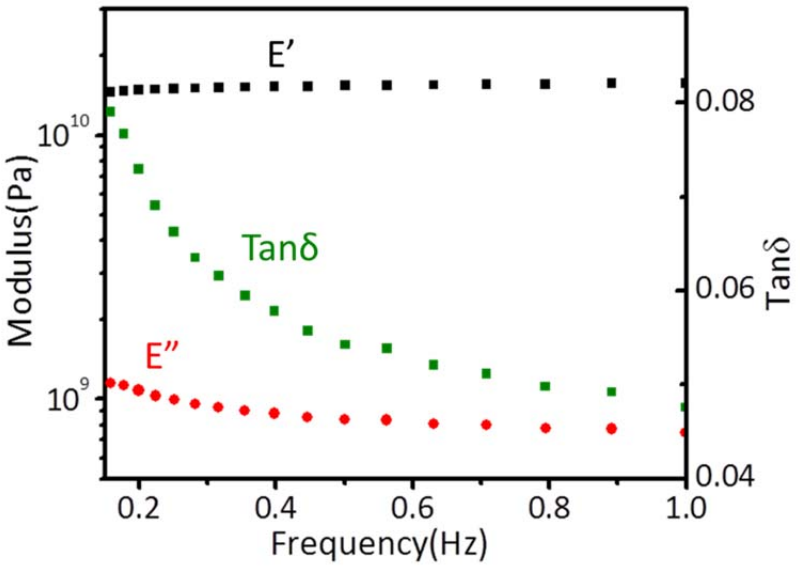

Figure 4.16. Dynamic Mechanical Analysis of $[1\%ANF/1\%EPX]_6$.

4.4 References

1. Sahimi, M., *Applications of Percolation Theory*. Taylor & Francis Inc. : Bristol, **1994**; pp 258.
2. Sun, Y. G.; Rogers, J. A., Inorganic Semiconductors for Flexible Electronics. *Adv. Mater.* **2007**, 19, 1897—1916.
3. Allen, B. L.; Kichambare, P. D.; Star, A., Carbon Nanotube Field-Effect-Transistor-Based Biosensors. *Adv. Mater.* **2007**, 19, 1439—1451.
4. Mecklenburg, M.; Schuchardt, A.; Mishra, Y. K.; Kaps, S.; Adelung, R.; Lotnyk, A.; Kienle, L.; Schulte, K., Aerographite: Ultra Lightweight, Flexible Nanowall, Carbon Microtube Material with Outstanding Mechanical Performance. *Adv. Mater.* **2012**, 24, 3486—3490.
5. Schaedler, T. A.; Jacobsen, A. J.; Torrents, A.; Sorensen, A. E.; Lian, J.; Greer, J. R.; Valdevit, L.; Carter, W. B., Ultralight Metallic Microlattices. *Science* **2011**, 334, 962—965.
6. Kyrylyuk, A. V.; Hermant, M. C.; Schilling, T.; Klumperman, B.; Koning, C. E.; van der Schoot, P., Controlling Electrical Percolation in Multicomponent Carbon Nanotube Dispersions. *Nat Nano* **2011**, 6, 364—369.
7. Hu, L.; Hecht, D. S.; Gruner, G., Percolation in Transparent and Conducting Carbon Nanotube Networks. *Nano Lett.* **2004**, 4, 2513—2517.
8. Shin, M. K.; Lee, B.; Kim, S. H.; Lee, J. A.; Spinks, G. M.; Gambhir, S.; Wallace, G. G.; Kozlov, M. E.; Baughman, R. H.; Kim, S. J., Synergistic Toughening of Composite Fibres by Self-Alignment of Reduced Graphene Oxide and Carbon Nanotubes. *Nat Commun* **2012**, 3, 650.
9. Ramanathan, T.; Abdala, A. A.; Stankovich, S.; Dikin, D. A.; Herrera Alonso, M.; Piner, R. D.; Adamson, D. H.; Schniepp, H. C.; Chen, X.; Ruoff, R. S.; Nguyen, S. T.; Aksay, I. A.; Prud'Homme, R. K.; Brinson, L. C., Functionalized Graphene Sheets for Polymer Nanocomposites. *Nature Nanotech.* **2008**, 3, 327—331.
10. Zhu, J.; Shim, B. S.; Di Prima, M.; Kotov, N. A., Transparent Conductors from Carbon Nanotubes Lbl-Assembled with Polymer Dopant with Π−Π Electron Transfer. *J. Am. Chem. Soc.* **2011**, 133, 7450—7460.
11. Shim, B. S.; Zhu, J.; Jan, E.; Critchley, K.; Ho, S. S.; Podsiadlo, P.; Sun, K.; Kotov, N. A., Multiparameter Structural Optimization of Single-Walled Carbon Nanotube Composites: Toward Record Strength, Stiffness, and Toughness. *ACS Nano* **2009**, 3, 1711—1722.
12. Podsiadlo, P.; Kaushik, A. K.; Arruda, E. M.; Waas, A. M.; Shim, B. S.; Xu, J. D.; Nandivada, H.; Pumplin, B. G.; Lahann, J.; Ramamoorthy, A.; Kotov, N. A., Ultrastrong and Stiff Layered Polymer Nanocomposites. *Science* **2007**, 318, 80—83.
13. Twardowski, T. E., *Introduction to Nanocomposite Materials: Properties, Processing, Characterization*. DEStech Publications, Inc. : Lancaster, **2007**; pp 533.
14. Decher, G., Fuzzy Nanoassemblies: Toward Layered Polymeric Multicomposites. *Science* **1997**, 277, 1232—1237.

15. Putz, K. W.; Compton, O. C.; Palmeri, M. J.; Nguyen, S. T.; Brinson, L. C., High-Nanofiller-Content Graphene Oxide–Polymer Nanocomposites Via Vacuum-Assisted Self-Assembly. *Adv. Funct. Mater.* **2010**, 20, 3322—3329.
16. Walther, A.; Bjurhager, I.; Malho, J.-M.; Pere, J.; Ruokolainen, J.; Berglund, L. A.; Ikkala, O., Large-Area, Lightweight and Thick Biomimetic Composites with Superior Material Properties Via Fast, Economic, and Green Pathways. *Nano Lett.* **2010**, 10, 2742—2748.
17. Kulkarni, D. D.; Choi, I.; Singamaneni, S. S.; Tsukruk, V. V., Graphene Oxide−Polyelectrolyte Nanomembranes. *ACS Nano* **2010**, 4, 4667—4676.
18. Wu, Z. C.; Chen, Z. H.; Du, X.; Logan, J. M.; Sippel, J.; Nikolou, M.; Kamaras, K.; Reynolds, J. R.; Tanner, D. B.; Hebard, A. F.; Rinzler, A. G., Transparent, Conductive Carbon Nanotube Films. *Science* **2004**, 305, 1273—1276.
19. Podsiadlo, P.; Sui, L.; Elkasabi, Y.; Burgardt, P.; Lee, J.; Miryala, A.; Kusumaatmaja, W.; Carman, M. R.; Shtein, M.; Kieffer, J.; Lahann, J.; Kotov, N. A., Layer-by-Layer Assembled Films of Cellulose Nanowires with Antireflective Properties. *Langmuir* **2007**, 23, 7901—7906.
20. Yano, H.; Sugiyama, J.; Nakagaito, A. N.; Nogi, M.; Matsuura, T.; Hikita, M.; Handa, K., Optically Transparent Composites Reinforced with Networks of Bacterial Nanofibers. *Adv. Mater.* **2005**, 17, 153—155.
21. Capadona, J. R.; Van Den Berg, O.; Capadona, L. A.; Schroeter, M.; Rowan, S. J.; Tyler, D. J.; Weder, C., A Versatile Approach for the Processing of Polymer Nanocomposites with Self-Assembled Nanofibre Templates. *Nat. Nanotechnol.* **2007**, 2, 765—769.
22. Anseth, K. S.; Bowman, C. N.; BrannonPeppas, L., Mechanical Properties of Hydrogels and Their Experimental Determination. *Biomaterials* **1996**, 17, 1647—1657.
23. Gurav, J. L.; Jung, I. K.; Park, H. H.; Kang, E. S.; Nadargi, D. Y., Silica Aerogel: Synthesis and Applications. *J Nanomater* **2010**, 2010, 1—11.
24. Schaefer, D. W.; Keefer, K. D., Structure of Random Porous Materials: Silica Aerogel. *Phys. Rev. Lett.* **1986**, 56, 2199—2202.
25. Xu, Y. X.; Sheng, K. X.; Li, C.; Shi, G. Q., Self-Assembled Graphene Hydrogel Via a One-Step Hydrothermal Process. *ACS Nano* **2010**, 4, 4324—4330.
26. Chen, Z.; Ren, W.; Gao, L.; Liu, B.; Pei, S.; Cheng, H.-M., Three-Dimensional Flexible and Conductive Interconnected Graphene Networks Grown by Chemical Vapour Deposition. *Nature Mater.* **2011**, 10, 424-428.
27. Kim, K. H.; Vural, M.; Islam, M. F., Single-Walled Carbon Nanotube Aerogel-Based Elastic Conductors. *Adv. Mater.* **2011**, 23, 2865—2869.
28. Bryning, M. B.; Milkie, D. E.; Islam, M. F.; Hough, L. A.; Kikkawa, J. M.; Yodh, A. G., Carbon Nanotube Aerogels. *Adv. Mater.* **2007**, 19, 661—664.
29. Klemm, D.; Kramer, F.; Moritz, S.; Lindström, T.; Ankerfors, M.; Gray, D.; Dorris, A., Nanocelluloses: A New Family of Nature-Based Materials. *Angew. Chem.* **2011**, 50, 5438—5466.
30. Nakayama, A.; Kakugo, A.; Gong, J. P.; Osada, Y.; Takai, M.; Erata, T.; Kawano, S., High Mechanical Strength Double-Network Hydrogel with Bacterial Cellulose. *Adv. Funct. Mater.* **2004**, 14, 1124—1128.

31. Hough, L. A.; Islam, M. F.; Hammouda, B.; Yodh, A. G.; Heiney, P. A., Structure of Semidilute Single-Wall Carbon Nanotube Suspensions and Gels. *Nano Lett.* **2006**, 6, 313—317.
32. Cai, J.; Liu, S.; Feng, J.; Kimura, S.; Wada, M.; Kuga, S.; Zhang, L., Cellulose–Silica Nanocomposite Aerogels by in Situ Formation of Silica in Cellulose Gel. *Angew. Chem.* **2012**, 51, 2076—2079.
33. Chang, C.; Zhang, L., Cellulose-Based Hydrogels: Present Status and Application Prospects. *Carbohydr. Polym.* **2011**, 84, 40—53.
34. Yang, M.; Cao, K.; Sui, L.; Qi, Y.; Zhu, J.; Waas, A.; Arruda, E. M.; Kieffer, J.; Thouless, M. D.; Kotov, N. A., Dispersions of Aramid Nanofibers: A New Nanoscale Building Block. *ACS Nano* **2011**, 5, 6945—6954.
35. Vollrath, F.; Knight, D. P., Liquid Crystalline Spinning of Spider Silk. *Nature* **2001**, 410, 541—548.
36. Sawyer, L. C.; Grubb, D. T.; Meyers, G. F., *Polymer Microscopy*. Springer New York, **2008**.
37. Paakko, M.; Vapaavuori, J.; Silvennoinen, R.; Kosonen, H.; Ankerfors, M.; Lindstrom, T.; Berglund, L. A.; Ikkala, O., Long and Entangled Native Cellulose I Nanofibers Allow Flexible Aerogels and Hierarchically Porous Templates for Functionalities. *Soft Matter* **2008**, 4, 2492—2499.
38. Shen, D. Y.; Molis, S. E.; Hsu, S. L., Vibrational Spectroscopic Characterization of Rigid Rod Polymers: Iv. Crystalline Modifications of Poly(P-Phenylene Terephthalamide). *Polym. Eng. Sci.* **1983**, 23, 543—547.
39. Venkatachalapathi, Y. V.; Mierke, D. F.; Taulane, J. P.; Goodman, M., Gas-Phase Ir Spectra of Substituted Alkylamides. *Biopolymers* **1987**, 26, 763—773.
40. Ashby, M. F., *Materials Selection in Mechanical Design*. Elsevier: Maryland Heights, **2005**.
41. Kim, K. H.; Oh, Y.; Islam, M. F., Graphene Coating Makes Carbon Nanotube Aerogels Superelastic and Resistant to Fatigue. *Nat Nano* **2012**, 7, 562—566.
42. Pääkkö, M.; Ankerfors, M.; Kosonen, H.; Nykänen, A.; Ahola, S.; Österberg, M.; Ruokolainen, J.; Laine, J.; Larsson, P. T.; Ikkala, O.; Lindström, T., Enzymatic Hydrolysis Combined with Mechanical Shearing and High-Pressure Homogenization for Nanoscale Cellulose Fibrils and Strong Gels. *Biomacromolecules* **2007**, 8, 1934—1941.
43. Piggott, M. R.; Harris, B., Compression Strength of Carbon, Glass and Kevlar-49 Fibre Reinforced Polyester Resins. *J. Mater. Sci.* **1980**, 15, 2523—2538.
44. Greenwood, J. H.; Rose, P. G., Compressive Behaviour of Kevlar 49 Fibres and Composites. *J. Mater. Sci.* **1974**, 9, 1809—1814.
45. Xu, G. H.; Zhang, Q.; Zhou, W. P.; Huang, J. Q.; Wei, F., The Feasibility of Producing Mwcnt Paper and Strong Mwcnt Film from Vacnt Array. *Appl. Phys. A: Mater. Sci. Process.* **2008**, 92, 531—539.
46. Sriupayo, J.; Supaphol, P.; Blackwell, J.; Rujiravanit, R., Preparation and Characterization of A-Chitin Whisker-Reinforced Poly(Vinyl Alcohol) Nanocomposite Films with or without Heat Treatment. *Polymer* **2005**, 46, 5637—5644.

47. Roohani, M.; Habibi, Y.; Belgacem, N. M.; Ebrahim, G.; Karimi, A. N.; Dufresne, A., Cellulose Whiskers Reinforced Polyvinyl Alcohol Copolymers Nanocomposites. *Eur. Polym. J.* **2008**, 44, 2489—2498.
48. Evstrapov, A.; Esikova, N.; Antropova, T. V., Spectral Characteristics and Structure of Porous Glasses. *Optica Applicata* **2005**, 35, 753—759.
49. Krimm, S.; Liang, C. Y.; Sutherland, G. B. B. M., Infrared Spectra of High Polymers. V. Polyvinyl Alcohol. *J. Polym. Sci.* **1956**, 22, 227—247.
50. Launey, M. E.; Ritchie, R. O., On the Fracture Toughness of Advanced Materials. *Adv. Mater.* **2009**, 21, 2103—2110.
51. Ritchie, R. O., The Conflicts between Strength and Toughness. *Nat. Mater.* **2011**, 10, 817—822.
52. Dikin, D. A.; Stankovich, S.; Zimney, E. J.; Piner, R. D.; Dommett, G. H. B.; Evmenenko, G.; Nguyen, S. T.; Ruoff, R. S., Preparation and Characterization of Graphene Oxide Paper. *Nature* **2007**, 448, 457—460.
53. Bonderer, L. J.; Studart, A. R.; Gauckler, L. J., Bioinspired Design and Assembly of Platelet Reinforced Polymer Films. *Science* **2008**, 319, 1069—1073.
54. Zhu, J.; Andres, C. M.; Xu, J.; Ramamoorthy, A.; Tsotsis, T.; Kotov, N. A., Pseudonegative Thermal Expansion and the State of Water in Graphene Oxide Layered Assemblies. *ACS Nano* **2012**, 6, 8357—8365.
55. Jain, A.; Vijayan, K., Kevlar 49 Fibres: Thermal Expansion Coefficients from High Temperature X-Ray Data. *Curr. Sci.* **2000**, 78, 331—335.
56. Olsson, R. T.; Azizi Samir, M. A. S.; Salazar Alvarez, G.; BelovaL; StromV; Berglund, L. A.; IkkalaO; NoguesJ; Gedde, U. W., Making Flexible Magnetic Aerogels and Stiff Magnetic Nanopaper Using Cellulose Nanofibrils as Templates. *Nat Nano* **2010**, 5, 584—588.
57. Henderson, J. D.; Mullarky, R. H.; Ryan, D. E., Tissue Biocompatibility of Kevlar Aramid Fibers and Polymethylmethacrylate, Composites in Rabbits. *J. Biomed. Mater.* **1987**, 21, 59—64.
58. Mandal, B. B.; Grinberg, A.; Seok Gil, E.; Panilaitis, B.; Kaplan, D. L., High-Strength Silk Protein Scaffolds for Bone Repair. *Proc. Natl. Acad. Sci.* **2012**, 109, 7699—7704.
59. Yamamura, N.; Sudo, R.; Ikeda, M.; Tanishita, K., Effects of the Mechanical Properties of Collagen Gel on the in Vitro Formation of Microvessel Networks by Endothelial Cells. *Tissue Eng* **2007**, 13, 1443—1453.
60. Kojima, Y.; Usuki, A.; Kawasumi, M.; Okada, A.; Fukushima, Y.; Kurauchi, T.; Kamigaito, O., Mechanical-Properties of Nylon 6-Clay Hybrid. *J. Mater. Res.* **1993**, 8, 1185-1189.
61. Glotzer, S. C.; Solomon, M. J., Anisotropy of Building Blocks and Their Assembly into Complex Structures. *Nature Materials* **2007**, 6, 557-562.
62. Rogers, J. A.; Someya, T.; Huang, Y. G., Materials and Mechanics for Stretchable Electronics. *Science* **2010**, 327, 1603-1607.
63. Bockstaller, M. R.; Thomas, E. L., Optical Properties of Polymer-Based Photonic Nanocomposite Materials. *J Phys Chem B* **2003**, 107, 10017-10024.
64. Murugan, R.; Ramakrishna, S., Development of Nanocomposites for Bone Grafting. *Compos Sci Technol* **2005**, 65, 2385-2406.

65. Simon, P.; Gogotsi, Y., Materials for Electrochemical Capacitors. *Nat. Mater.* **2008**, 7, 845-854.
66. Futaba, D. N.; Hata, K.; Yamada, T.; Hiraoka, T.; Hayamizu, Y.; Kakudate, Y.; Tanaike, O.; Hatori, H.; Yumura, M.; Iijima, S., Shape-Engineerable and Highly Densely Packed Single-Walled Carbon Nanotubes and Their Application as Super-Capacitor Electrodes. *Nat. Mater.* **2006**, 5, 987-994.
67. Baughman, R. H.; Zakhidov, A. A.; de Heer, W. A., Carbon Nanotubes - the Route toward Applications. *Science* **2002**, 297, 787-792.
68. De Volder, M. F.; Tawfick, S. H.; Baughman, R. H.; Hart, A. J., Carbon Nanotubes: Present and Future Commercial Applications. *Science* **2013**, 339, 535-9.
69. Lundstrom, M. S., Graphene the Long and Winding Road. *Nature Mater.* **2011**, 10, 566-567.
70. Rao, C.; Sood, A.; Subrahmanyam, K.; Govindaraj, A., Graphene: The New Two-Dimensional Nanomaterial. *Angew. Chem.* **2009**, 48, 7752—7777.
71. Deville, S.; Saiz, E.; Nalla, R. K.; Tomsia, A. P., Freezing as a Path to Build Complex Composites. *Science* **2006**, 311, 515—518.
72. Erb, R. M.; Libanori, R.; Rothfuchs, N.; Studart, A. R., Composites Reinforced in Three Dimensions by Using Low Magnetic Fields. *Science* **2012**, 335, 199—204.
73. Podsiadlo, P.; Kaushik, A. K.; Arruda, E. M.; Waas, A. M.; Shim, B. S.; Xu, J.; Nandivada, H.; Pumplin, B. G.; Lahann, J.; Ramamoorthy, A.; Kotov, N. A., Ultrastrong and Stiff Layered Polymer Nanocomposites. *Science* **2007**, 318, 80—83.
74. Mallick, P. K., *Fiber-Reinforced Composites: Materials, Manufacturing, and Design*. CRC Press: Boca Raton, FL, **2008**; pp 619
75. Dzenis, Y., Materials Science - Structural Nanocomposites. *Science* **2008**, 319, 419—420.
76. Cambridge Materials Selector Database (Grantadesign.Com).
77. Chen, H.; Muller, M. B.; Gilmore, K. J.; Wallace, G. G.; Li, D., Mechanically Strong, Electrically Conductive, and Biocompatible Graphene Paper. *Adv. Mater.* **2008**, 20, 3557—3561.
78. Rafiee, M. A.; Rafiee, J.; Wang, Z.; Song, H. H.; Yu, Z. Z.; Koratkar, N., Enhanced Mechanical Properties of Nanocomposites at Low Graphene Content. *ACS Nano* **2009**, 3, 3884-3890.
79. Suhr, J.; Koratkar, N.; Keblinski, P.; Ajayan, P., Viscoelasticity in Carbon Nanotube Composites. *Nat. Mater.* **2005**, 4, 134-137.
80. Zandiatashbar, A.; Picu, C. R.; Koratkar, N., Control of Epoxy Creep Using Graphene. *Small* **2012**, 8, 1676—1682.
81. Spitalsky, Z.; Tsoukleri, G.; Tasis, D.; Krontiras, C.; Georga, S. N.; Galiotis, C., High Volume Fraction Carbon Nanotube–Epoxy Composites. *Nanotechnology* **2009**, 20, 405702.
82. Guan, Y.; Yang, S. G.; Zhang, Y. J.; Xu, J.; Han, C. C.; Kotov, N. A., Fabry-Perot Fringes and Their Application to Study the Film Growth, Chain Rearrangement, and Erosion of Hydrogen-Bonded Pvpon/Paa Films. *J. Phys. Chem. B* **2006**, 110, 13484-13490.

83. Eichhorn, S. J.; Dufresne, A.; Aranguren, M.; Marcovich, N. E.; Capadona, J. R.; Rowan, S. J.; Weder, C.; Thielemans, W.; Roman, M.; Renneckar, S.; Gindl, W.; Veigel, S.; Keckes, J.; Yano, H.; Abe, K.; Nogi, M.; Nakagaito, A. N.; Mangalam, A.; Simonsen, J.; Benight, A. S.; Bismarck, A.; Berglund, L. A.; Peijs, T., Review: Current International Research into Cellulose Nanofibres and Nanocomposites. *J. Mater. Sci.* **2010**, 45, 1—33.
84. Meyers, M. A.; Chawla, K. K.; Hosford, W. F.; MyiLibrary, *Mechanical Behavior of Materials*. Cambridge University Press: Cambridge ; New York, **2009**; pp 856.
85. Studart, A. R., Towards High-Performance Bioinspired Composites. *Adv. Mater.* **2012**, 24, 5024-5044.
86. Cao, K.; Siepermann, C. P.; Yang, M.; Waas, A. M.; Kotov, N. A.; Thouless, M. D.; Arruda, E. M., Reactive Aramid Nanostructures as High-Performance Polymeric Building Blocks for Advanced Composites. *Adv. Funct. Mater.* **2012**, DOI: 10.1002/adfm.201202466.
87. Ariga, K.; Hill, J. P.; Ji, Q., Layer-by-Layer Assembly as a Versatile Bottom-up Nanofabrication Technique for Exploratory Research and Realistic Application. *Phys. Chem. Chem. Phys.* **2007**, 9, 2319-2340.
88. Cho, J.; Char, K.; Hong, J. D.; Lee, K. B., Fabrication of Highly Ordered Multilayer Films Using a Spin Self-Assembly Method. *Adv. Mater.* **2001**, 13, 1076—1078.
89. Bao, W. Z.; Miao, F.; Chen, Z.; Zhang, H.; Jang, W. Y.; Dames, C.; Lau, C. N., Controlled Ripple Texturing of Suspended Graphene and Ultrathin Graphite Membranes. *Nature Nanotech.* **2009**, 4, 562—566.
90. Nelson, J. B.; Riley, D. P., The Thermal Expansion of Graphite from 15°C to 800°C. *Proc. Phys. Soc.* **1945**, 57, 477—486.
91. Mounet, N.; Marzari, N., First-Principles Determination of the Structural, Vibrational and Thermodynamic Properties of Diamond, Graphite, and Derivatives. *Phys. Rev. B* **2005**, 71, 205214.
92. Grigoriadis, C.; Haase, N.; Butt, H. J.; Mullen, K.; Floudas, G., Negative Thermal Expansion in Discotic Liquid Crystals of Nanographenes. *Adv. Mater.* **2010**, 22, 1403—1406.
93. Lifshitz, I., Thermal Properties of Chain and Layered Structures at Low Temperatures. *Zh. Eksp. Teor. Fiz.* **1952**, 22, 475—486.

CHAPTER V

Conclusions and Perspective

The research, presented in this work, has demonstrated layer-by-layer assembly (LBL) and its alternatives towards the fabrication of high performance multifunctional nanocomposites. Those approaches allow easy control over compositions, structures, alignments, and interfacial interactions to give targeted multifunctions. Chapter II describes a new type carbon nanotube coating combining transparency, flexibility, strength, conductivity, smoothness and environmental stability based on LBL. Chapter III describes vacuum assisted flocculation (VAF) method for fabricating strong and tough graphene composites, as well as the strong and stiff graphene oxide composites with unique negative and tunable thermal expansion. Chapter IV presents a novel aramid nanofiber (ANF) network and gelation-assisted layer-by-layer deposition (GLBL) approach towards ANF composites with high strength, toughness, transparency, minimal thermal expansion and environmental stability.

Those results are only a tip of the iceberg for future research directions. Potential development of new materials with enhanced multifunctionality can be achieved through some adjustments of procedures or materials. For example, as suggested in Chapter II, polymers with stronger electron-withdrawing functional groups can be selected to improve the doping effect thus the conductivity. High quality graphene can also be used

to replace carbon nanotube to improve the combined properties. Chapter III still limits the discussion to aqueous components. The inclusion of water-insoluble polymers by VAF can further expand the functionalities of the composites, such as the damping property, and further enhance the already impressive mechanical performance. The ANF network described in Chapter IV can be integrated with other polymers. Especially, monomers of any choice can polymerize inside the network. Other soluble polymer can be directly incorporated into the network without the polymerization step. Considering such a versatile selection of polymers, various functions and related enhancement should be observed.

Further research can also be directed to the applications of the high performance materials. The carbon nanotube coating can be applied in an electronic device, such as a touch screen or a solar cell, to evaluate the performance and compare it with other commercially available products. The strong and tough graphene or aramid composite films can be used for micro-containers, packaging materials or building blocks for MEMs. The unique hydrothermally induced negative thermal expansion can be explored for extremely sensitive humidity sensor, or highly responsive actuators. Moreover, the biocompatibility of some of these strong and tough films can be used for bio-implant device coatings for better cell attachment and long-term use.

Scalability is still challenging the LBL assembly for industrially producing multifunctional nanocomposites, despite some efforts have been exercised this work through the development of VAF and GLBL. In the future studies, spraying can be used to uniformly dispense components on the surface to effectively address the scale-up issues. The porous percolation network can also be explored during the spraying

procedure to quickly build up the coating in a short time. Other environmental factors, such as the temperature, can be used to accelerate the evaporation of solvent or even remove the rinsing step.

The nanomaterials used for nanocomposites should not only be limited to carbon nanotube, graphene, aramid nanofiber investigated in this work. Metallic nanoparticles, such as gold, silver or copper can be exploited for their high conductivity and optical properties. Their combination with polymers can make stretchable conductors for wearable electronics. Semiconductive nanoparticles can also be manipulated in the composites. Optical properties can be changed through the modulation of the band gaps by electrical field, which can be used for electrochromic glass. Other nanoparticles, such as ZnO, can be engineered to convert mechanical energy to electric energy due to its amazing piezoelectric properties. Dielectric nanoparticles, such as boron nitride nanotubes or nanosheets and cellulose nanocrystals, can be used for transparent, insulating, strong and tough materials. The design principles examined in this work can be used to successfully transfer the nanoscale properties to the macro scale performances.

The science and engineering of nanocomposite is still in its infancy. In Chapter III, I have shown that various theoretical models effective for conventional composites give poor prediction for the nanocomposites. In those materials, structures are more complicated, nanoparticles are more size-distributed, and the interfacial interactions are more difficult to quantify. However, following the general design principles with the right processing techniques, high performance nanocomposites can still be attained with fewer trials. It is nevertheless possible that, in the future, designing nanocomposites can

be as straightforward as designing chemical reactors nowadays with the development of more powerful computation tools.